Development of an Advanced 10 kHz High Harmonic Source and its Application to Angle- and Phase-Resolved Photoelectron Streaking Spectroscopy

Jürgen Schmidt

München 2016

Development of an Advanced 10 kHz High Harmonic Source and its Application to Angle- and Phase-Resolved Photoelectron Streaking Spectroscopy

Jürgen Schmidt

Dissertation
an der Fakultät für Physik
der Ludwig–Maximilians–Universität
München

vorgelegt von
Jürgen Schmidt
aus Riedlingen

München, den 17.11.2016

Erstgutachter: Prof. Dr. Ulf Kleineberg
Zweitgutachter: Prof. Dr. Wolfgang Zinth
Tag der mündlichen Prüfung: 18.01.2017

Contents

Summary **xiii**

1 Introduction **1**

2 Fundamentals **5**
2.1 Few-cycle laser pulses . . . 5
2.1.1 Material dispersion . . . 6
2.1.2 Carrier-envelope phase . . . 10
2.2 Nonlinear optics and strong field effects . . . 14
2.2.1 Optical perturbation theory . . . 14
2.2.2 High-order harmonic generation . . . 18
2.3 Photoelectron emission spectroscopy on solids . . . 26
2.3.1 Angle-resolved PES . . . 27
2.3.2 Photoelectron streaking . . . 28

3 Beamline development **33**
3.1 Laser front end and pulse shaping . . . 33
3.1.1 The 10 kHz laser system . . . 33
3.1.2 Nonlinear pulse compression by SPM . . . 35
3.2 Vacuum line and experimental end station . . . 41
3.2.1 HHG chamber . . . 41
3.2.2 Differential pumping . . . 44
3.2.3 XUV beam monitor . . . 48
3.2.4 ARPES chamber . . . 49
3.2.5 XUV spectrometer . . . 52
3.2.6 Electron spectrometer . . . 58
3.2.7 Sample preparation and handling . . . 72
3.2.8 Carrier-envelope phase tagging and data mapping . . . 73

4 Few-cycle driven HHG at 10 kHz and its polarization control via multilayer optics **77**
4.1 Few-cycle driven HHG at 10 kHz . . . 77
4.2 Generation of circularly polarized HH radiation . . . 88

4.2.1 Wave-plate design and fabrication process 89
4.2.2 Transmission and phase shift characteristics 91
4.2.3 Dispersion behavior 99

5 Time-, angle- and CEP-resolved PES 101
5.1 Calibration and performance of the electron spectrometer 101
5.2 High harmonic (AR)PES on W(110) 104
5.2.1 Surface contamination 106
5.2.2 Space charge distortion 107
5.3 Angle- and CEP-resolved photoelectron streaking 110
5.3.1 CEP-related evaluation 110
5.3.2 Angle-related evaluation 118
5.3.3 Wave-packet reconstruction, relative time delays and wave-packet spread 118
5.3.4 Prospects for band structure resolved streaking 123

6 Conclusion and outlook 127

A Technical aspects of device synchronization for CEP-tagging 131

B Time of flight filtering 133

C Beam alignment concept 137

Acknowledgments 152

List of Figures

2.1 Dispersion . . . 9
2.2 Frequency comb. . . . 11
2.3 Stereographic single-shot ATI phase-meter. . . . 13
2.4 Simulation of SPM-induced spectral broadening of a femtosecond pulse . . 18
2.5 HHG three step model - Principle. . . . 19
2.6 HHG three step model - Classical calculation. . . . 22
2.7 Photoelectron streaking - Principle . . . 31

3.1 Layout of the 10 kHz few-cycle laser front end. . . . 34
3.2 Mode transmission and coupling efficiency of a hollow core fiber. . . . 38
3.3 SPM-induced spectral broadening of amplified NIR pulses in neon. . . . 39
3.4 SPM-induced spectral broadening of amplified NIR pulses in argon. . . . 40
3.5 Spectral reflectivity and dispersion characteristics of the optical mirror compressor. . . . 41
3.6 Vacuum back end of the beamline. . . . 42
3.7 Vibration isolation scheme of the HHG chamber . . . 43
3.8 Differential pumping - Simulation model . . . 44
3.9 Differential pumping - Simulation and setup. . . . 47
3.10 XUV beam monitor . . . 48
3.11 Spatio-temporal alignment of the delay unit. . . . 50
3.12 Sketch of the ARPES experimental chamber . . . 51
3.13 XUV spectrometer. . . . 52
3.14 Spherical imaging grating - Nomenclature and Rowland circle geometry. . . 53
3.15 Characteristics of the spherical varied line-space grating. . . . 57
3.16 The Themis 1000 angle-resolving spectrometer . . . 58
3.17 Themis 1000 - Alignment of the excitation spot and definition of the optical axis. . . . 60
3.18 MCP delay-line detector - Principle. . . . 62
3.19 MCP delay-line detector - Time calibration. . . . 64
3.20 Themis 1000 - Data conversion and energy resolution. . . . 65
3.21 MCP delay-line detector - Time response and time-offset correction. . . . 67
3.22 Magnetic field compensation - Coil field distribution . . . 70
3.23 Magnetic field compensation - Estimation of residual stray fields. . . . 71

3.24 Electron bombardment heater. 72
3.25 CEP tagging - Setup. 73
3.26 CEP tagging - Data synchronization. 74

4.1 HHG - NIR pulse properties of sub-6 fs pulses as used for HHG. 78
4.2 HHG from neon - Pressure dependence, phase-matching and cutoff, focal length: 40 cm. 79
4.3 HHG - NIR pulse properties of sub-10 fs pulses as used for HHG. 79
4.4 HHG from neon - Pressure dependence, phase-matching and cutoff, focal length: 30 cm. 80
4.5 HHG from argon - Pressure dependence, phase-matching and cutoff, focal length: 30 cm. 81
4.6 HHG - Detailed pressure dependence for neon and argon at 66 eV. 82
4.7 HHG - Chirped driver pulses. 83
4.8 HHG - Different axial nozzle positions: phase-matching and cutoff. 85
4.9 HHG - Different axial nozzle positions: beam profile and yield. 86
4.10 HHG - Temporal output stability. 87
4.11 XUV quarter wave-plate - Design and spectral behavior. 89
4.12 XUV quarter wave-plate - Spectral ellipticity and polarization orientation. 90
4.13 XUV quarter wave-plate - Transmission measurement. 92
4.14 XUV polarimetry - Setup. 93
4.15 XUV polarimetry - Spectral behavior of the analyzer mirror. 94
4.16 XUV polarimetry - Influence of pre-filtering. 96
4.17 XUV polarimetry - Results. 97
4.18 XUV polarimetry - True versus estimated maximum ellipticity. 99
4.19 XUV polarimetry - Data selection process. 100

5.1 Themis 1000 - Image quality for high and low retardation ratios. 102
5.2 Themis 1000 - Experimental characterization of the resolving power. 103
5.3 HHG PES - NIR pulse parameters and HHG spectrum. 104
5.4 HHG PES - Principal spectrum from W(110). 105
5.5 HHG PES - Influence of surface contamination. 106
5.6 HHG PES - Influence of space charge. 108
5.7 Streaking - Influence of NIR field induced space charge. 109
5.8 HHG PES - CEP resolved. 111
5.9 CEP-resolved streaking - Exemplary spectrograms for selected CEP ranges. 112
5.10 CEP-resolved streaking - Absolute gauge calibration of the phase-meter. . 113
5.11 CEP-resolved streaking - Illustration of the XUV-NIR phase-locking mechanism. 115
5.12 CEP-resolved streaking - Experimental observation of the XUV-NIR phase-locking. 116
5.13 CEP-resolved streaking - Variation of the initial kinetic energy of the photoelectrons. 118

5.14 Angle-resolved streaking - Variation of the streaking amplitude. 119
5.15 Complete electron wave packet and vector potential reconstruction of the angle-integrated streaking trace for a cosine-pulse. 120
5.16 Angle-resolved wave packet spread and emission delay for a cosine-pulse. . 121
5.17 HHG XUV broadband Fermi surface imaging. 123
5.18 Concepts for improving energy resolution. 124
5.19 Transformation of the spectrogram for long XUV pulses. 126

A.1 CEP tagging - Effect of erroneous data assignment. 131
A.2 Trigger pulse behavior of the CFD and TDC. 132

B.1 Concept of ToF filtering. 134
B.2 MCP gain degradation without ToF filtering. 135

C.1 Beam alignment concept. 138

List of Tables

2.1 Time-bandwidth product. 8

3.1 Reflectivity parameters of the mirrors for the beam monitor. 48
3.2 Lens modes of the Themis 1000. 59

4.1 Summary of the results of the polarimetry measurement. 98

5.1 Summary of resolution values of the electron spectrometer. 103

Zusammenfassung

Der Fortschritt in der Ultrakurzzeitspektroskopie zur Untersuchung der Elektronendynamik in Materie ist während des letzten Jahrzehnts entscheidend durch zwei Entwicklungen vorangetrieben worden: die Verbesserung optischer Kompressionstechniken zur Erzeugung von ultrakurzen Laserpulsen, die nur wenige elektrische Feldschwingungen enthalten (few-cycle Pulse) und die Generierung von Attosekunden-Pulsen mittels höherer harmonischer Erzeugung sowie die Entwicklung zugehöriger Mess- und Spektroskopieverfahren. Die Phase der Feldschwingung bezüglich der Einhüllenden bestimmt maßgeblich die Wechselwirkung eines few-cycle Pulses mit einem elektronischen System. Durch gezielte Kontrolle dieser Phase lassen sich elektronische Prozesse auf einer Zeitskala kürzer als eine Feldschwingungsperiode steuern. Die Dynamik des Prozesses wird mittels einer Anrege-Abtast Messung unter Verwendung von Attosekundenpulsen mit höchster Zeitauflösung abgetastet. Die zur höheren harmonischen Erzeugung benötigten Treiberpulse stammen konventionell aus Titan-Saphir basierten Multipass Laserverstärkern, die gewöhnlich Pulsenergien von wenigen mJ bei einer Repetitionsrate von 1-3 kHz liefern. Speziell bei Photoemissions-Experimenten sind jedoch höhere Repetitionsraten förderlich, da die anwendbare Strahlungsintensität durch Raumladungseffekte begrenzt ist, und die Messstatistik bzw. die Aufnahmezeit damit direkt von der Repetitionsrate abhängen. In dieser Arbeit wird eine komplette Attosekunden-Messinfrastruktur für zeit-, winkel- und phasenaufgelöste Photoemission-Messungen mit erhöhter Repetitionsrate von 10 kHz entwickelt, aufgebaut und charakterisiert. Zudem wird eine Methode implementiert, die es ermöglicht zirkularpolarisierte höhere harmonische Strahlung zu erzeugen. Dies stellt seit den Anfängen der höheren harmonischen Erzeugung eine generelle Schwierigkeit dar. In dieser Arbeit wird hierfür eine auf Multischicht-Technologie basierende Wellenplatte für den extremen UV Bereich entwickelt sowie ihre Tranmissions- und Phasencharakteristik (Polarisationszustand) vermessen. Die Verfügbarkeit zirkularpolarisierter harmonischer Strahlung erweitert deutlich das Spektrum anwendbarer Messmethoden in der Attosekundenspektroskopie.
Eines der Hauptmessverfahren in der Attosekundenspektrospie ist das Photoelektronen-Streaking. Dieses hat sich mittlerweile als nützliches Werkzeug bei der Untersuchung von Elektronendynamiken in Festkörpern etabliert. Als prominenteste Beispiele sind hierfür die Messung relativer Zeitverzögerungen bei der Photoemission sowie die direkte Beobachtung der zeitlichen Entwicklung des Wellenpakets eines Photoelektrons während seines Transports im Festkörper auf der Attosekunden-Zeitskala zu nennen. Als weiterer Teil dieser Arbeit wurde ein erweitertes Streaking-Messverfahren konzipiert und umgesetzt, das zusätzlich zur herkömmlichen Methode die Phase des beteiligten few-cycle Pulses sowie den Emissionswinkel der Photoelektronen auflöst. Damit werden nun zwei wichtige Parameter mitberücksichtigt, die wesentliche Information über die probenspezifische Bandstruktur und die Verteilung des Streaking-Feldes, das gleichzeitig als Anregepuls dienen kann, enthalten. Die Verwendung eines winkelabbildenden Flugzeitspektrometers in Kombination mit einer Phasen-Tagging Methode erlaubt schließlich die simultane Aufzeichnung aller Parameter ohne Datenverlust. Erste Messungen mit der erweiterten Streaking-Methode wurden an einer Wolfram-Probe durchgeführt.

PUBLICATION LIST

Parts of this work have been published in the following articles.

Journals

1. J. Schmidt, S.H. Chew, A. Gliserin, A. Guggenmos, J. Zou and U. Kleineberg. *Carrier-Envelope phase tagged and angle-resolved photoelectron streaking.* In preparation, to be submitted in Applied Physics Letters.

2. J. Schmidt, A. Guggenmos, S.H. Chew, A. Gliserin, M. Hoegner, J. Zou, C. Spaeth and U. Kleineberg. *Development of a 10 kHz High Harmonic Source up to 140 eV Photon Energy for Ultrafast Time-, Angle- and Phase-Resolved Photoelectron Emission Spectroscopy on Solid Targets.* Submitted to Rev. Sci. Instr.

3. S.H. Chew, A. Gliserin, J. Schmidt, H. Bian, S. Nobis, F. Schertz, M. Kübel, Y.Y. Yang, B. Loitsch, T. Stettner, J.J. Finley, C. Späth, H. Ouacha, A.M. Azzeer and U. Kleineberg, *Applied Physics B* **122** (2016), 102.

4. J. Schmidt, A. Guggenmos, M. Hofstetter, S.H. Chew and U. Kleineberg, *Opt. Express* **23** (2015), 33564.

5. M. Kübel, A.S. Alnaser, B. Bergues, T. Pischke, J. Schmidt, Y. Deng, C. Jendrzejewski, J. Ullrich, G.G. Paulus, A.M. Azzeer, U. Kleineberg, R. Moshammer and M.F. Kling, *New Journal of Physics* **16** (2014), 065017.

6. A.S. Alnaser, M. Kübel, R. Siemering, B. Bergues, N.G. Kling, K.J. Betsch, Y. Deng, J. Schmidt, Z.A. Alahmed, A.M. Azzeer, J. Ullrich, I. Ben-Itzhak, R. Moshammer, U. Kleineberg, F. Krausz, R. de Vivie-Riedle and M.F. Kling, *Nature Communications* **5** (2014), 3800.

7. M. Kübel, K.J. Betsch, N.G. Kling, A.S. Alnaser, J. Schmidt, U. Kleineberg, Y. Deng, I. Ben-Itzhak, G.G. Paulus, T. Pfeifer, J. Ullrich, R. Moshammer, M.F. Kling and B. Bergues, *New Journal of Physics* **16** (2014), 033008.

8. A. Guggenmos, R. Rauhut, M. Hofstetter, S. Hertrich, B. Nickel, J. Schmidt, E.M. Gullikson, M. Seibald, W. Schnick and U. Kleineberg, *Opt. Express* **21** (2013), 21728.

9. S.H. Chew, F. Süßmann, C. Späth, A. Wirth, J. Schmidt, S. Zherebtsov, A. Guggenmos, A. Oelsner, N. Weber, J. Kapaldo, A. Gliserin, M.I. Stockman, M.F. Kling and U. Kleineberg, *Applied Physics Letters* **100** (2012), 051904.

Proceedings

1. J. Schmidt, A. Guggenmos, S.H. Chew, A. Gliserin and U. Kleineberg: *Carrier-Envelope-Phase- and Angle-resolved Photoelectron Streaking Measurements on W(110)*, In *Conference on Lasers and Electro-Optics*. The Optical Society (2016).

2. K. Pearce, R. Dehde, A. Spreen, C. Späth, M. Wendl, J. Schmidt and U. Kleineberg: *Modulation of extraordinary optical transmission through nanohole arrays using ultrashort laser pulses*, In *Nanophotonics VI*, edited by D. L. Andrews, J.-M. Nunzi and A. Ostendorf. SPIE-Intl Soc Optical Eng (2016).

3. A. Guggenmos, J. Schmidt, S. Heinrich, B. Nickel, F. Krausz and U. Kleineberg: *Multilayer Mirrors for VUV-XUV Attosecond Pump-Probe Experiments*, In *Frontiers in Optics 2015*. The Optical Society (2015).

4. A. Guggenmos, M. Hofstetter, R. Rauhut, C. Späth, S. Hertrich, B. Nickel, S. Yang, E.M. Gullikson, J. Schmidt, M. Seibald, W. Schnick, F. Krausz and U. Kleineberg: *Broadband multilayer mirror and diffractive optics for attosecond pulse shaping in the 280-500 eV photon energy range*, In *XVIIIth International Conference on Ultrafast Phenomena*, edited by M. Chergui, A. Taylor, S. Cundiff, R. de Vivie-Riedle and K. Yamagouchi, Volume 41. EDP Sciences (2013) Page 01011.

5. S.H. Chew, K. Pearce, S. Nobis, C. Späth, A. Spreen, S. Radünz, Y. Yang, J. Schmidt and U. Kleineberg: *Spatiotemporal characterization and control of lightfield nanolocalization on metallic nanostructures by nonlinear-PEEM*, In *Plasmonics: Metallic Nanostructures and Their Optical Properties X*, edited by M. I. Stockman. SPIE-Intl Soc Optical Eng (2012).

Book chapters

1. S.H. Chew, K. Pearce, C. Späth, A. Guggenmos, J. Schmidt, F. Süßmann, M.F. Kling, U. Kleineberg, E. Mårsell, C.L. Arnold, E. Lorek, P. Rudawski, C. Guo, M. Miranda, F. Ardana, J. Mauritsson, A. L'Huillier and A. Mikkelsen: *Imaging Localized Surface Plasmons by Femtosecond to Attosecond Time-Resolved Photoelectron Emission Microscopy - "ATTO-PEEM"*. Wiley-Blackwell, 2015.

Chapter 1

Introduction

High harmonic generation (HHG) has enabled the development of coherent and broadband radiation sources, spectrally ranging from the extreme ultra-violet (XUV) up to the soft x-ray region, at a table top size. Furthermore, it forms the basis for the creation of the shortest laser pulses to date [43,158] with durations in the order of the orbit-time of bound electrons (attoseconds), thus allowing the real-time observation and control of atomic-scale electron dynamics [44, 68]. Due to these outstanding characteristics, it has already found numerous applications in ultrafast time-resolved XUV spectroscopy [130, 138, 151], microscopy [150], interferometry [81,160] and diffraction experiments [133,162]. The advance of new high harmonic sources and related measurement techniques is closely linked to laser development on the one hand and to the development of advanced XUV optics on the other hand. Especially the precise shaping of the pulse structure and its dispersion/phase control are of utmost relevance in this context. The refinement of pulse compression techniques eventually lead to the generation of few-cycle laser pulses, merely comprising few field oscillations, which turned out to be beneficial for the HHG process initiated from gas targets [29]. Owing to their steep rise in intensity these pulses promote the creation of harmonics near the spectral cutoff due to low fractional ionization levels within the field cycles before the highest field amplitude is reached. The successful application of few-cycle pulses is mainly attributed to the development of techniques which allow the control of their carrier-envelope phase (CEP) either by means of its stabilization [52, 69, 89, 117] or its single-shot measurement [22, 59, 105, 116, 122, 152] for CEP tracking. The exact control of the sub-cycle field evolution by the CEP entails the ability for steering electron motion on a sub-fs time scale, which has been demonstrated for instance in multi-photon ionization [77], charge migration in molecules [3] or plasmonic excitation [76].

In the context of HHG, CEP-controlled few cycle pulses form a natural gate for the highest harmonics by confining their generation to the field cycle with the highest field strength, thereby producing a spectral continuum at the harmonic cutoff from which, with the appropriate optics, almost any arbitrary spectral content regarding central photon energy, bandwidth and chirp [46–48, 55] can be extracted. In this way it is possible to create isolated attosecond pulses which are inherently synchronized to the driving laser pulse.

When applied to a pump-probe setup, these pulses can be used to track electron dynamics with unprecedented time resolution. One prominent application in this respect is the photoelectron streaking technique [44,54,65,73], in which a photo-emitted electron, ionized by an attosecond XUV pulse, is subsequently streaked in the electric field of the laser pulse. Upon varying the relative delay between these two pulses, characteristic modulations in the kinetic energy spectra of the photo-electrons are observed which contain information about the electron wave packet and the laser field. Originally conceived for attosecnd metrology, this technique has finally proved to be as well successful in measuring relative time delays in the photoemission process [19, 96, 97, 131] and the evolution of electron wave packets during their photo-induced transport in solids [100] on an attosecond time scale. The first measurement of photoemission time delays on solids was performed by Cavaleri *et al.* in 2007 [19] and refined by Neppl *et al.* in 2012 [96], which triggered an intense discussion about the involved mechanisms, especially the role of band structure dispersion, electron (de-)localization of initial states and laser field screening effects. All these factors have been theoretically predicted to considerably affect the photoemission process in solids, e.g. the evolution of a photo-ionized electron wave packet during its transport to the sample surface on a sub-femtosecond time scale [62, 72, 82, 156, 157]. Although simple ballistic transport models have been successfully applied to fit experimental data of non-resonant photoelectron excitations [96,97], there's also experimental indication that this model may break down for resonant excitations [140]. In this case the band structure of the solid plays a significant role [140]. Furthermore, the screening of the electric field inside the metal has been only accounted for so far by a parameter for the screening depth, simply serving as an additional fit parameter in order to match the anticipated transport model to the experimental data [97]. The highly nonlinear nature of the exponentially decaying screening field together with its transient character, however, may suggest an additional dependency of the photoelectron transport processes in solids on the CEP. The latter assumption is further supported by the experimental observation of a CEP sensitivity in the nonlinear multi-photon ionization process from metal tips [75,76,108]. Additionally, the penetrating evanescent laser field may perturb the band structure as a function of its CEP, at least within the first few surface layers, which may further influence electron excitation, transport and emission. Access to the band structure is obtained by recording the photoelectrons angle-resolved (ARPES). Photoelectron streaking measurements which systematically include band structure and CEP effects have not been experimentally conducted so far, since the conventional measurement scheme employs phase-stabilized laser pulses with a defined and fixed CEP value and records an angle-integrated photoemission signal within a narrow emission cone. Therefore, the first objective of this thesis is to conceive the concept of an extended photoelectron streaking scheme which additionally incorporates angle- and CEP resolution and to demonstrate the feasibility of such an experiment by means of a proof-of-principle measurement on a tungsten surface. Compared to the conventional time-resolved ARPES technique, angle-resolved streaking measurements not only yields the rate of a dynamic electron process but the complete evolution of the electron wave packet over time. We believe that this type of measurement scheme will be able to provide a more complete understanding of the delay mechanisms in the photoemission process and a deeper insight

into the atomic-scale electron dynamics in solids in general. While conventional photoelectron streaking typically applies a spectrally broadband excitation bandwidth of several electron volt in order to generate wave packets of only tens to hundreds of attoseconds in duration, a trade-off between time- and energy resolution has to be made when the band structure of a solid is to be reasonably resolved. This trade-off certainly depends on the specific dispersion relation behavior of the sample under investigation.

Another objective of this thesis was the design, the construction and the characterization of a corresponding HHG beam-line which is applicable for conducting the CEP- and angle-resolved streaking measurements as discussed above. The entire beam-line has been basically set up from scratch, including the implementation of the setups for pulse shaping and characterization, diagnostics, the vacuum-line and the experimental end station together with the measurement concept. Generally, important parameters in the design of a HHG source are the high harmonic flux, its cutoff energy and the repetition rate. For photoemission experiments, performed with femtosecond or even sub-femtosecond pulses, the applicable radiation intensity, however, is limited by space charge distortions [104, 107]. Therefore, the data acquisition rate is ultimately linked to the repetition rate, making the latter the primary key parameter in order to avoid disproportionately long acquisition times. This is of particular importance when a multi-dimensional dataset, as it is obtained in this work, has to be populated by photoemission events. On the other hand, it is desirable to reach a sufficiently high cutoff energy which ensures spectroscopic access to electronic states of different binding levels. In our design we follow the most common way of generating high harmonic radiation by means of the nonlinear interaction of intense, ultrashort laser pulses with a noble gas target in the free gas jet configuration. This typically requires intensities in the 10^{14}–10^{15} W/cm^2 range. At the beginning of this work, predominantly ultrashort near-infrared laser pulses from Ti:Sapphire based multi-pass amplifiers with repetition rates of 1–3 kHz have been employed for this purpose [18,35,40,91]. Relying on this proven technology, a prototype of a commercial 10 kHz multi-pass amplifier system has been set up as laser front end for the new beam-line. Although the increased repetition rate comes at the expense of a reduced output power and reduced stability, the resultant high harmonic output is shown to reach photon energies well beyond 100 eV with feasible flux for photoemission spectroscopy. Its viability is further confirmed by the successful realization of angle- and CEP-resolved photoelectron streaking measurements. Meanwhile, ongoing effort has been put into the development of high harmonic sources which boost the repetition rate to multi-hundred kHz [51, 74, 118] or even MHz [17, 26, 114] by means of alternative amplifier technologies or intra-cavity HHG designs. However, up to now this tremendous increase of the repetition rate often comes along with a (greatly) reduced cutoff energy or harmonic yield. And although harmonic output has been demonstrated from these sources, many of them still lack proof of their applicability to real experiments. Also, pulse compression down to the few-cycle regime for CEP sensitive measurements has not yet been demonstrated with MHz rate harmonic sources. Nevertheless, the 10 kHz HHG beam-line, developed in the course of this thesis, is considered as an intermediate step in the fast-advancing process of high repetition rate HHG source developments. Fur-

thermore, in order to facilitate CEP-sensitive studies, the laser source is not actively phase stabilized, but the CEP is tracked shot-by-shot by an appropriate phase-meter [122] which is synchronized to the electron spectrometer used for photoemission spectroscopy.

The last issue which is addressed in this thesis is the generation of circularly polarized high harmonic radiation. This task has been representing a major difficulty since the advent of HHG. The nature of the HHG process only allows linearly polarized harmonic radiation to be efficiently generated from an isotropic gas target with a single driving laser beam [7, 15, 16]. For this reason, the majority of HHG sources are designed for linearly polarized high harmonic radiation and, consequently, their application is restricted to (spectroscopic) techniques which also rely on linear polarization. On the other hand, the availability of circularly polarized high harmonic radiation greatly extends the spectroscopic possibilities and the range of material classes that can be investigated by ultrafast HHG spectroscopy. The great potential of circularly polarized XUV radiation has been extensively demonstrated using large-scale synchrotron sources, for instance by means of spin-resolved photoemission on topological insulators [103,148] or circular dichroism techniques in absorption [11, 132], reflection or in photoemission [13, 88, 129] applied to magnetic and chiral samples. The pulse duration of these sources, and hence the time resolution in pump-probe experiments, however, is still limited to ∼100 fs [56]. So far, only few concepts for the generation of circularly polarized high harmonic radiation have been suggested [6,64,146,161]. These are, however, either relatively inefficient or experimentally quite complex. Using our in-house multilayer fabrication capabilities we have implemented a multilayer based XUV phase retarder in transmission [128]. Although the concept was already proposed two decades ago [71], it has never been fabricated for and applied to high harmonic radiation. Here we have designed, fabricated and characterized a XUV quarter wave plate as an ultra thin free-standing multilayer foil for harmonic radiation at 66 eV for an exemplary XMCD application at the Ni M-edge [80].

The structure of this thesis is organized as follows: After a brief summary of the theoretical fundamentals of few-cycle pulses, HHG and the principle of attosecond streaking spectroscopy, the development of the 10 kHz HHG beam-line is presented in chapter 2. The characterization of the high harmonic output as well as its polarization control via transmissive multilayer optics and the determination of the polarization states by means of XUV polarimetry are summarized in chapter 3. The results obtained by the angle- and CEP resolved photoelectron streaking scheme are given in chapter 4. Finally, an outlook concludes this work.

Chapter 2

Fundamentals

2.1 Few-cycle laser pulses

The development of mode-locking techniques in laser resonators and the continuous refinement of laser pulse compression techniques has lead to the generation of ultrashort laser pulses in the femtosecond range and finally to few-cycle pulses whose duration is limited to only a few electric field oscillations. Owing to their large spectral bandwidth, the frequency response of light-matter interactions such as the field induced polarization of dielectric media cannot be considered constant any more. This characteristic is commonly referred to as dispersion. As a consequence, the pulse experiences a reshaping of its (temporal) structure while passing through dispersive media. For the following discussion, light is described in the classical way as electromagnetic wave and represented by the electric field vector. The complex notation is used and the complex conjugate part is omitted for simplicity. In this way, an ultrashort laser pulse is described as [1] [14]

$$\mathbf{E}(\mathbf{r},t) = \mathbf{A}(\mathbf{r},t)e^{i\phi(\mathbf{r},t)} \tag{2.1}$$

with $\phi(\mathbf{r},t)$ being the phase and $\mathbf{A}(\mathbf{r},t)$ a (bell-shaped) envelope function. The general form of the phase term can be approximated by Taylor-expanding it according to

$$\phi(t) = \sum_{j=0}^{\infty} D_j(t_0)(t-t_0)^j \tag{2.2}$$

with the derivatives

$$D_j = \frac{1}{j!}\left.\frac{\partial^j \phi}{\partial t^j}\right|_{t_0} \tag{2.3}$$

The zero-order term $D_0 = \Phi_{\mathrm{CEP}}$ is called carrier-envelope phase (CEP) and represents the offset between the envelope and the underlying fast oscillation of the electric field. The CEP plays a major role for few-cycles pulses and is further discussed in the next section.

[1] Vector quantities are denoted in bold letters

The first-order phase coefficient $D_1 = \omega_0$ is the carrier frequency and the higher-order terms D_j with $j > 1$ are referred to as temporal chirp factors of order $(j-1)$. Chirp results in a time-dependent frequency of the field oscillations in which the instantaneous frequency is obtained as

$$\omega(t) = \frac{d}{dt}\phi(t). \tag{2.4}$$

According to the sign of the linear chirp factor, the pulse is said to be positively chirped if $D_2 > 0$ and negatively chirped if $D_2 < 0$.

2.1.1 Material dispersion

In order to describe the frequency-dependent response of dispersive media to the laser field it is convenient to describe the problem in the Fourier domain. In this domain the solution of the one-dimensional (plane-wave and propagation direction along the z-axis) homogeneous Helmholtz wave equation [2]

$$\left[\frac{\partial^2}{\partial z^2} + \frac{\omega^2 \epsilon(\omega)}{c_0^2}\right] \hat{E}(\omega) = 0 \tag{2.5}$$

is given by

$$\hat{E}(z,\omega) = \hat{E}_0(\omega) \mathrm{e}^{-ik(\omega)z} \tag{2.6}$$

where $\hat{E}(z=0,\omega) = \hat{E}_0(\omega)$, and the wave vector is given by

$$k(\omega) = \frac{\omega}{c_0}\sqrt{\epsilon(\omega)} = \frac{\omega}{c_0} n(\omega) \tag{2.7}$$

with $n(\omega)$ being the linear index of refraction describing the material response. The general frequency-dependent behavior of the wave vector can be again approximated by a Taylor series

$$k(\omega) = \sum_{j=0}^{\infty} K_j (\omega - \omega_0)^j \tag{2.8}$$

with

$$K_j = \frac{1}{j!} \left.\frac{\partial^j k(\omega)}{\partial \omega^j}\right|_{\omega_0}. \tag{2.9}$$

[2] Quantities labeled by a top hat are Fourier-transformed

Using equation 2.7, the first four terms explicitly read

$$K_0 = k_0 = \frac{\omega_0}{c_0} n(\omega_0) \tag{2.10}$$

$$K_1 = \left.\frac{\partial k(\omega)}{\partial \omega}\right|_{\omega_0} = \frac{n(\omega_0)}{c_0} + \left.\frac{\omega_0}{c_0}\frac{\partial n(\omega)}{\partial \omega}\right|_{\omega_0} \tag{2.11}$$

$$K_2 = \left.\frac{1}{2}\frac{\partial^2 k(\omega)}{\partial \omega^2}\right|_{\omega_0} = \left.\frac{1}{c_0}\frac{\partial n(\omega)}{\partial \omega}\right|_{\omega_0} + \left.\frac{\omega_0}{2c_0}\frac{\partial^2 n(\omega)}{\partial \omega^2}\right|_{\omega_0} \tag{2.12}$$

$$K_3 = \left.\frac{1}{6}\frac{\partial^2 k(\omega)}{\partial \omega^2}\right|_{\omega_0} = \left.\frac{1}{2c_0}\frac{\partial^2 n(\omega)}{\partial\, \omega^2}\right|_{\omega_0} + \left.\frac{\omega_0}{6c_0}\frac{\partial^3 n(\omega)}{\partial \omega^3}\right|_{\omega_0}. \tag{2.13}$$

The zeroth-order term constitutes the inverse of the phase velocity

$$v_{\mathrm{ph}} = \frac{1}{K_0} = \frac{\omega_0}{k_0} = \frac{c_0}{n(\omega_0)} \tag{2.14}$$

which measures the propagation speed of the carrier frequency component of the pulse, while the propagation speed of the pulse envelope is given by the inverse of the first-order term, denoted as group velocity

$$v_{\mathrm{gr}} = \frac{1}{K_1} = \left.\frac{\partial \omega(k)}{\partial k}\right|_{k_0}. \tag{2.15}$$

The second-order dispersion term $\frac{\partial^2 k(\omega)}{\partial \omega^2} = 2K_2$ is called group velocity dispersion (GVD), indicating that the group velocity itself is frequency-dependent. The next higher-order terms ($j!K_j$, $j > 2$) are simply denoted as third-order dispersion (TOD), fourth-order dispersion (FOD) etc. Dispersion terms of second-order and higher generally introduce chirps and cause a broadening and reshaping of the pulse envelope. This is exemplary shown for the presence of GVD and a Gaussian parametrization of the pulse envelope

$$E(z=0,t) = E_0\ \mathrm{e}^{-\left(\frac{t^2}{\tau^2}\right)}\ \mathrm{e}^{-i\omega_0 t} \tag{2.16}$$

where τ is a measure for the pulse duration. Substituting its Fourier transform

$$\hat{E}(0,\omega) \propto E_0\ \mathrm{e}^{\frac{1}{4}\tau^2(\omega-\omega_0)^2} \tag{2.17}$$

and the phase terms 2.10-2.12 into equation 2.6 leads to the Fourier integral ($\Gamma = K_2$)

$$E(z,t) \propto \int \mathrm{e}^{-\left(\frac{1}{4}\tau^2 + i\Gamma z\right)\Omega^2} \mathrm{e}^{i\Omega(t-K_1 z)}\, \mathrm{d}\Omega \tag{2.18}$$

for the back transformation into the time domain. Here, $\Omega = (\omega - \omega_0)$ has been used. The solution of the integral is tabulated [1] and reads

$$E(z,t) \propto E_0 \exp\left[-\frac{(t-K_1 z)^2}{\tau^2 + \left(\frac{4\Gamma z}{\tau}\right)^2}\right] \exp\left[i\frac{(t-K_1 z)^2 4\Gamma z}{\tau^4 + (4\Gamma z)^2} + i\omega_0\left(t - \frac{k_0}{\omega_0} z\right)\right]. \tag{2.19}$$

Shape	Formula	P
Gaussian	$e^{-\frac{t^2}{2\tau^2}}$	0.441
Hyperbolic secant	$\frac{1}{\cosh(t/\tau)}$	0.315
Exponential	$e^{-\frac{t}{2\tau}}$	0.140
Lorentzian	$\frac{1}{1+(t/\tau)^2}$	0.142

Table 2.1: Values of the time-bandwidth product for different pulse shapes.

The first exponential term is real-valued and describes the new shape of the envelope. It has been broadened to the new width of

$$\tau_2(z) = \sqrt{\tau^2 + \left(\frac{4\Gamma z}{\tau}\right)^2}. \tag{2.20}$$

Moreover, the phase of the pulse now contains an additional term which is quadratic in time, constituting a linear chirp η of

$$\eta(z) = \frac{4\Gamma z}{\tau^4 + (4\Gamma z)^2}. \tag{2.21}$$

Both effects arise from the impact of GVD. This example illustrates that any chirped pulse exhibits a pulse duration which is larger than the theoretical minimum determined by its spectral bandwidth. Generally, the product of pulse duration and spectral bandwidth follows the universal inequality

$$\Delta t \Delta\omega \geq P, \tag{2.22}$$

which constitutes the classical analog to the quantum-mechanical time-energy uncertainty principle. The minimum value P is only obtained by a chirp-free pulse, and its magnitude depends on the shape of the envelope and the definition of pulse duration. Values of P for various pulse shapes and FWHM pulse duration are summarized in table 2.1. Practically, dispersion effects are derived from the frequency-dependent linear index of refraction which is usually approximated by the Sellmeier equation. Dispersion values of relevant technical glasses commonly used in laser science as well as the quantitative broadening and reshaping of Gaussian pulses due to higher dispersion orders are shown in figure 2.1. As can be seen from the figure, even the dispersion of air matters for few-cycle pulses and the broadening effect due to GVD is significant. The temporal broadening caused by TOD is generally less pronounced, but still can considerably affect the duration of few-cycle pulses, e.g. as a remainder of an incomplete optical pulse compression. While GVD (and all even higher order dispersion terms) broadens the pulse symmetrically and preserves the pulse shape in the specific case of a Gaussian envelope shape, TOD (and all odd higher order dispersion terms) produces an asymmetric pulse shape with a single-sided ringing. Optical pulse compression techniques aim at minimizing higher order dispersion primarily by eliminating the most significant GVD accumulated while passing dispersive media such as glass (lenses, windows or beam splitters) or even air in the case of few-cycle pulses. For this purpose,

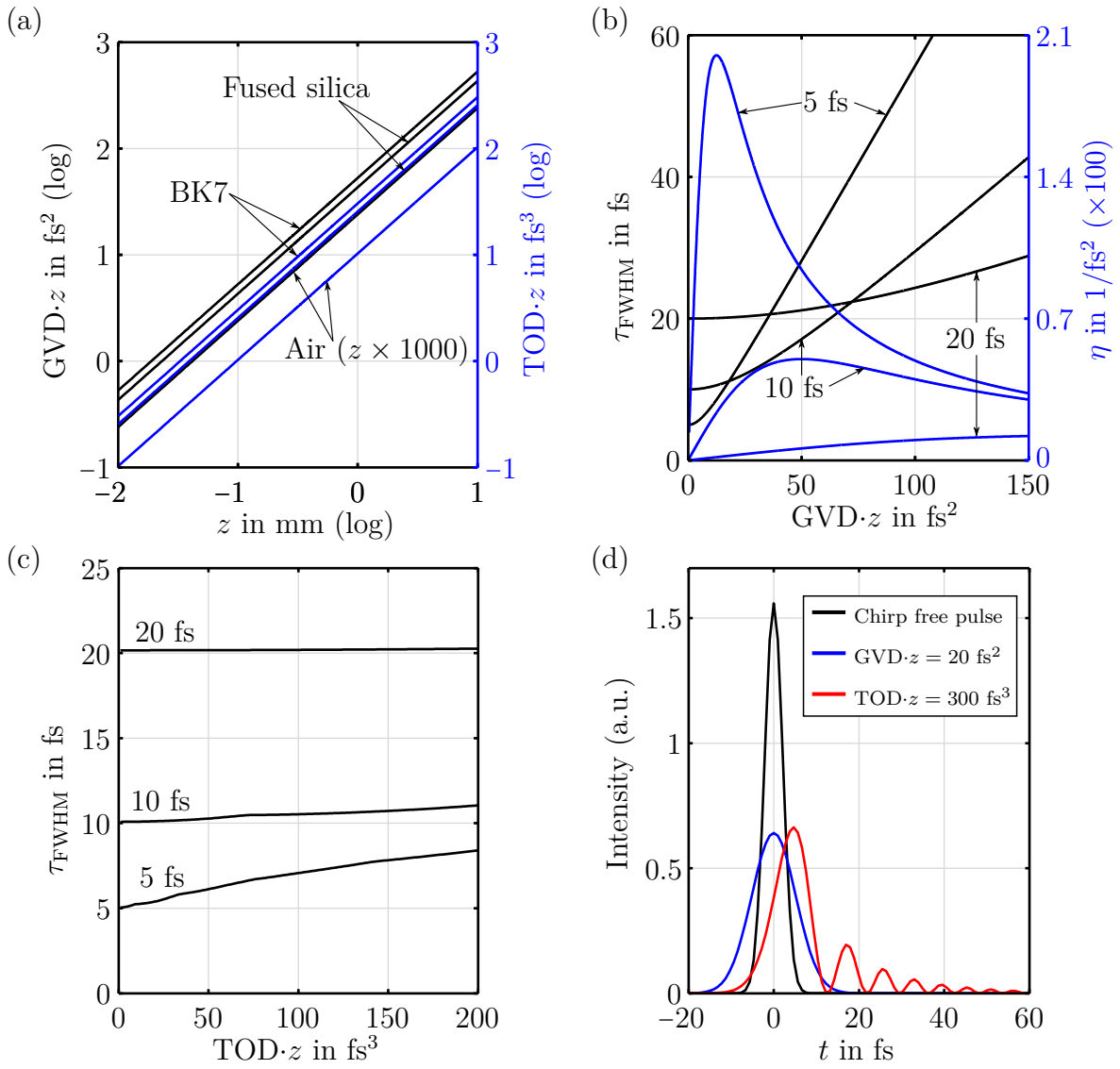

Figure 2.1: Dispersion. (a): Second order dispersion of air and common laser glasses. (b): Pulse broadening and chirp due to second order dispersion. (c): Pulse broadening due to third order dispersion. (d): Temporal pulse form reshaping due to pure GDD and TOD.

the pulse is sent through a setup of dispersive media which exhibit the opposite sign of second-order dispersion. This can be achieved by prisms, gratings, multilayer mirrors or fibers in the anomalous dispersion regime. Usually it is not possible to completely remove the GVD and higher-order dispersion at the same time.

2.1.2 Carrier-envelope phase

Few-cycle pulses may contain less than two optical field cycles, and thus the electric field strength changes considerably after one optical cycle. Therefore, the CEP, i.e. the alignment of the field oscillation with respect to its envelope, significantly affects the precise evolution of the electric field, see figure 2.2. Consequently, the CEP constitutes a critical and important quantity in light-matter interactions of few-cycle pulses and strongly influences any nonlinear optical process which depends on the instantaneous field strength rather than on the cycle-averaged intensity. CEP effects have been demonstrated on gases [59, 77, 87], molecules [3, 84] and solids [8, 34, 76, 159], revealing its enormous potential to precisely manipulate and control ultrafast electronic dynamics. Since the carrier wave advances with v_{ph}, see equation 2.14, and the field envelope with v_{gr}, see equation 2.15, the net dispersion experienced by a pulse circulating inside a laser resonator of length L introduces a shift of the CEP after each round trip by

$$\Delta\Phi_{\mathrm{CEP}} = \omega_0 L \left(\frac{1}{v_{\mathrm{gr}}} - \frac{1}{v_{\mathrm{ph}}} \right). \tag{2.23}$$

The electric field $E_{\mathrm{pt}}(t)$ of a pulse train with repetition rate $f_r = \tau_r^{-1}$ from a mode-locked laser cavity therefore can be written as

$$E_{\mathrm{pt}}(t) = \sum_{n=-\infty}^{+\infty} A_{\mathrm{p}}(t - n\tau_r) \mathrm{e}^{i(\omega_0 t - n\tau_r\omega_0 + n\Delta\Phi_{\mathrm{CEP}} + \Phi_{\mathrm{CEP}})} \tag{2.24}$$

where $A_{\mathrm{p}}(t)$ is the envelope of a single pulse, and n an integer number representing the round trip number. The Fourier transform of equation 2.24 reads

$$\hat{E}_{\mathrm{pt}}(\omega) = \int_{-\infty}^{+\infty} E_{\mathrm{pt}}(t) \mathrm{e}^{-i\omega t} \, \mathrm{d}t \tag{2.25}$$

$$= \sum_{n=-\infty}^{+\infty} \mathrm{e}^{i(-n\omega_0\tau_r + n\Delta\Phi_{\mathrm{CEP}} + \Phi_{\mathrm{CEP}})} \int_{-\infty}^{+\infty} A_{\mathrm{p}}(t - n\tau_r) \mathrm{e}^{-i(\omega-\omega_0)t} \, \mathrm{d}t \tag{2.26}$$

$$= \mathrm{e}^{i\Phi_{\mathrm{CEP}}} \hat{A}(\omega - \omega_0) \sum_{n=-\infty}^{+\infty} \delta(\omega\tau_r - \Delta\Phi_{\mathrm{CEP}} - 2\pi n). \tag{2.27}$$

The last equation is obtained by substituting $(t - n\tau_r) \to t'$ and using the sum representation of the Dirac-distribution. Equation 2.27 is only non-zero if the argument of the Dirac-distribution equals zero, which is the case for the frequency components

$$f_n = \frac{\Delta\Phi_{\mathrm{CEP}}}{2\pi\tau_r} + \frac{n}{\tau_r} = f_{\mathrm{CEO}} + n f_r. \tag{2.28}$$

The frequency representation of a pulse train is therefore a spectrum of equidistant lines separated by f_r with an offset of f_{CEO}, distributed under the envelope function $\hat{A}(\omega-\omega_0)$, see figure 2.2. This is referred to as a frequency comb. The CE-offset frequency f_{CEO}

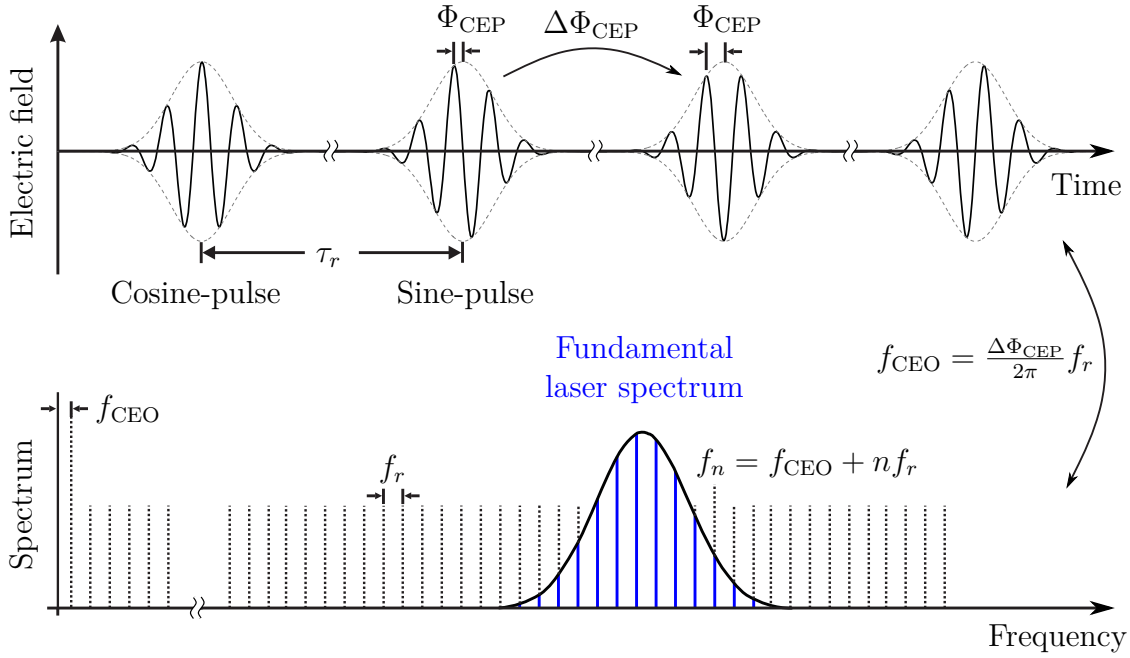

Figure 2.2: Exemplary field evolution in a laser pulse train of repetition rate f_r consisting of few-cycle pulses and corresponding frequency comb in the Fourier domain. Figure adapted from [95].

describes the rate of change of the CEP within the pulse train. However, practically both f_r and f_{CEO} are perturbed by noise fluctuations preventing the frequency comb from being stable, and hence rendering the CEP of consecutive pulses random. For this reason, it is necessary to either actively stabilize the CEP to a constant value or to measure it on a single-shot basis in order to keep track of its instantaneous value. The latter approach is used in this work, and the corresponding measurement technique is described in section 2.1.2.

CEP control and measurement

The successful application of few-cycle pulses is closely related to the ability for controlling their carrier-envelope phase. Due to stochastic environmental perturbations, the CEP value of consecutive laser pulses from an ultrafast laser oscillator appears random by nature [52]. The conventional approach to controlling the CEP is to actively stabilize it by heterodyning different harmonics of an octave-spanning laser pulse and locking the beat signal to a frequency reference [112, 117, 141]. When this reference coincides with the down-sampled repetition rate of the amplifier system, an output pulse train with a constant CEP value is

obtained. Recent advances in CEP stabilization techniques demonstrated long-term locking stability of more than 10 hours with a RMS phase noise of a few hundred mrad after the amplifier system using the feedforward method [69, 89]. An alternative approach employs methods for tracking and recording the CEP of a non-stabilized laser source on a single-shot basis in parallel to the actual data acquisition [59,77]. This techniques is referred to as CEP-tagging. It is quite beneficial for systematic studies of CEP-dependent processes as a continuous variation of the CEP value over its full 2π range is intrinsically provided by the pulse train, omitting the need for a manual scanning of the CEP. Furthermore, the random change of consecutive CEP values prevents the accumulation of systematic errors, e.g. by a gradual sample drift. Additionally, it has been shown that the intensity-CEP cross-talk of the common ATI phase-meter (see below) is lower than from stabilization setups, therefore giving a lower CEP uncertainty related to intensity fluctuations [116, 122, 147]. The tagging method measures and evaluates the CEP-dependent response of a highly CEP-sensitive process. The common type of phase-meter exploits the process of above-threshold ionization (ATI) for this purpose [105, 122, 152]. Especially the high-energy tail of the ATI spectrum, formed by rescattered photoelectrons, has proven to be favorable as it shows a pronounced CEP-distinctive variation of its low-energy and high-energy shoulder, see figure 2.3(b) upper panel. Two of those spectra are simultaneously measured by a stereographic arrangement of two opposing ToF spectrometers whose drift tubes are parallelly aligned to the axis of laser polarization, figure 2.3(a). In this way, one spectrum always corresponds to the field-inverted (CEP shift of 180°) version of the other spectrum. Finally, a value describing the asymmetry between both spectra is calculated according to

$$A_{1,2} = \frac{L_{1,2} - R_{1,2}}{L_{1,2} + R_{1,2}}, \tag{2.29}$$

where L and R describe the integrated electron yield of the left and the right spectrum, respectively. The index 1 refers to a spectral integration in the low energy region and index 2 to an integration in the high energy region. Moreover, it has been shown that the asymmetry value behaves sinusoidal with respect to the CEP while the phase of this relationship is energy dependent, see figure 2.3(b) lower panel. Therefore, by properly choosing the integration regions so that

$$A_1 \propto \sin\left(\Phi_{\mathrm{CEP}} + \Phi_{\mathrm{CEP}}^{\mathrm{offset}}\right) \tag{2.30}$$

$$A_2 \propto \cos\left(\Phi_{\mathrm{CEP}} + \Phi_{\mathrm{CEP}}^{\mathrm{offset}}\right), \tag{2.31}$$

one ends up with a circular Lissajous-figure when A_1 is plotted against A_2 in a parametric plot with Φ_{CEP} being the parameter. This is commonly referred to as parametric asymmetry plot (PAP). A PAP for 2 million consecutive few-cycle laser shots is shown in figure 2.3(c). Each count in the plot represents a laser shot. This representation turned out to be very convenient, since the CEP value of a laser pulse is directly related to the polar angle ϑ of the corresponding count in the PAP by

$$\Phi_{\mathrm{CEP}} = \vartheta + \Phi_{\mathrm{CEP}}^{\mathrm{offset}}, \tag{2.32}$$

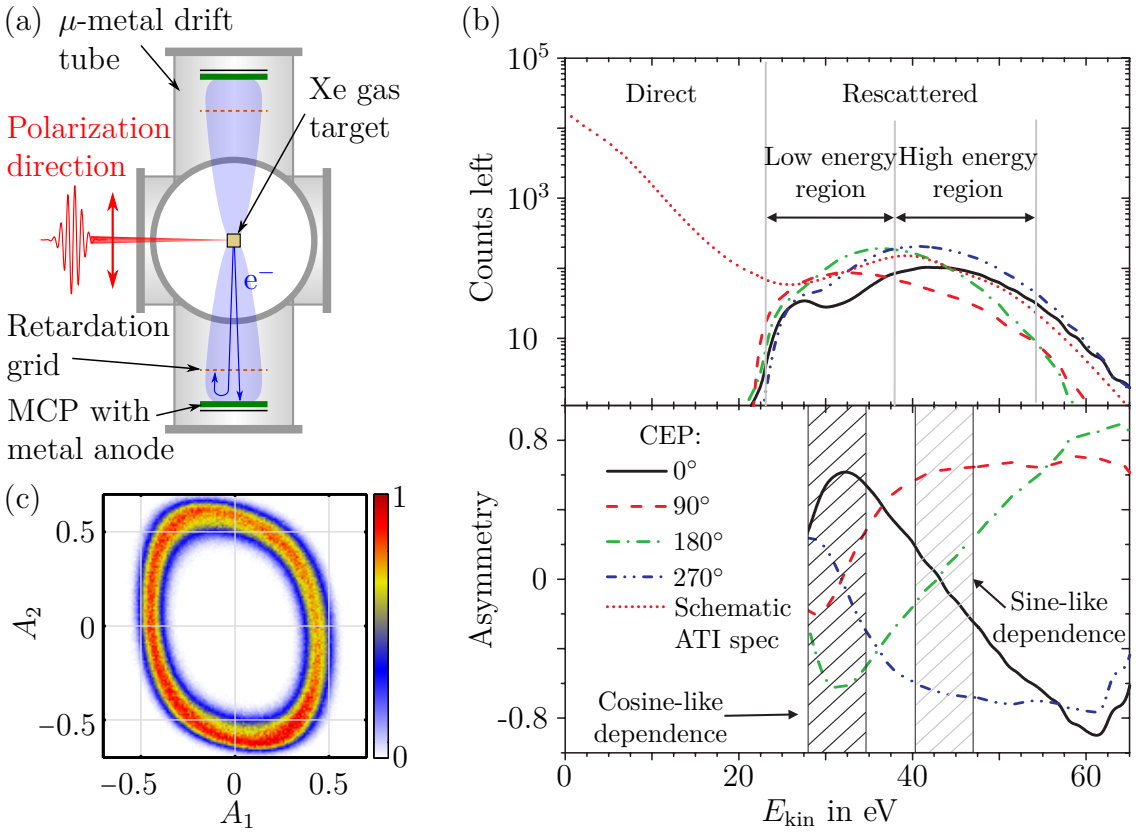

Figure 2.3: (a): Setup of the stereographic, single-shot ATI phase-meter. (b): CEP-dependent ATI spectra of rescattered photoelectrons, recorded from one detector of the phase-meter (top), and asymmetry calculation showing a sine- and cosine-like behavior for the indicated energy regions. Figure adopted from [116]. (c): Parametric asymmetry plot of 2 million consecutive few-cycle laser shots, revealing a mean pulse duration of 5.2 fs FWHM.

where $\Phi_{\mathrm{CEP}}^{\mathrm{offset}}$ is a generally unknown offset value which depends on the exact position of integration windows. It should be mentioned that, depending on the actual adjustments of the integration windows, the relation between ϑ and Φ_{CEP} is not necessarily linear, but it can always be linearized using the angular point-density distribution of the PAP [122]. It is also intuitive that the asymmetry between the left-side and right-side ATI spectra increases with shorter pulse duration, as in this case the variation of maximum field strength between consecutive optical cycles increases. A larger asymmetry value entails a larger radius of the circular distribution in the PAP. The relation between FWHM pulse duration τ and radius R in the PAP was experimentally investigated and empirically determined as [121]

$$\tau = \gamma + \sqrt{\frac{-\delta}{\ln(1-R)}} \tag{2.33}$$

with $\gamma = 1.6063 \pm 0.2593$ and $\delta = 9.7317 \pm 1.5069$. Using this equation, a pulse duration of 5.1 fs is deduced from the PAP in figure 2.3(c). In this way, the output of the stereo-

ATI phase-meter additionally allows for an estimation of the single-shot pulse duration and hence for a convenient real-time evaluation of the laser performance. The real-time calculation of the asymmetry values according to equation 2.29 from the raw MCP signals is performed by the phase-meter processing unit (PMPU), consisting of 4 gated integrators with adjustable gate width and gate position as well as an analog arithmetic unit.

2.2 Nonlinear optics and strong field effects

2.2.1 Optical perturbation theory

The compression of laser pulses down to the femtosecond and few-cycle regime entails the generation of extremely high optical peak intensities and ,correspondingly, high electric field strengths so that the assumption of a linear relationship between field induced polarization and field strength is not appropriate any more. Instead, the polarization response is expanded in a power series with respect to the field strength according to

$$\hat{\mathbf{P}} = \epsilon_0 \left(\underline{\chi}^{(1)} \hat{\mathbf{E}} + \underline{\chi}^{(2)} \hat{\mathbf{E}}^2 + \underline{\chi}^{(3)} \hat{\mathbf{E}}^3 + \dots \right) \tag{2.34}$$

$$= \hat{\mathbf{P}}_{\mathrm{L}}^{(1)} + \hat{\mathbf{P}}_{\mathrm{NL}}^{(2)} + \hat{\mathbf{P}}_{\mathrm{NL}}^{(3)} + \dots \tag{2.35}$$

with the nth-order susceptibility $\underline{\chi}^{(n)}$. In component notation the second-order nonlinear polarization, for instance, is given as

$$\hat{P}_i^{(2)}(\omega_l) = \sum_{jk} \sum_{(mn)} \chi_{ijk}^{(2)}(\omega_l, \omega_m, \omega_n) \hat{E}_j(\omega_m) \hat{E}_k(\omega_n) \tag{2.36}$$

where the multiplication of the involved electric field strengths implies a wave mixing process which leads to the generation of the new side-band frequency components $\omega_l = \omega_m \pm \omega_n$. This is commonly referred to as optical sum-frequency generation (SFG) and difference-frequency generation (DFG), respectively. The corresponding displacement vector then reads

$$\hat{\mathbf{D}} = \hat{\mathbf{D}}^{(1)} + \hat{\mathbf{P}}^{(\mathrm{NL})} \tag{2.37}$$

with

$$\hat{\mathbf{D}}^{(1)} = \epsilon_0 \hat{\mathbf{E}} + \hat{\mathbf{P}}_{\mathrm{L}}^{(1)} \qquad \text{and} \qquad \hat{\mathbf{P}}^{(\mathrm{NL})} = \hat{\mathbf{P}}_{\mathrm{NL}}^{(2)} + \hat{\mathbf{P}}_{\mathrm{NL}}^{(3)} + \dots \tag{2.38}$$

Deriving the wave equation in the common way yields

$$\left[\nabla_\perp^2 + \frac{\partial^2}{\partial z^2} + \frac{\omega^2 \epsilon(\omega)}{c_0^2} \right] \hat{\mathbf{E}} = -\mu_0 \omega^2 \hat{\mathbf{P}}^{\mathrm{NL}} \tag{2.39}$$

where the nonlinear polarization now appears on the right hand side as an inhomogeneity. The general solution for this equation is given by the sum of the solution for the homogeneous equation discussed before and a particular solution. Again the dispersion relation $k^2(\omega) = \frac{\omega^2 \epsilon(\omega)}{c_0^2}$ is used. Introducing a complex wave vector

$$\tilde{k} = k + i\beta \quad \text{with} \quad |k| \gg |\beta| \tag{2.40}$$

also accounts for absorption.

Second-order nonlinearity Fortunately, a number of symmetry conditions can usually be applied to the nonlinear susceptibility tensor which heavily simplify the summation in 2.36 and which may break down the vector relation 2.39 to a scalar relationship. On that condition, equation 2.39 can be recast in the case of a second-order nonlinearity to

$$\left[\nabla_\perp^2 + \frac{\partial^2}{\partial z^2} + (k_3 + i\beta_3)^2\right] \hat{E}_3(\mathbf{r},\omega_3) = -\frac{4\omega^2}{c_0^2} d_{\text{eff}}(\omega_3)\hat{E}_1(\mathbf{r},\omega_1)\hat{E}_2(\mathbf{r},\omega_2) \tag{2.41}$$

where d_{eff} is an effective second-order susceptibility and $\omega_i = \omega - \omega_{i,0}$. The general form of the solution for the fields is assumed to be

$$\hat{E}_i(\mathbf{r},\omega) = \hat{A}_i(\mathbf{r},\omega-\omega_{i,0})e^{ik_{i,0}z}. \tag{2.42}$$

with $\hat{A}_i$ being a complex envelope. Inserting equation 2.42 into 2.41 and defining $\Delta k = k_{3,0} - k_{1,0} - k_{2,0}$ yields

$$\begin{aligned}\left[\nabla_\perp^2 + \frac{\partial^2}{\partial z^2} + 2ik_{3,0}\frac{\partial}{\partial z} - k_{3,0}^2\right] \hat{A}_3(\mathbf{r},\omega-\omega_{3,0}) + [\tilde{k}_3(\omega)]^2\hat{A}_3(\mathbf{r},\omega-\omega_{3,0}) \\ = -\frac{4\omega^2}{c_0^2} d_{\text{eff}}(\omega)\hat{A}_1(\mathbf{r},\omega-\omega_{1,0})\hat{A}_2(\mathbf{r},\omega-\omega_{2,0})e^{-i\Delta kz}\end{aligned} \tag{2.43}$$

The wave vector $k_i(\omega)$ is again expanded according to 2.8. Since $K_i^{(1)}$,$K_i^{(2)}$ (the order of the dispersion terms are here indexed as superscripts as the subscripts are used to label the waves) and β_i are considered small compared to $k_{i,0}$, only terms with a linear combination of these coefficients are sustained after squaring down, and one obtains

$$\begin{aligned}\left[-\frac{i}{2k_{3,0}}\left(\nabla_\perp^2 + \frac{\partial^2}{\partial z^2}\right) + \frac{\partial}{\partial z} - iK_3^{(1)}(\omega-\omega_{3,0})\right. \\ \left. -\frac{i}{2}K_3^{(2)}(\omega-\omega_{3,0})^2 + \frac{\beta_3}{2}\right] \cdot \hat{A}_3(\mathbf{r},\omega-\omega_{3,0}) \\ = i\frac{2\omega^2}{k_{3,0}c_0^2} d_{\text{eff}}(\omega)\hat{A}_1(\mathbf{r},\omega-\omega_{1,0})\hat{A}_2(\mathbf{r},\omega-\omega_{2,0})e^{-i\Delta kz}.\end{aligned} \tag{2.44}$$

Assuming the second-order response is instantaneous (frequency independent), an inverse Fourier transform can be performed:

$$\begin{aligned}\left[-\frac{i}{2k_{3,0}}\left(\nabla_\perp^2 + \frac{\partial^2}{\partial z^2}\right) + \frac{\partial}{\partial z} - K_3^{(1)}\frac{\partial}{\partial t} + \frac{i}{2}K_3^{(2)}\frac{\partial^2}{\partial t^2} + \frac{\beta_3}{2}\right] \cdot A_3(\mathbf{r},t) \\ = i\frac{2}{k_{3,0}c_0^2}\left(\omega_{3,0} + i\frac{\partial}{\partial t}\right)^2 d_{\text{eff}}A_1(\mathbf{r},t)A_2(\mathbf{r},t)e^{-i\Delta kz}\end{aligned} \tag{2.45}$$

For the last transformation the relation $\omega^2 = (\omega-\omega_{i,0})^2 + 2(\omega-\omega_{i,0})\omega_{i,0} + \omega_{i,0}^2$ and thus $\mathcal{F}^{-1}[\omega^2 G(\omega-\omega_{i,0})] = -\frac{\partial^2 G(t)}{\partial t^2} + 2i\omega_{i,0}\frac{\partial G(t)}{\partial t} + \omega_{i,0}^2 = \left(\omega_{i,0} + i\frac{\partial}{\partial t}\right)^2 G(t)$ was used. Equations

for the complex field envelopes $A_1(\mathbf{r},t)$ and $A_2(\mathbf{r},t)$ can be derived accordingly. The resulting set of coupled wave equations describe the field evolution of ultrashort pulses in a dispersive, nonlinear medium of second-order, and therefore form the basis of SFG, DFG and SHG. The term Δk is called phase mismatch and is of fundamental importance for any frequency conversion process (see also section 2.2.2). It describes the dephasing of the fields while propagating through the nonlinear medium, and thus determines the efficiency of the conversion process. The process is most efficient when $\Delta k = 0$, which corresponds to momentum conservation in the quantum-mechanical point of view. Practically, special measures are employed to minimize the phase mismatch.

Third order nonlinearity Third-order nonlinearity based on $\underline{\chi}^{(3)}$ is associated with a four wave mixing process involving the frequencies $\omega_1, \omega_2, \omega_3$ and ω_4. In the case of a single laser beam it is $\omega = \omega_1 = \omega_2 = \omega_3$, and the polarization response with $P^{(3)}(\omega_4 = 3\omega)$ leads to third harmonic generation (THD) while the response that oscillates with the fundamental frequency $P^{(3)}(\omega_4 = \omega)$ contributes to a change of the refractive index δn in the material, thereby modulating the phase of the original wave. Since a real intensity distribution is spatially and temporally non-uniform, the wave itself modulates its phase both in space and time which is known as spatial and temporal self-phase modulation (SPM). In this case the nonlinear polarization reads

$$\hat{P}(\omega) = 3\epsilon_0 \chi^{(3)}(\omega = \omega - \omega + \omega)\hat{E}(\omega)\hat{E}^*(-\omega)\hat{E}(\omega) \tag{2.46}$$

The nature of SPM simplest reveals for a quasi-monochromatic plane wave, turning equation 2.39 into

$$\left[\frac{\partial^2}{\partial z^2} + \frac{\omega_0^2}{c_0^2}\left(\epsilon + 3\chi^{(3)}|A(z)|^2\right)\right] A(z) = 0 \tag{2.47}$$

An extended effective dielectric constant becomes evident, which is given as

$$\epsilon_{\text{eff}} = \epsilon + 3\chi^{(3)}|A(z)|^2 \tag{2.48}$$

Using the general relation $n = \sqrt{\epsilon_{\text{eff}}}$ for the index of refraction, one obtains

$$n = \sqrt{\epsilon + 3\chi^{(3)}|A(z)|^2} = n_1\sqrt{1 + \frac{3\chi^{(3)}|A(z)|^2}{\epsilon}} \tag{2.49}$$

The square root can be approximated by a truncated Taylor expansion so that

$$n = n_1 + \frac{3\chi^{(3)}|A(z)|^2}{2n_1} = n_1 + n_2 I(z) \tag{2.50}$$

where n_2 is the nonlinear index of refraction. An approximate solution of equation 2.47 is obtained by

$$A(z) = E_0 \exp i\left[k_0 n_1 z + k_0 \int_0^z n_2 I(z')\,\mathrm{d}z'\right] \tag{2.51}$$

The nonlinear index of refraction links the evolution of the phase to the pulse intensity. A radial intensity variation therefore induces a lens effect which is known as Kerr-lensing, forming the basis of the Kerr-lens mode-locking technique in femtosecond laser oscillators. A temporal variation of the intensity modulates the instantaneous frequency of the pulse, and thus may produce additional frequency components. A more rigorous derivation of the SPM-affected field evolution of ultrashort pulses including dispersion effects follows the steps of the previous paragraph. Substituting equation 2.46 and 2.42 in 2.39 and performing the inverse Fourier transform yields

$$\left[-\frac{i}{2k_0}\left(\nabla_\perp^2+\frac{\partial^2}{\partial z^2}\right)+\frac{\partial}{\partial z}-K_1\frac{\partial}{\partial t}+\frac{i}{2}K_2\frac{\partial^2}{\partial t^2}+\frac{\beta}{2}\right]\cdot A(\mathbf{r},t) = i\frac{3}{2k_0c_0^2}\left(\omega_0+i\frac{\partial}{\partial t}\right)^2\chi^{(3)}|A(\mathbf{r},t)|^2A(\mathbf{r},t) \quad (2.52)$$

Using the approximation

$$\omega_0^2\left(1+\frac{i}{\omega_0}\frac{\partial}{\partial t}\right)^2=\omega_0^2\left(1+\frac{2i}{\omega_0}\frac{\partial}{\partial t}-\frac{1}{\omega_0^2}\frac{\partial^2}{\partial t^2}\right)\approx\omega_0^2\left(1+\frac{2i}{\omega_0}\frac{\partial}{\partial t}\right) \quad (2.53)$$

and the relation

$$\frac{\partial}{\partial t}(|A|^2A)=2|A|^2\frac{\partial A}{\partial t}+A^2\frac{\partial A^*}{\partial t} \quad (2.54)$$

finally results in

$$\left[-\frac{i}{2k_0}\left(\nabla_\perp^2+\frac{\partial^2}{\partial z^2}\right)+\frac{\partial}{\partial z}+\left(\frac{6\omega_0}{k_0c_0^2}\chi^{(3)}|A|^2-K_1\right)\frac{\partial}{\partial t}+\frac{i}{2}K_2\frac{\partial^2}{\partial t^2}+\frac{\beta}{2}\right]\cdot A(\mathbf{r},t) = i\frac{3\omega_0^2}{2k_0c_0^2}\chi^{(3)}|A(\mathbf{r},t)|^2A(\mathbf{r},t)-\frac{3\omega_0}{k_0c_0^2}\chi^{(3)}A^2\frac{\partial A^*}{\partial t}. \quad (2.55)$$

This equation forms the basis of SPM-induced spectral broadening of ultrashort laser pulses in nonlinear fiber compressors, see section 3.1.2. Also note the intensity-dependent contribution to the group velocity, which leads to the phenomena of self-steepening , i.e. the peak of a pulse is slowed down more than the edges, leading to a steepening of the trailing edge of the pulse. The last equation is often referred to as nonlinear optical Schroedinger equation. A simulation using equation 2.55 is shown in figure 2.4 for SPM-induced spectral broadening as exploited in nonlinear pulse compressors (see section 3.1.2). The simulation uses typical values of argon as the gas medium in a 1 m long hollow core fiber. The spectral width broadens monotonically with increasing distance but quickly starts saturating due to chirp-induced pulse broadening. The output spectrum is highly modulated as a result of spectral interference. Furthermore, TOD causes an asymmetric shape. The output pulse can be compressed when the accumulated chirp is removed.

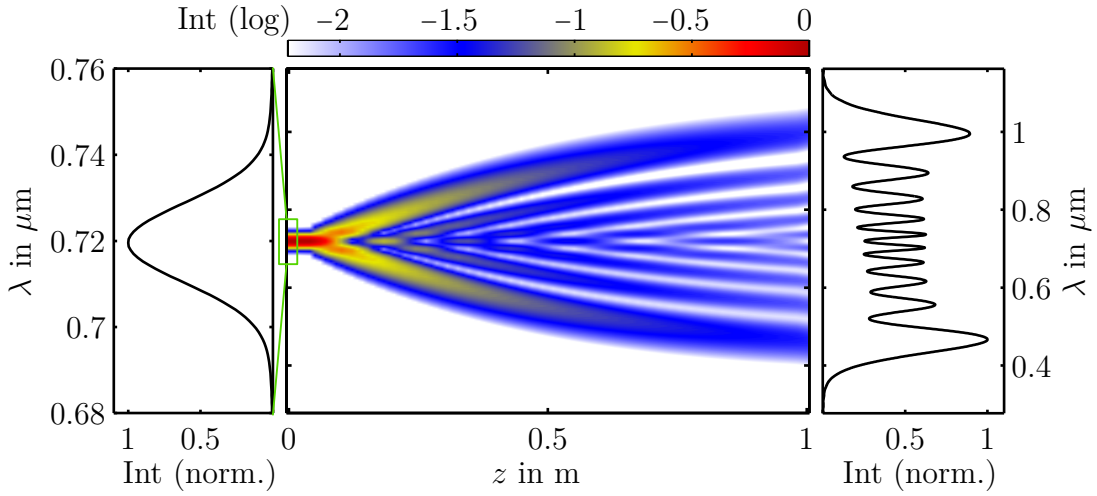

Figure 2.4: Simulation of SPM-induced spectral broadening of a femtosecond pulse in a 1 m long hollow core fiber filled with argon. Parameters: $p = 500$ mbar, GDD $= 12$ fs^2/m, TOD $= 5.1$ fs^3/m, $n_2 = 1 \cdot 10^{-19}$ cm^2/W, $\tau = 25$ fs, $E = 400\,\mu$J, $w_{1/e} = 90\,\mu$m. See text for explanations.

2.2.2 High-order harmonic generation

The frequency up-conversion of laser radiation to large integer multiples (up to several hundred [21,111]) of its original frequency is known as high harmonic generation (HHG). It results from highly nonlinear interaction of high-intensity laser pulses with matter. Usually the interaction target is a noble gas. In this case HHG requires laser intensities in the order of $10^{14}-10^{15}$W/cm^2. It allows the generation of broadband radiation up to the extreme UV (XUV) or even to the soft x-ray range with high spatial and temporal coherence [120] on a table-top size and also forms the basis for the generation of isolated attosecond pulses. The HHG process and the properties of high harmonic radiation are described in more detail in the following. We restrict the discussion to high harmonics generated from a gas target as this is the most established technique which we also go for in our setup, although there are concepts for and experimental approval of high harmonic generation from solids, the generation mechanism however is different. The generation of high order harmonics can not be described by perturbation theory any more, since the electric field strength associated with the required intensities is now comparable to the inner atomic field, and hence, the assumption of a material polarization slightly perturbed by higher order electric field terms breaks down. Instead, HHG can be successfully described by a semi-classical three step model developed by Corkum [31] and Kulander [79], as summarized in figure 2.5. According to this model, gas atoms or molecules are first field-ionized in the strong electric field of an ultrashort high-intensity laser pulse close to its field maximum and the released electrons, which have zero initial velocity, are subsequently accelerated in the laser field away from their parent ions. The Coulomb potential of the ionized atoms is neglected in the strong field approximation (SFA). When the electric laser field reverses, the electrons are first decelerated and then accelerated back towards their parent ions,

thereby gaining energy from the electric field of the laser. Finally they can recombine with a certain probability with their parent ions, emitting a high energy photon. The emitted photon energy is a direct consequence of the electron's kinetic energy, acquired during its round trip in the laser field, at the time of recombination.

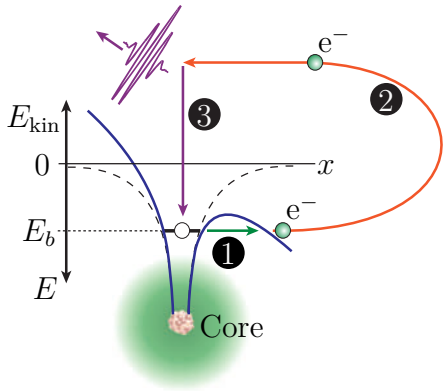

Figure 2.5: HHG three step model. (1): Tunnel ionization. (2): Acceleration in the laser field. (3): Recombination and photoemission. Figure adapted from [68].

Ionization A prerequisite for HHG is the ionization of atoms in the laser field. The predominant ionization mechanism for HHG is tunnel ionization. In this case the electric field strength of the laser pulse is comparable to the inner atomic field and the atomic Coulomb potential V_C gets heavily deformed by the potential V_L of the strong laser field. The net inner potential V_i that a bound electron experiences then reads

$$V_i(r,t) = V_C(r,t) + V_L(r,t) = -\frac{e^2}{4\pi\epsilon_0 r} + eE(t)r \tag{2.56}$$

forming a potential barrier with finite width which the electron can tunnel through. Tunnel ionization is the dominant ionization mechanism when the ponderomotive potential U_p of the laser field is much larger than the ionization potential I_p of the atom. This is usually expressed in terms of the Keldysh parameter γ [63]

$$\gamma = \sqrt{\frac{I_p}{2U_p}}. \tag{2.57}$$

The ponderomotive potential is the cycle-averaged energy which a free electron acquires while exposed to the laser field and which is given as

$$U_p = \frac{e^2 E_L^2}{4m_e\omega_L^2} \propto I\lambda^2 \tag{2.58}$$

The Keldysh parameter can also be expressed in terms of the tunneling time τ_{tunnel} and the laser period T_L which may give a more intuitive access in understanding this parameter

$$\gamma = 4\pi \frac{\tau_{\text{tunnel}}}{T_L}. \tag{2.59}$$

The tunneling time τ_{tunnel} is the time it takes for an electron to tunnel through the potential barrier formed by 2.56. For tunnel ionization this time has to be short compared to the time of one optical cycle T_L so that the oscillating laser field is effectively static during the tunneling process. This is called *quasi static limit*. If $\tau_{\text{tunnel}} \gg T_L$, the tunnel barrier is already vanished in the course of the oscillating nature of the laser field before the electron tunneled through it and, consequently, tunnel ionization is suppressed. The tunnel ionization rate w in a gas target under the influence of a laser pulse is commonly calculated using the ADK formula [5], which is valid for arbitrary atoms in an arbitrary initial electronic configuration and is given by (in atomic units)

$$w_{\text{ADK}}(t) = C^2_{n^*l^*} f_{ml} \left(\frac{3E_L(t)}{\pi(2I_p)^{3/2}} \right)^{\frac{1}{2}} I_p \left(\frac{2(2I_p)^{3/2}}{E_L(t)} \right)^{2n^* - |m| - 1} \exp\left[-\frac{2(2I_p)^{3/2}}{3E_L(t)} \right] \tag{2.60}$$

where

$$n^* = \frac{Z}{\sqrt{2I_p}}, \tag{2.61}$$

$$l^* = n^* - 1, \tag{2.62}$$

$$C^2_{n^*l^*} = \frac{2^{2n^*}}{n^*\Gamma(n^* + l^* + 1)\Gamma(n^* - l^*)}, \tag{2.63}$$

$$f_{lm} = \frac{(2l+1)(l+|m|)!}{2^{|m|}(|m|)!(l-|m|)!}. \tag{2.64}$$

l and m are the angular and magnetic quantum number, respectively, n^* and l^* are effective quantum numbers including quantum effects and the degree of ionization Z and the parameters C_{n^*l} and f_{ml} take into account the atomic species as well as the initial electronic configuration. Using equation 2.60 one can calculate the time dependent density of free electrons $n_e(t)$ for an initial gas density n_0 as

$$n_e(t) = n_0 \left(1 - \exp\left[-\int_{\infty}^{t} w(t')\, \mathrm{d}t' \right] \right) \tag{2.65}$$

which is a critical quantity for the HHG process, since a high background of free electrons adds a contribution to the total refractive index experienced by the laser field and hence affects the propagation properties of the driving laser pulse and the harmonic radiation. The transverse distribution of this free electron induced change of refractive index follows the spatially bell-shaped intensity distribution of the pulse profile, forming an effective lens which defocuses the pulse while propagation through the gas medium. Additionally,

the index change affects the dephasing behavior between high harmonics and laser pulse, hence influencing the phase matching condition, which will be discussed in more detail later. Furthermore, a strong depletion of neutral gas atoms in the interaction zone before it is reached by the maximum field amplitude of the pulse, which in turn leads to the highest harmonic orders in the HHG process, deteriorates the achievable high harmonic flux in the cutoff region. For these reasons, the use of few-cycle laser pulses for driving the high harmonic process has proven to be advantageous for an efficient generation of high harmonic radiation.

Electron acceleration Once the electron is freed it gets subsequently accelerated in the laser field. Principal properties of the evolution of the electron wave-packet can be intuitively investigated using classical mechanics [31, 79]. This approach already gives valuable insight into the basic internal processes which establish the characteristics of high harmonic radiation. The Coulomb force of the ion core is neglected and only the electric field of the laser is considered. Also, the initial position and velocity of the freed electron is assumed to be zero at the instant of ionization. The equation of motion for the electron then reads

$$m_e \mathbf{a}(t) = e\mathbf{E}(t) = E_0 \cos(\omega t + \phi)\mathbf{x} + \alpha E_0 \sin(\omega t + \phi)\mathbf{x} \quad (0 \leq \alpha \leq 1) \tag{2.66}$$

where α is introduced to account for arbitrary polarization ($\alpha = 0$ corresponds to linear, $\alpha = 1$ to circular polarization; $\mathbf{x}$ is the unit vector in x-direction). The electron motion is easily obtained by integration

$$v_x(t) = \int_{t_0}^{t} \frac{eE_x(\tau)}{m_e}\, \mathrm{d}\tau = \frac{eE_0}{m_e\omega} \sin(\omega t + \phi) + v_{d,x} \,, \tag{2.67a}$$

$$x(t) = \int_{t_0}^{t} v_x(\tau)\, \mathrm{d}\tau = -\frac{eE_0}{m\omega^2} \cos(\omega t + \phi) + v_{d,x} t + x_0 \,, \tag{2.67b}$$

where t_0 is the instant of ionization, $v_{d,x} = -\frac{eE_0}{m_e\omega}\sin(\omega t_0 + \phi)$ is the drift velocity and $x_0 = \frac{eE_0}{m\omega^2}\cos(\omega t_0 + \phi) - v_{d,x} t_0$. Accordingly, it is

$$v_y(t) = -\alpha \frac{eE_0}{m_e\omega} \cos(\omega t + \phi) + v_{d,y} \,, \tag{2.68a}$$

$$y(t) = \alpha \frac{eE_0}{m\omega^2} \sin(\omega t + \phi) + v_{d,y} t + y_0 \,. \tag{2.68b}$$

The electron describes an oscillatory motion around the position determined by the drift velocity v_d. Its average quiver energy per field cycle is given by 2.58. Depending on the initial phase $\Phi_L^{\mathrm{ion}} = \omega t_0 + \phi$, the electron may periodically re-encounter its parent ion, recombining and emitting high harmonic radiation. For linearly polarized light, several classes of electron trajectories are possible which are displayed in the position-velocity map in figure 2.6 using equations 2.67a and 2.67b. The majority of electrons are generated at unfavorable phases, moving on trajectories which never return to the parent ion, as

for $\Phi_L^{\text{ion}} = -45°$. These electrons do not contribute to high harmonic generation but form a free electron background in the gas interaction zone, affecting the propagation conditions for laser pulse and harmonics. Electrons on trajectories which return to the ion core generally acquire different kinetic energies during their excursion, visualized by the intersection of those traces with the velocity axis in figure 2.6. Tunneling ionization is most likely at the peak of the electric field, i.e. at $\Phi_L = 0°$ when the potential barrier is lowest, but those electrons return to the ion core with zero kinetic energy. For an ionization phase of $\Phi_L^{\text{ion}} = 17°$ the electrons gain the highest energy upon the arrival at their parent ion, producing the highest photon energies (cut-off of the harmonic spectrum) after recombination. At lower energies, there are typically two types of electron trajectories which contribute to HHG, short and long ones, which exhibit different excursion times but end at the ion core with the same kinetic energy as for $\Phi_L^{\text{ion}} = 3°$ and $\Phi_L^{\text{ion}} = 45°$. The harmonic output properties are in this case determined by the interference of both trajectories.

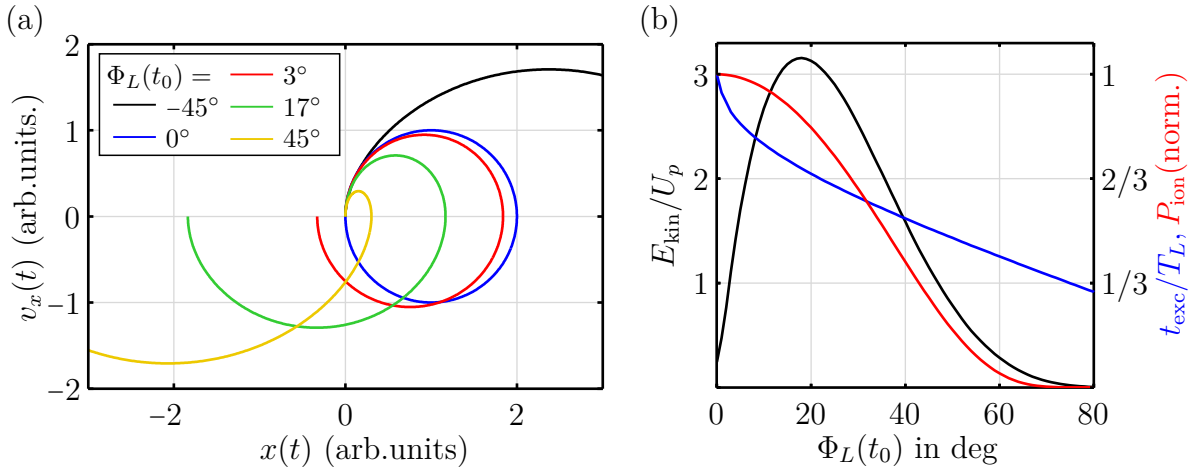

Figure 2.6: HHG three step model. (a): Classical electron trajectories for different ionization phases. (b): Kinetic energy of the accelerated electrons at recombination, ionization probability P_{ion} for a NIR intensity of $I = 3.8 \cdot 10^{14}$ W/cm^2 and the electron excursion time t_{exc}. U_p: ponderomotive potential, T_L: oscillation period of the NIR field.

As it is also obvious from equations 2.67a-2.68b, with increasing degree of ellipticity, the electron gets displaced from the parent ion position after its excursion by an increasing offset in y-direction and, consequently, the recombination probability and hence the efficiency for high harmonic generation quickly drops to zero. This has been confirmed experimentally [15]. For this reason, HHG is most efficient when excited with linearly polarized laser pulses, in turn producing harmonic radiation with linear polarization. However, the availability of circularly polarized high harmonic radiation would greatly extend the spectroscopic possibilities in attosecond physics. So far only few concepts for its production have been conceived and experimentally realized [64, 144, 146, 161]. However, these are either rather inefficient or quite complex in their implementation. Our approach of gen-

erating harmonic radiation with circular polarization will be dealt with in more detail in section 4.2.

Recombination Upon its return to the ion core, the accelerated electron can recombine to the ground state. In this case, the energy difference is released as a high-energy photon. According to energy conservation, the emitted photon energy is given by

$$E_{\mathrm{ph}} = \hbar\omega = I_P + E_{\mathrm{kin}}(\phi_{\mathrm{ion}}). \tag{2.69}$$

The return energy as a function of the ionization phase Φ_L^{ion} can be calculated using equations 2.67a and 2.67b and is plotted in figure 2.6(b), together with the corresponding electron excursion time, determined by $x(t_{\mathrm{exc}}) = 0$ for $t_{\mathrm{exc}} > t_0$. Also shown is the phase-dependent ionization probability according to 2.60. As apparent from the figure, the highest return energy $E_{\mathrm{kin}}^{\mathrm{max}} = 3.17U_p$ is obtained for an ionization phase of $\Phi_L^{\mathrm{ion}} = 17°$, thereby defining the cutoff energy of the HHG process as

$$E_{\mathrm{ph}}^{\mathrm{cutoff}} = I_p + 3.17U_p. \tag{2.70}$$

Although the ionization probability for this phase is still quite high, it is noted that the phase with the highest ionization probability does not promote the HHG process since these photo-ionized electrons return to the ion core with zero kinetic energy. The excursion time of the accelerated electrons is in the order of a quarter oscillation period, and decreases with increasing phase values. Therefore, photoelectrons ionized at $\Phi_L^{\mathrm{ion}} < 17°$ move on long trajectories while those ionized at $\Phi_L^{\mathrm{ion}} > 17°$ move on short trajectories. Since $U_p \propto \lambda I^2$, a higher cutoff energy 2.70 may be obtained by either increasing the wavelength or the peak intensity. However, both changes generally reduce the conversion efficiency of the HHG process. The quantum nature of the electron leads to a transverse spread of the wave packet during its excursion in the continuum. This spread gets more pronounced the longer the excursion time, which greatly reduces the recombination probability for long wavelengths. A higher intensity, on the other hand, may increase the dephasing between harmonics and the driving laser field due to plasma induced dispersion and nonlinearities, thereby preventing the coherent buildup of the harmonic field.

Intrinsic phase Another important quantity in HHG is the intrinsic (dipole) phase of the harmonic emission. This phase is not addressed by the semi-classical description but follows from a quantum-mechanical formulation. An approximate solution of the TDSE for the HHG process is given by the Lewenstein-model [83], which is valid in a low frequency, high intensity limit ($U_p > I_p$). The evolution of the electron wave function $|\psi(t)\rangle$ in the presence of a NIR laser field is described by [3]

$$i\frac{\partial}{\partial t}|\psi(t)\rangle = \hat{H}(t)\,|\psi(t)\rangle \tag{2.71}$$

[3] Atomic units are used for the remainder of this paragraph.

with the Hamilton operator

$$\hat{H} = \frac{1}{2}(\mathbf{p} - \mathcal{A}_L(t))^2 + V_{\text{eff}}(\mathbf{r}) + \mathbf{E}_L(t)\mathbf{r}. \tag{2.72}$$

Here, $\mathbf{E}_L(t) = A_L(t)\,\mathrm{e}^{-i\omega_L t}\,\mathbf{n}_L$ is the NIR laser field, with $\mathbf{n}_L$ being the polarization direction, and $\mathcal{A}_L(t)$ its vector potential in Coulomb gauge so that $\mathbf{E}_L(t) = -\frac{\partial \mathcal{A}_L}{\partial t}$. $V_{\text{eff}}(\mathbf{r})$ describes an effective potential formed by the ion and the remaining bound electrons. However, within the strong field approximation the influence of $V_{\text{eff}}(\mathbf{r})$ is considered to be small and can be neglected. The ionization process, described as the transition from the ground state $|0\rangle$ to the continuum state $|\mathbf{v}\rangle$ with kinetic momentum $\mathbf{v}$, is represented by the dipole matrix

$$M(\mathbf{v}) = \langle \mathbf{v}|\mathbf{r}\cdot\mathbf{n}_L|0\rangle\,. \tag{2.73}$$

The inverse process of recombination is given as the complex conjugate and describes the transition from the continuum to the ground state

$$M^*(\mathbf{v}) = \langle 0|\mathbf{r}\cdot\mathbf{n}_L|\mathbf{v}\rangle\,. \tag{2.74}$$

The high harmonic response is described by the time-dependent dipole moment $\mu_n(t) = \langle\psi(t)|\mathbf{r}\cdot\mathbf{n}_L|\psi(t)\rangle$ along the direction $\mathbf{n}_L$ where $|\psi(t)\rangle$ solves equation 2.71. An approximate solution of 2.71 allows the dipole moment to be calculated by [83]

$$\mu_n(t) \propto \int_{\mathbf{p}} \int_{-\infty}^{t} [M^*(\mathbf{p}-\mathcal{A}_L)] \times [A_L(t')M(\mathbf{p}-\mathcal{A}_L)]\,\mathrm{e}^{-i\omega_L t'} \times \exp[-i\Phi_v(\mathbf{p},t,t')]\,\mathrm{d}t'\,\mathrm{d}\mathbf{p}. \tag{2.75}$$

Here the canonical momentum $\mathbf{p} = \mathbf{v} + \mathcal{A}_L$ is used. The classical action of the laser field now appears in a phase term which is known as a Volkov phase and which reads

$$\Phi_v(\mathbf{p},t,t') = \int_{t'}^{t} \left(\frac{1}{2}\left[\mathbf{p} - \mathcal{A}_L(t'')\right]^2 + I_p\right)\mathrm{d}t''. \tag{2.76}$$

Equation 2.75 reflects the same three steps as described in the semi-classical model: ionization, recombination and propagation. However, in the quantum-mechanical formulation the additional phase term 2.76 shows up which accounts for the phase of the electron wave packet accumulated during its field-dressed propagation in the continuum. This intrinsic (dipole) phase has far-reaching implications for the temporal, spatial and spectral structure of the high harmonic radiation. Especially the wave packets which arise from long- and short trajectories acquire quite different phase accumulations, leading to high harmonic contributions with differing characteristics. Moreover, the intensity dependence of the intrinsic phase causes an inherent negative chirp in the harmonic emission near the cutoff when the process is driven by few-cycle pulses. It also causes the spatial divergence of the emission to be dependent on the gas target position relative to the laser focus. Equation 2.75 forms the basis of the HHG simulations employed in section 5.3. In order to calculate the high harmonic field, the nonlinear source term in the wave equation 2.39 is substituted by the high harmonic dipole moment 2.75.

Phase matching As already outlined in section 2.2.1, phase matching is of ultimate importance for the constructive, and thus efficient buildup of harmonic radiation. Any dephasing of the involved fields while propagating through the nonlinear medium greatly diminishes the harmonic output due to destructive interference. Perfect phase matching between the driving laser field and the q-th harmonic field requires the phase mismatch Δk to vanish

$$\Delta k = qk_L - k_q \stackrel{!}{=} 0, \tag{2.77}$$

with k_L and k_q being the wave vector of the fundamental and the harmonic field, respectively. Phase shifts are naturally introduced by the focusing of the laser beam, by nonlinear phase modulations, by the dipole phase and by the gas medium causing dispersion. Considering the refractive indices associated with both the density of neutral gas atoms and the plasma background, generated by ionization events with non-returning electrons, the wave vector can be expressed, in the adiabatic limit, as [61, 109, 110]

$$k(\lambda) = \frac{2\pi}{\lambda} + \frac{2\pi N_a n(\lambda)}{\lambda} - N_e r_e \lambda + \frac{1}{z_R} + \frac{2\pi}{\lambda} n_2 I + \frac{\partial \Phi_{\text{dipole}}}{\partial z} \tag{2.78}$$

where N_a and N_e are the densities of neutral atoms and electrons, respectively, $n(\lambda)$ is the refractive index per unit neutral atom density, and z_R the Rayleigh length. The terms in 2.78 describe, in the order of their appearance, the vacuum dispersion, the dispersion of the neutral gas, the plasma dispersion, the Gouy phase shift, nonlinear dispersion and the phase delay caused by the intrinsic dipole phase. An additional term accounting for fiber dispersion arises if the high harmonics are generated in a wave guide [37]. Substituting equation 2.78 into 2.77 and using $\lambda_q = \lambda_L/q$ yields for the phase mismatch

$$\Delta k = \frac{2\pi q}{\lambda}(1-\eta)p\Delta n - \eta p N_{\text{atm}} r_e \lambda \left(\frac{q^2-1}{q}\right) + \frac{1}{z_R}(q-1) + \frac{2\pi}{\lambda} q n_2 I_L - \frac{\partial \Phi_{\text{dipole}}}{\partial z} \tag{2.79}$$

$$= \Delta k_{\text{neutral}} + \Delta k_{\text{plasma}} + \Delta k_{\text{Gouy}} + \Delta k_{\text{nonlin}} + \Delta k_{\text{dipole}} \tag{2.80}$$

Here, η is the ionization fraction, N_{atm} the gas density at atmospheric pressure, and $\Delta n = n_L^{\text{atm}} - n_q^{\text{atm}}$ the difference between the refractive indices of the neutral gas at atmospheric pressure. The phase-mismatch also defines a coherence length

$$L_{\text{coh}} = \frac{\pi}{\Delta k}$$

over which high harmonic radiation can be efficiently generated. Equation 2.79 provides a general guideline for reducing the phase mismatch in the free gas jet geometry. Due to the anomalous dispersion of the plasma, it can be used to counteract the dispersion of other terms by tuning the gas pressure p [61] or the ionization fraction η, which in turn is affected by adjusting the laser intensity. The contribution from the Gouy phase can be controlled by the focusing geometry and by the position of the gas jet relative to the focus. In this way, adjusting the phase mismatch allows for a spectrally selective enhancement of the macroscopic high harmonic yield. In addition, since the two trajectory

types acquire a differing dipole phase, phase matching adjustments can be used to favor one type. In general, phase matching sensitively depends on the specific pulse and target properties and is usually empirically adjusted to the particular needs of the experiment by means of the afore mentioned parameters. Incomplete phase-matching and re-absorption of the harmonic radiation in the gas jet limit the usable interaction length with the gas target. For few-cycle pulses, the phase mismatch 2.79 generally grows nonlinearly with increasing propagation distance which entails non-adiabatic phase matching effects [42, 142]. Furthermore, the high peak intensities associated with these pulses may provoke a considerable reshaping of the pulse structure due to nonlinear interactions with the gas target such as SPM, self-steepening and so on, making phase matching a rather complex issue.

Isolated XUV pulses Each successful recombination process gives rise to a short burst of XUV radiation, leading to the emission of a sub-fs XUV pulse. Since the high harmonic generation process is repeated every half-cycle of the driving laser field, a train of attosecond pulses is generated. The corresponding spectrum is determined by the interference of all contributing XUV bursts. Due to the temporal periodicity of $T_L/2$, it only consists of the odd harmonics of the fundamental laser frequency. The simplest way of creating an isolated XUV pulse is by band-pass filtering the spectrum in such a way that only a single high harmonic peak is extracted. The duration of the resulting XUV pulse is in this case determined by the spectral width of the harmonic peak. The line width of an harmonic peak in turn is determined by the number of half-cycles which contribute to the harmonic emission of that particular energy. The less half-cycles contribute, the broader the high harmonic line width. Therefore, in order to generate a broadband XUV continuum supporting the shortest isolated XUV pulses, the high harmonic generation process has to be confined to a single optical half-cycle. Several gating techniques have been developed for this purpose [28]. A few-cycle pulse, for instance, naturally confines the generation of harmonic emission with the highest energies to that half-cycle with the highest field strength (provided its CEP is properly controlled), thus providing a spectral continuum near the cutoff energy. In this case, the XUV pulse duration is limited by the width of the applied band-pass filter, enabling the generation of sub-100 as XUV pulses using appropriate broadband filters [43]. The XUV band-pass filters employed in this work are based on reflective multilayer optics, which additionally serve as a focusing element, if necessary. By engineering the multilayer structure, tailored filter characteristics regarding bandwidth, central energy and XUV chirp can be produced.

2.3 Photoelectron emission spectroscopy on solids

Photoelectron spectroscopy (PES) is a powerful tool for the investigation of the electronic structure of matter. The technique is based on the photoelectric effect in which energetic radiation is employed to liberate electrons from a sample. By measuring the energy- and angle-distribution of the released photoelectrons, valuable information about their

initial energetic state can be extracted. The photoemission process can be semi-classically described by a three step model: optical excitation of an electron in the bulk, transport of the excited electron to the surface, and finally the escape of the photoelectron into vacuum. Beside this approach, a more rigorous quantum-mechanical description has been developed which treats the photo-ionization, the electron transport, its transmission and detection as a single coherent process. This so-called one-step model includes bulk, surface and vacuum states in the Hamiltonian describing the crystal, and therefore, this model also accounts for quantum interference and resonance effects. However, the more intuitive three-step model has phenomenologically proven to be rather successful for the discussion of PES data, and thus a brief summary of the model is presented here.

2.3.1 Angle-resolved PES

Excitation By the absorption of a photon of energy $E_{\mathrm{ph}} = \hbar\omega$ an electron is excited from its initial state $|\varphi_i\rangle$ to a final state $|\varphi_f\rangle$. The probability for this transition is given by the corresponding matrix element

$$P_{\mathrm{exc}} \propto \langle\varphi_f|H_{\mathrm{int}}|\varphi_i\rangle \tag{2.81}$$

where H_{int} is the Hamiltonian of the interaction. Both states are associated with an initial energy $E_i(\mathbf{k}_i)$ and a final energy $E_f(\mathbf{k}_f)$, in which the energy generally depends on the momentum of the electron according to the dispersion of the crystal band structure. Energy and momentum conservation implies for the final state

$$E_f(\mathbf{k}_f) = \hbar\omega - E_i(\mathbf{k}_i) \tag{2.82}$$

$$\mathbf{k}_f = \mathbf{k}_i + \mathbf{G} \tag{2.83}$$

where $\mathbf{G}$ is a reciprocal lattice vector of the crystal. The wave vector of the photon can be neglected in the XUV spectral range. Owing to the conservation laws 2.82 and 2.83, this step contains all the information about the intrinsic electronic structure of the material.

Electron transport After excitation the electrons move to the surface with the (group) velocity

$$v_e(\mathbf{k}_f) = \frac{\partial E_f(\mathbf{k}_f)}{\hbar\partial\mathbf{k}_f}. \tag{2.84}$$

During this transport process the electrons may experience scattering processes which cause energy loss and a redistribution of their momenta. Due to the stochastic nature of the scattering process, these electrons have lost the link to their initial state and they only contribute to a continuous, decaying low-energy background signal in the photoemission spectrum. This background has to be subtracted by appropriate techniques [136, 143, 145]. The inelastic mean free path of free electrons in solids as a function of their kinetic energy has been investigated and follows a universal curve with slight element-specific deviations, see for example [134, 155]. This curve has a minimum in the relevant energy range of XUV

excitation with a mean free path of only a few Angström. Hence, XUV PES is extremely surface sensitive and primary photoelectrons, which haven't undergone a scattering process, can only be expected from the first few top layers.

Surface transmission The final state of a photo-excited electron within the solid is commonly approximated by a free-electron-like state with a parabolic energy-momentum dispersion. The vertex of this parabola is set to a value V_0 so that the final-state energy matches the electron's kinetic energy in vacuum once it has left the solid

$$E_f(\mathbf{k}_f) = \frac{\hbar^2 k_f^2}{2m} - V_0 = E_{\text{kin}} = \frac{\hbar^2 (k_f^{\text{vac}})^2}{2m}. \tag{2.85}$$

Here, the energy values are referenced to the vacuum level. According to the energy conservation 2.82 it follows

$$E_{\text{kin}} = \hbar\omega - E_i(\mathbf{k}_i) = \hbar\omega - E_B(\mathbf{k}_i) - \phi_W. \tag{2.86}$$

The work function ϕ_W is introduced in the last equation since the binding energy E_B is traditionally referenced to the Fermi-energy level. The term V_0 in 2.85 can be formally considered as a potential step the electrons have to overcome when leaving the surface, thus breaking the translational symmetry along the surface normal. Therefore, only the momentum component parallel to surface is conserved when the electron transmits the surface, i.e. $k_{f||}^{\text{vac}} = k_{f||}$. The initial parallel momentum component is then obtained as

$$k_{i||} = k_{f||}^{\text{vac}} = \frac{\sqrt{2mE_{\text{kin}}}}{\hbar} \sin(\theta). \tag{2.87}$$

Using equation 2.85 the perpendicular momentum is calculated to be

$$k_{i\perp} = \frac{\sqrt{2m}}{\hbar} \sqrt{E_{\text{kin}} \cos^2(\theta) + V_0}. \tag{2.88}$$

The value of V_0 can be estimated by specific experimental methods [32,57] or it is calculated by a priori assumptions for the dispersion of the final state $E_f(\mathbf{k}_f)$. In this way the band structure of a crystal can be reconstructed from the angle-distribution of the kinetic energy of the liberated photoelectrons, i.e. quantities accessible by the experiment.

2.3.2 Photoelectron streaking

Photoelectron streaking constitutes an extension of PES to a pump-probe scheme using the inherently synchronized XUV/NIR pulses from a HHG process. The technique has been originally conceived for attosecond metrology, i.e. the temporal characterization of the attosecond pulses, by mapping time onto energy via a field-dressed photoemission process. The impact of the NIR laser field on the electron wave packet, photo-emitted by the XUV pulse, gives rise to a characteristic shift and deformation of the photoelectron

spectra as a function of the relative delay between XUV and NIR pulse, which is commonly referred to as a streaking trace or spectrogram. By applying a modified FROG-algorithm to this streaking trace, it is possible to completely reconstruct the evolution of the NIR dressing field as well as the temporal structure (including the phase) of the electron wave packet [41], which possibly represents the time structure of the XUV pulse provided the former is a direct imprint of the latter. On the other hand, photoelectron streaking has been demonstrated to be a powerful tool for the investigation of electron transport dynamics on the attosecond time scale. By the simultaneous streaking of different energy levels/bands in gases and solids, an attosecond-scaled delay in the photoemission process has been observed, which triggered a lively and still ongoing debate on the exact mechanisms behind that delay. This finally resulted in the formation of the new research field of attosecond chronoscopy. Moreover, a temporal broadening of photo-excited electron wave packets during their transport in a solid, due to their emission from different depths, could be directly observed in the time-domain by the photoelectron streaking technique. Very recently, the resonant excitation of photoelectrons to unoccupied bands of solids have revealed a strong dependence of the photoemission delay on the dispersion of the band structure [140]. Interestingly, the observed behavior could not be explained by the group velocity dynamics of the involved band dispersion within the scope of a ballistic transport model. Regarding these aspects from previous work, the importance of the extended photoelectron streaking technique which is presented in section 5.3 is manifold: Theoretical approaches for the explanation of the photoemission delay in solids are based on quite different assumptions concerning the role of band structure effects and the properties of the NIR field inside the crystal, leading to discrepancies in their predictions. An angle- and CEP-resolved streaking scheme, however, provides experimental access to the band structure for different NIR field configurations, thereby being able to explicitly discern their influence on the electron wave packet propagation dynamics inside a solid. Moreover, the direct observation of the temporal evolution of electron wave packets (with sub-fs resolution) initiated from different states of the band structure, potentially perturbed and controlled by the CEP of the NIR laser field, may not only contribute to answer open questions about the photoemission process but also allows a deeper and more complete insight into the time-domain behavior of electron dynamics in solid matter in general.

In the following section, the principle of the standard photoelectron streaking method is briefly discussed, as it forms the basis for the evaluation of the streaking traces presented in this work. A basic insight into the streaking technique is already obtained by a semi-classical description in which a photoelectron is instantaneously accelerated in the oscillating linearly polarized electric field $E(t)$ after its release from the surface, thereby experiencing a momentum shift $\Delta p_{||}$ (parallel to the polarization axis) which is calculated, by integrating the classical equation of motion, as

$$\Delta p_{||}(\tau) = m\dot{r}_{||} = -e\int_{\tau}^{\infty} A(t)\cos(\omega_L t + \Phi_{\mathrm{CEP}})\,\mathrm{d}t = -e\mathcal{A}_L(\tau) \tag{2.89}$$

assuming the instant of photoemission is τ. Here, $\mathcal{A}_L(t)$ is the vector potential of the

field in the Coulomb gauge. Within the adiabatic approximation, i.e. $dA/dt \ll A\omega_L$ the integral in 2.89 can be evaluated so that

$$\Delta p_{||}(\tau) = \frac{eA(\tau)}{\omega_L} A(t)\sin(\omega_L\tau + \Phi_{\mathrm{CEP}}) = \sqrt{4U_p(\tau)m_e}\sin(\omega_L\tau + \Phi_{\mathrm{CEP}}). \tag{2.90}$$

The final electron momentum for an arbitrary polarization direction is given by the trigonometric relation $p_f^2 = p_i^2 + 2p_f\Delta p_{||}\cos\Theta - \Delta p_{||}^2$, where Θ is the angle between the polarization axis and the final momentum direction of the electron. The corresponding final kinetic energy then approximately reads

$$E_{\mathrm{kin},f}(\tau,\Theta) = \frac{p_f^2}{2m} \approx E_{\mathrm{kin},i} + 2U_p(\tau)\cos(2\Theta)\sin(\omega_L t + \Phi_{\mathrm{CEP}}) + \sqrt{8U_p(\tau)E_{\mathrm{kin},i}}\cos(\Theta)\sin(\omega_L t + \Phi_{\mathrm{CEP}}). \tag{2.91}$$

The last relation shows that the laser field induced modulation of the final kinetic energy critically depends both on the release time τ and on the observation direction of the electrons. In most cases the observation direction is chosen close to the polarization axis ($\Theta = 0$). On that condition, the second term in 2.91 strongly dominates for typical NIR and XUV parameters used in streaking experiments ($U_p \sim 50$ meV, $E_{\mathrm{kin},i} \sim 50$ eV) and the energy shift reduces to

$$\Delta E_{\mathrm{kin},f}(\tau,\Theta) \approx \sqrt{8U_p(\tau)E_{\mathrm{kin},i}}\cos(\Theta)\sin(\omega_L t + \Phi_{\mathrm{CEP}}) \propto \mathcal{A}_L(\tau). \tag{2.92}$$

Equation 2.92 demonstrates that in the parallel detection geometry the vector potential of the field can be directly sampled by varying the release time τ of the photoelectrons.
Considering the photoelectron in a quantum-mechanical sense as a wave packet with finite temporal duration, it gets apparent from equation 2.92 that the structure of this wave packet will be modified while it is mapped onto the kinetic energy space by the influence of the NIR field as a function of its release time τ, which in turn manifests as a change of the shape of the corresponding energy spectrum. The discussion so far suggests an intuitive interpretation of the streaking trace in which the evolution of the center of gravity as a function of τ represents the vector potential of the NIR laser field whereas the spectral fine structure encodes information about the temporal structure of the electron wave packet. A more rigorous quantum-mechanical description follows the same steps as in section 2.2.2. The Hamilton operator of the TDSE is now given as [4]

$$\hat{H} = \frac{1}{2}(\mathbf{p} - \mathcal{A}_L(t))^2 + V_{\mathrm{eff}}(\mathbf{r}) + \mathbf{E}_X(t+\tau)\mathbf{r}. \tag{2.93}$$

This Hamiltonian already implies an approximation: only the XUV pulse $\mathbf{E}_X(t) = A_X(t)\cdot \mathrm{e}^{-i\omega_X t}\,\mathbf{n}_X$ (with $\mathbf{n}_X$ being the polarization direction) is assumed to contribute to the ionization of the atomic system, while solely the NIR field affects the final momentum state

[4] Atomic units are again used for the remainder of this paragraph.

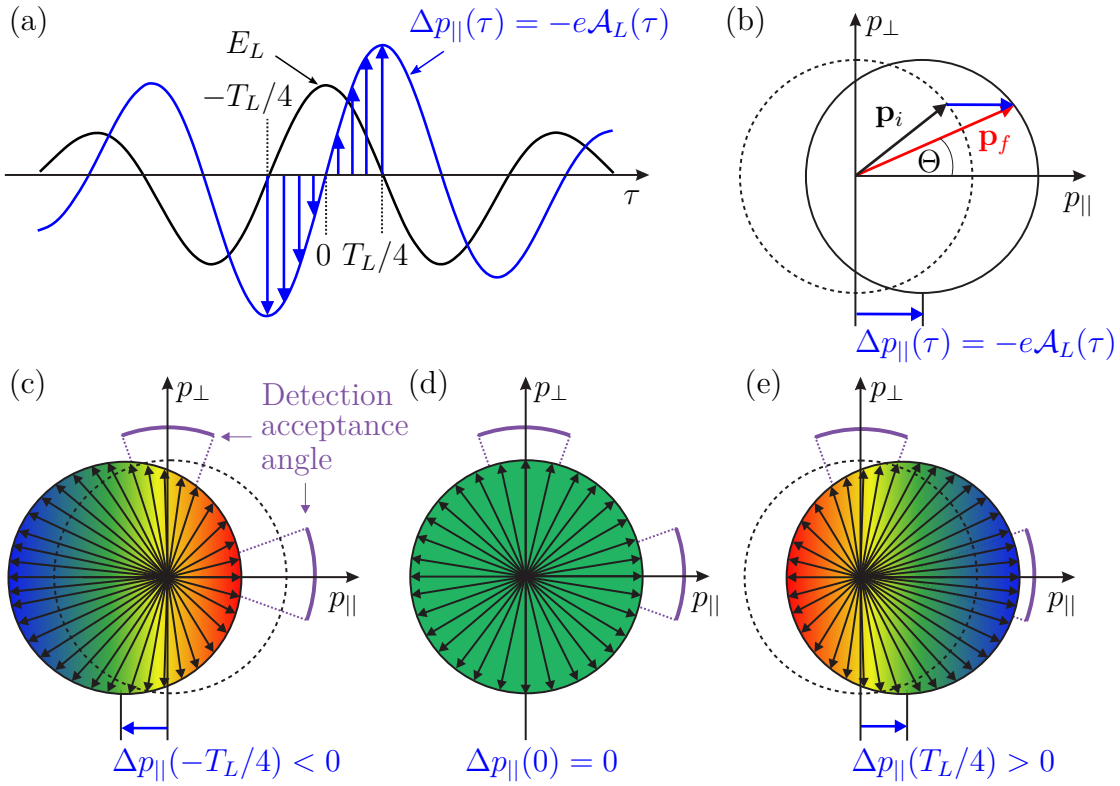

Figure 2.7: The principle of photoelectron streaking. (a): photoelectrons which are released into the NIR field $E_L(t)$ at the instant τ experience a momentum shift $\Delta p_{||}$ which is proportional to the instantaneous vector potential $\mathcal{A}(\tau)$. (b)-(e): Illustration of the streaking effect for an isotropic angle distribution of initial momenta. The laser-field induced perturbation of the initial momentum distribution results in a periodic broadening of the measured electron spectra for an observation angle of $\Theta = 90°$ while an observation angle of $\Theta = 0°$ results in an alternating energy shift. Figure adapted from [95].

of the photo-ionized wave packet via its vector potential $\mathcal{A}_L(t)$. $V_{\text{eff}}(\mathbf{r})$ is again neglected within the strong field approximation. The transition amplitude for populating the final continuum states $|\mathbf{p}\rangle$ with momenta $\mathbf{p}$ is then obtained as [67]

$$\langle \mathbf{p}|\psi(t)\rangle \propto \int_{-\infty}^{+\infty} A_X(t+\tau) M(\mathbf{p} - \mathcal{A}_L(t))\ \mathrm{e}^{-i\Phi_v(\mathbf{p},t)}\, \mathrm{e}^{i(p^2/2 - p_i^2/2)t}\, \mathrm{d}t \tag{2.94}$$

with the Volkov phase

$$\Phi_v(\mathbf{p}, t) = \int_t^{\infty} \left(\mathbf{p}\mathcal{A}_L(t') - \frac{1}{2}\mathcal{A}_L^2(t') \right) \mathrm{d}t', \tag{2.95}$$

describing the NIR field-dressed evolution of the electron wave function in the continuum. Note that the ionization potential and the XUV photon energy define the initial momentum p_i of the photo-ionized electron wave packet in 2.94 according to 2.86 as $p_i^2/2 = \omega_X - E_B -$

ϕ_W. The response of the atomic system is described by the dipole matrix $M \approx \langle \mathbf{p}|\mathbf{r}\cdot\mathbf{n}_X|0\rangle$ evaluated between the ground state $|0\rangle$ and the final state $|\mathbf{p}\rangle$ approximated as the plane wave of a quasi-free electron with final momentum $\mathbf{p}$. The spectrogram of the streaking measurement is finally given by

$$S(E,\tau) = S(p^2/2,\tau) = |\langle p, \psi(t)\rangle|^2 \,. \tag{2.96}$$

It is advantageous to recast equation 2.94 in a form which is compatible with a common FROG spectrogram $S(\omega,\tau)$ given as

$$S(\omega,\tau) = \left| \int P(t) G(t+\tau) e^{i\omega t}\, \mathrm{d}t \right|^2 \tag{2.97}$$

In this way, the structure of the pulse $P(t)$ and the gate function $G(t)$ can be easily reconstructed using efficient FROG algorithms. The central momentum approximation (CMA) is usually applied for this purpose. Within the CMA, the momentum dependence of the dipole matrix element and the Volkov phase is removed by substituting $\mathbf{p} \to \mathbf{p}_c \approx \mathbf{p}_i$ where $\mathbf{p}_c$ is the central momentum of the unstreaked photoelectron spectrum. Hence, the dipole matrix element just contributes a constant value to equation 2.94 and can be neglected. With this approximations it is $P(t) = A_X(t)$ and $G(t) = \exp[-i\Phi_v(\mathbf{p}_c, t)]$. By reconstructing $P(t)$ and $G(t)$ from the streaking spectrogram one gets the complete temporal information of the XUV pulse as well as the laser vector potential. In this work we employ the LSGPA algorithm as discussed in [41], which is typically referred to as FROG-CRAB (complete reconstruction of attosecond bursts). The assumption of a constant dipole matrix element may be justified in the case of non-resonant excitations. As electrons are the mediating particles which are finally detected in the setup of a streaking measurement, it is common to refer to the reconstructed wave form as an electron wave packet. According to the given approximations, the interpretation is quite intuitive: the electron wave packet can be thought of a representation of the temporal emission profile of the photoelectrons. Provided that the photoelectrons immediately experience the streaking field, the reconstructed electron wave packet constitutes an imprint of the temporal structure of the ionizing XUV field. In solids, however, the photoelectrons first undergo a transport process to the sample surface before they feel the streaking field. This may change the structure of the initial wave packet depending on solid-state-specific characteristics, revealing information about the dynamics related to solid-state effects. This is one strength of the angle-resolved streaking technique. However, this intuitive picture doesn't hold when the excitation process is resonant. In this case, the structure of the wave packet now contains information about the (spectrally non-uniform and thus time-dependent) dipole matrix element [153]. However, this 'distortion' may be exploited to gain valuable information about the transition dynamics itself. It should also be noted that the CMA is a poor approximation when the XUV pulse length exceeds the half period of an optical field cycle [41]. In this case, the reconstructed wave packet becomes inaccurate and especially the phase may exhibit severe deviations.

Chapter 3

Beamline development

In the course of this thesis an entire high harmonic beamline was planned, designed, constructed and assembled, from the laser front end up to the experimental end station including the implementation of all required setups and techniques for laser pulse shaping, dispersion management, high harmonic generation, beam characterization, sample preparation and handling and the engineering of most of the mechanical assemblies such as the vacuum system, the differential pumping system, the XUV spectrometer, the delay unit and the sample load lock system. The design, test and performance of the individual parts are presented in the subsequent chapters.

3.1 Laser front end and pulse shaping

3.1.1 The 10 kHz laser system

The laser front end of the beamline provides the laser pulses which drive the HHG process and comprises all setups and techniques for pulse creation, amplification and shaping. It is designed to deliver few-cycle pulses with a center wavelength in the near-infrared (NIR) at an enhanced repetition rate of 10 kHz. The increase of the repetition rate from 1-3 kHz of prevailing high harmonic sources to 10 kHz marks a valuable improvement for time-resolved PES experiments which are prone to space charge distortions. The outline of the laser front end is illustrated in figure 3.1. A commercial femtosecond laser source (Femtopower Compact Pro, Femtolasers GmbH), consisting of a Kerr-lens mode-locked Ti:Sapphire laser oscillator followed by a Ti:Sapphire multi-pass chirped pulse amplification (CPA) system, outputs a pulse train of $\sim 400\,\mu$J pulse energy and 25 fs FWHM pulse duration centered at 780 nm. Pulse compression is performed by a grating compressor in combination with an acousto-optical dispersion filter (AODF) for optimizing the temporal pulse structure. The 10 kHz amplifier system was a prototype at that time derived from a 3 kHz system. Accordingly, it suffered from initial deficiencies which have been remedied gradually. Therefore, not all stages of measurements presented in this work could benefit from the latest features and improvements of the system (as it is described in this section).

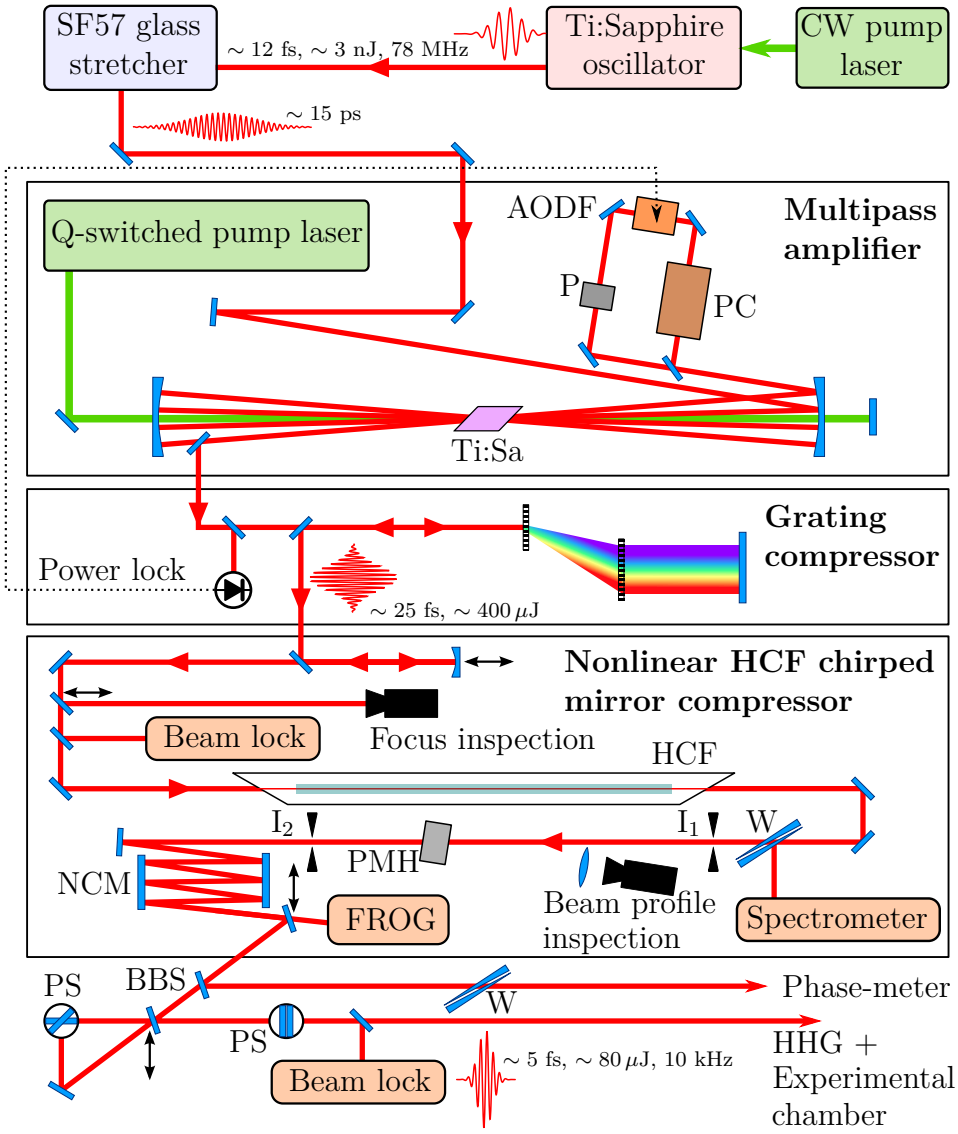

Figure 3.1: Layout of the 10 kHz few-cycle laser front end. AODF: acousto-optical dispersion filter, P: polarizer, PC: pockels cell, HCF: hollow-core fiber, I: alignment iris, W: glass wedges, PMH: power meter head, NCM: negatively chirped mirrors, BBS: low-GDD broadband beam-splitter, PS: periscope, in crossed-mirror and parallel-mirror configuration.

A major problem was related to insufficiencies in the thermal management which lead to significant drifts in output parameters. An improved cooling capacity with higher stability and a power feedback loop could solve the issue. A photodiode after the amplifier section provides now a feedback signal for the transmission function of the AODF in order to stabilize and smooth the long-term power output. The output pulses from the CPA are further compressed to the few-cycle regime by an external nonlinear fiber compressor (see next section) before they are focused into the HHG target. Naturally, the increased repetition rate comes at the expense of a reduced pulse energy compared to systems at lower rates, requiring a medium with sufficiently high nonlinearity in the hollow core fiber compressor and a tighter focusing geometry for the HHG process. Few-cycle pulses with a duration of 5 fs pulses and an energy of 150–170 μJ centered at 720 nm are finally obtained after the external compressor setup. Before the pulses are fed into the vacuum system for HHG and to the experiment, 30% of their energy is reflected by a broadband low-GDD beam splitter to a stereographic ATI phase-meter for CEP tagging, see section 2.1.2. Moreover, the polarization direction of the laser pulses, and thus the polarization direction of the high harmonic radiation can be adapted to different experimental requirements. It can be switched between horizontal and vertical by directing the beam either via a parallel or a crossed periscope into the vacuum chamber. This scheme inherently supports spectrally broadband pulses without impairing their polarization's degree of linearity, as opposed to approaches which use (intrinsically narrow-band) NIR wave-plates. A high degree of linearity is absolutely essential for an efficient high harmonic conversion from gas targets [15].

3.1.2 Nonlinear pulse compression by SPM

Goal of this setup is to generate sub-7 fs few-cycle laser pulses as a driver for the high harmonic generation process and as an excitation source which enables CEP sensitive measurements. The pulse duration obtained at the output of the multi-pass amplifier is limited to about 25 fs due to gain narrowing. Further compression down to sub-7 fs has to be done in an external setup and is achieved by spectral super-continuum generation by means of self phase modulation (SPM) followed by appropriate chirp compensation. The use of noble gas as a nonlinear medium filled into a hollow core fiber has established as a standard method for this purpose with the given pulse energies. The fiber guides the focused laser beam over a sufficiently long distance so that the desired spectral content can build up. Furthermore, the magnitude of nonlinearity can be conveniently adjusted by changing the gas pressure in the fiber and, opposed to a solid nonlinear medium, material damage is of no concern. On the other hand, ionization losses can be quite high, reducing the total throughput of the compressor setup below 50%. For the design process of the hollow core fiber compressor it is essential to understand the spatial and temporal pulse evolution inside the fiber. The temporal evolution regarding material dispersion and nonlinear polarization response was dealt with in section 2.2.1. In this section, we focus on the spatial field distribution of guided modes in the fiber core which is important for an efficient coupling of power from the laser pulse into the fiber modes. The proper coupling condition in turn determines the focusing requirements. A hollow fiber represents a

step-index fiber with a refractive core index of $n_i = 1$ and the refractive index n_e of the glass cladding. The cylindrical axis of the fiber is aligned to the z-axis. Customarily, the ansatz [2]

$$\hat{\mathbf{E}}(\mathbf{r},\omega) = \mathbf{F}(x,y)\hat{A}(z,\omega)\exp[i\beta(\omega)z] \tag{3.1}$$

is used to describe the field inside the fiber, where the electric field is separated into the transverse mode distribution $\mathbf{F}(x,y)$ and the spectral mode amplitude $\hat{A}(z,\omega)$ with the propagation constant $\beta(\omega)$. The solution of the wave equation for $F(x,y)$ under the constraints of the cylindrical fiber geometry [92,137] leads to a set of natural modes sustained by the fiber, designated by HE_{nm}. It turns out that only the HE_{1m} modes are quasi linearly polarized [38] where either the x- or y-field component dominates while the component in z-direction gets negligibly small. Only these modes are of interest regarding an excitation with a linearly polarized laser pulse. Their transverse field distribution is given by

$$\mathbf{F}(x,y)_{1m} \propto J_0\left(u_{1m}\frac{r}{a}\right)\mathbf{x} \tag{3.2}$$

where $r = \sqrt{x^2+y^2}$, J_0 is the zeroth-order Bessel function, a the bore radius of the fiber and u_{1m} the m-th root of J_0. Here we have set the polarization direction to the x-direction without loss of generality. The HE_{11} mode is referred to as fundamental mode of a hollow core fiber. The propagation constant β is obtained from the boundary conditions, i.e. from the continuity of fields at the core-cladding interface. For the HE_{1m} modes it is determined as

$$\beta_{1m} = k\left[1 - \frac{1}{2}\left(\frac{u_{1m}\lambda}{2\pi a}\right)^2\left(1 - i\frac{\lambda(\nu^2+1)}{2\pi a\sqrt{\nu^2-1}}\right)\right] \tag{3.3}$$

where $k = \frac{2\pi}{\lambda}$ and $\nu = \frac{n_e}{n_i}$. As usual, the attenuation constant of the mode is given by the imaginary part of the propagation constant

$$\alpha_{1m} = \mathrm{Im}\{\beta_{1m}\} = \left(\frac{u_{1m}}{2\pi}\right)^2\frac{\lambda^2}{2a^3}\,\mathrm{Re}\left\{\frac{\nu^2+1}{\sqrt{\nu^2-1}}\right\}. \tag{3.4}$$

As evident from equation 3.4, the intrinsic modal attenuation increases with the mode order and can be made, in principle, arbitrarily small for the fundamental mode by choosing an appropriate bore radius according to the λ^2/a^3 dependency. In reality, another loss mechanism is introduced by fiber bending which provokes additional power leakage through the fiber cladding. Including this bending loss the attenuation constant has to be corrected for by an additional attenuation term and is then described by [38]

$$\alpha_{1m}(R) = \alpha_{1m}(\infty)\left[1 + \frac{4}{3}\left(\frac{2\pi a}{u_{1m}}\right)^4\left(\frac{a}{R}\right)^2\right] \tag{3.5}$$

with the bending radius R. $\alpha_{1m}(\infty)$ is the attenuation constant (3.4) for the straight fiber ($R = \infty$). Equation 3.5 shows that the fundamental mode is most affected by bending losses. Therefore, it has to be ensured that this loss channel is minimized by a rigid

construction and precise fabrication of the fiber mount. For fiber lengths ≤ 1 m bending losses can be kept small compared to the intrinsic modal loss. Finally, a third source for power loss if given by gas ionization. This loss mechanism can make up a major part of the beam attenuation and also determines the choice of gas type and sets an upper limit for the beam intensity.
For an efficient power coupling into the fiber good mode matching between laser pulse and fundamental fiber mode is required. Mode mismatch leads to an increase of losses and to the excitation of higher order modes which significantly lowers the output beam quality. The power P_m^c which is coupled into the m-th order mode can be estimated by the overlap integral

$$P_m^c = \iint_A \mathbf{E}_i \times \mathbf{H}_{1m} \cdot \mathbf{z} \, \mathrm{d}A \tag{3.6}$$

where $\mathbf{E}_i$ is the electric field of the incident beam and $\mathbf{H}_{1m}$ the magnetic field of the excited fiber mode. Integration is performed over the fiber cross section. Using a Gaussian field distribution of the incident beam $\mathbf{E}_i(r) = E_0 e^{-r^2/w^2}\mathbf{x}$, polarized in x-direction, and the magnetic field of the excited mode according to equation 3.2 as $\mathbf{H}_{1m} = H_0 J_0\left(u_{1m}\frac{r}{a}\right)\mathbf{y}$, polarized in y-direction, the coupling efficiency $\eta_m = \frac{P_m^c}{P_{\mathrm{in}}}$ is calculated as [93]

$$\eta_m = \frac{|\int_0^a e^{-\frac{r^2}{w^2}} J_0\left(u_{1m}\frac{r}{a}\right) r \, \mathrm{d}r|^2}{\int_0^{\mathrm{inf}} e^{-\frac{2r^2}{w^2}} r \, \mathrm{d}r \int_0^a J_0^2\left(u_{1m}\frac{r}{a}\right) r \, \mathrm{d}r}. \tag{3.7}$$

The total power loss after propagating a distance z in the fiber is finally given by

$$L_{\mathrm{tot}} = 1 - \sum_m \eta_m e^{-2\alpha_{1m} z}. \tag{3.8}$$

The coupling efficiencies of the fundamental and the next 3 higher modes ($m = 1, 2, 3, 4$) as function of the normalized beam waist $\frac{w}{a}$ are plotted in figure 3.2. Also plotted is the intrinsic modal transmission efficiency through the fiber as function of fiber length z for these modes. The fiber parameters are $a = 125$ μm and $n_e = 1.5$ (corresponds to typical values of the fiber used in this work). The intrinsic transmission losses are lowest for the fundamental mode HE_{11}. Furthermore, this mode allows the highest coupling efficiency. Therefore, it is highly favorable to only excite this mode. Best coupling condition is obtained with a normalized beam waist of $\frac{w}{a} = 0.64$, yielding a coupling efficiency to the fundamental mode larger than 90% while the efficiency for the next higher mode HE_{12} is only 0.5%. Hence, good mode discrimination can be expected for this launch condition even for a short fiber length. This is also quite beneficial for the subsequent HHG process. However, an evaluation of equation 3.8 suggests a slightly smaller normalized beam waist than 0.64 in order to minimize the total loss, especially in the case of a short fiber length or a large bore size. On the other hand, coupling into the fiber with slightly larger values than 0.64 does not significantly impair mode discrimination and coupling efficiency, but usually leads to increased fiber-end heating which shortens the lifetime of the fiber

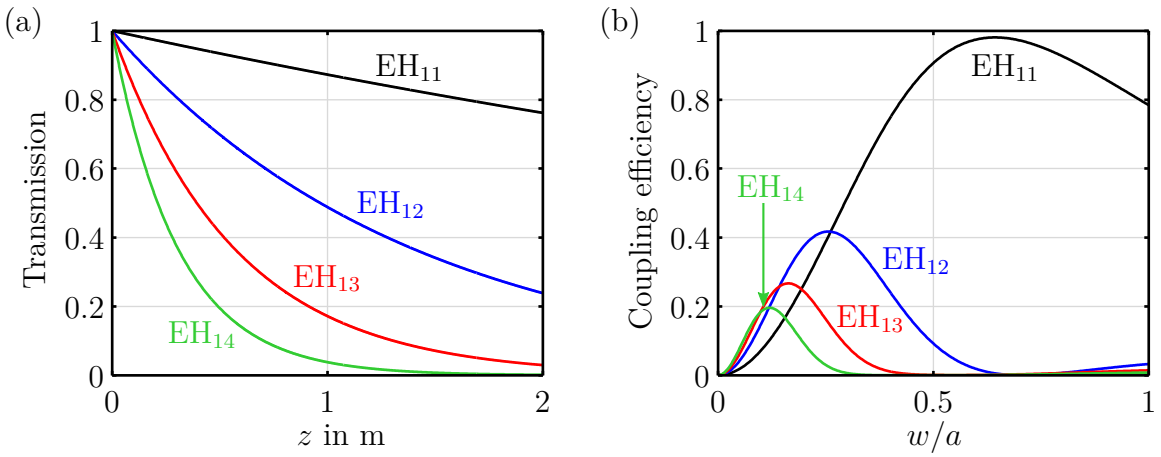

Figure 3.2: Efficiency characteristics of the hollow core fiber. (a): Mode transmission efficiency. (b): Mode coupling efficiency.

input face [98]. Typically, values for $\frac{w}{a}$ between 0.6 and 0.7 are a good choice. It is also noted that, in practice, any spatio-temporal pulse distortions, fiber misalignment and fiber manufacturing tolerances may heavily reduce the total transmission efficiency below the theoretical expectation value and can also cause a different fractional distribution of the modal coupling efficiencies.

The focus profile as it is used to couple the laser pulses into a fused silica hollow core fiber with a bore diameter of 300 μm is shown in figure 3.3(a). The normalized beam waist has a mean value of 0.66, which is close to the theoretical optimum. Figure 3.3 shows the amount of spectral broadening achieved by a fiber length of 1 m filled with neon. The intensity at the focal plane is $7.4 \cdot 10^{13}$ W/cm^2. The spectral broadening factor F, defined as

$$F = \frac{\Delta\lambda_{\mathrm{HCF}}^{\mathrm{RMS}}}{\Delta\lambda_{\mathrm{Amp}}^{\mathrm{RMS}}}$$

is only 3.1 at a pressure of 1500 mbar. The fragile Brewster windows at the end faces of the vacuum chamber which houses the fiber do not support a pressure above $\approx$ 2000 mbar, and therefore, they set a limit for the applicable gas pressure. Better spectral broadening for the given laser intensity at more practical pressures below 1000 mbar is achieved with argon which exhibits a considerably higher nonlinearity than neon [12]. SPM broadened output spectra are shown in figure 3.4 for different gas pressures. Also shown are the corresponding temporal intensity profiles after chirp compensation, reconstructed from NIR FROG measurements. The FROG device uses a four-wave mixing process with a resultant signal beam of the fundamental frequency. Hence, the setup does not suffer from phase mismatch generated by temporal and spatial walk-off. The finite crystal thickness of 70 μm however induces a systematic error of a few percent. A spectral broadening factor of $F = 7.5$ is obtained at a pressure of 900 mbar which results in an octave-spanning output

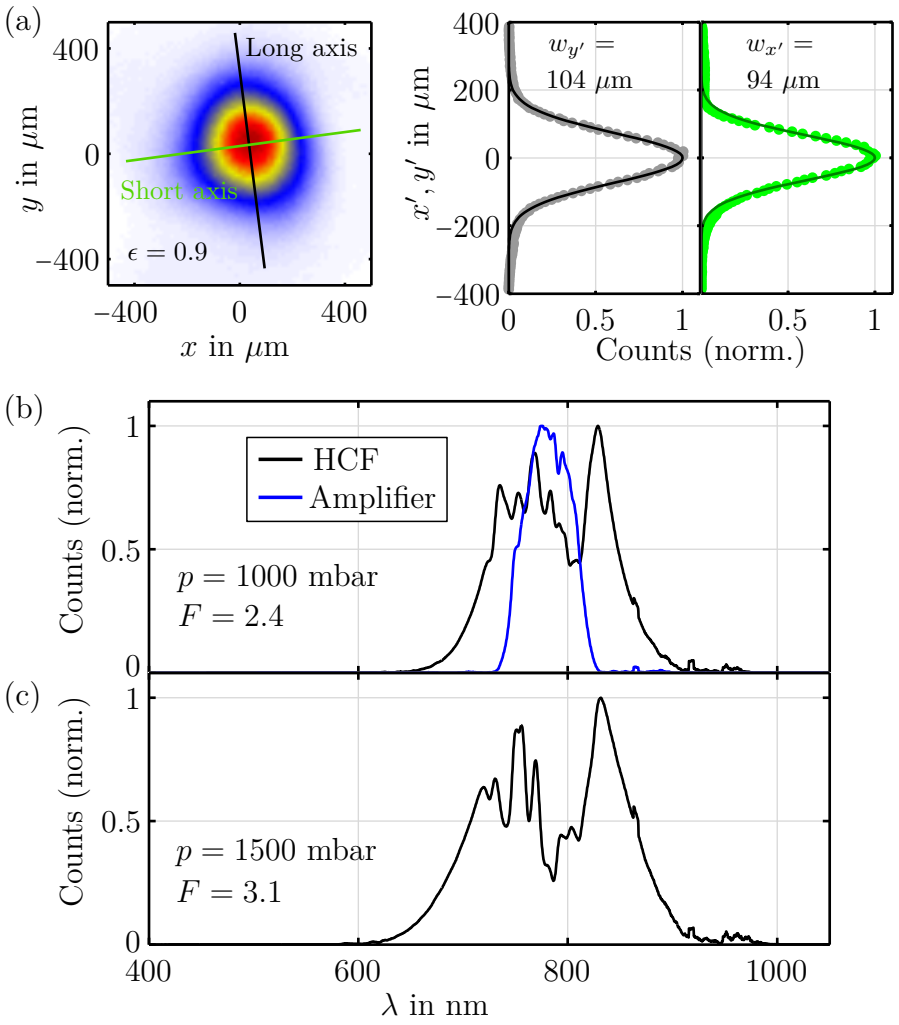

Figure 3.3: SPM-induced spectral broadening of the amplified NIR pulses in neon. (a): Focal beam profile as used for coupling to the fiber as well as cross-sections along the short and long axis. ϵ: beam ellipticity. (b): HCF input and output spectrum at a gas pressure of 1000 mbar. (c): HCF output spectrum at a gas pressure of 1500 mbar.

spectrum that supports sub-5 fs pulses. The overall throughput is typically 45% where ionization losses in argon make up the dominant loss mechanism. Chirp compensation is achieved by multiple reflections on dispersive multilayer mirrors in combination with a thin pair of adjustable glass wedges. The mirrors have been fabricated in house (courtesy of V. Pervak). Two designs have been developed whose spectral reflectivity and dispersion characteristics are shown in figure 3.5. The first design supports a bandwidth from 600-1000 nm while the bandwidth of the second design was increased to 470-1050nm. Mirror pairs are operated at two distinct angles of incidence in order to reduce their spectral dispersion ripple which is characteristic to multilayer optics. Sub-7 fs pulses were obtained with the first design (not shown in this summary), while the second design could achieve

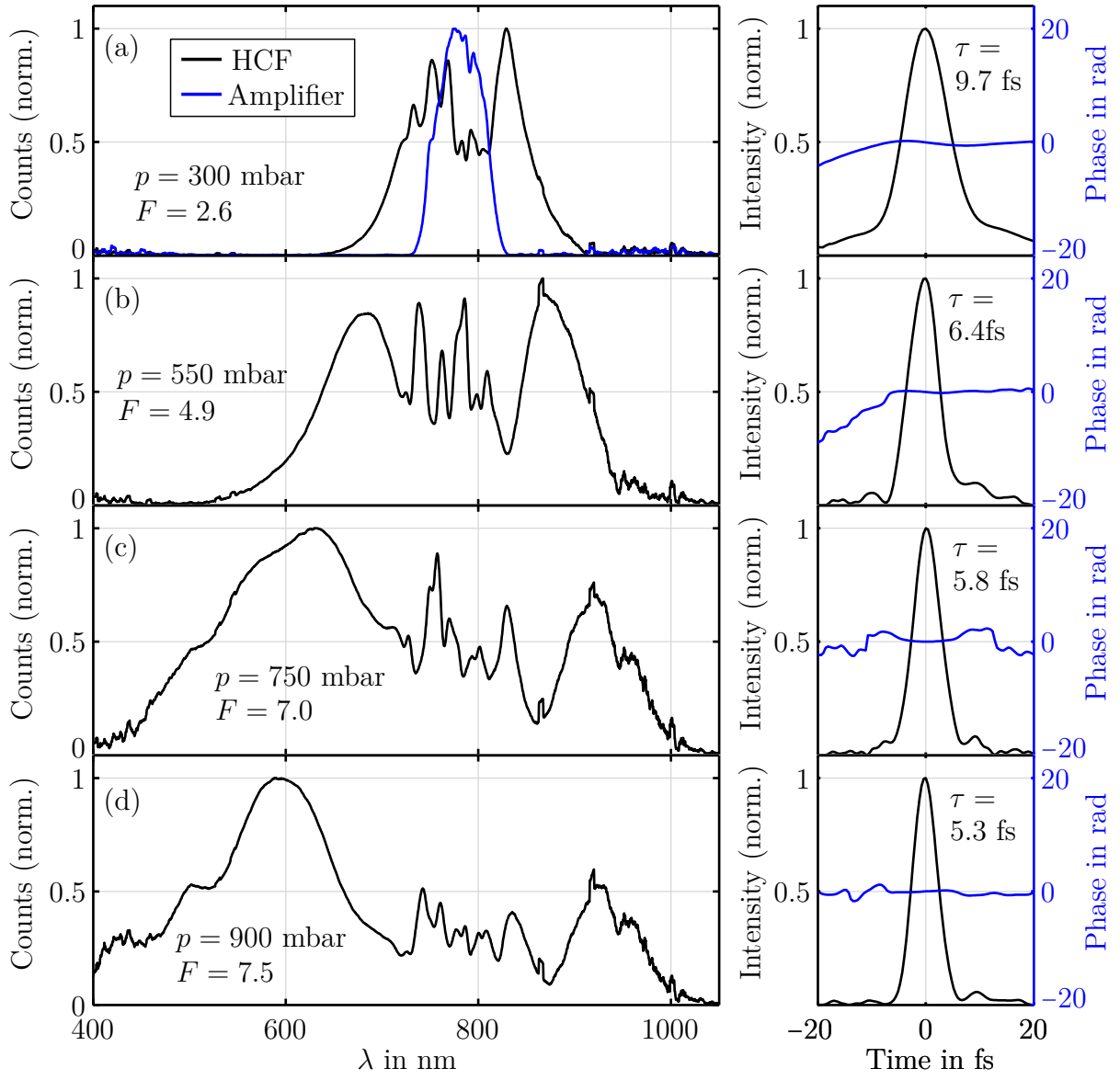

Figure 3.4: SPM-induced spectral broadening of the amplified NIR pulses in argon. (a:) HCF input and output spectrum at a gas pressure of 300 mbar. (b): HCF output spectrum at a gas pressure of 550 mbar, (c): 750 mbar and (d): 900 mbar. Right column: Corresponding temporal intensity structure reconstructed from FROG measurements. The value indicates the FWHM pulse duration.

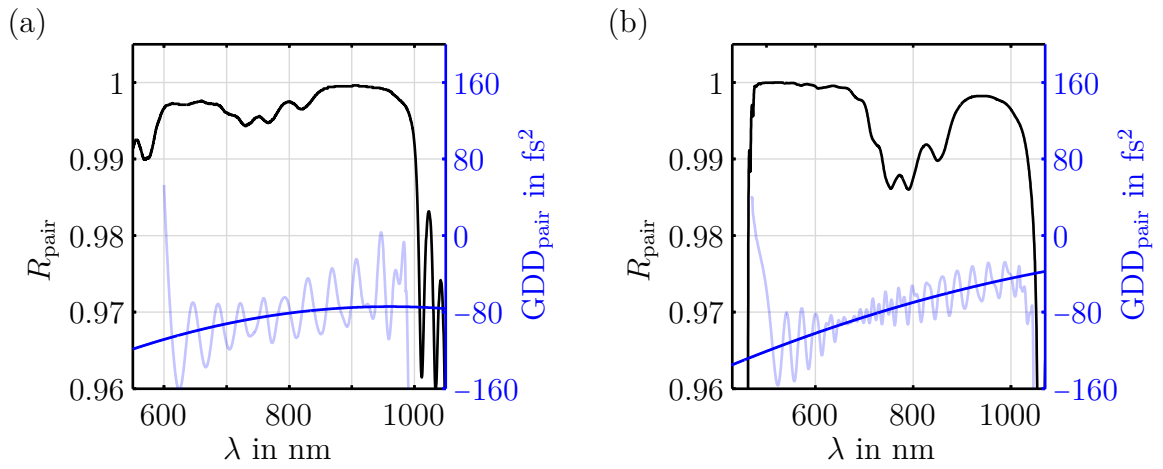

Figure 3.5: Spectral reflectivity and dispersion characteristics of the optical mirror compressor as obtained from multilayer simulations. Shown are the properties for a single mirror pair. Each mirror pair is operated at two distinct angles of incidence to reduce dispersion ripple (light blue lines). The blue lines are polynomial fits of second order to approximate the dispersion behavior. (a): First mirror design supporting a bandwidth from 600-1000 nm. (b): Second mirror design with increased bandwidth from 470-1050 nm.

sub-5 fs pulses as demonstrated in figure 3.4. A set of 5 mirror pairs was used for this measurement and all the following experiments.

3.2 Vacuum line and experimental end station

This section describes the entire vacuum part of the beam line. An overview of the involved parts and devices as well as their arrangement is shown in figure 3.6. The following sections provide a description, design considerations as well as test and characterization results of the individual parts.

3.2.1 HHG chamber

The high harmonic target chamber comprises all parts necessary for the high harmonic generation process, i.e. folding mirrors, the focusing mirror, the gas nozzle and necessary motorized tables and mechanics. It is equipped with a 600 l/s turbo pump to handle the high gas load. The chamber is part of the optical table, vibration dampers prevent the transmission of vibrations from the vacuum pump on the optical setup. All components inside the chamber are mounted onto a breadboard which is firmly attached to the optical table but decoupled from the chamber body, see figure 3.7. Likewise, the port with the entrance window is also decoupled from the chamber body by a flexible bellow and fixed to a rigid post which is part of the optical table. This scheme provides highest beam stability inside the vacuum system towards the gas nozzle and finally towards the sample target in

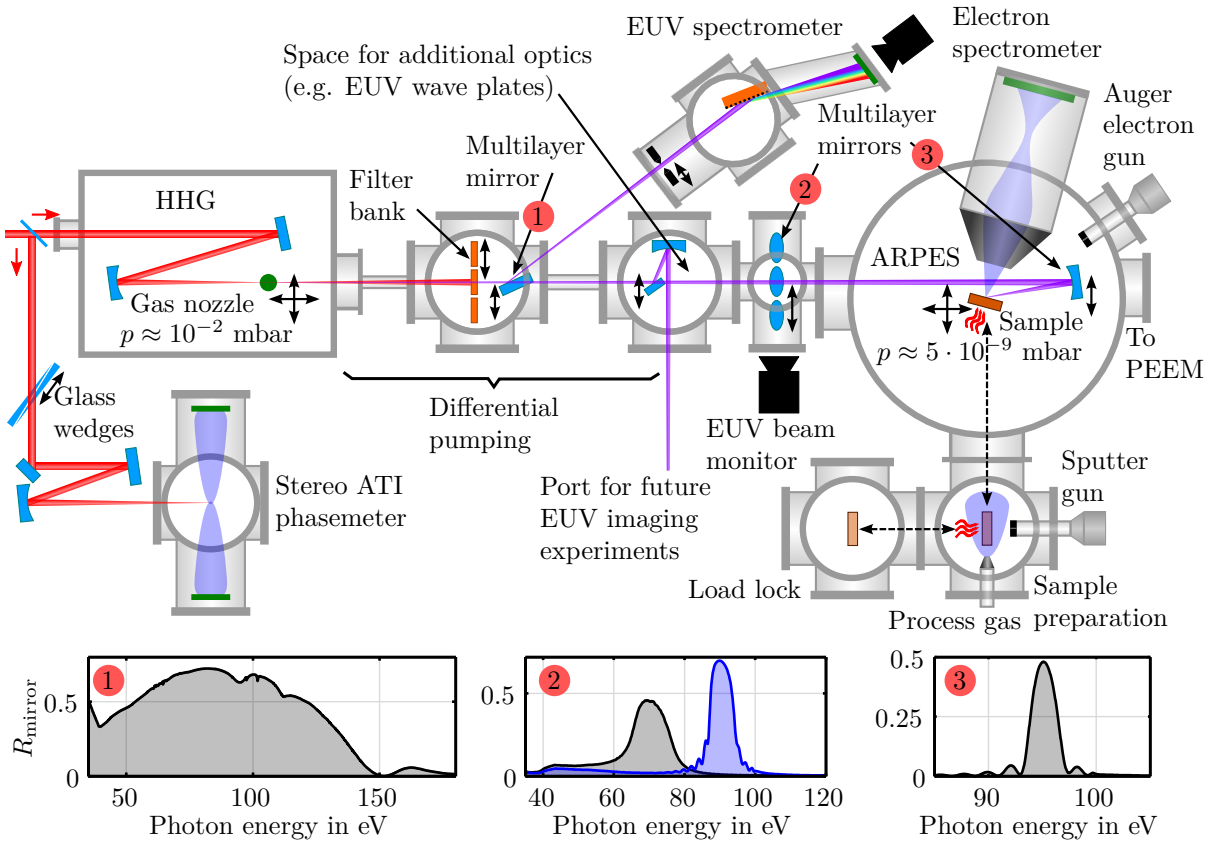

Figure 3.6: Vacuum back end of the beamline, including the phase-meter, the HHG chamber, the differential pumping system, the XUV beam diagnostics (beam monitor and spectrometer) as well as the experimental end station with the electron spectrometer and the setup for sample handling and preparation. The 3 graphs at the bottom depict the reflectivity of the multilayer mirrors used for the XUV spectrometer, the XUV beam monitor and the streaking experiment.

the experimental chamber. The chamber allows an easy adaption of the focal length up to 80 cm without complicated folding geometry. Furthermore, chamber and breadboard provide enough space for additional optics such as beam splitters, wave-plates, polarizers or nonlinear crystals (e.g. for SHG) as it would be required for further manipulation of the driving laser pulse and for multi- or bi-chromatic excitation of the harmonic process, which is subject of ongoing theoretical considerations and experimental developments. The placement of additional parts to the vicinity of the gas target ensures best stability and beam drift performance. In this way, the HHG setup can be easily adapted to future needs and requirements. High harmonic radiation is generated by interaction of the few-cycle pulses with noble gas in a free gas jet configuration. The gas nozzle is either formed by a thin metal tube (nickel, stainless steel) which is closed at one side or a tapered glass capillary which is used in end-fire geometry. The other end of the tube/capillary is connected to the gas line with a gas flow regulator. The metal tube nozzle contains a mechanically drilled orifice in the front and back wall which allows the laser beam to

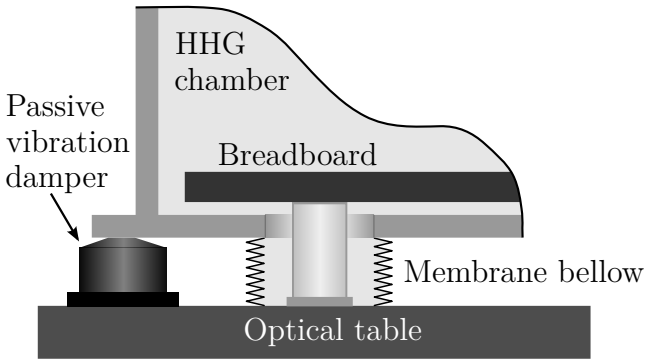

Figure 3.7: Construction of the vibration isolation scheme for the HHG chamber. The breadboard is firmly fixed to the optical table while the chamber body is connected to it via vibration dampers with low resonance frequency ($f_R = 3.5$ Hz) and a transmissibility of smaller than -40 dB for $f > 50$ Hz.

transmit the nozzle and interact with the gas inside the tube. The diameter of the orifice is a critical design parameter as it determines the stability of the harmonic output yield (see section 4.1) on the one hand and the gas load in the main chamber on the other hand. While the backing pressure in the nozzle determines the phase-matching of the HHG process (which may require quite high backing pressures for certain gas types), the maximum allowable gas load is limited by the turbo pump. Therefore, it has to be ensured that the pumping capacity allows for optimum phase-matching adjustments. The latter requirement suggests a rather small hole size. On the other hand, any interaction of the laser beam with the nozzle material, e.g. at the rim of the orifice, is highly unfavorable as thermally and chemically induced gradual changes of the orifice geometry cause significant instabilities in the harmonic output. It was found that, with respect to our focusing geometry and HHG in neon, an orifice diameter of 150-200 μm allows optimum phase-matching adjustments and provides good stability at the same time. Moreover, in order to minimize instabilities induced by beam drifts, the laser beam is actively stabilized in position and angle before it enters the HHG chamber. For this purpose, the weak reflex from the entrance window serves as a reference beam which is sent to two position sensitive detectors. These create a feedback signal for two motorized mirror mounts in front of the chamber which finally keep the beam axis stationary. The nozzle itself is mounted on a motorized table which allows the precise 3D-alignment of the orifice with respect to the laser beam and its axial focus position for phase matching adjustments. Furthermore, as already mentioned before, the polarization direction can be switched between vertical and horizontal by means of two different periscope configurations without impairing the polarization's degree of linearity of the broadband NIR pulses. Horizontal polarization is used throughout this work. However, the lateral deflection of the XUV beam to an alternative experimental end station for future XUV imaging experiments, as indicated in figure 3.6, requires vertical polarization since the deflecting multilayer mirrors are operated in Brewster geometry. Horizontal polarization corresponds in this case to p-polarization,

heavily degrading the reflectivity performance.

3.2.2 Differential pumping

The purpose of the differential pumping section is to bridge the pressure difference between the high harmonic chamber, which is at a moderate vacuum level, and the experimental chamber which is ideally kept at ultra high vacuum (UHV) conditions. The ultimate pressure limit in the HHG chamber is 10^{-2} mbar (operation limit of the turbo pump). The vacuum requirements in the experimental chamber, however, are quite stringent in order to keep the sample surface clean and free of contamination during the data acquisition time t_{aq}. Due to the high surface sensitivity of XUV PES (see section 2.3.1), even one monolayer of adsorbate on the sample surface may considerably disturb the measurement. The mono-time t_1, i.e. the time it takes for residual gas particles in an atmosphere of pressure p at room temperature to form one monolayer on an area unit is given by (assuming a sticking coefficient of unity) [90]

$$t_1 \approx 3.6 \cdot 10^{-6} \frac{1}{p} \tag{3.9}$$

where p is in mbar and t_1 in seconds. In order to minimize the impact of contamination during the measurement it has to be ensured that $t_{\mathrm{aq}} \lesssim t_1$. A background pressure of $p = 10^{-9}$ mbar results in a mono-time of $t_1 \approx 1\mathrm{h}$ which is reasonable for a typical PES measurement. A physical separation of HHG and experimental chamber in order to support a large pressure difference is difficult to implement in the XUV regime and not always possible. Only ultra-thin metal foils (typical thickness below 1 μm) can be used for this purpose. Their fragility requires special care and restricts their applicability. For this reason, we have designed a differential pumping system which is able to maintain a pressure difference of at least 6 orders of magnitude (from 10^{-2} mbar to at least 10^{-8} mbar) even without physical separation. Main goal is the development of suitable vacuum connections

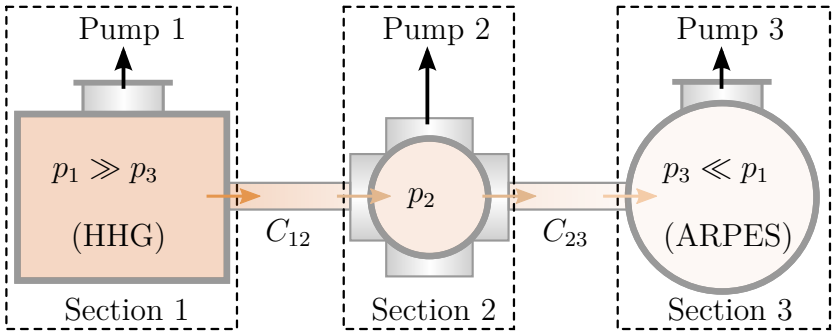

Figure 3.8: Model for simulating the pressure distribution in the vacuum line. The number of sections n is given by the number of vacuum vessels within which the pressure is assumed to be constant. The gas flow between them is governed by the mutual conductivities $C_{i,i+1}$, $i < n$.

between the chambers which restricts the gas flow, and hence the balancing of the pressure

gradient, usually with the help of additional pumping stations in between. In order to keep the physical dimension of the system compact we only use one additional intermediate pumping station. The required pumping speed S for this pumping station is to be determined as well. For this purpose, the entire vacuum line is modeled as a series of 3 vacuum segments consisting of HHG chamber, intermediate pumping station and experimental chamber with mutual flow conductances C between adjacent segments. For each segment n the net gas flow Q_n (in mbar·l/s) which sums up all incoming and outgoing gas flows reads

$$Q_n = R_n + (p_{n-1} - p_n)C_{n-1,n} - (p_n - p_{n+1})C_{n,n+1} - S_n p_n \quad n = 1, 2, 3 \tag{3.10}$$

where R_n considers the total parasitic gas inflow such as from desorption, outgassing and potential leaks as well as the gas stream from the HHG gas nozzle (only for $n = 1$). The second and third term describe the gas flow from and to the adjacent segment with higher and lower pressure, respectively, and finally the last term represents the gas outflow through the attached vacuum pumps. At equilibrium it is $Q_n = 0$ and the set of equations 3.10 can be summarized in matrix form as

$$\mathbf{R} = \mathbf{p} \cdot (\mathbf{C} + \mathbf{S}) \tag{3.11}$$

with a tridiagonal conductance matrix $\mathbf{C}$ and a sparse diagonal matrix for the pumping speeds $\mathbf{S}$. The values for R_n are obtained by measuring (or reasonably estimating from experience) the end pressure $p_{0,n}$ for each segment when encapsulated, i.e. without any connection to adjacent segments. Consequently, R_n is given by

$$R_n = S_n p_{0,n}. \tag{3.12}$$

Using equations 3.11 and 3.12 one can iteratively determine the required pumping speed S_2 of the intermediate pumping station as well as the corresponding conductance values $C_{n,m}$ required to fulfill the above given pressure constraint for the experimental chamber. We restrict the following calculations to the molecular-flow pressure regime which is a good approximation for the high and ultra high vacuum range. In this case, the conductance values are independent on pressure and can be generally expressed for an arbitrary pipe geometry as

$$C = C_A \cdot \mathcal{P} \tag{3.13}$$

where C_A is the conductance of the entrance aperture of the pipe and $\mathcal{P}$ is the free molecule transmission probability which depends on the specific pipe geometry. Formulas for both quantities and different geometries can be found in [90]. Only round geometries are relevant in our case for which it is

$$C_A = 9.1 \cdot d^2 \tag{3.14}$$

where d is in cm, and

$$\mathcal{P} = \left(1 + \frac{3}{8}\frac{l}{r}\right)^{-1} \xi^{-1}. \tag{3.15}$$

ξ is a correction factor depending on the ratio $\frac{l}{r}$ [10]. The total transmission probability of a serial concatenation of apertures and pipes can be calculated by

$$\mathcal{P}_{\text{tot}}^{-1} = 1 + \sum_{i=1}^{m} \frac{A_e}{A_i} \left[(\mathcal{P}_i^{-1} - 1) + \left(\frac{A_i}{A_{B,i}} - 1 \right) \right] \tag{3.16}$$

where A_e is the cross section of the entrance aperture of the entire setup, A_i and $\mathcal{P}_i$ are the cross section and transmission probability of the i-th pipe and $A_{B,i}$ is the cross section of the exit aperture of the i-th pipe. From equations 3.13-3.16 it is obvious that long and narrow pipes are highly favorable. The best pipe geometry is certainly a conical pipe whose opening angle is adapted to the beam divergence. Such a pipe geometry is difficult to fabricate, but it can be approximated by a straight pipe filled with segments of round apertures of gradually increasing diameter. The available lab space sets a constraint for the length of the differential pumping system of 1 m, which leaves a length of approximately 40 cm for connection pipe 1 and 30 cm for pipe 2. Figure 3.9 shows simulated expectation values for different design parameters. The range of conductivity values required to maintain a pressure difference from $p_1 \leq 5 \cdot 10^{-3}$ mbar to $p_3 \geq 10^{-8}$ mbar is depicted as green region in figure 3.9(a) with the assumption of $p_{0,3} = 10^{-9}$ mbar. Simple standard DN16/DN25 straight vacuum tubes are not applicable as indicated, whereas modified tubes with a set of additional apertures inside can shift the conductivity value into the suitable range. The number and diameters of an appropriate set of apertures is found by using equation 3.16. A set of 5 apertures per pipe turned out to be sufficient. The conical shape represents the ideal case and sets the limit of what is possible. Pipe 1 holds an in-vacuum extension with a long but small bore diameter. A cross-section of this pipe is shown in figure 3.9(c). Using this final pipe design, the expected pressure p_3 in the experimental chamber as a function of pumping speed S_2 (intermediate chamber) for different initial pressures $p_{0,3}$ is plotted in figure 3.9(b). It can be seen that the end pressure p_3 saturates with increasing pumping speed. Therefore, the benefit of an expensive pump with highest pumping speed is only marginal. Moreover, the presented design does not support end pressures $p_3 \leq 10^{-9}$ mbar even when the initial pressure $p_{0,3}$ is well below this value.

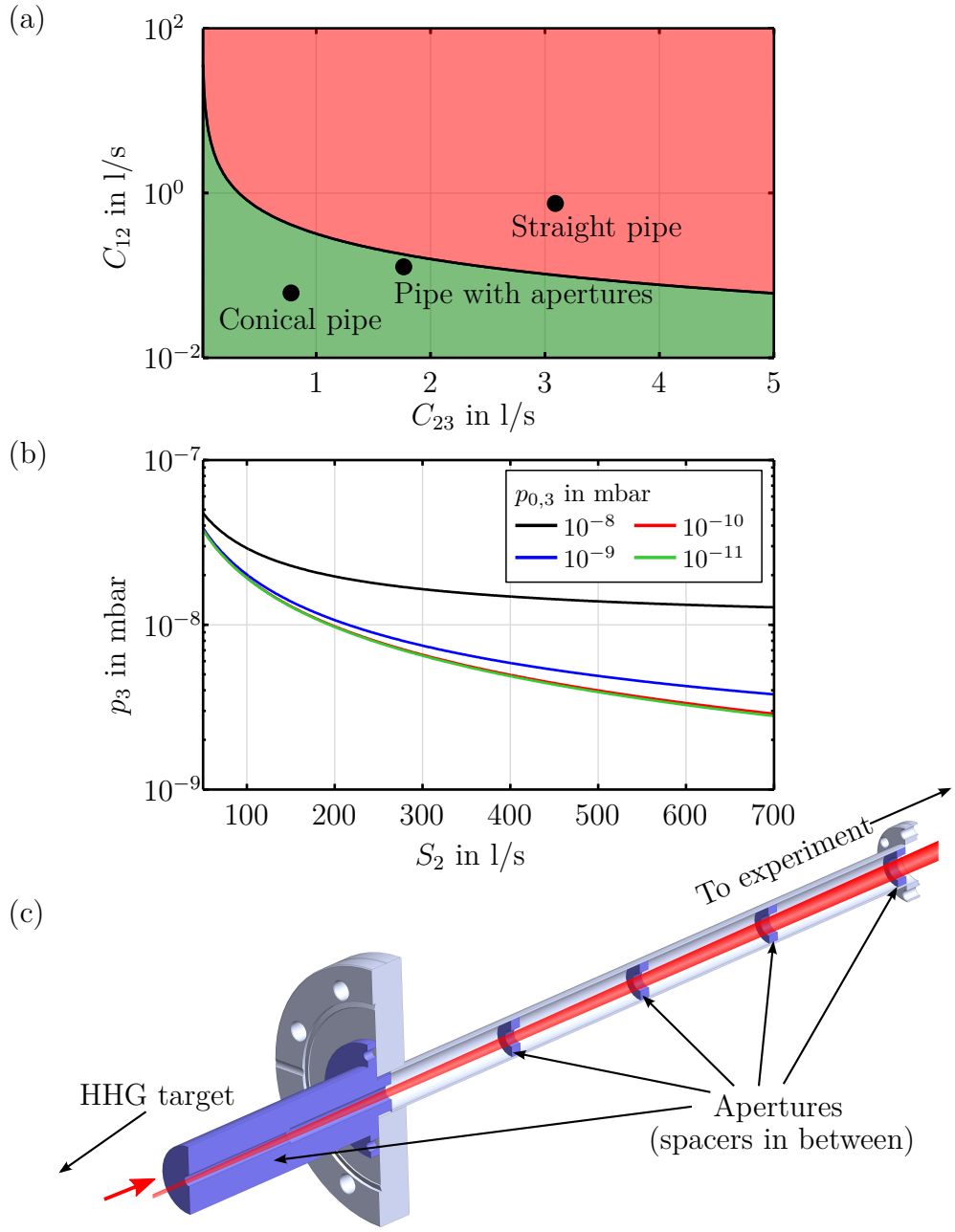

Figure 3.9: Differential pumping. (a): Range of conductivity values to maintain a pressure difference from $5 \cdot 10^{-3}$ to 10^{-8} mbar (green section). While a straight standard DN16 tube is not suitable, its flow conductivity is sufficiently improved by adding apertures whose diameter are adapted to the required beam divergence. (b): Expected end pressure p_3 in the experimental (ARPES) chamber as a function of pumping speed S_2 in the intermediate chamber for different initial pressures $p_{0,3}$. (c): Image of the first connection pipe (HHG chamber to intermediate chamber) with an extended aperture at the front and four more apertures within the pipe.

3.2.3 XUV beam monitor

The XUV beam monitor setup in front of the experimental chamber was developed to facilitate the optimization of desired XUV beam parameters. It allows the imaging of the XUV beam profile, flux and position over selectable energy ranges. In this way, it simultaneously serves as a simplified spectrometer, flux monitor and alignment reference mark. It comprises a set of XUV multilayer mirrors with distinct energy regions which reflect the beam to a XUV sensitive, thermo-electrically cooled low-noise CCD camera (PIXIS, Princeton Instruments). The spectral reflectivity characteristics of the mirrors are plotted in figure 3.10. A spectral range from 50 eV to 90 eV is currently covered. Specific

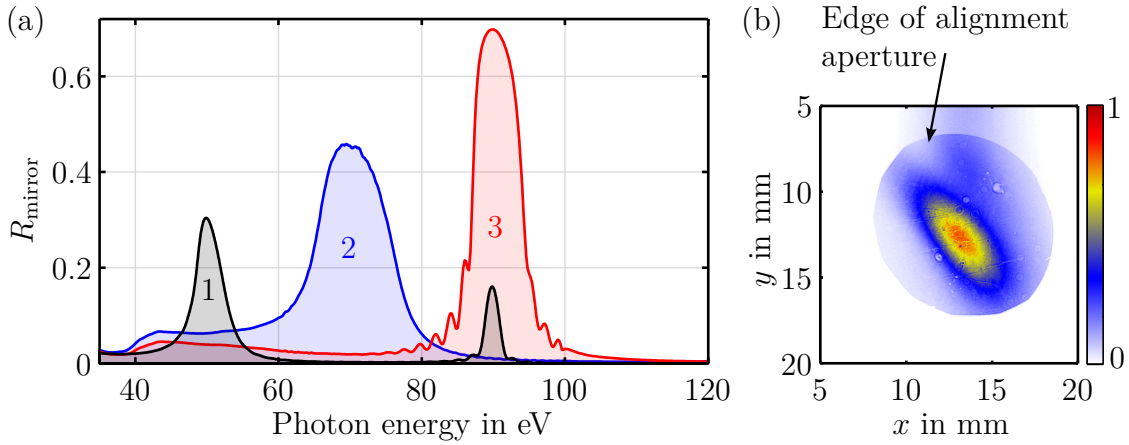

Figure 3.10: (a): Simulated spectral reflectivity of the multilayer mirrors (courtesy of A. Guggenmos) used in the beam monitor setup. The reflection regions are centered around 50 eV, 70 eV and 90 eV. (b): Typical XUV beam profile measured with mirror 3, also showing the boundary of the alignment aperture which defines the nominal beam axis.

reflectivity values are summarized in table 3.1. The mirrors are mounted on a motorized, high-precision linear table for a reproducible and precise alignment of each mirror. In this way, the setup provides a quick and convenient way to reproducibly align both the XUV beam and related transmissive XUV optics (e.g. XUV wave-plates, pellicle filters etc.) onto the beam path and to optimize the spatial beam profile as well as the harmonic flux at the same time within a selected spectral region of interest. For XUV beam alignment

Mirror	$\boldsymbol{E_c}$ in eV	$\boldsymbol{R}_{\mathrm{max}}$ in %	$\boldsymbol{\Delta E}_{\mathrm{FWHM}}$ in eV
1	49.9	30.4	4.3
2	69.6	45.8	11.3
3	90.0	69.8	7

Table 3.1: Reflectivity parameters of the multilayer mirrors for the beam monitor setup.

purposes, the setup is also equipped with an in-vacuum iris which marks a defined beam position.

3.2.4 ARPES chamber

The experimental chamber for angle-resolved photoemission studies is designed as a cylinder with the sample positioned on the symmetry axis. This configuration enables easy access to the sample surface from different directions by a multitude of ports. The chamber is additionally equipped with an electron gun ($E_{\mathrm{kin}} \leq 3000$ eV) for Auger spectroscopy in order to check the cleanness of the sample surface. The normal of the sample surface is aligned to the spectrometer axis. The XUV/NIR beam is focused onto the sample by a concentrically split multilayer mirror which simultaneously acts as a delay unit for time-resolved measurements. For this purpose, the inner part of the mirror is attached to a piezo-driven translation table for nanometer-precise positioning allowing the adjustment of sub-fs delays. The two mirror segments are embedded into a mechanical setup of nested multi-axis tip-tilt and translational stages to enable their independent alignment for a spatio-temporally coincident adjustment of their foci on the sample. In order to minimize the transmission of vibrations from the vacuum pumps to the delicate delay unit, sacrificing its sub-fs stability, the breadboard is placed on specifically designed vacuum-compatible passive vibration isolators with good damping of mechanical high frequency noise, see figure 3.12. In this way, superior stability of the delay unit is achieved. The entire delay unit can be retracted from the beam axis in order to let the beam pass to a second experimental chamber containing a photoemission electron microscope for micro-spectroscopic studies on nano-structured samples. The two beams are focused onto the sample at a grazing angle of 30°. Additionally, the foci of the beams can be inspected from outside the chamber. For this purpose, the sample holder is moved out of the beam axis so that a lens can image the in-vacuum foci with a magnification factor of ≈ 5 to the outside onto a CCD camera. This inspection tool is essential to adjust the spatio-temporal overlap of the two foci for time-resolved pump-probe experiments. The spatio-temporal alignment procedure of the delay unit is depicted in figure 3.11. Both mirror segments are illuminated by the NIR pulse. The two resultant foci are adjusted in such a way that a concentrically symmetric interference pattern (concentric interference rings) is formed, see figure 3.11(a). The temporal overlap is found by recording the intensity of the interference signal at the center of the combined foci profile as a function of the piezo-stage position. Although the temporal structure of the pulses is modified by dispersion introduced by the vacuum window and the imaging optics, the piezo position where the envelope of the interference signal peaks already provides a good approximation of the 'zero delay' between the two pulses, see figure 3.11(b). It is crucial that this imaging process is free of astigmatism as the latter would totally distort the image of the focus from the outer mirror segment. Adjusting a precise spatial overlap of the foci would then not be possible any more.
Furthermore, the sample holder is equipped with a heater which allows in-situ heating of the sample up to 1700° C by electron bombardment. This is especially useful to quickly condition and/or flash-anneal the sample between subsequent acquisition cycles, e.g. in order to remove accumulated adsorbent from its surface. A sample garage is installed to conveniently store up to 8 sample within the main chamber under UHV conditions. Additionally, the chamber body is embedded into a triaxial coil setup which allows the

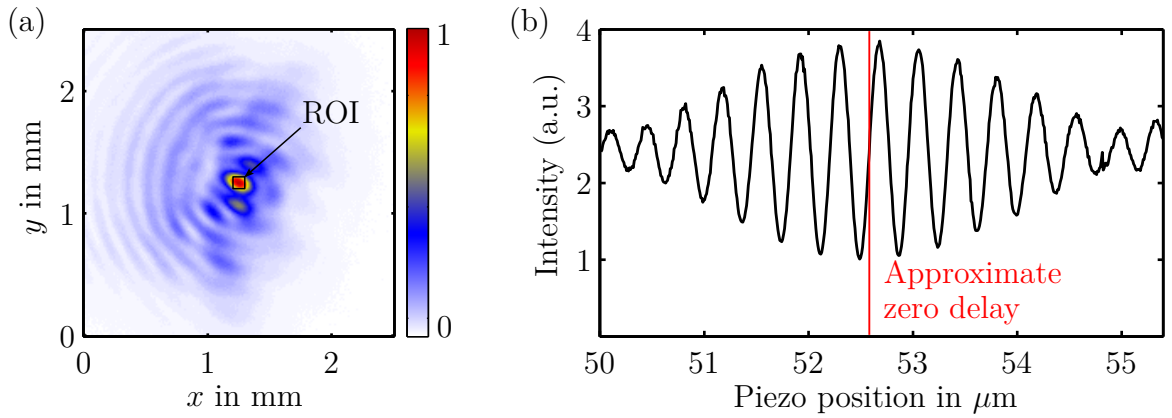

Figure 3.11: Spatio-temporal alignment of the delay unit. (a): Image of the NIR beam foci after the delay unit, spatially well overlapped, with concentric interference rings. (b): Intensity of the interference signal, spatially averaged over the region-of-interest as shown in (a), as a function of the piezo delay. The position where the envelope of the signal peaks marks the approximate zero delay between pump- and probe pulse, indicated by a red line.

compensation of magnetic stray fields (predominantly the earth's magnetic field). The remanent magnetic field strength within the critical volume of interest is kept in this way below 2 μT resulting in a maximum angle error of 0.2° for electrons of 90 eV kinetic energy (see section 3.2.6).

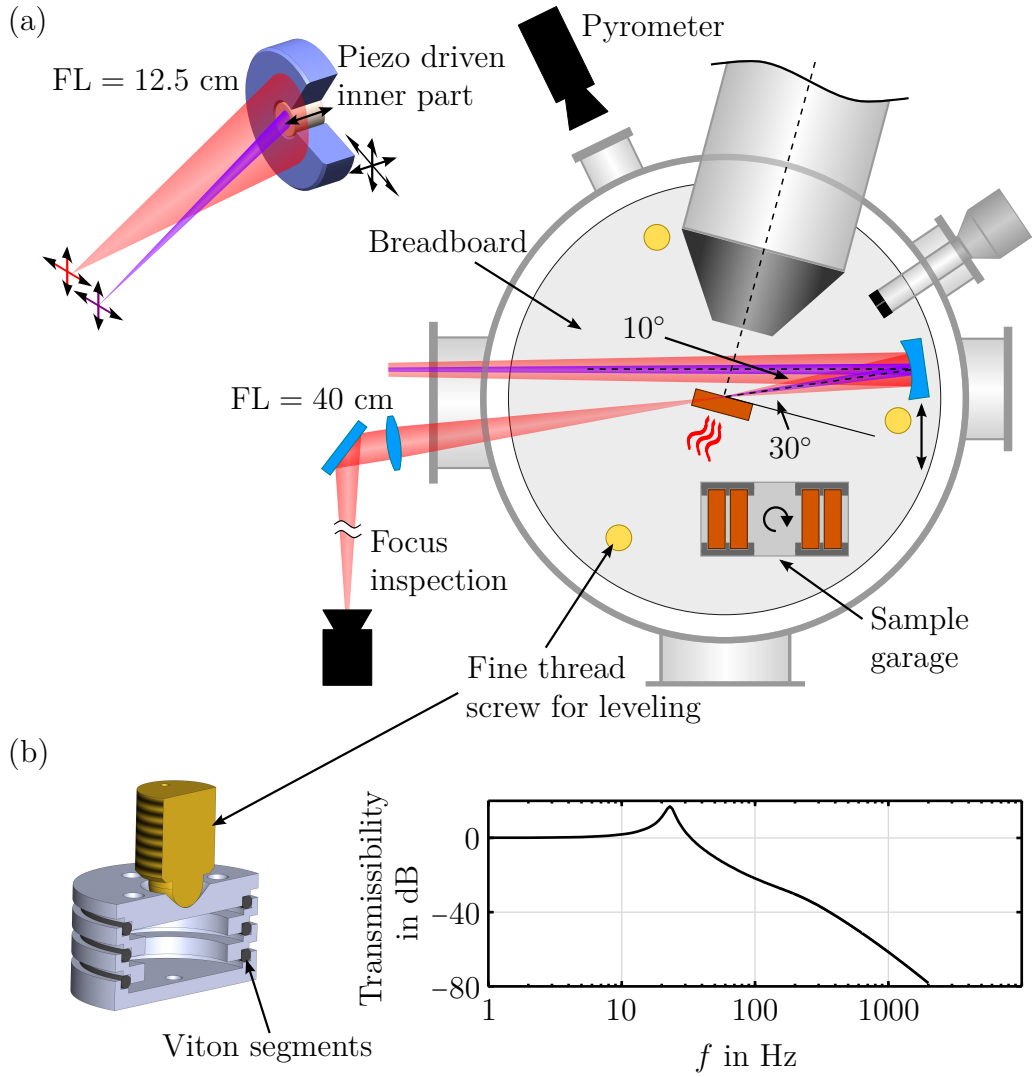

Figure 3.12: Sketch of the ARPES experimental chamber with peripheral devices. (a): Chamber geometry and construction of the concentrically split multilayer mirror as delay unit. The multi-axes mount of the mirror allows the adjustment of all degrees of freedom needed to ensure the spatio-temporal overlap of the foci and to align them onto the sample. An external focus inspection setup is used to adjust the overlap. The temporal overlap is found interferometrically by scanning the piezo translator. FL: focal length (b): Construction of the in-vacuum vibration dampers to reduce the transmission of high-frequency noise from the pumps into the optical setup, in particular into the delay unit. Visco-elastic viton rubber segments are used as a vacuum-compatible damping material between metal plates. This design is well proven for high-precision UHV environments [27,99,101,102,124]. An estimation of the (one-dimensional, vertical) transfer function for our design of the vibration damper is also plotted. Values for the stiffness and damping constants of the viton segments are taken from [101]. Resonance occurs at $f_R \approx 20$ Hz, damping is achieved for frequencies $f > 30$ Hz.

3.2.5 XUV spectrometer

For the spectral characterization of the harmonic radiation a XUV flat field spectrometer was developed and built in house. The main focus of the design process lies in a versatile setup with good resolving power as well as good overall efficiency and in a mechanically simple and robust construction with full UHV compatibility, which makes it a flexible and easy to use device for routine measurements, see figure 3.13. The spectrometer incorporates

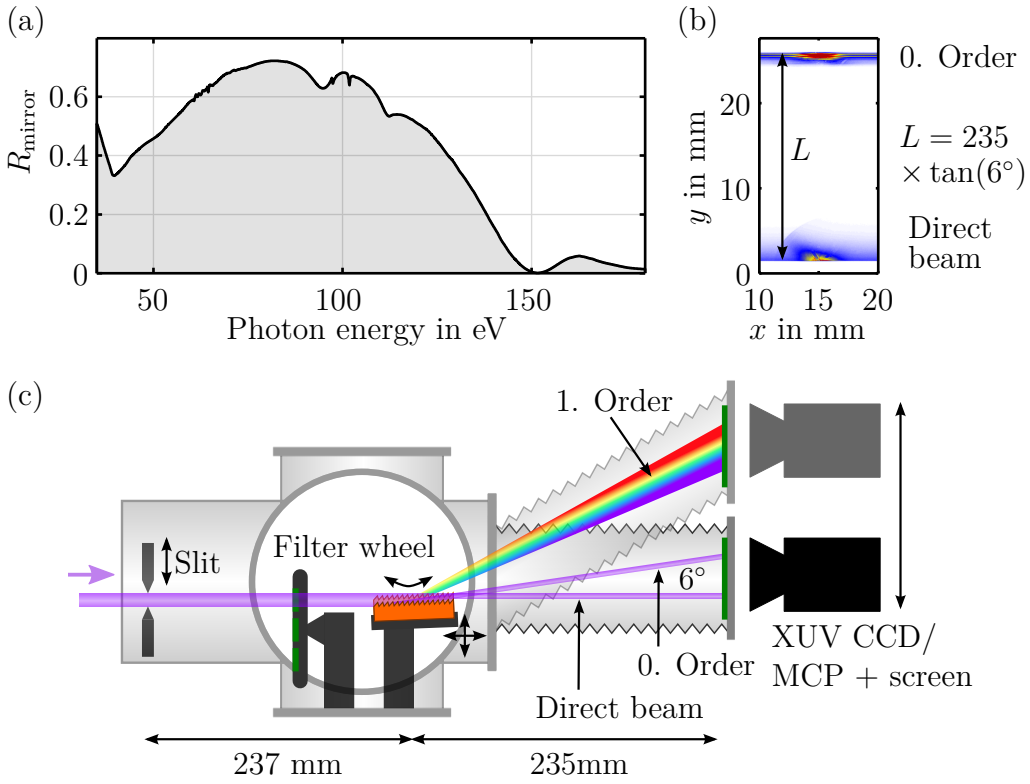

Figure 3.13: (a): Braodband multilayer mirror used to outcouple the beam to the XUV spectrometer for spectral characterization. The mirror is illuminated at 15° grazing incidence. (b): Image on the detector as used for the angle alignment of the grating. The separation between the zeroth diffraction order and the direct beam is determined by the nominal angle of incidence for the grating and the distance between grating and detector. (c): Sketch of the XUV spectrometer. The detector unit is flexibly connected to the spectrometer chamber, allowing its movement along the flat-field plane of the grating in order to additionally get access to the direct beam and the zeroth diffraction order which facilitates the alignment process. The grating can be moved out of the beam axis for this purpose.

a concave grazing incidence gold grating with varied line spacing (Hitachi) which produces a spectral flat field image in a specified spectral range. This flat field image allows for a relatively simple detection scheme, by simply placing a suitable position sensitive detector onto the flat field plane. This is in contrast to the mechanically much more complex Rowland circle scheme where a point or line detector has to be moved along a circular trajectory. These two common concepts are briefly discussed in the next paragraph. The spectrometer body also contains a filter wheel which can be loaded with 8 metal filters for pre-filtering the radiation and for energy calibration. Additionally, it is equipped with an entrance slit whose width is continuously adjustable from 0 to 6 mm so that the device can be adapted either to a high resolution mode (small slit width) or to a high throughput mode (big slit width), according to the needs and the available radiation flux. For the construction process of the spectrometer it is essential to understand the imaging properties of concave diffraction gratings with varied line spacing. Using Fermat's principle, an image is formed when the optical path length $\mathrm{d}S = n(l)\,\mathrm{d}l$ is minimized

$$\delta \int_A^B \mathrm{d}S = 0 \tag{3.17}$$

where A and B are object and image point, respectively. The following notation refers to figure 3.14. We assume straight grooves and the origin O of a rectangular coordinate system is placed at the center of the grating surface with the x-axis being parallel to the normal of the grating surface at O. The y-axis is perpendicular and the z-axis parallel to the grooves. Points on the grating surface are denoted by (ζ, η, ξ) where $\zeta = F(\eta, \xi)$ describes the form of the grating surface. A spherical surface with radius R is assumed. Image points are denoted by primed coordinates, see figure 3.14. The optical path length

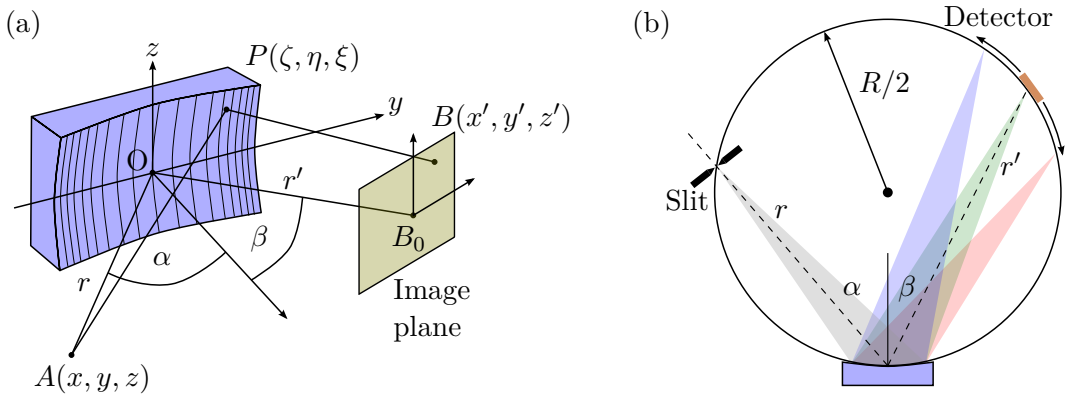

Figure 3.14: Spherical imaging grating. (a): Nomenclature. (b): Rowland circle geometry for a standard spherical grating without varied line-spacing.

from a source point A to the image point B is

$$S = \overline{AP} + \overline{PB} + Nm\lambda\eta \tag{3.18}$$

where N is the line density and m the diffraction order. The last term in 3.18 accounts for the phase advance due to diffraction. In order to satisfy equation 3.17 the following conditions have to be fulfilled

$$\frac{\partial S}{\partial \eta} = 0, \frac{\partial S}{\partial \xi} = 0. \tag{3.19}$$

That is, (x', y', z') are determined so that the optical path is stationary with respect to η and ξ. In order to find the imaging condition with increasing degree of precision, the path length S is expanded in a power series around the origin according to

$$S(\eta, \xi) = S_{00} + \eta S_{10} + \eta^2 S_{20} + \xi^2 S_{02} + \eta^3 S_{30} + \eta \xi^2 S_{12} + \dots \tag{3.20}$$

with $S_{ij} = \frac{\partial^i \partial^j}{\partial \eta^i \partial \xi^j} S$. Using $r = \sqrt{x^2 + y^2 + z^2}$ and $r' = \sqrt{x'^2 + y'^2 + z'^2}$ as well as the direction cosines $\cos\alpha = \frac{x}{r}$, $\sin\alpha = \frac{y}{r}$ and $\cos\beta = \frac{x'}{r'}$, $\sin\beta = \frac{y'}{r'}$ the first terms in 3.20 yield

$$S_{00} = r + r' \qquad (*) \tag{3.21}$$

$$S_{10} = Nm\lambda - (\sin\alpha + \sin\beta) \qquad \text{(grating equation)} \tag{3.22}$$

$$S_{02} = \frac{1}{2}\left(\frac{1}{r} - \frac{\cos\alpha}{R}\right) + \frac{1}{2}\left(\frac{1}{r'} - \frac{\cos\beta}{R}\right) \qquad \text{(sagittal focus)} \tag{3.23}$$

$$S_{20} = \frac{1}{2}\left(\frac{\cos^2\alpha}{r} - \frac{\cos\alpha}{R}\right) + \frac{1}{2}\left(\frac{\cos^2\beta}{r'} - \frac{\cos\beta}{R}\right) \qquad \text{(meridional focus)} \tag{3.24}$$

$$S_{30} = \frac{1}{2}\left(\frac{\cos^2\alpha}{r} - \frac{\cos\alpha}{R}\right)\frac{\sin\alpha}{r} + \frac{1}{2}\left(\frac{\cos^2\beta}{r'} - \frac{\cos\beta}{R}\right)\frac{\sin\beta}{r'} \qquad \text{(primary coma)} \tag{3.25}$$

$$S_{12} = \frac{1}{2}\left(\frac{1}{r} - \frac{\cos\alpha}{R}\right)\frac{\sin\alpha}{r} + \frac{1}{2}\left(\frac{1}{r'} - \frac{\cos\beta}{R}\right)\frac{\sin\beta}{r'} \qquad \text{(astigmatic coma)} \tag{3.26}$$

Applying condition 3.19 requires all terms S_{ij} beyond S_{00} to be equally zero for an ideal image formation. Any terms which are not equal to zero lead to image distortions. Setting $S_{10} = 0$ gives the common grating equation which determines the diffraction angle β for a given wavelength with respect to the incidence angle α and line density N. The term S_{20} is the focus in the direction of dispersion (meridional direction) while the next higher order term S_{30} is the most significant source of aberration in that direction, and hence these are the most important terms to be minimized. Therefore, setting $S_{20} = 0$ yields

$$r = R\cos\alpha \tag{3.27}$$

$$r' = R\cos\beta \tag{3.28}$$

This is the Rowland circle condition. It implies that, in order to meet Fermat's principle, source point and image point have to lie on a circle of diameter R which is tangent to the grating surface in O. It also ensures that the first meridional aberration term S_{30} is minimized. This means for the spectrometer design that entrance slit (source), grating and

detector (image) have all to be arranged on the Rowland circle for best imaging properties. Moreover, the detector has to be moved along this circle geometry when an extended spectral range is to be recorded. The remaining terms of 3.20 are not explicitly minimized by the Rowland circle condition, which is usually not very destructive. S_{02} describes the focus perpendicular to the dispersion direction (sagittal direction), however, defocusing in that direction is not crucial for spectroscopic applications since it does not degrade the resolving power. The term S_{12} primarily leads to image curvature. Higher order terms also result in some kind of aberration, however, with decreasing significance.

The circular focal line of the standard concave grating requires a complex and costly mechanical detector mount which is able to move the detector along this circular geometry. In order to simplify the construction efforts and the mechanical complexity, aberration corrected flat field gratings are used which produce a straight focal line so that the detector only has to be moved along a single direction in order to record a full spectrum. This flat field image is achieved by varying the grating line density, usually in the form of a polynomial

$$N(\eta) = N_0 \left(1 + \frac{2b_2}{R}\eta + \frac{3b_3}{R^2}\eta^2 + \frac{4b_4}{R^3}\eta^3 + \dots\right). \tag{3.29}$$

Repeating the calculation from above now results in new expansion coefficients $\tilde{S}_{ij}$

$$\tilde{S}_{10} = S_{10} \tag{3.30}$$

$$\tilde{S}_{02} = S_{02} - N_0 m\lambda \frac{\tan\theta}{2R} \tag{3.31}$$

$$\tilde{S}_{20} = S_{20} + N_0 m\lambda \frac{1}{R}\left(b_2 - \frac{\tan\theta}{2}\right) \tag{3.32}$$

$$\tilde{S}_{30} = S_{30} + N_0 m\lambda \frac{1}{R^2}\left(b_3 - b_2\tan^2\theta\right) \tag{3.33}$$

$$\tilde{S}_{12} = S_{12} - N_0 m\lambda \frac{b_2\tan\theta}{R^2}. \tag{3.34}$$

From this new set of equations following conclusions can be drawn: the grating equation, represented by $\tilde{S}_{10}$, remains unchanged. The sagittal focus $\tilde{S}_{02}$ is modified by an additional term containing the tilt angle of the grooves θ, however, in practice θ is strongly limited by mechanical manufacturing constraints and can not be chosen arbitrarily in order to fully minimize $\tilde{S}_{02}$. The first benefit of the varied line spacing shows up in the meridional focus $\tilde{S}_{20}$ in which the focal line now can be affected by the design parameter b_2. By properly choosing the value of this parameter, the focal curve can be changed from circular to nearly flat within a certain spectral range, see figure 3.15(a). In addition, the second order line density coefficient b_3 can be adjusted to minimize the primary coma $\tilde{S}_{30}$ which is not automatically zero any more as it was the case in the Rowland circle geometry. By carefully optimizing the combination of θ and b_2, even the term of astigmatic coma $\tilde{S}_{12}$ can be significantly reduced. As a result, the image from aberration corrected gratings with varied line spacing is nearly free of line curvature. This greatly facilitates the analysis of

the spectrum. If necessary, higher order aberrations could also be reduced to a certain degree by adjusting the higher order coefficients in 3.29.

From the discussion above it gets clear that the great advantage of the concave grating with varied line spacing lies in its ability to generate a spectral flat-field image while simultaneously minimizing the two most significant sources of aberrations, namely primary coma and astigmatic coma whereas the latter is not minimized in the Rowland circle scheme. This results in a mechanically simpler, compacter and potentially less expensive spectrometer design and also simplifies the analysis of the spectrum. However, there are also disadvantages which should be mentioned. Since the spectral flat field image is spatially contracted due to the shorter focal distance, see figure 3.15(a), the separation of energy components within the image plane is smaller compared to the Rowland circle setup and hence the spectral resolution is lower. Furthermore, the complex design of the varied line space grating requires higher manufacturing efforts which are costly and may increase manufacturing imperfections. The major restriction, however, is the fact that the flat field characteristic and the aberration performance is only valid within a limited spectral range. Beyond this range, aberrations increase destructively and the focal line bends off from the ideal flat field curve, which is illustrated in figure 3.15(c).
The Hitachi grating which we use as a standard in our spectrometer covers a spectral range from 62–248 eV (5–20 nm). It requires a source distance of 237 mm at an angle of $\alpha = 87°$ to the surface normal. The resulting flat field has a height of 25.3 mm which completely fits onto the XUV CCD chip (Pixis, Princeton Instruments) without moving the camera. Nevertheless, the camera can slide in a straight guide along the extension of the flat field focal line in order to be able to also image the zeroth diffraction order as well as the non-diffracted direct XUV beam, see figure 3.13. The latter turned out to be useful for alignment purposes. Also for alignment reasons, the grating can be moved off the beam axis and is additionally mounted on a motorized goniometer for an on-line adjustment of the angle of incidence. Furthermore, grating-slit distance and grating-detector distance can be adjusted independently to adapt the spectrometer to imaging properties of alternative gratings. In order to determine the required alignment precision, the imaging properties of our standard grating is investigated with respect to variations of the nominal imaging parameters. As a measure for the goodness of alignment we use the deviation of the focal line from the flat field. It turns out that the angle of incidence is the most critical parameter in the alignment procedure, see figure 3.15(b). Practically, the following procedure is used to adjust the correct angle of incidence: first the direct beam is imaged and centrically aligned to the entrance slit. Then the grating is driven back into the beam so that the latter is clipped half-way. Next, it is tilted so that the distance s between the center of the specular reflection (zeroth diffraction order) and the center of the blanked portion of the direct beam on the detector plane becomes

$$s = L_1 \tan(6°) \tag{3.35}$$

where L_1 can be any preset but known grating-detector distance measured along the straight beam axis (see figure 3.13(b)). s is easily determined with the known pixel size of

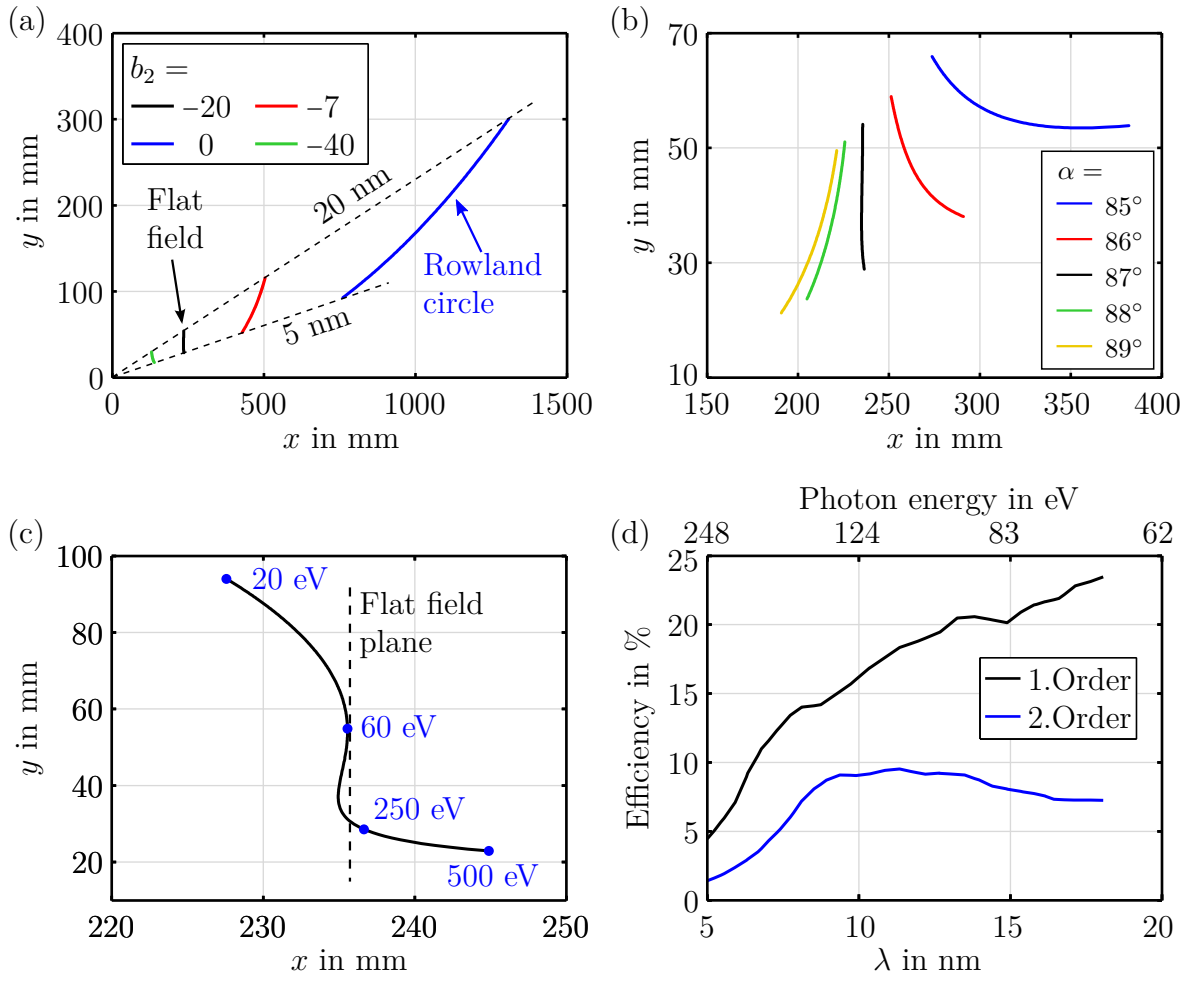

Figure 3.15: Characteristics of the spherical varied line-space grating for XUV spectroscopy. (a): Variation of the focal line with grating parameter b_2 between 60 eV (20 nm) and 250 eV (5 nm). The focal line can be tuned to an almost flat shape (flat-field). (b): Deformation of the flat-field as a function of the angle of incidence α. The nominal value is $\alpha = 87°$. (c): Shape of the focal line for an extended energy range. Beyond the nominal range the focal start deviating from the flat-field considerably. (d): Estimated total efficiency of the spectrometer including diffraction efficiency of the grating and detection efficiency of the XUV CCD chip.

the CCD chip. With $L_1 = 235.5$ mm, α can be easily adjusted within $\pm 0.5°$ of the nominal value. Energy calibration is done by means of a thin Al-filter which exhibits a sharp absorption edge at 72 eV. This edge can be easily identified in the spectrum. Finally, the relation between photon energy (wavelength) and position along the flat field in y-direction is obtained as

$$y(\lambda) = L_2 \cot \beta(\lambda) \tag{3.36}$$

where L_2 is the grating-detector distance in x-direction, nominally given as $L_2 = 235.3$ mm. Moreover, alignment errors of L_2 and α are corrected for by software post-processing using an iterative algorithm which adapts the energy axis 3.36 of the spectrum under the additional constraints of a second calibration mark (usually the absorption edge of Si at 100 eV) and the equidistance of neighboring high harmonic peaks. In this way, an accurate and precise energy scaling is obtained.

3.2.6 Electron spectrometer

The angle-resolving electron spectrometer, which is used in this work, is the *Themis 1000* from Specs Surface Analysis GmbH. It is a time-of-flight (ToF) spectrometer equipped with an electro-statical lens system which images the emission angle of photo-excited electrons onto a time- and position-resolving detector. The lens and drift sections consist of a series of conical and straight metal tubes which can be individually supplied by a voltage. Different

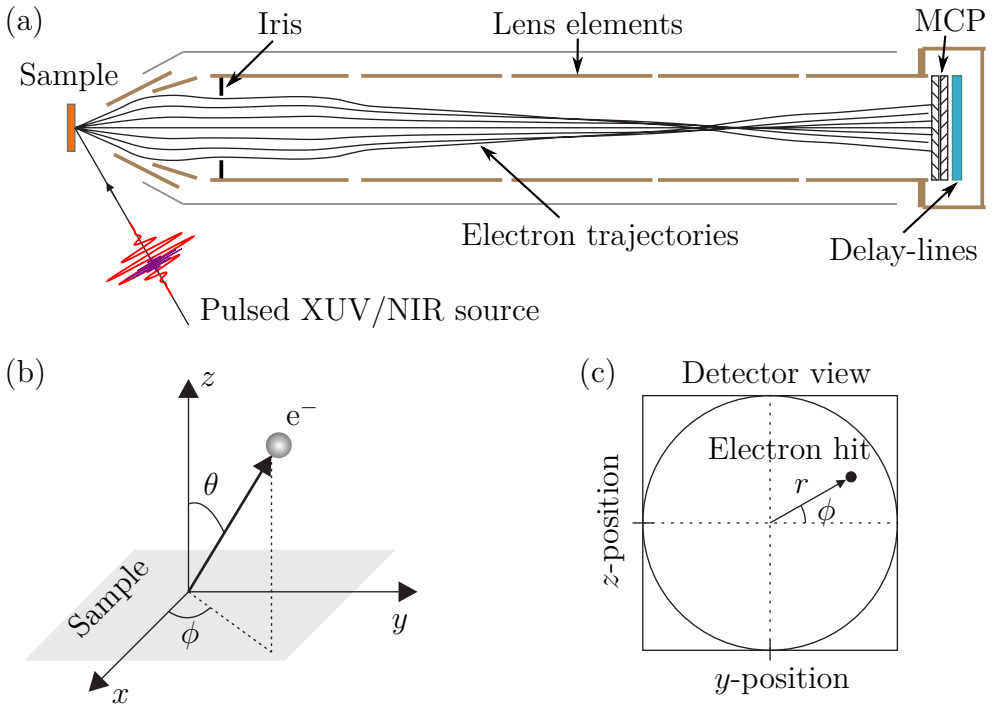

Figure 3.16: The Themis 1000 angle-resolving spectrometer. (a): Sketch of the lens system. (b): Geometry of the photoemission direction. (c): Detector view.

Lens mode	Abbr.	Magnification/ collection angle	min RR	max RR
Low angular dispersion	LAD	±7°	0.07	30
Wide angle mode	WAM	±15°	0.1	10
Drift mode	DM	±1.3°	0	∞
High magnification	HM	10	0.2	1000

Table 3.2: Lens modes of the Themis 1000 used in this work.

lens settings allow the spectrometer to be adapted to various lens modes with different imaging characteristics. According to the convention of hemispherical analyzers, the initial start energy, i.e. the kinetic energy of the electron at the sample, is referred to as E_{kin} and the final energy, i.e. the kinetic energy when the electron hits the detector, as pass energy E_{pass}. The lens behavior, and hence a particular imaging characteristic of the spectrometer only depends on the retardation ratio

$$\mathrm{RR} = \frac{E_{\mathrm{kin}}}{E_{\mathrm{pass}}}. \tag{3.37}$$

This ratio defines how strong the electron is accelerated or decelerated while passing the lens setup. In this way, it affects the time-energy dispersion which in turn determines the energy resolution and chromaticity of the imaging system. Two types of lens modes can be adjusted: a position-resolving mode and several angle-resolving modes. The angle modes differ by their collection angle and the range of valid retardation ratios. The characteristics of the three most important angle modes, used in this work, are summarized in table 3.2. The position-resolving mode is only used to estimate the beam spot size on the sample. A mechanical iris is installed inside the third lens tube whose diameter can be manually adjusted in order to reduce the collection angle or to block scattered electrons. A defined working distance (distance between sample and the first lens element) of 53.3 mm is necessary for the lens system to work properly. This distance is adjusted by a special gauge designed for this purpose. A μ-metal shield around the lens system reduces magnetic stray fields, predominantly the earth's magnetic field, inside the spectrometer and ensures high imaging quality, see also section 3.2.6.

In contrast to spectroscopic imaging techniques which are based on a field retarder or a hemispherical energy analyzer, the concept of ToF-optics in combination with a delay-line detector has the advantage of being able to measure *all* randomly incoming particles both in position and in time on a true counting basis, thus eliminating data loss and reducing acquisition time. This is of particular interest for pump-probe photoemission experiments in the femto- and attosecond time scale where space charge effects heavily limit the maximum number of photoelectrons per laser pulse, see section 5.3. On the other hand, a large amount of particles which are not of interest such as secondary (scattered) electrons, usually making up the majority of all generated photoelectrons, are also inevitably measured, leading to a strong background signal which may degrade the detector performance

by driving it into saturation or into the multi-hit regime. Furthermore, the specific settings of the lens system often produce focal points on the detector plane for particles at energies outside the spectroscopic energy-window of interest. This leads to a locally high flux-density of particles on the active area of the detector which may cause a heavy impairment of the detection quality. The latter turned out to be a particular problem for the photoelectron streaking measurements which were performed in the course of this work, see appendix B.

Alignment of the excitation spot

While the parasitic focusing behavior of the lens system may be destructive for the detector on the one hand, it can also be exploited for the alignment of the excitation spot onto the optical axis of the lens system on the other hand, provided the total particle flux is kept at a safe level. Good alignment of the excitation spot is achieved when the resultant chromatic focal spots are all aligned to a single position on the detector. This position marks the location of the optical axis and should be (close to) the 0-position. The alignment of the focal spots is best evaluated in the xt- and yt-diagram as shown in figure 3.17. In case the

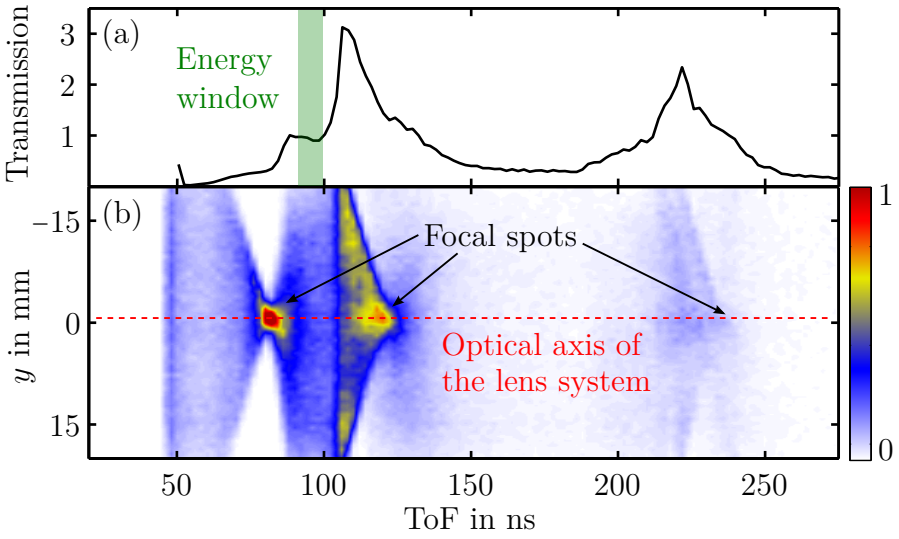

Figure 3.17: Alignment of the excitation spot on the sample and definition of the optical axis of the lens system. The sample is irradiated by electrons with $E_{\mathrm{kin}} = 1000$ eV from the electron gun. The lens adjustments are $U_{\mathrm{kin}} = U_{\mathrm{pass}} = 100$ V in LAD mode. The corresponding energy window for a valid data transformation is depicted as green-shaded area. (a): Transmission function for the given lens setting, calculated from the corresponding ToF-spectrum which is referenced to a spectrum obtained in drift mode (lenses off). (b): The excitation spot is properly positioned on the sample when all chromatic focal points are aligned in a row, which also defines the location of the optical axis of the lens system.

optical axis does not coincide with the 0-position of the detector, the recorded position values have to be corrected correspondingly so that the real position of the optical axis

is used as conversion center for the data transformation (see section 3.2.6). Also note that the energy-dependent transmission function of the spectrometer generally assumes a complicated nonlinear shape outside the adjusted energy window, as depicted in figure 3.17(a). Therefore, any spectral features located outside the valid energy range are in general meaningless. It is good practice to check the alignment after every change of the lens settings as it turned out that the exact location of the optical axis slightly depends on the lens settings.

MCP Delay-line Detector

The detector system of the spectrometer is a 3D delay-line detector (DLD) from Surface Concept GmbH which is able to measure both the position and the hit time (x, y, t) of an impinging electron. It consists of two micro-channel plates (MCP) with a delay-line anode. An impinging particle that strikes the inner wall of a micro-channel triggers a collision-induced electron avalanche by means of repeated and cascaded secondary electron emission. The channels are usually tilted by a small angle in order to improve efficiency. Furthermore, the gain of the multiplier process can be increased by combining two MCP plates with their biased channels rotated by 180° from each other, also known as chevron configuration. In this way a gain of more than 10^6 is typically achieved. The resultant electron cloud is finally accelerated by an electrical potential toward the delay-line anode consisting of two electrically isolated meander-like wire structure (delay-lines) which are crossed by 90° to each other. The principle of the delay-line measurement is shown in figure 3.18(a). At the position where the electron cloud from the MCPs passes the two delay-lines electrical pulses are induced whose transit times t_{x1},t_{x2} and t_{y1},t_{y2} to both ends of each delay-line are precisely measured. The hit position can then be deduced from the corresponding transit time differences $\Delta t_x = t_{x2} - t_{x1}$ for the x-position and $\Delta t_y = t_{y2} - t_{y1}$ for the y-position, respectively. Additionally, a position-independent time coordinate t_{hit} is obtained as

$$t_{\text{hit}} = \frac{t_{x1} + t_{x2} + t_{y1} + t_{y2}}{4}. \tag{3.38}$$

The measurement of the transit times is performed by a fast time-to-digital converter (TDC) whose timing unit is started by a reference pulse which is synchronized to the release of the photoelectrons. The reference signal is deduced by the laser pulses itself. The actual time-of-flight for a photo-emitted electron is then given as

$$\text{ToF} = t_{\text{hit}} - t_{\text{offset}}, \tag{3.39}$$

where t_{offset} accounts for delays in the electronic circuits and for the time offset between the start of the TDC timing unit and the actual instant of photoemission. t_{offset} is usually determined experimentally, see next paragraph.

The prerequisite for an ultimate performance of the delay-line detector is an accurate and precise time measurement. Therefore, special care has to be bestowed on the conditioning of the electrical signals which are fed into the start- and the stop-channels of the TDC. A typical signal chain for this purpose is shown in figure 3.18(b). It comprises a low-noise

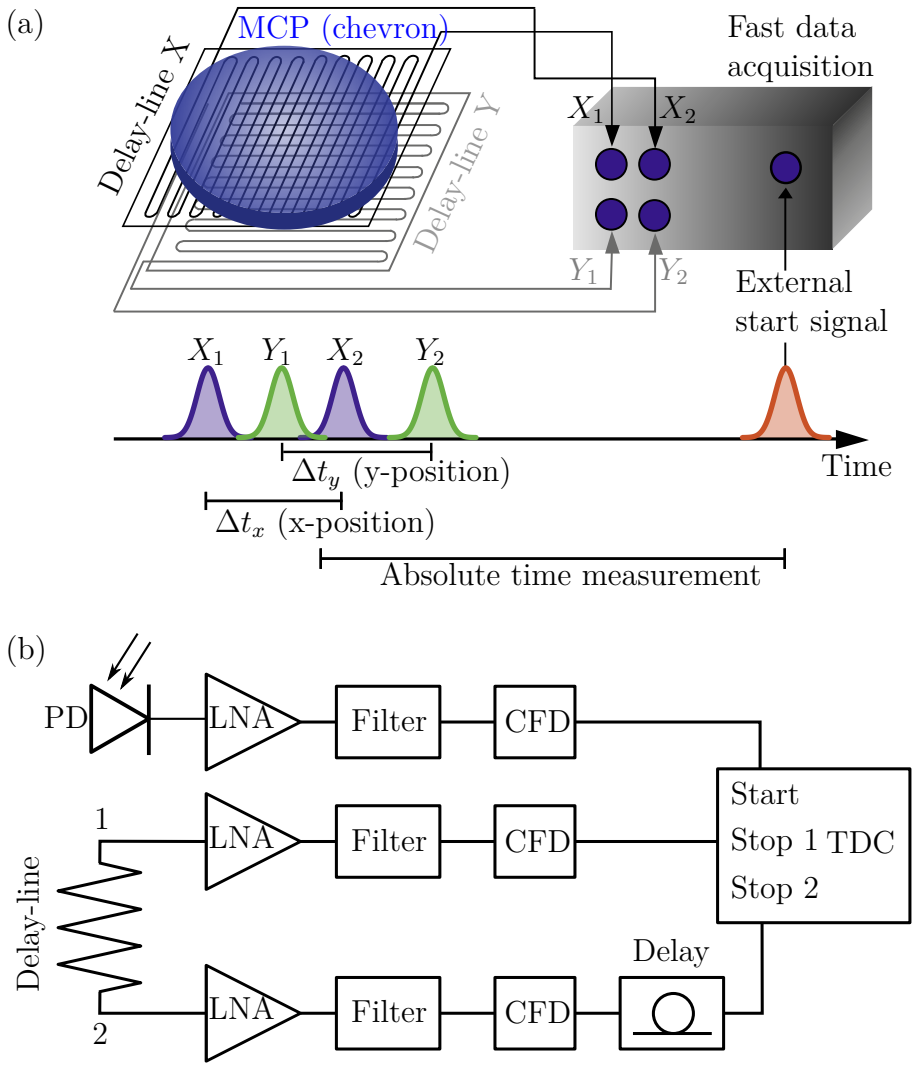

Figure 3.18: MCP delay-line detector. (a): Operating principle of the detector. (b): Electronic signal chain of the DLD data acquisition. PD: photodiode, LNA: low-noise amplifier, CFD: constant-fraction discriminator, TDC: time-to-digital converter.

amplifier (LNA), a specific filter circuit and a constant-fraction discriminator (CFD). Key element is the CFD whose release time, in contrast to a standard constant-level discriminator, is not affected by incoming pulse height fluctuations which are inherent to all involved signal sources (due to laser pulse fluctuations for the signal from the photodiode and due to the statistical nature of the electron-multiplying process in the MCPs for the signal from the delay-line). However, this is only true for pulses with a non-varying pulse shape. Therefore, the main task of the filter circuit is to provide a smooth and more or less constant pulse shape as input for the CFD. Consequently, the fine-tuning of these circuits and the mutual matching of their parameters is both critical and delicate for a precise time measurement. Even a slight detuning may drastically impair the time resolution of the setup. Furthermore, the working principle of the DLD implies a natural dead time given by the transit time of the induced electrical pulses on the delay-lines, which is typically ≈ 15 ns [139]. A second particle event within this dead time would mess up the proper assignment of the transit-time quadruples at the TDC stop-channels to the corresponding particle event. This is usually referred to as multi-hit regime. As a consequence, the quadruple is either discarded, leading to no detector count, or it is accepted but corrupted, leading to a fake count at a wrong position and/or ToF value. As the energy-time dispersion of the relevant photoelectrons in our experiments entails a ToF spread smaller than 15 ns (see figure 3.20), the maximum usable detector count rate is ultimately determined by the repetition rate of the laser pulses. Delay-line detectors exhibit an extremely low dark-count rate, and therefore provide a superior signal-to-noise ratio.

Determination of t_{offset} The following procedure has proven to be useful in order to experimentally determine the DLD time offset: when using the electron gun, the elastically scattered electrons can be identified in the time-of-flight spectrum as a sharp peak with a high slope at the high-energy side, see figure 3.19(a). The corresponding time-of-flight $t_{\mathrm{tof}}^{\mathrm{elastic}}$ is indicated by a red line. The spectrum is taken in drift mode and the iris in the spectrometer is closed to reduce the acceptance angle below 0.1°. In drift mode the electrons move field-free along straight trajectories toward the detector, and their theoretical energy-dependent time-of-flight can be easily calculated. Considering the geometric distance between sample and detector, the DLD time offset is given as

$$t_{\mathrm{offset}} = t_{\mathrm{tof}}^{\mathrm{elastic}} - \frac{1486.6}{\sqrt{E_{\mathrm{kin}}[\mathrm{eV}]}} \tag{3.40}$$

where E_{kin} is the primary kinetic energy of the electrons when leaving the electron gun. This primary energy is well-known.
For XUV radiation, a photon peak can be observed in the spectrum which is temporally located before the actual energy spectrum of the electrons, see figure 3.19(b). It arises from scattered XUV light on the sample which hits the detector and induces a signal in the form of a sharp peak. The position of this peak $t_{\mathrm{tof}}^{\mathrm{XUV}}$ is again indicated by a red line. In this case the DLD time offset is obtained as

$$t_{\mathrm{offset}} = t_{\mathrm{tof}}^{\mathrm{XUV}} - 2.94\,\mathrm{ns} \tag{3.41}$$

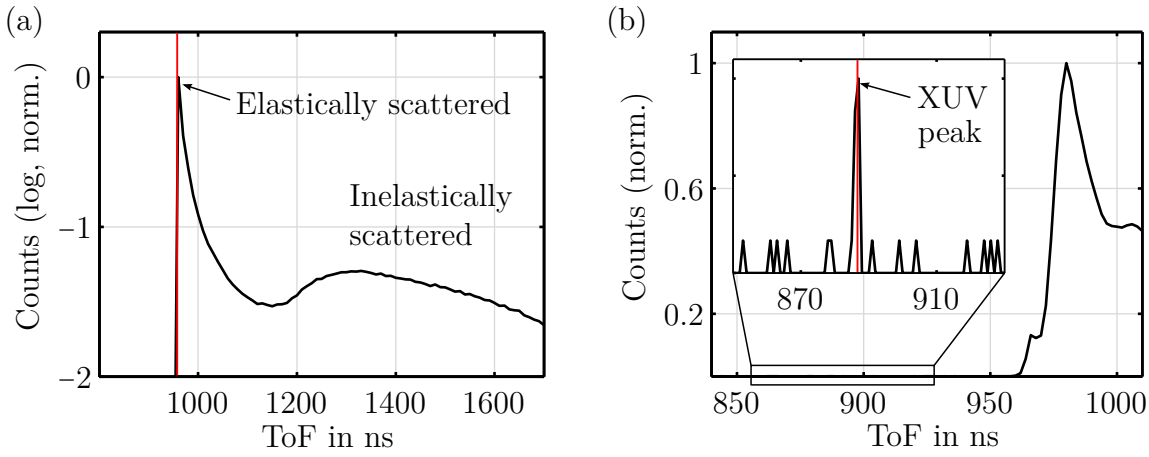

Figure 3.19: Time calibration of the DLD detector using the (a): Electron gun and (b): XUV radiation.

where the last term accounts for the time the light needs to propagate from the sample to the detector using the speed of light.

Data conversion

The conversion of the raw data triplet (x, y, t), provided by the detector system, into the physically more relevant quantities $(\alpha, \beta, E_{\text{kin}})$ is based on the simulation of electron trajectories from the sample to the detector plane. A ray-tracing algorithm for electro-optics calculates in consideration of the adjusted lens settings the ToF and the hit position on the detector for a set of electrons which are launched with varying kinetic energies and emission angles from a point source at the working distance and on the optical axis of the lens system. Due to the rotational symmetry of the system it is sufficient to only consider the radial distance r and the polar emission angle θ, see figure 3.16(c). The result of the ray-tracing simulation is a 2-dimensional, functional assignment $(\theta, E_{\text{kin}}) \rightarrow (r, t)$ which needs to be inverted to $(r, t) \rightarrow (\theta, E_{\text{kin}})$ in order to get the conversion function for the raw data. Values between the initial sampling grid are spline-interpolated. Note that the inversion process requires a one-to-one mapping between the two parameter sets (r, t) and (θ, E_{kin}), which is usually not satisfied for the entire energy range of the detected photoelectrons. Also note that the software does not cancel the calculation or inform the user when the condition for a one-to-one mapping is not fulfilled, the resultant conversion function is just not meaningful in this case. However, within the allowed lens settings for the *Themis 1000*, a successful, i.e. meaningful, conversion can be guaranteed for the energy range $E_{\text{kin}} = q(U_{\text{kin}} \pm 0.1 U_{\text{pass}})$ in LAD mode and $E_{\text{kin}} = q(U_{\text{kin}} \pm 0.05 U_{\text{pass}})$ in WAM mode, where U_{kin} and U_{pass} are the adjusted lens potentials. Figure 3.20 shows a representation of the conversion function for $U_{\text{kin}} = 70$ V and $U_{\text{pass}} = 600$ V in WAM mode (a typical adjustment which was used to obtain a broadband overview-spectrum) as a combined 2-dimensional contour plot for the emission angle and the kinetic energy. Additionally, the

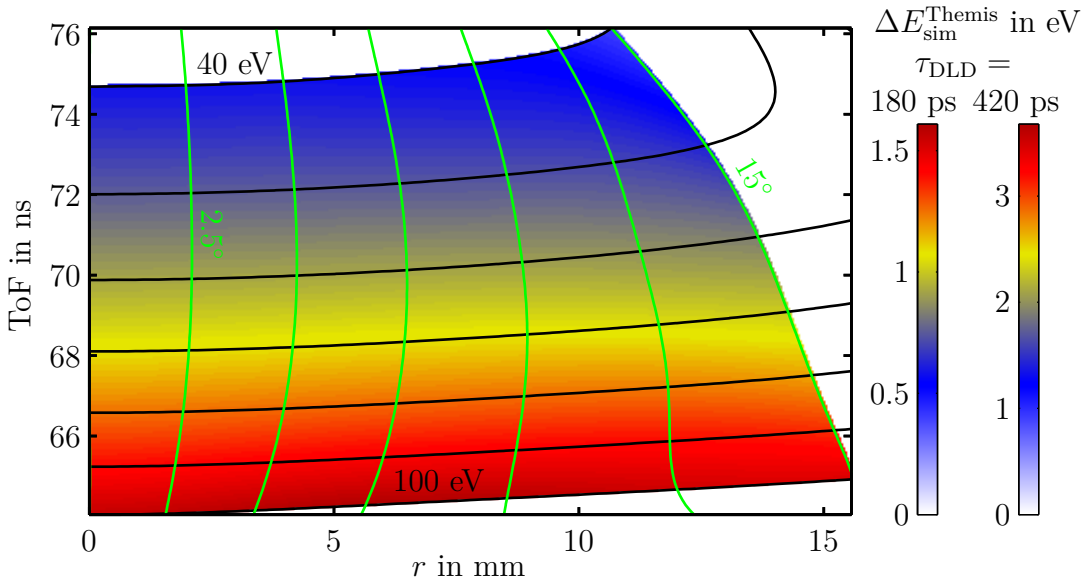

Figure 3.20: Illustration of the data conversion function for the lens settings $U_{\mathrm{kin}} = 70$ V and $U_{\mathrm{pass}} = 600$ V in WAM mode. Isolines of the kinetic energy are drawn in black from 40 eV to 100 eV in 10 eV steps, isolines of the emission angle are plotted in green from 2.5° to 15° in 2.5° steps. Overlaid is the theoretically expected energy resolution based on the given conversion function with a FWHM DLD time resolution of 420 ps (measured) and 180 ps (more typical), resulting in an energy resolution of 3.7 eV and 1.6 eV, respectively.

conversion function enables the calculation of the full differential for the energy and the angle, thereby providing an estimation of the theoretical expectation value for the energy and angle resolution. The energy resolution can be approximated as

$$\Delta E = \sqrt{\left(\frac{\partial E}{\partial t}\Delta t\right)^2 + \left(\frac{\partial E}{\partial r}\Delta r\right)^2 + \frac{\partial^2 E}{\partial t \partial r}\Delta t \Delta r + (\mathrm{RR} q \Delta U_{\mathrm{pass}})^2}. \tag{3.42}$$

The last term accounts for a possible ripple on the lens potentials. Similarly, the angle resolution is obtained as

$$\Delta\theta = \sqrt{\left(\frac{\partial \theta}{\partial t}\Delta t\right)^2 + \left(\frac{\partial \theta}{\partial r}\Delta r\right)^2 + \frac{\partial^2 \theta}{\partial t \partial r}\Delta t \Delta r}. \tag{3.43}$$

The expected energy resolution according to equation 3.42 is also shown in figure 3.20 for two different DLD time resolutions. A rather poor resolution value of 420 ps was measured with our detector (see next section) while a value of 180 ps represents a more typical value achieved by optimized DLD systems. Only the shaded area is used for the data conversion. As can be seen from the figure, the energy resolution generally depends on the position and the ToF, however, in order to compare it to experimentally obtained values derived from the slope of the Fermi-edge (corresponding to the shortest ToF) of

angle-integrated spectra, we define the theoretical value in this case as the maximum of the position- and time-dependent resolution. Additionally, the energy resolution strongly depends on the adjusted retardation ratio, and therefore a general statement about its magnitude cannot be made, but the expected resolution can always be estimated for any specific case by evaluating the corresponding conversion function. A natural consequence of the data transformation process by means of the conversion function is the compensation for chromatic lens aberrations within the valid kinetic energy range.

DLD time resolution

The basis for a reasonable energy and angle resolution of the spectrometer is the accurate and precise time measurement of the DLD detector. It is found that the time measurement suffers from imperfections corrupting the overall performance of the spectrometer. By feeding the femtosecond laser pulses directly onto the multichannel plates, the time response of the detector is investigated and the results are summarized in figure 3.21. The time response is strongly dependent on the electron hit position, manifesting as a time offset which makes up the same order as the width of the time response itself, considerably broadening the area-integrated time resolution of the detector. In order to obtain a position dependent time-offset map, the detector area is divided into a raster of small segments for each of which the time response is extracted by fitting a Gaussian function to the position-integrated ToF data. The time-offset values obtained from this raster are then interpolated to the original pixel grid of the detector. The resultant time-offset map is shown in figure 3.21(c). It can be seen that the largest offset occurs at the rim of the detection area. Therefore, only electron events within a limited area around the center part, indicated by the green circle, are considered for the data conversion. Additionally, the time values of the raw data stream are corrected according to the time-offset map. The latter step improves the corresponding energy resolution of the spectrometer up to 10% as indicated by the evaluation of the width of the Fermi edge in figure 3.21(e). Nevertheless, the temporal width of the detector response after correction is with 420 ps FWHM still by a factor 2–3 too large (a typical time resolution of an optimized delay-line anode is 180 ps). This discrepancy can either arise from timing jitter in the start signal or the stop signal of the TDC. Any timing jitter in the start signal is minized by the usage of a CFD as a trigger discriminator. As opposed to a standard constant level discriminator the CFD derives its trigger time from a constant fraction of the pulse amplitude rather from a constant predefined signal level, thus eliminating timing jitter which is caused by amplitude fluctuations. Furthermore, measuring the time response of the DLD with different laser sources and trigger mechanisms gives similar results as presented above. A closer inspection of the delay-line circuitry finally revealed mistuned components in the internal electronic signal chain as the reason for the poor time resolution. Unfortunately, the measurements performed in the course of this thesis could not yet benefit from an optimized delay-line circuitry due to this finding. However, a significant improvement of the spectrometer's performance regarding energy and angle resolution can be expected for upcoming measurements.

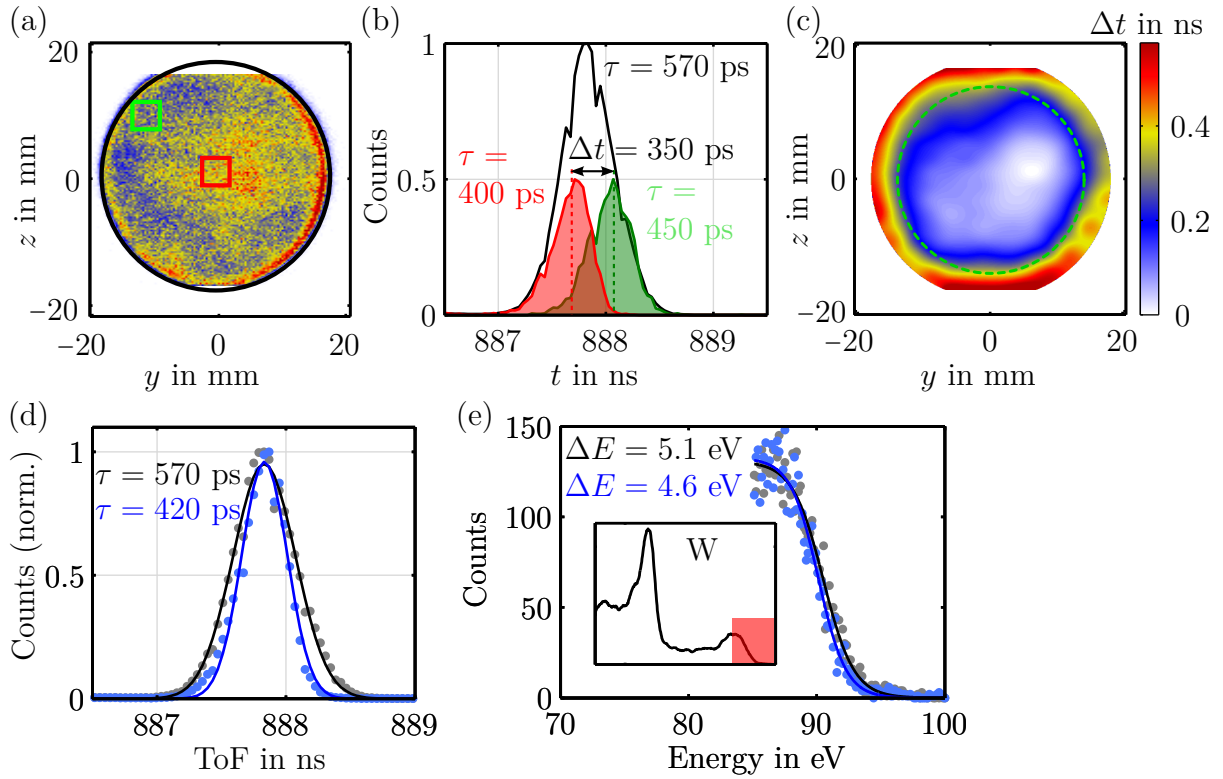

Figure 3.21: Time response of the DLD detector, measured by illuminating it with femtosecond laser pulses. The time response is found to be strongly position dependent. τ describes the FWHM width of the indicated curves. (b): Time response for different exemplary selected areas as illustrated in (a). A significant time offset between different hit positions is observed, leading to considerable broadening of the area-integrated time resolution to nearly 600 ps. (c): Position dependent time-offset map which is used to correct the measured time events from the detector. Only hit events within the green circle are used for the data transformation. (d): Area-integrated time resolution with and without time-offset correction according to the map in (c). (e): Effect of the time correction on the energy resolution of the spectrometer in LAD mode at low RR, measured on W(110). The energy resolution is improved by 10%.

Magnetic field compensation

For a reliable and accurate angle-energy mapping of the electrons, it is crucial that their trajectories are not distorted by external electric or magnetic fields. Generally, it is much easier to compensate for DC fields than for AC fields which is why the latter have to be avoided in any case. External (static) electric fields are basically compensated for within the chamber by the metal vessel (Faraday cage) while the compensation of external (static) magnetic fields require special attention. A common method is to build an enclosure made of a metal with high magnetic permeability, typically a Fe-Ni alloy (such as μ-metal), around the volume to be shielded. Such a material exhibits a high magnetic permeance, efficiently guiding magnetic field lines around the shielded volume. As the magnetization

inside such a material already saturates at low magnetic fields, several layers of material are usually employed for an efficient shielding. In this way, high damping of magnetic fields is achieved within such an enclosure. However, any cold working/mechanical shaping process of these alloys downgrades their permeability which has to be recovered by subsequent annealing under vacuum or inert gas atmosphere, making constructions of these materials quite costly. Our spectrometer incorporates two layers of 2 mm thick μ-metal to screen external magnetic fields to an uncritical level. The space between sample and the spectrometer's front lens, however, is not encapsulated by this shield, and therefore electrons are exposed to external stray fields over the length of the spectrometer's working distance. For cost reasons, the construction of the entire chamber from μ-metal was not suitable. Instead, the chamber and its flange components are made from a stainless steel alloy with reduced Ni content and a highly stable austenitic structure (316L/EN 1.4404 and 316LN/EN 1.4406 or EN 1.4429) which gives a very low magnetic permeability of $\mu_m < 1.005$. This ensures a negligible remanent magnetization of the material and allows the use of external coils for magnetic field compensation. Additionally, all components in the close vicinity of the unscreened volume are made of non-magnetic materials (Aluminum, Titanium and Molybdenum) in order to reduce locally inhomogeneous stray fields which cannot be accurately compensated for. The main magnetic stray field is the earth's magnetic field which has a strength of the order of $B_E \approx 50\ \mu$T at an inclination angle of $\alpha_B = 60°$. The spectrometer axis is nearly aligned to the geographic North, i.e. the vertical field component $B_{E,z} = B_E \sin(\alpha_B)$ is the most disturbing one. In order to estimate the influence of stray fields, we calculate the angle deviation of an on-axially emitted electron of initial energy E_{kin} under the influence of a field component perpendicular to the initial emission direction (representative B_z). Using the Lorentz force the lateral drift distance is

$$y = -\frac{eB_z\Delta l^2}{2\sqrt{2m_e E_{\mathrm{kin}}}}, \tag{3.44}$$

where Δl is the on-axis distance over which the electron experiences the stray field, which can be approximated as the spectrometer's working distance. Determining the ratio between the initial velocity v_x of the electron and the velocity component v_y induced by the magnetic field, one gets the angle deviation $\delta\alpha$ as

$$\delta\alpha = \arctan\left(-\frac{eB_z\Delta l}{\sqrt{2m_e E_{\mathrm{kin}}}}\right). \tag{3.45}$$

Although a stray magnetic field cannot directly change the value of E_{kin}, it can do so indirectly due to the correlation between angle and energy in the mapping from position/ToF to angle and energy in the data conversion process. It is obvious from equation 3.44 and 3.45 that the distorting influence of a given magnetic stray field decreases with increasing initial kinetic energy of the electron.

A triaxial compensation system was designed in order to compensate for (homogeneous) magnetic stray fields. It consists of three coil pairs whose center axes are perpendicularly aligned to each other, giving full 3D control of the resultant field generated by the coils.

Ideal compensation coils would be Helmholtz coils consisting of a pair of ring coils separated by a distance which equals half the ring diameter. Under this condition, the magnetic field is homogeneous in the central region and parallel to the center axis. For practical construction reasons however, squared coils are chosen. Also, the Helmholtz condition is relaxed in order to avoid a nested coil design. In this case, the coil windings can simply be attached to a rectangular support frame around the measurement chamber. An analysis of the field distribution near the center axis of a squared coil pair reveals that the loss of homogeneity of such a non-ideal coil design is acceptable if the volume which is to be shielded is small compared to the coil dimensions and if the distance between the coils of a pair is not larger than their arm length. The volume which has to be screened is of cylindrical shape with a length of $L = 53.3$ mm (working distance) and a diameter of $D = 30$ mm (opening diameter of the front lens). The two horizontally aligned coil pairs have an arm length of $a_{1,2} = 0.7$ m and a distance of $d_{1,2} = 0.7$ m, the vertically aligned coil pair has an arm length of $a_3 = 0.7$ m and a distance of $d_3 = 0.5$ m. The representatively simulated field distribution of the vertical coil pair is shown in figure 3.22. Each coil consists of 12 turns of copper wire (2.5 mm^2 cross-section). Corresponding coil pairs are connected in series with counter-rotating winding direction. The simulation confirms a good field homogeneity within the volume of interest despite of the non-ideal arm length to distance ratio. A maximum field variation smaller than 0.5 μT is obtained. The magnitude of the coil current is chosen so that the vertical component of the earth's magnetic field $B_{E,z}$ is completely compensated for at the origin. Practically, the coil currents are pre-adjusted with the help of a calibrated fluxgate sensor which is placed between sample and spectrometer. In this way the resultant magnetic field can be suppressed to $B_{\mathrm{res}} \leq 3$ μT. In order to verify the the quality of the compensation scheme experimentally, and for fine tuning of the coil currents the sample is illuminated by a focused electron beam with an initial kinetic energy of $E_{\mathrm{kin},i} = 1000$ eV. The inelastically scattered electrons are imaged with the spectrometer using its drift mode, i.e. with all lenses switched off. The acceptance angle of the spectrometer is reduced to approximately $\Delta\alpha = \pm 0.5°$ by means of the internal iris. Hence, for ideal conditions the electrons form a nicely round and centered illumination spot on the detector. Any deviation in shape and position reveals uncompensated stray fields. The result is shown in figure 3.23. The scattered electrons form a broadband energy spectrum ranging from zero kinetic energy up to $E_{\mathrm{kin},i}$, which allows the investigation of stray field effects as a continuous function of kinetic energy. The non-uniform deformation of the beam spot for slow electrons ($E_{\mathrm{kin}} < 10$ eV) reveals the presence of minor inhomogeneous stray fields to which, however, the faster electrons ($E_{\mathrm{kin}} > 10$ eV) are not sensitive. The energy dependent shift of the electron spot is illustrated by yE- and zE-slices. This representation is also useful for the fine tuning of the coil currents. The left and mid-left panels show a well adjusted stray field compensation. In this case only the slow electrons experience a small lateral shift caused by the field-induced angle deflection given in equation 3.45. The lateral drift distance of the electron spot on the detector plane can be derived from equation 3.44 to

$$y \approx -\frac{eB_z \Delta l}{m_e} t_{\mathrm{ToF}} \tag{3.46}$$

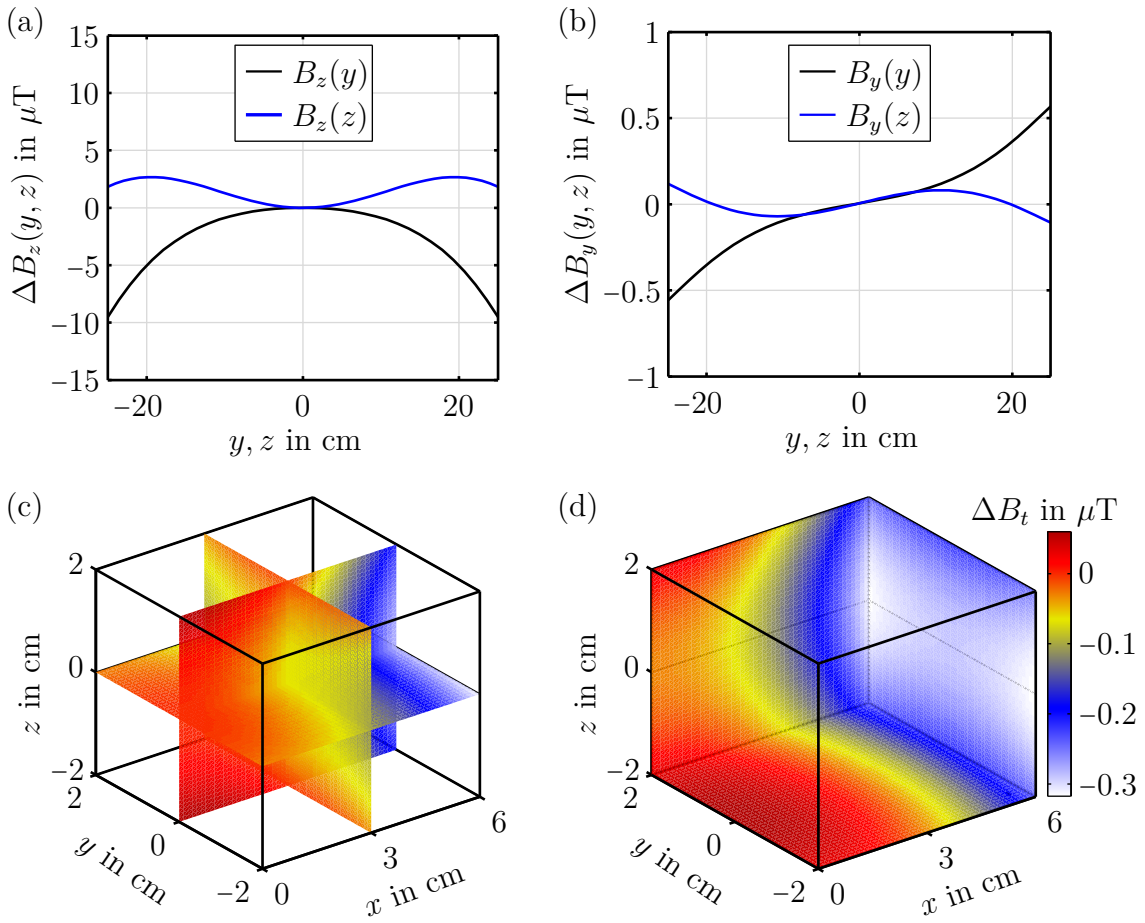

Figure 3.22: Calculated magnetic field distribution of the vertical compensation coil. (a): B_z-field component. (b): B_y-field component. (c), (d): Distribution of the total magnetic field strength $B_t = \sqrt{B_x^2 + B_y^2 + B_z^2}$ within the volume of interest. The field strength is displayed relative to the field strength at the origin which coincides with the sample position. The simulation shows that the coils produce a sufficiently homogeneous field distribution with a maximum variation of smaller than 0.5 μT within the volume of interest.

for magnetic fields and

$$y \approx \frac{eE_y \Delta l}{m_e(L_{\text{tube}} + \Delta l)} t_{\text{ToF}}^2 \tag{3.47}$$

for electric fields, where L_{tube} is the length of the spectrometer tube from the inlet to the detector plane. Note the different exponential relation in the time-of-flight for the two field types. Fitting a quadratic function to the center of gravity of the electron distribution in the yE- and zE-plane (green lines) allows the determination of the residual magnetic field from the linear term and the residual electric field from the quadratic term. The maximum values are $|B|_{y,\text{res}} < 1.2$ μT and $|E|_{z,\text{res}} < 27$ mV/cm. The right and mid-right panels in figure 3.23(c) illustrate a poorly adjusted stray field compensation. The different

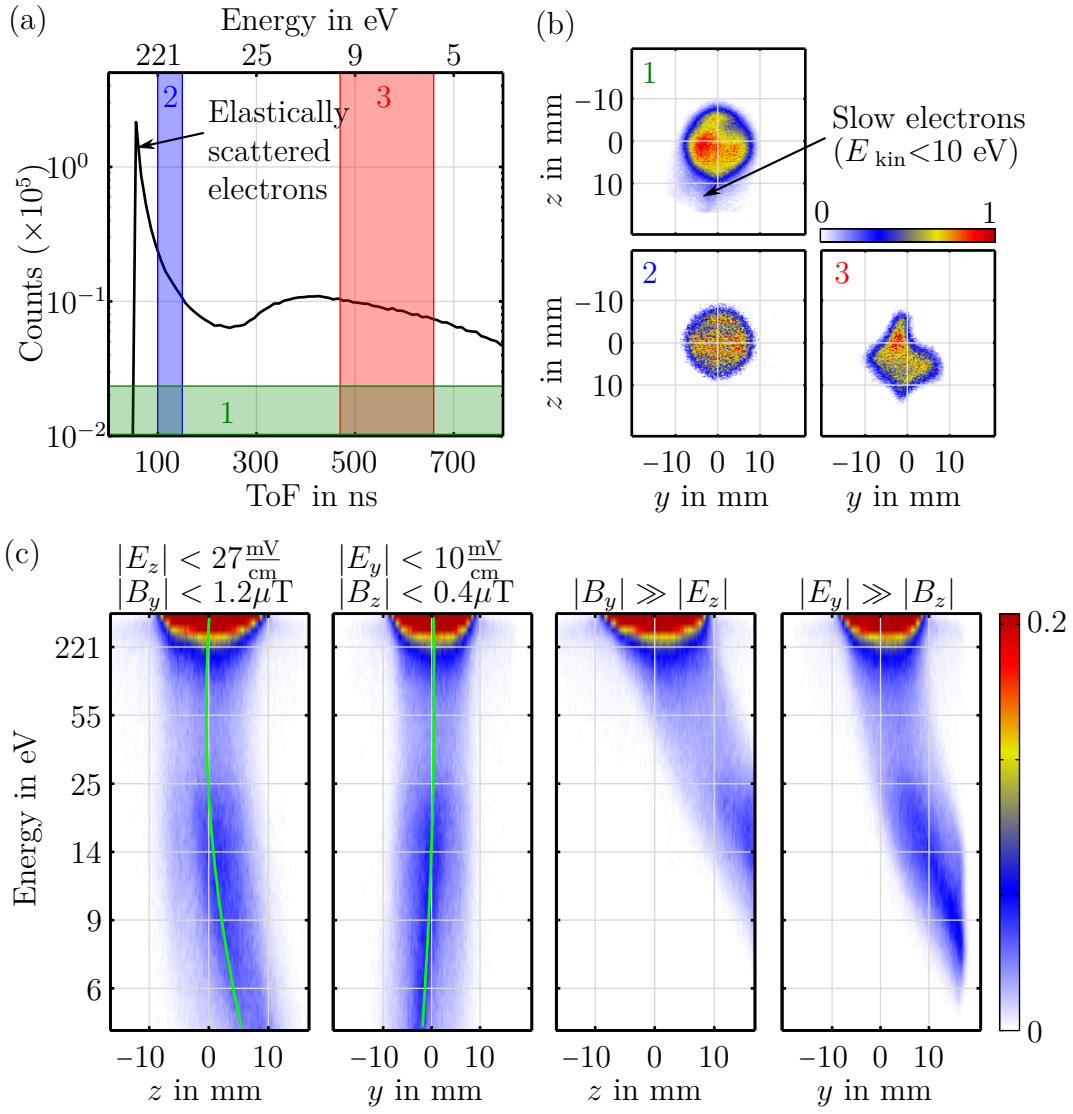

Figure 3.23: Illustration and estimation of residual stray fields using the spectrometer in drift mode. (a): Energy spectrum of scattered electrons. The prominent peak is formed by elastically scattered electrons (with an initial kinetic energy of $E_{\mathrm{kin},i} = 1000$ eV). (b): Beam spots for different energy selections. The irregular shape of the beam spot formed by slow electrons indicates inhomogeneous residual stray fields. (c): yE- and zE-slices indicating the lateral drift of the electron spot due to stray fields with good compensation (left and mid-left, the estimated residual fields are given above the plots) and bad compensation (right and mid-right).

deflection behavior (linear and quadratic) can be clearly identified depending on whether the magnetic or the electric field dominates.

3.2.7 Sample preparation and handling

For a convenient sample exchange and sample preparation, a separate vacuum system was constructed which is attached to experimental chamber. It consists of two small vacuum chambers separated by a gate valve. One chamber acts as a load lock and is equipped with an additional sample garage and an in-vacuum pincer grip on a wobble-stick manipulator to load the sample into the receptacles of the second chamber. The latter comprises a long-range transfer rod to convey the sample to the experimental chamber, a process gas inlet, an evaporation system for the in-situ preparation of coatings, a high-power heater and an ion sputter gun. This equipment allows the preparation/cleaning of a multitude of (metal) samples, which usually requires subsequent cycles of sputtering and annealing, sometimes under a special process gas atmosphere [94]. The heater is able to heat the sample well above 2000°C within tens of seconds, see figure 3.24(b). Such high temperatures are necessary for the preparation of tungsten [154], which is the

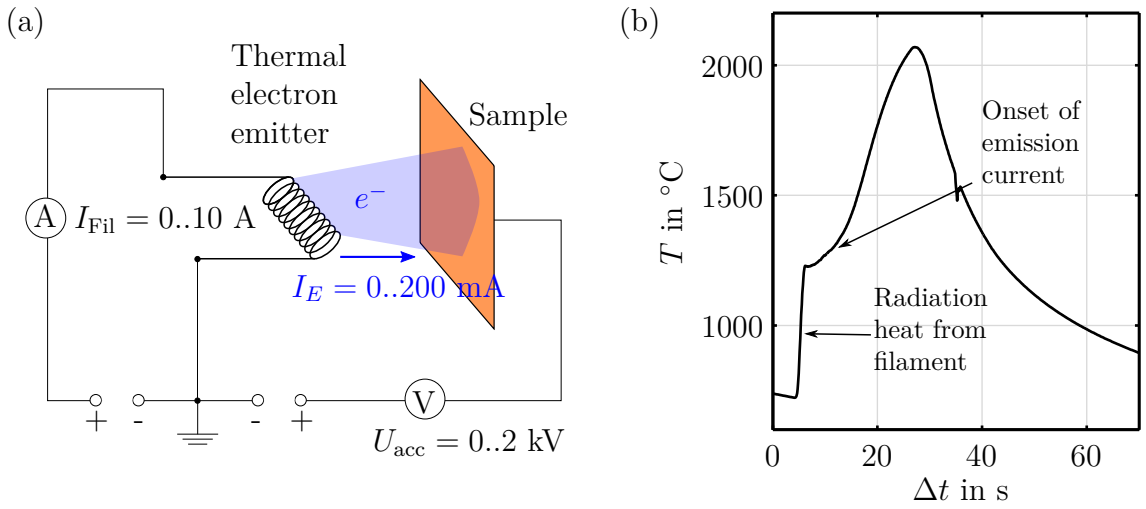

Figure 3.24: (a): Electron bombardment heater. Electrons emitted from a hot filament are accelerated and directed onto the sample by a high voltage. I_{Fil}: filament current, I_E: emission current, U_{acc}: acceleration voltage. (b): Typical high temperature flash of a tungsten sample at $P = 180$ W of applied electrical power. The power is increased gradually. Before electron emission from the filament sets in, the sample is already heated by radiation heat to about 1200°C.

primary sample used in this work. The heating mechanism is based on the bombardment of accelerated electrons. This technique is very efficient due to its highly-directed and local heat input. The heater assembly is completely made of refractory metals and high-temperature ceramics as isolators. The sample temperature is monitored by a pyrometer.

The principle of electron bombardment heating is depicted in figure 3.24(a). Moreover, the entire sample preparation and handling system is mounted on a mobile rack and can flexibly be moved and attached to other experimental chambers.

3.2.8 Carrier-envelope phase tagging and data mapping

The setup of the CEP-tagging method for phase-resolved streaking measurements is shown in figure 3.25. The data acquisition process collects the data streams from the ATI phase-meter as well as from the delay-line detector and keeps track of the delay time τ. The two data streams are not intrinsically aligned to each other due to the stochastic characteristic of the delay-line detector. Therefore, an appropriate mapping of their data entries is required. This synchronization process calls for some special considerations and the modifi-

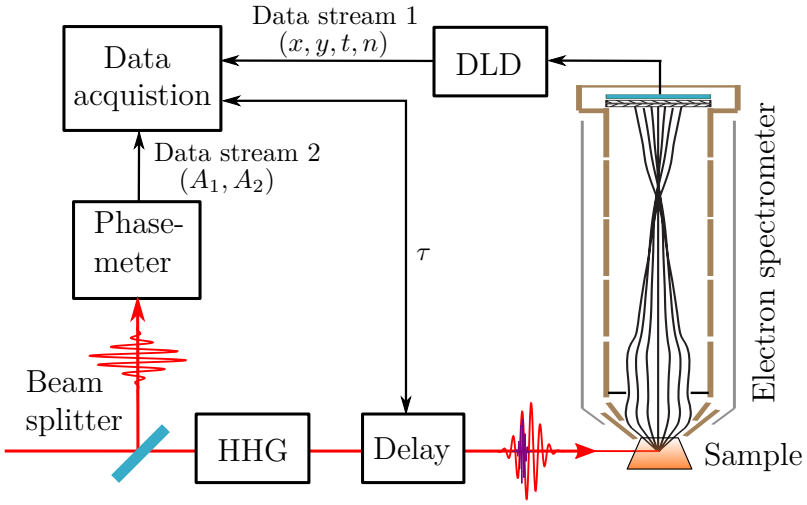

Figure 3.25: Setup of the phase-tagged photoelectron streaking experiment. The data streams from the ATI phase-meter and from the delay-line detector are acquired simultaneously. Their data entries, however, are not mutually aligned, but require appropriate mapping as the DLD events occur probabilistically.

cation of existing hardware. The fundamental difficulty is to ensure the correct assignment of the asymmetry pairs to the corresponding DLD events. While a pair of asymmetry values is delivered from the phase-meter for every laser shot, the occurrence of an event detected by the DLD is probabilistic, generally not providing a data entry on a single-shot basis. Therefore, a mechanism which keeps track of the laser shot number for every data entry is required. In collaboration with Surface Concepts GmbH, the performance of the TDC was extended by this functionality by adding an electronic counter to the internal FPGA circuit which is incremented by a logic signal applied to an additional external input (*Tag*-input). The current counter value is appended to each output DLD data triplet. The *Tag*-input is triggered by the same signal (provided by the photodiode) which is used to trigger the timing unit of the TDC (*Start*-input) and the PMPU (*Trig-in*-input). In this

manner, each data entry in the DLD stream is tagged by a number n which is associated with the corresponding laser shot that created the event for this entry, see figure 3.26(a). This additional information finally allows the proper assignment of the DLD events to the

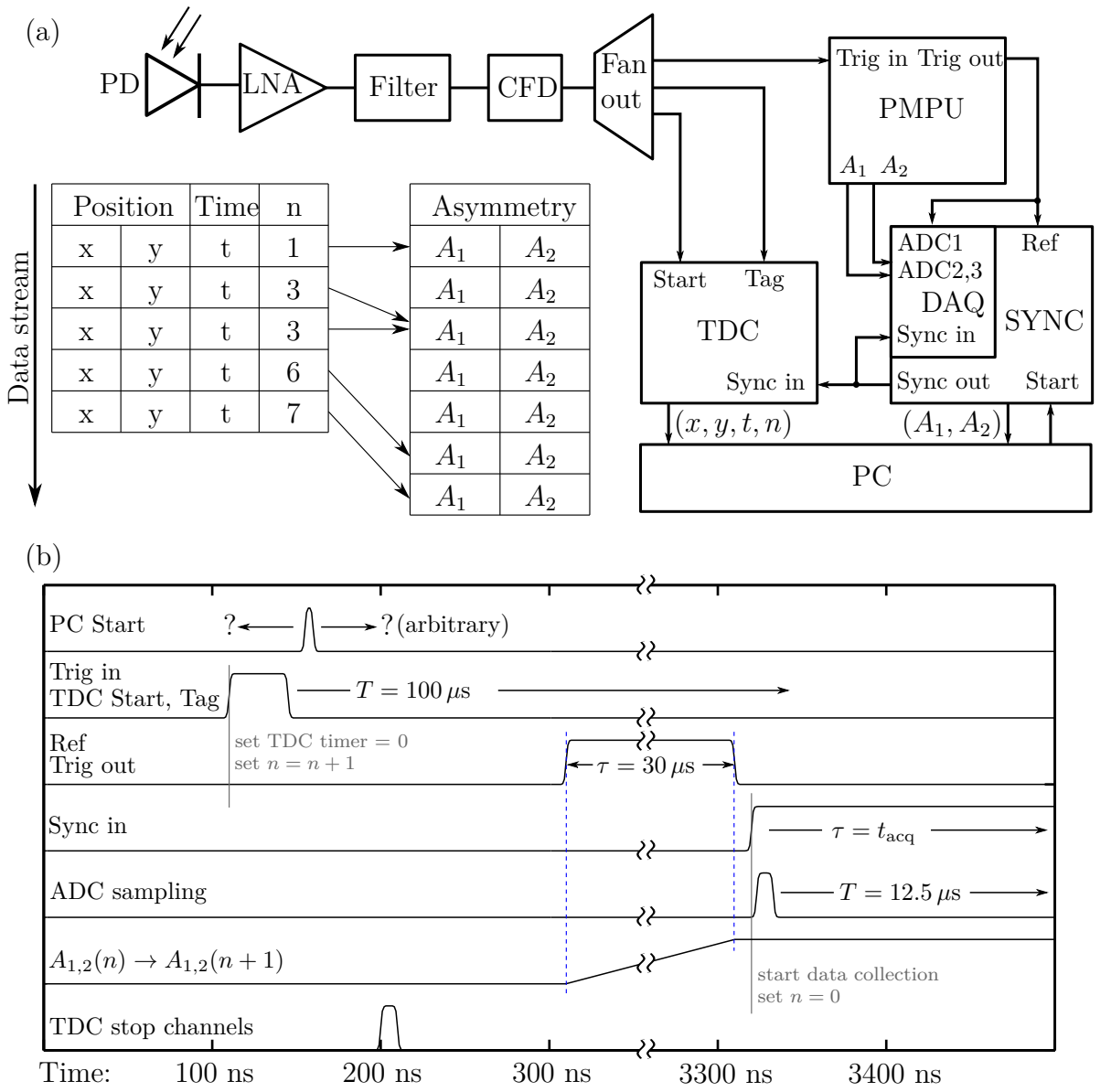

Figure 3.26: Synchronization of the data streams from the ATI phase-meter and the electron spectrometer. (a): Schematic of the data acquisition/synchronization setup and illustration of the data assignment process. LNA: low-noise amplifier, CFD: constant-fraction discriminator, PMPU: phase-meter processing unit, TDC: time-to-digital converter, DAQ: data acquisition unit. (b): Time-sequence of the relevant signals for the synchronization setup.

corresponding asymmetry values. The reliable and correct operation of this implementation is of vital importance, since due to the random nature of the CEP for consecutive laser

pulses any slippage of the *Tag*-counter or any loss of even a single counter event would render the dataset useless. Technical pitfalls related to this issue are discussed in appendix A. In a next step, it has to be ensured that the onset of data recording from both streams is consistent between different acquisition cycles. This assures conformity of datasets from different acquisitions. However, the instant of user interaction for starting data collection is arbitrary. Therefore, a latching mechanism is used in order to schedule the onset of data recording to a well-defined and consistent instant of time. This requires a precise knowledge of the temporal sequence of the involved signals, which is visualized in diagram 3.26(b). The latch for the onset of data recording is provided by the falling edge of the signal at the *Ref*-input. This is a forwarded trigger signal from the CFD which is delayed by the PMPU data processing time and broadened to a width which corresponds to the time it takes to output the new asymmetry values (transition time). Once the user has initiated data acquisition by a software trigger, a synchronization unit waits for the next falling edge of the *Ref*-signal, then generates a *Sync*-signal which sets the *Tag*-counter of the TDC to zero, and which initiates the sampling signal for the ADCs of the DAQ unit. In order to prevent the acquisition of asymmetry values during their transition time, only those values are accepted which coincide with a low logic level of the *Ref*-signal.

Chapter 4

Few-cycle driven HHG at 10 kHz and its polarization control via multilayer optics

In this section we present the high harmonic output of the beam line, characterized by the home-build XUV spectrometer, see section 3.2.5, and the XUV beam monitor, see section 3.2.3. Due to the reduced pulse energy provided by the laser amplifier at 10 kHz and subsequent additional power losses (nonlinear fiber compressor, silver mirrors, power splitting to the phase-meter), a remaining pulse energy of 70-80 μJ is available at the gas target for HHG. It was experimentally found that a focusing geometry with a F-number of 40-60 provides suitable harmonic output beyond 100 eV for the given pulse parameters. The Rayleigh length associated with this geometry limits the coherence length of the HHG process. Accordingly, the length of the gas target has to be adapted to the coherence length for an efficient conversion. Various excitation parameters have been scanned in order to investigate the high harmonic output.

4.1 Few-cycle driven HHG at 10 kHz

The gas cell is formed by a thin metal tube with two tiny bore holes in beam direction which basically confine the gas volume to the inner diameter of the tube. A tube diameter slightly below one millimeter has been empirically found to be most efficient for the intended focusing geometry which implies focal lengths of 30-40 cm. The high harmonic output for neon, using a focal length of 40 cm, as a function of the backing pressure in the metal tube is shown in figure 4.2. The spectral NIR pulse properties and the corresponding PAP are depicted in figure 4.1, indicating a FWHM pulse duration of 5.7 fs. The peak intensity at the focal plane is estimated to be $I \approx 6 \cdot 10^{14}$ W/cm^2. An iris in the NIR beam path is used to optimize the high harmonic yield by adjusting the peak intensity and the Rayleigh length for best phase-matching. The yield is further optimized regarding the nozzle position relative to the focal plane (typically few millimeter off-focus). The upper

panel in figure 4.2 shows the transmission characteristics of the metal foils used to filter the high harmonic spectrum and to block the NIR field. The structure of the spectra exhibits discrete harmonic peaks below 90 eV and a broad continuum near the cutoff energy, which is typical for HHG driven by few-cycle pulses. However, it is reminded that the spectra are recorded CEP-integrated as the laser system is not CEP-stabilized. Therefore, the high-energy continuum appears broader than it actually is since the harmonic spectrum becomes most CEP-sensitive near the cutoff which manifests in a CEP-dependent shifting of the harmonic peaks [58, 118] (see also the simulation in figure 5.8).

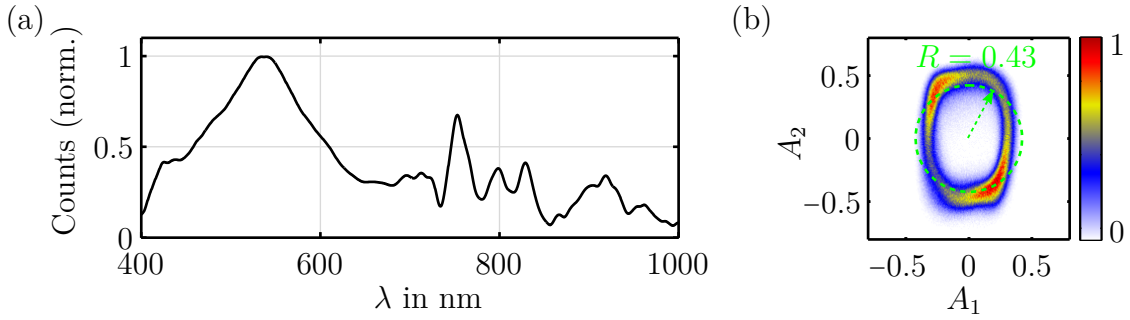

Figure 4.1: Spectral NIR pulse properties as used for HHG (figure 4.2) and characterization of the pulse length. (a): Spectrum after SPM broadening in the HCF. (b): Parametric asymmetry plot for 2 million consecutive laser shots indicating a mean pulse duration of 5.7 fs.

The graph also shows the pressure-dependent phase-matching behavior in which the green line indicates the evolution of the optimum pressure for best phase-matching as a function of harmonic energy. From this it is apparent that lower photon energies require a higher backing pressure for best phase-matching where optimum phase-matching in the cutoff region is achieved at a backing pressure of $p_{\mathrm{opt}} = 200$ mbar. The logarithmic plots at the bottom of the figure represent spectra at p_{opt} which reveal a cutoff energy around 130 eV. The absolute flux of the high harmonic output is determined by means of the XUV beam monitor, considering the quantum efficiency of the low-noise CCD chip as well as the transmission and reflection characteristics of the involved XUV optics. The overall flux is finally calculated by integrating over the entire spatial XUV beam profile. Utilizing mirror 3 of the XUV beam monitor (see figure 3.10 and table 3.1) a lower limit of the high harmonic flux is estimated to be $5 \cdot 10^9$ photons/s within a bandwidth of 8% around the central energy of 90 eV.
Figure 4.4 shows harmonic spectra generated from neon with a shorter focal length of 30 cm and changed NIR pulse properties. The corresponding pulse spectrum and the associated PAP are given in figure 4.3, exhibiting a longer mean pulse duration of 9.1 fs. These pulse properties and focusing condition are applied to all of the following high harmonic spectra measurements.

It is noted that a XUV sensitive CCD camera (Pixis, Princeton Instruments) is used as a detector for the following measurements while a multi-channel plate with phosphor screen was used for the measurement in figure 4.2. Therefore, a drop of the signal strength

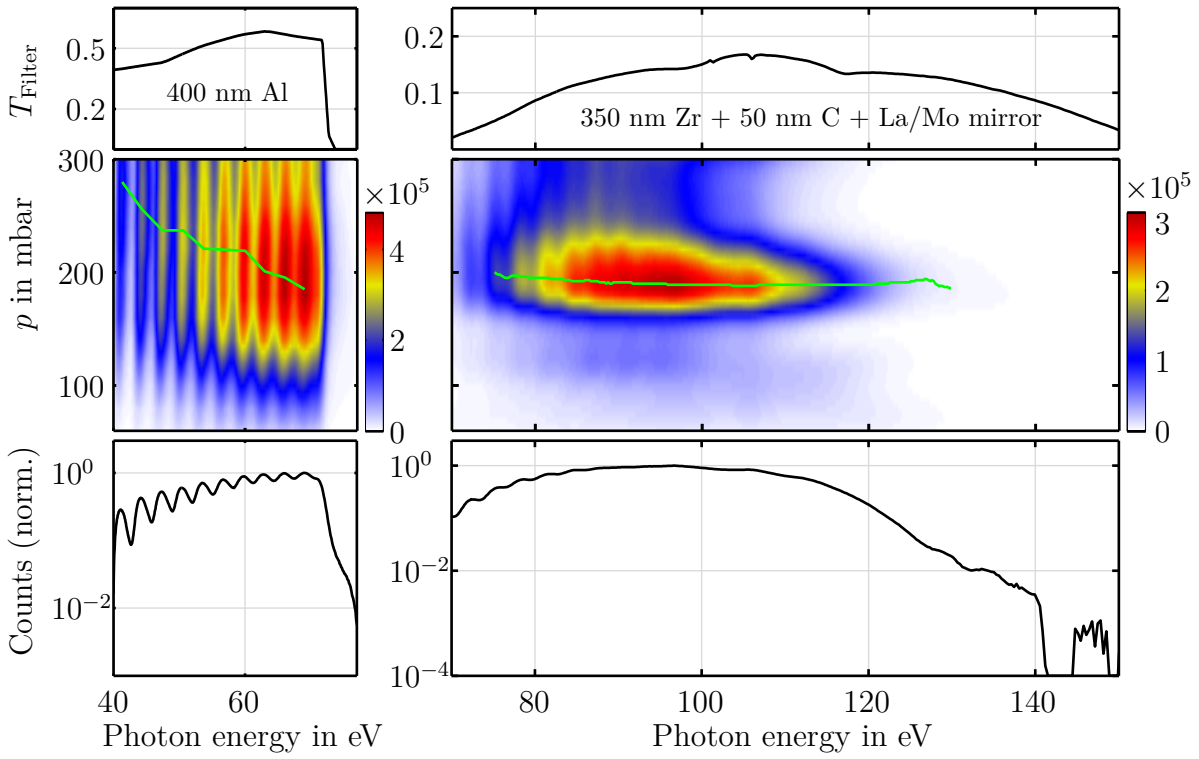

Figure 4.2: Pressure dependence of the harmonic yield generated from neon. The NIR beam is focused with $f = 40$ cm. Cutoff: ~ 130 eV. Top: Filter and multilayer mirror transmission. The green line indicates the evolution of the optimum pressure for best phase-matching. The profile in the lower panel is drawn for a pressure of 200 mbar.

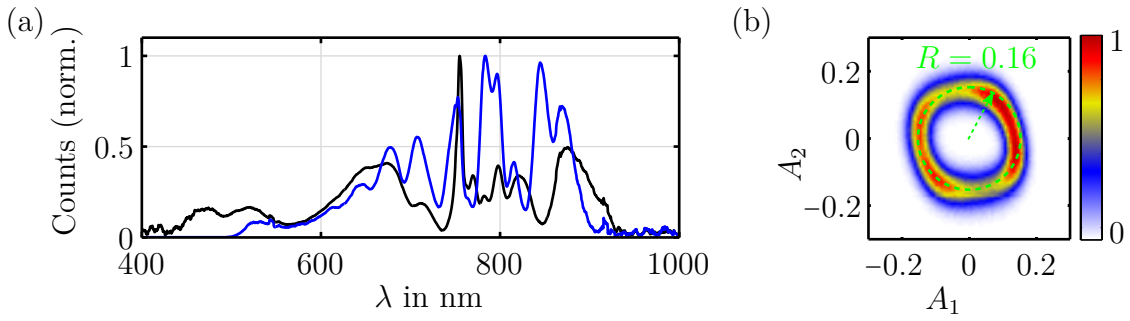

Figure 4.3: Spectral NIR pulse properties of sub-10 fs pulses as used for HHG and characterization of the pulse length. (a): Spectra after SPM broadening in the HCF. The spectra varied slightly in width and shape on a daily basis (black and blue line) (b): Parametric asymmetry plot for 3 million consecutive laser shots corresponding to the blue spectrum in (a) indicating a mean pulse duration of 9.1 fs.

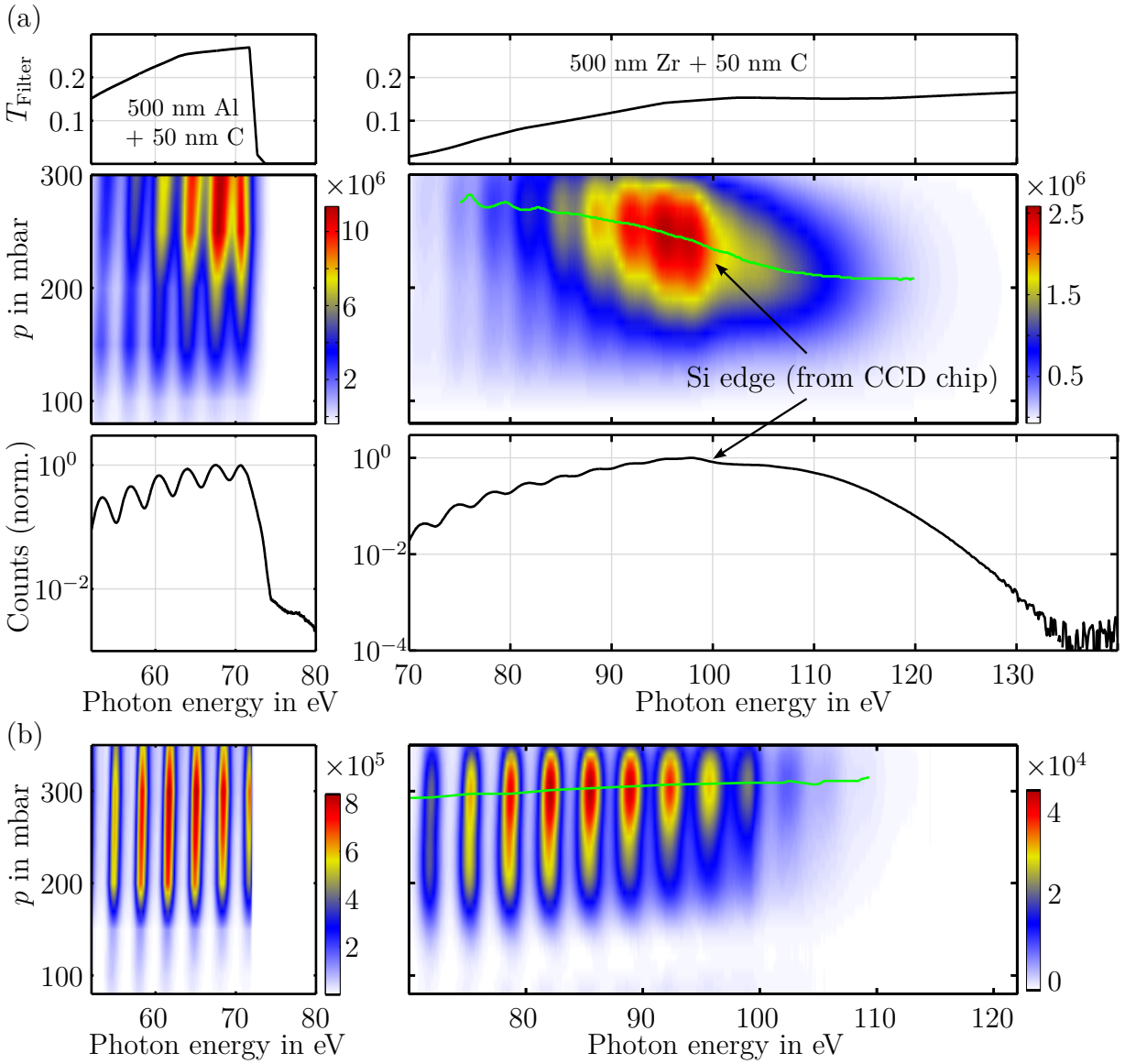

Figure 4.4: (a): Pressure dependence of the harmonic yield generated from neon with a focal length of 30 cm. Cutoff: $\sim$ 130 eV. Top: Filter and multilayer mirror transmission. The pressure-dependent phase matching behavior near the cutoff region is more pronounced (green line) for the shorter focal length. The profile in the lower panel is drawn for a pressure of 220 mbar. (b): Pressure dependence of the harmonic spectra for a positively chirped NIR driver pulse. The phase-matching behavior as well as the line width have changed considerably (see also figure 4.7).

at 99.6 eV is generally observed in the subsequent spectra due to the L-absorption edge of silicon in the CCD chip. This should not be confused with a real feature in the harmonic spectra. Due to the tighter focusing condition, the pressure-dependent phase matching behavior near the cutoff region is more pronounced (see figure 4.4(a)). However, its exact evolution is sensitively affected by the properties of the driving NIR pulse, as indicated in part (b) of the figure in which the pulse has been chirped by inserting ~ 200 μm of glass. Furthermore, the line width of the harmonic peaks changes, which will be discussed later in this section.

High harmonic spectra generated from argon are depicted in figure 4.5. The achieved

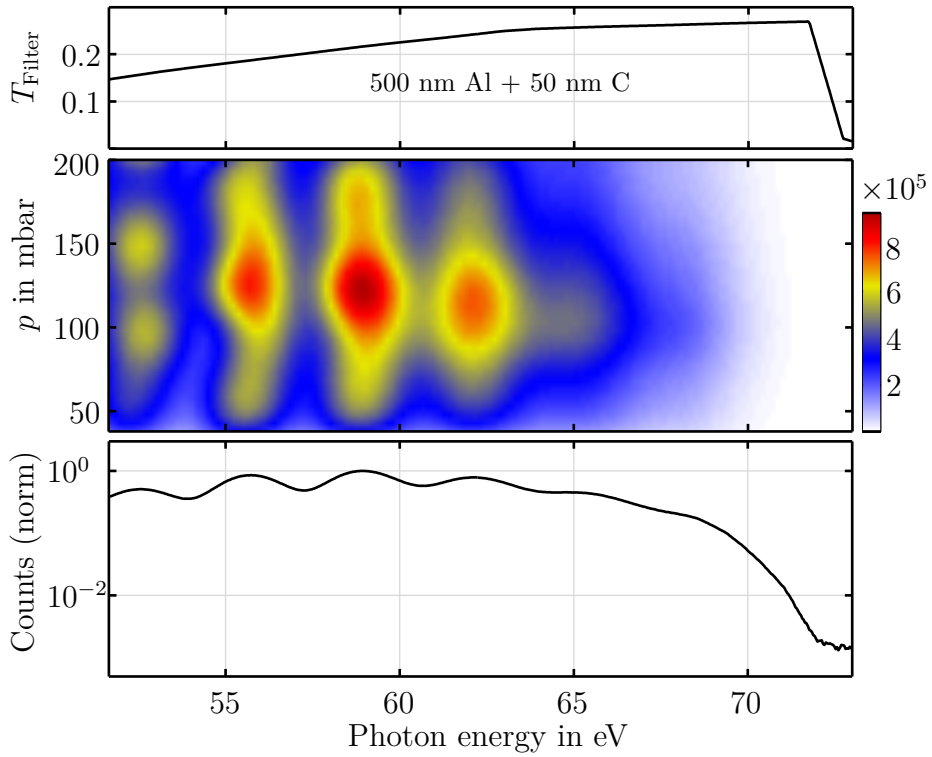

Figure 4.5: Pressure dependence of the harmonic yield generated from argon with a focal length of 30 cm. Cutoff: < 75 eV. The observed cutoff energy is phase-matching limited due to exceeding a critical ionization level. Top: Filter and multilayer mirror transmission.

cutoff energy is significantly lower than from neon. This fact is well-known, and is the result of exceeding a critical ionization level in the gas medium which prevents further efficient phase-matching [109, 111]. Phase-matching primarily aims at balancing the negative contributions of dispersion, e.g of the electron plasma, with the positive contributions of dispersion, e.g. of the neutral gas atoms. Once the ionization level becomes so high that plasma dispersion overwhelms the other contributions, the conversion process gets inevitably phase-mismatched. This phase-matching limitation reduces the effective cutoff

energy below the theoretical limit given by equation 2.70. This effect is more pronounced for argon than for neon since the ionization probability of argon is lower due to its smaller ionization potential. Especially long driver pulses are affected by this cutoff limitation. Due to their slow rise in intensity, the critical ionization level may already be reached well before the optical cycles with the highest field strength can contribute to the HHG process.

A more detailed plot of the pressure-dependent harmonic yield for a fixed photon energy at 66 eV is shown in figure 4.6. In this measurement the high harmonic signal is integrated over the full XUV beam profile and is recorded in steps of 10 mbar. In the low pressure

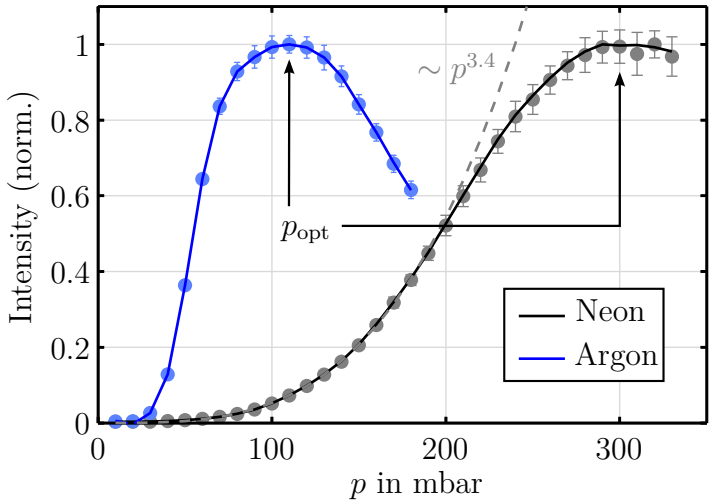

Figure 4.6: Detailed pressure dependence of the harmonic yield at 66 eV for argon and neon. Different regions can be observed: exponential growth in the low pressure region, saturation for increasing pressure and a maximum at p_{opt} when phase-matching is achieved. The optimum pressure for argon is considerably lower than for neon due to their different dispersive characteristics.

range the high harmonic yield increases exponentially. Opposed to the prediction of a quadratic increase with regard to gas density from a pure atomic response with constant coherence length [30], the actual exponential growth exhibits a higher exponent, e.g. 3.4 in the case of neon. This fast growth of the high harmonic signal can be explained by a pressure-dependent increase of the coherence length which reaches its maximum at p_{opt} [61]. Finally the yield saturates with increasing pressure and peaks at p_{opt} when the different dispersion contributions are balanced, i.e. when the phase-mismatch is minimized. The more dispersive the gas, the lower p_{opt} since in this case a lower gas density is required to match the dispersion of the neutral gas and the free electron background generated by ionization. Therefore, the optimum pressure obtained for argon is considerably lower than for neon.

The following measurement demonstrates the influence of chirp of the driving laser field on the structure of the HHG spectrum. Figure 4.7 shows high harmonic spectra driven by pulses with varying chirp. Different chirp values are easily adjusted by changing the

insertion depth of one of the glass wedges after the nonlinear fiber compressor. As a re-

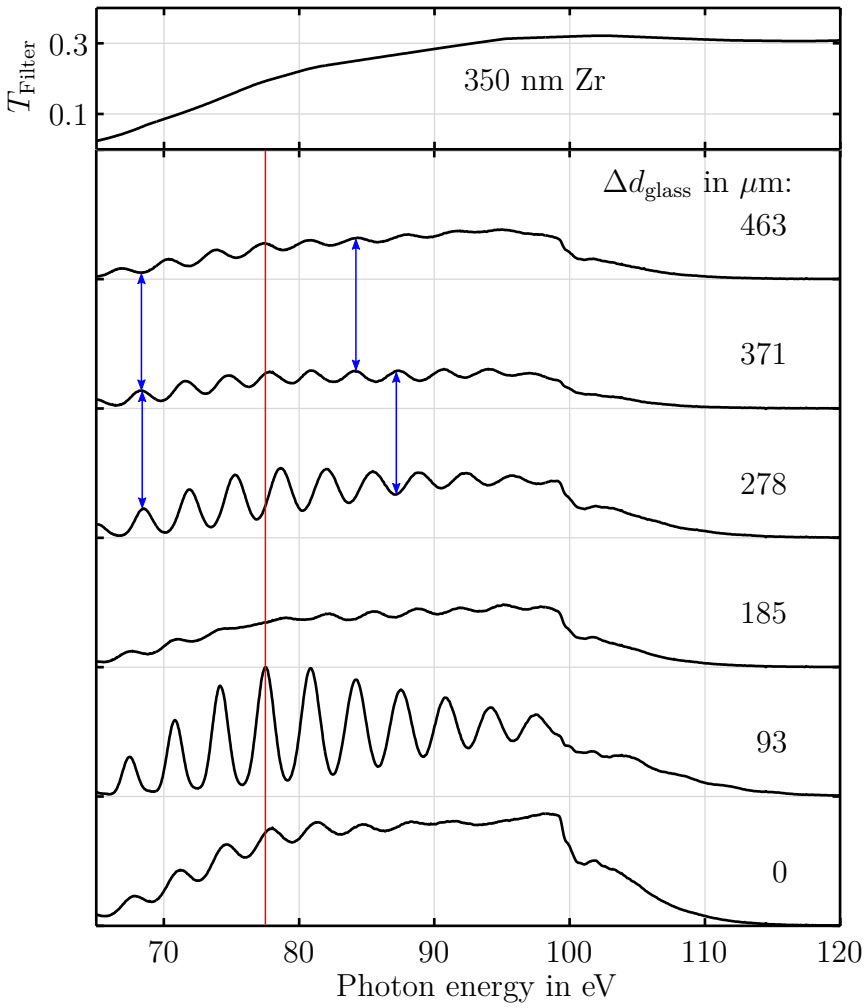

Figure 4.7: Variation of the harmonic spectra for chirped driver pulses. The chirp affects the substructure of the spectrum.It modifies both the line-width and the position of the harmonic peaks.

sult, both the spectral position of the harmonic peaks as well as their spectral width are modified. Note that this is not an explicit CEP effect as the measurement intrinsically integrates over the full 360° CEP range. The observed changes in the spectrum are a result of the interplay between the chirp of the NIR field and the intrinsic chirp of the harmonics induced by the atomic dipole phase. Depending on the exact chirp conditions of the NIR pulse, the laser and quantum phase can either subtract, leading to harmonic peaks of narrow line-width, or they can add up, causing spectrally broad harmonic peak widths, and hence near-continuum HHG emission [20, 119]. This behavior is quite obvious from figure 4.7. Additionally, it is observed that the harmonic peak positions shift with varying chirp factor and, furthermore, the peaks within a single spectrum are not strictly equidistant

any more. Peak positions along the red and blue guide-lines illustrate this behavior. Owing to the non-stationary carrier frequency of a chirped pulse, HHG events of subsequent half-cycles are not strictly periodic in time any more, leading to peak shifts and spectral asymmetry. However, peak shifts and spectral non-uniformity may also be introduced by ionization-induced [4] or non-adiabatic [60, 135] blue-shifting. Both processes are crucially affected by the intensity of the NIR pulse. As the employed method for adjusting the pulse chirp inherently alters the pulse duration, and thus its intensity evolution, the observed shifts are likely a result of different intermixing effects.

Next, the harmonic output as a function of nozzle position along the beam axis is presented in figure 4.8. The most prominent feature is the evolution of the cutoff energy, which reaches its highest value when the nozzle is positioned in the focal plane. The green circles represent the position-dependent evolution of the cutoff energy, where the cutoff is defined in this case as an arbitrary but constant signal value above the noise level. Also shown is a fit to the cutoff energy according to the scaling law of equation 2.70 using the common Gaussian transformation behavior of the beam waist in the vicinity of the focal plane. The fit shows good agreement with the measurement, and hence confirms the validity of the simple cutoff scaling law even for sub-10 fs pulses. Although the position of the gas nozzle in the focal plane promotes the highest cutoff energy, the position is unfavorable in terms of phase-matching due to the Gouy phase shift which considerably reduces the coherence length of the conversion process. Furthermore, a plasma-induced blue-shift of the harmonic peaks is apparent from the figure. The lower panel shows a detailed view of the 45th harmonic peak where the green line follows the position-dependent maximum of the peak, indicating a spectral shift of more than 1 eV. With increasing NIR intensity the peak shifts to higher photon energies. This is because plasma-induced blue-shifting is proportional to the ionization rate [4], and thus strongly depends on the NIR peak intensity. Therefore, plasma-induced spectral shifting is most pronounced close to the focal plane where the NIR intensity is highest.

A major disadvantage of the bore-drilled metal tubes as gas nozzles is that their positioning along the beam axis poses the risk of beam clipping. Interaction of the laser beam with the nozzle material may dramatically change the high harmonic output and may further induce instabilities, see next paragraph. In order to avoid such complications tapered glass capillaries in an end-fire geometry have been tested as an alternative nozzle type. Diameters of the tapered end between 80-200 μm have been tested. The laser beam is aligned slightly above the tapered end for this type of nozzle. The highest high harmonic yield at 90 eV (mirror three of the XUV beam monitor) could be achieved with an end diameter of 140 μm at a backing pressure of 650 mbar (which was actually the limit of the mass flow controller in the gas line). However, the flux was just one fourth of that obtained by the metal tubes. The lower yield is attributed to the poor spatial confinement of the gas volume along the beam direction once the gas leaves the end face of the capillary, thereby delivering an effective interaction length beyond the coherence length. Nevertheless, this type of nozzle is superior regarding long-term stability and less susceptible for beam clip-

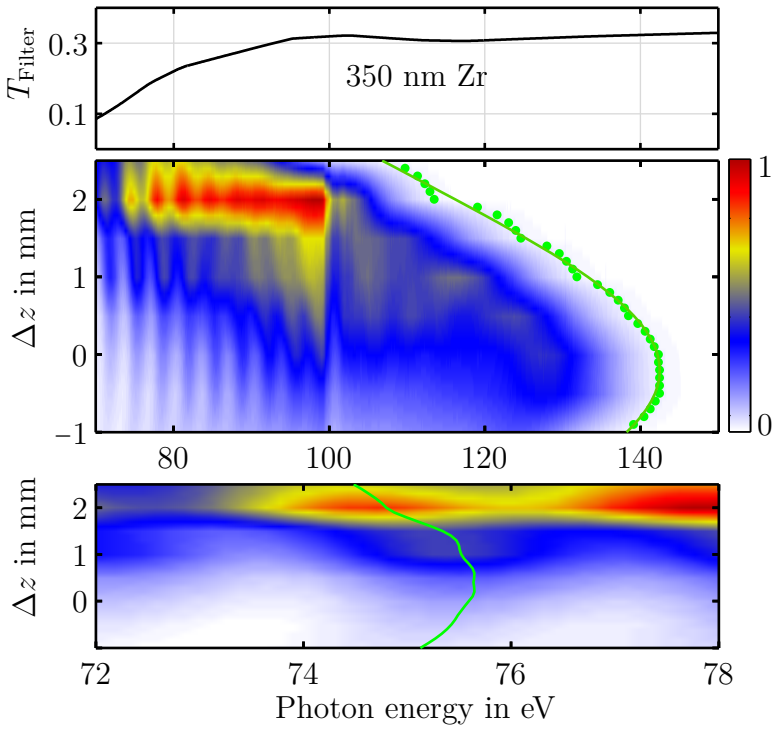

Figure 4.8: Harmonic spectra as a function of nozzle position along the beam axis. The cutoff energy shifts according to the scaling law 2.70 due to the varying pulse intensity (green dots and line in the middle panel). Also, a plasma induced blue-shift of the harmonic peaks is clearly discernible (lower panel).

ping. Therefore, we use this nozzle type in order to investigate the spatial far field profile of the XUV beam as it allows a convenient positioning of the nozzle along the beam axis without the risk of clipping and distorting the beam profile. The beam profiles are recorded with the XUV beam monitor using the 70 eV mirror (label two in figure 3.10 and table 3.1). Beam profiles for different nozzle positions relative to the laser focus are presented in figure 4.9. The spatially integrated signal strength is also shown. It is apparent that the beam diameter, and hence the beam divergence, as well as the ellipticity of the beam profile changes considerably. The divergence is smaller when the nozzle is positioned in front of the laser focus. This behavior is again a result of the intensity-dependent atomic dipole phase. The spatial intensity variation of the driving laser pulse induces a correspondingly spatial distribution of the intrinsic phase of the electron wave packet after its acceleration. This distribution leads to a curved phase front of the emitted high harmonic radiation which in turn defines its divergence. The sign of the phase front curvature of the NIR field, however, changes at the focal plane. As the HHG process is synchronized to the phase of the driving laser field, the degree of phase front curvature of the harmonic field is either reduced or enlarged depending on the nozzle position relative to the focus. The occurrence of an elliptical beam profile originates from an astigmatic focusing behavior

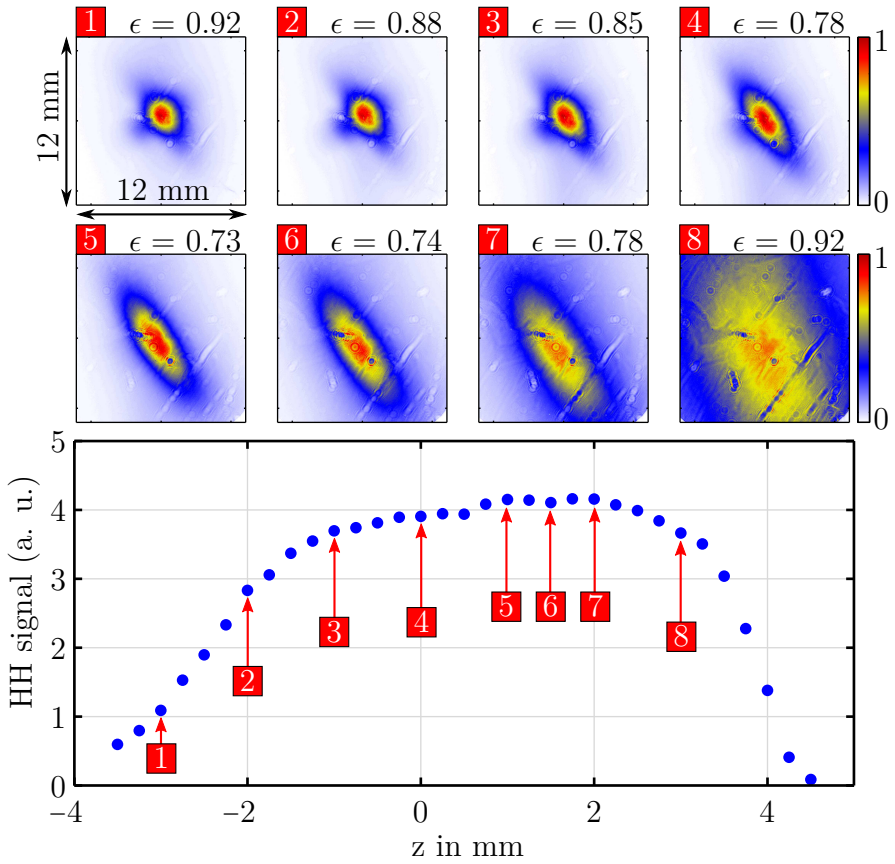

Figure 4.9: High harmonic beam profile and flux as a function of nozzle position along the beam axis (negative values indicate positions in front of the focal plane). A tapered glass nozzle in end-fire geometry and mirror 2 of the beam monitor (see figure 3.10) was used for this measurement. ϵ: beam ellipticity calculated according to ISO11146. Note that values of the ellipticity for a clipped beam profile are poor estimates.

of the NIR pulse, introduced by its non-normal incidence onto the HHG focusing mirror. Apparently, the impact of this astigmatism on the XUV beam profile can be minimized for a specific nozzle position (see profile 1 in figure 4.9), however, the overall yield at this position is greatly reduced. The signal strength naturally drops with increasing distance to the focal plane due to the decreasing NIR intensity. Typically, the position-dependent harmonic flux shows an additional dip at the focal position due to poor phase-matching induced by the Gouy phase shift [120]. This dip, however, is only rudimentary apparent in our case as the long axial elongation of the gas plume from the end-fire nozzle causes a smearing of the signal strength with respect to the nozzle position.

Besides a suitable flux and an appropriate cutoff energy, another important issue for the successful execution of HHG spectroscopy is the long-term stability of the high harmonic output, see figure 4.10. It is obvious that the harmonic signal strength follows the intensity fluctuations of the driving laser field. The long-term power drift and power fluctuations on the minute-scale are compensated for by means of the regulated transmission function of the

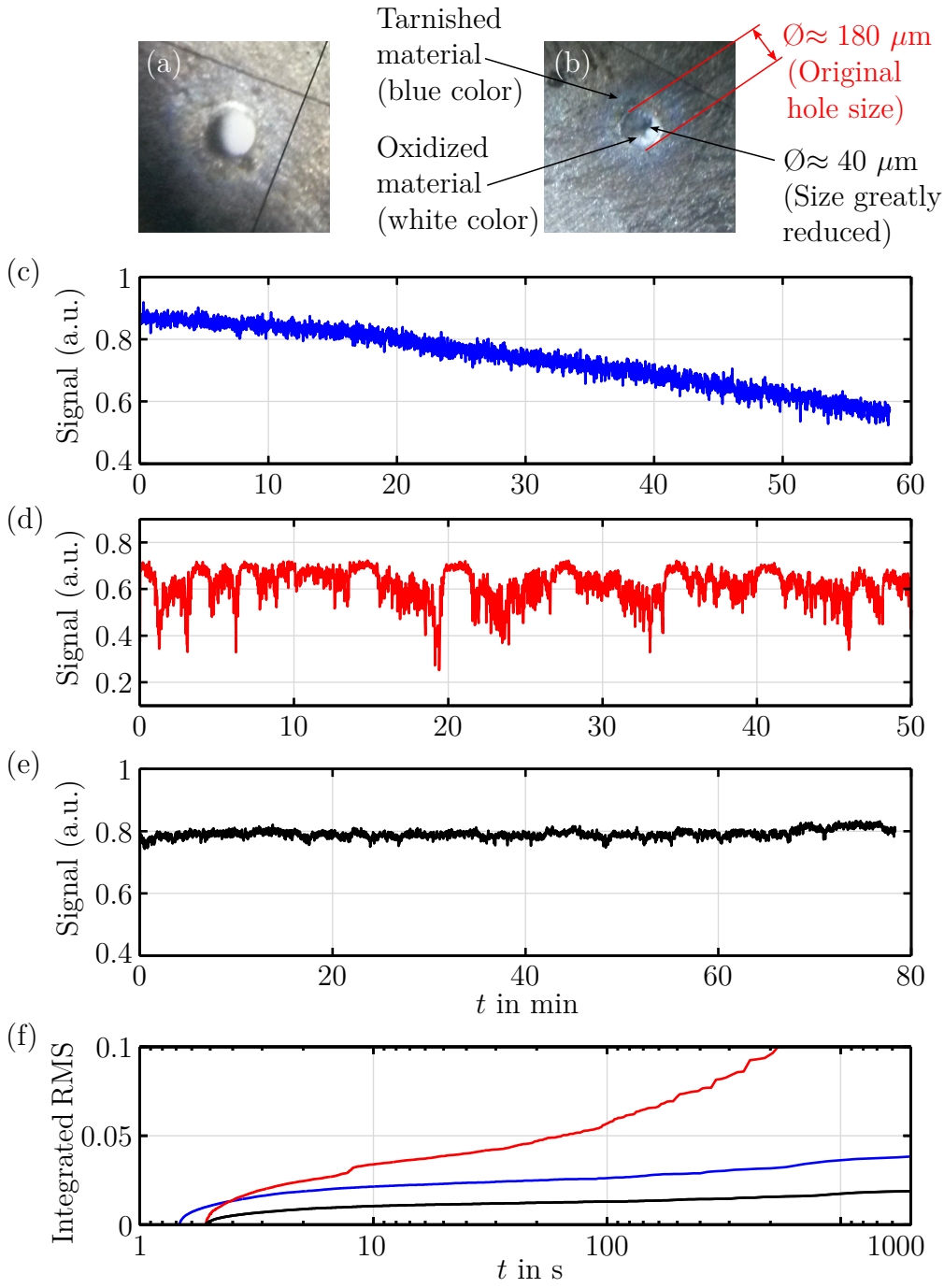

Figure 4.10: Temporal stability of the high harmonic output. (a): Freshly drilled nozzle orifice. (b): Orifice after several hours of operation. (c): Drift of harmonic yield due to thermally induced deformation of the nozzle orifice. (d): Unstable harmonic output due to a deformed nozzle outlet after several hours of operation. (d): Harmonic output with active beam pointing stabilization and a large size of the nozzle outlet. (e): Integrated RMS noise of the above signals.

acousto-optical dispersion filter in the amplifier section of the laser front end. Additionally, it is found that thermal effects, induced by peripheral beam parts striking the edge of the nozzle orifice, lead to significant instabilities and a considerable drop of the harmonic yield within an experimental acquisition cycle. Figure 4.10(b) shows how the nozzle orifice has deformed after an operation of several hours. The tarnished material indicates that the edge of the orifice experiences substantial heating which results in a chemical and structural modification of the material, in turn greatly reducing the size of the hole. This is a creeping process which leads to a gradual drop of the harmonic yield as plotted in 4.10(c). The new properties of the chemically and/or structurally modified material prevent the laser beam from drilling a new hole. Once the outlet has deformed, the harmonic output becomes highly instable as shown in 4.10(d). The transition time of this process is material dependent, where stainless steel has proven to be superior compared to nickel which was initially used. Refractory metals (tungsten, tantalum or molybdenum) or highly inert materials as fused silica glass or technical ceramics as nozzle material might further improve the long-time stability. Furthermore, our initial approach to let the laser beam drill the hole is not favorable in this respect. The stability of the harmonic output is improved when the hole is mechanically pre-drilled to a size which is considerably larger than the beam diameter at the focus. However, a trade-off between maximum backing pressure and gas load in the vacuum chamber has to be made. A hole diameter of 150-200 μm turned out to be feasible. Additionally, the beam pointing in front of the nozzle is actively stabilized in order to further minimize any interaction of the laser beam with the nozzle material which may be introduced by pointing fluctuations and drifts. By these measures, the overall stability of the output is considerably improved and a suitable long-term stability is achieved as demonstrated in figure 4.10(e) and (f).

4.2 Generation of circularly polarized HH radiation

In this section we present our approach to generating circularly polarized harmonic radiation. We employ a transmission multilayer structure as a XUV quarter wave-plate in order to transform harmonic radiation from linear into circular polarization. Although transmission wave-plates are conventional in the visible and NIR spectral range, they are quite extraordinary in the XUV and soft x-ray range due to the lack of strongly birefringent materials and the generally high absorption rate. Nevertheless, the usage and applicability of multilayer structures in transmission as phase retarders in order to generate circularly polarized x-rays was already proposed more than two decades ago [71] and tested with synchrotron radiation [66, 123]. However, these structures have never been developed for and applied to any high harmonic source so far. In this work, we have designed and produced a multilayer quarter wave-plate for the XUV range, apply it for the first time to high harmonic radiation, and demonstrate its usability for broadband applications. The design, the fabrication process, and its characterization using high harmonic radiation is presented in detail in the following subsections.

4.2.1 Wave-plate design and fabrication process

For a quarter wave-plate a phase shift of $\Delta\phi = 90°$ has to be introduced between two perpendicularly decomposed field components of the same amplitude. It has been found that a multilayer structure being used in transmission can introduce a substantial phase shift between s- and p-orientated field components near the Bragg angle if this angle is in the vicinity of the Brewster angle, which is close to 45° in the XUV range [71]. In this case, standing waves are formed within the periodic multilayer structure whose intensity is either concentrated in the spacer material for angles slightly smaller than the Bragg angle or in the absorber material for angles slightly bigger than the Bragg angle [70]. This gives rise to a strong phase retardation or phase advance, respectively, for the s-component, basically through refractive effects, whereas the p-component remains unaffected by this resonance due to the proximity to the Brewster angle.

Based on this behavior, a periodic molybdenum-silicon (Mo/Si) multilayer structure was designed (courtesy of A. Guggenmos) which creates the desired phase shift at an incident angle of 45° and 66 eV photon energy while simultaneously transmitting the s- and p-component at equal amounts. The design energy of 66 eV was chosen to create a test case for a real XMCD application at the Ni M-edge (binding energy of 66.2 eV and 68 eV). The composition of the multilayer stack and its calculated spectral behavior is depicted in figure 4.11. Optical constants for the simulation are taken from [53]. Oxide layers, rough-

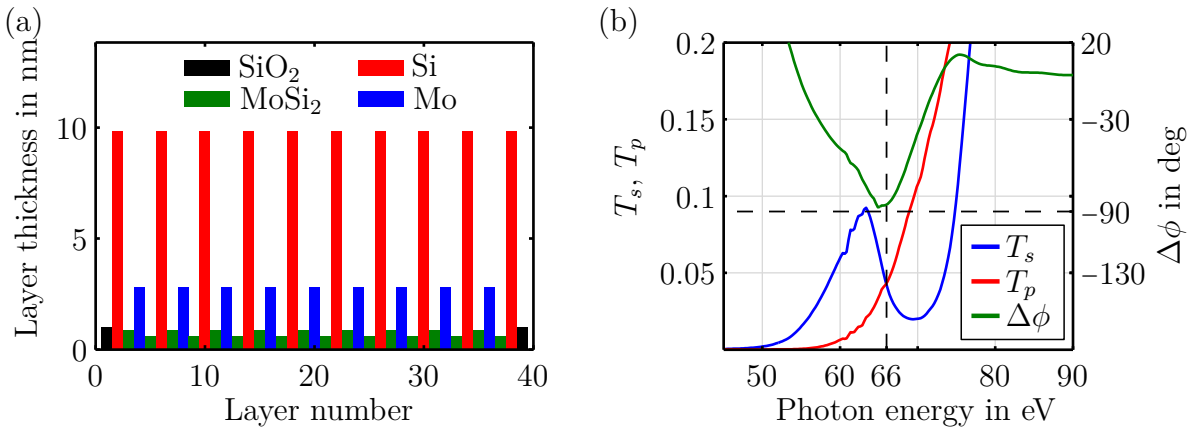

Figure 4.11: (a): Composition of the multilayer stack. The real design starts and ends with a natively formed SiO_2 layer. Asymmetric $MoSi_2$ layers are formed by material reaction at the Mo-Si-Mo interfaces. Their thickness depends on whether Mo is deposited on Si or vice versa [9]. (b): Simulated spectral transmission and phase difference of the XUV multilayer wave-plate for an angle of incidence of 45°. The Bragg condition is fulfilled at an energy of ≈ 70 eV, which results in a local transmission minimum. The wave-plate is designed for a nominal photon energy of 66 eV where T_s equals T_p and where a phase shift $\Delta\phi$ of nearly 90° is introduced.

ness values, as well as inter diffusion and interface reaction parameters are included into the simulation and are based on long-term experience in the production of XUV multilayer optics [47, 48, 55]. As it is evident from the simulation, the spectral s- and p-transmission

intersect at the design energy with an absolute value of almost 5%, and the introduced phase shift $\Delta\phi$ is close to 90°. The local minimum in s-transmission at 70 eV constitutes the Bragg reflection peak for the given angle of incidence. From the simulated transmission and phase behavior as shown in figure 4.11, the spectral ellipticity ϵ and orientation Φ of the polarization ellipse can be deduced, which give a directer insight into the spectral performance of the wave-plate. These quantities are plotted in figure 4.12 for different values of the incident angle α_1. The ellipticity peaks at 66 eV with a value of almost unity, i.e.

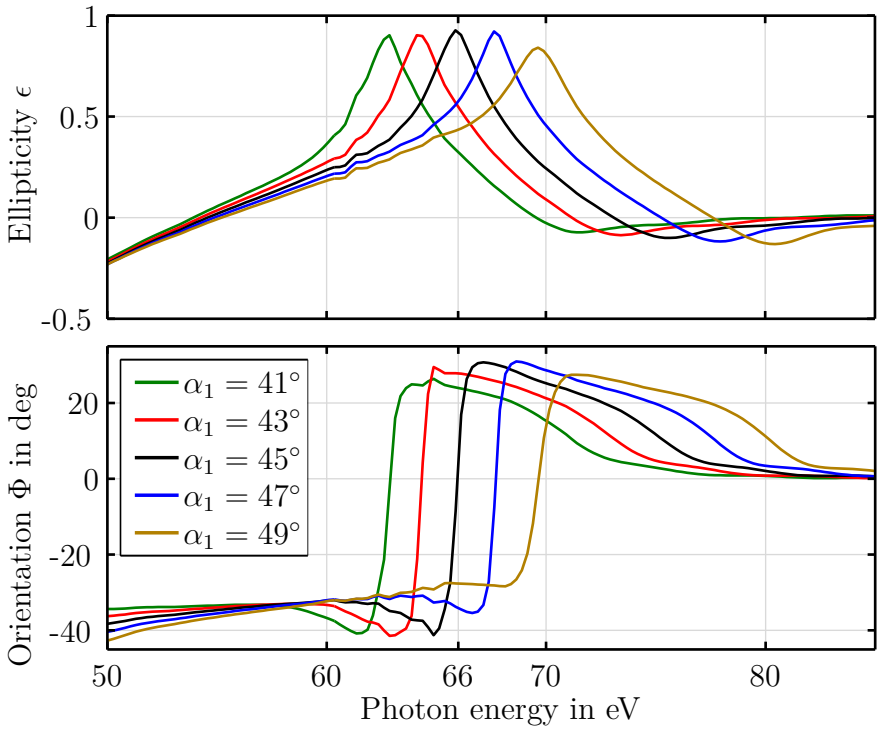

Figure 4.12: Calculated spectral ellipticity and polarization orientation of the transmitted radiation for different normal incident angles α_1. The polarization before the wave-plate is linear horizontal. The ellipticity at 66 eV and $\alpha_1 = 45°$ is nearly 1 and shifts by several eV in energy while its magnitude is only little affected when the incident angle is varied.

complete circular polarization. The spectral FWHM bandwidth of the ellipticity is with 4 eV remarkably high, indicating that ultrashort pulse durations in the attosecond range are supported with a high degree of ellipticity. The steep slope in the orientation angle around 66 eV indicates its strong sensitivity with respect to photon energy and incident angle. It should also be noted that a small variation of the incidence angle allows the spectral position of the peak ellipticity to be shifted by several electron volts while its magnitude is only little affected. This can be useful to tune the polarization state after the wave-plate.

An important and critical issue in the development of transmission multilayer structures is the fabrication procedure. In contrast to earlier approaches, our wave-plate is not fabricated on a support foil (e.g. silicon nitrid) but is designed as a free-standing multilayer

foil for best transmission efficiency with a total thickness smaller than 150 nm. The foil has a free aperture of 3 mm and is attached to a 1 inch sized metal ring to fit in any standard optic mount. While the production of high quality reflection multilayer structures, which are usually placed on a thick, super-polished solid substrate, is well developed, high quality free-standing transmission multilayer optics are still challenging to fabricate and require special attention regarding stability, contamination and film stress compensation. The fabrication process was optimized to produce transmission multilayers with reasonably good quality. All fabrication steps are done in a class 1000 clean room environment in order to keep the contamination level during sample handling as low as possible. As a temporary substrate we use a semiconductor grade silicon wafer which is spin-coated by a PMMA (polymethyl methacrylate) resist (thickness: 290 nm) and baked by 130° C. The multilayer structure is applied on top of the resist by ion beam deposition where each layer thickness can be controlled with sub-nm precision [48]. Interface reactions, inter-diffusion, and roughness effects as well as post-deposition oxide formation are taken into account (see fig. 4.11). In the next step, a metal ring is glued onto the structure. For improved stability, a thin adhesive Kapton foil is placed between multilayer stack and metal ring to reduce stress on the multilayer structure introduced by the glue during its curing time. Finally, the resist is dissolved by an appropriate solvent and the silicon wafer is carefully removed. In order to remove any remaining debris from the solvent, the multilayer foil is finally baked out at 100° C for one hour in a last step. It has to be mentioned that due to interface and surface stress, the multilayer foil is usually not perfectly even, but slightly wavy.

4.2.2 Transmission and phase shift characteristics

In order to verify the functioning of the wave-plate, we first measured its spectral transmission in s- and p-orientation with our HHG source. High harmonic radiation is generated in neon with horizontal polarization. A 200-400nm thick Al filter blocks the NIR light. The transmitted spectrum is measured with the flat-field XUV spectrometer presented in section 3.2.5. The measurement geometry is shown in figure 4.14. The measured transmission spectra T_m are normalized by a reference spectrum T_{ref} which is taken without the wave-plate in order to eliminate any substructure of the harmonic spectrum. In this way, the true transmission function $T^{(s,p)}$ of the wave-plate is obtained by

$$T^{(s,p)} = \frac{T_m^{(s,p)}}{T_{\mathrm{ref}}}. \tag{4.1}$$

The nominal angle of incidence is $\alpha_1 = 45°$ with an error of $\pm 0.5°$. Figure 4.13 shows the result in an energy range around the design energy. The measurement agrees well with the simulation as characteristic features are well reproduced. The local peak near 63 eV and the minimum at 70 eV (Bragg condition) are clearly replicated in s-orientation while in p-orientation the transmittance is monotonically increasing over the depicted energy range, also in coincidence with the simulation. The slight spectral shift of the local peak transmittance at 63 eV in s-orientation is attributed to small alignment errors in the angle

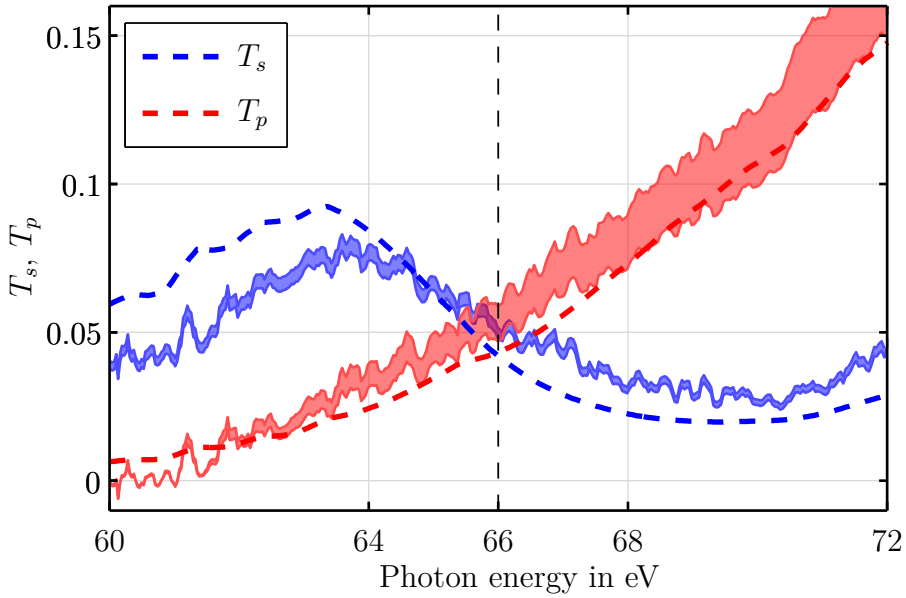

Figure 4.13: Measured transmission function of the wave-plate in s- and p-orientation. The shaded area represents the estimated error interval caused by a drifting harmonic intensity during the acquisition time. The simulated behavior is shown for comparison (dashed lines).

of incidence. The shaded area represents an estimation of the error interval, which is deduced by a drifting harmonic intensity over the acquisition time (see figure 4.10, the pointing of the NIR beam has not yet been stabilized at that time).

induced by a slight drifts of the harmonic intensity over time, as illustrated in figure 4.10. The mean transmission efficiency within the measurement error is $\approx 5\%$.

In the next step, we determine the polarization state, i.e. ellipticity and polarization orientation, of the harmonic radiation after inserting the wave-plate into the beam path. Ellipticity and polarization orientation are a direct consequence of the introduced phase shift. For this we perform a simplified polarimetry measurement by recording the beam intensity after a rotating analyzer mirror, which acts as a polarizer, as a function of its rotation angle β_2 (Rabinovitch setup [115]) while keeping the azimuthal angle β_1 of the wave-plate fixed. The geometry of the measurement setup is shown in figure 4.14. In the following, we introduce a reference (x, y)-coordinate system whose x-axis coincides with the direction of initial laser polarization. Azimuthal angles along the beam axis are positive for counter-clockwise rotation when viewed in beam direction. Additional (s, p)-coordinate systems are firmly attached to each optical element with the s-axis being perpendicular and the p-axis being parallel to the plane of incidence. The analyzer multilayer mirror is operated near the Brewster angle in order to suppress reflections in p-orientation while still having reasonable reflectivity in s-orientation (making it an XUV polarizer [33]). The simulated spectral reflectivity of the mirror is plotted in figure 4.15. The reflectivity in s-orientation has a peak value of 34% at 66 eV and a reflection bandwidth of 4.6 eV (FWHM)

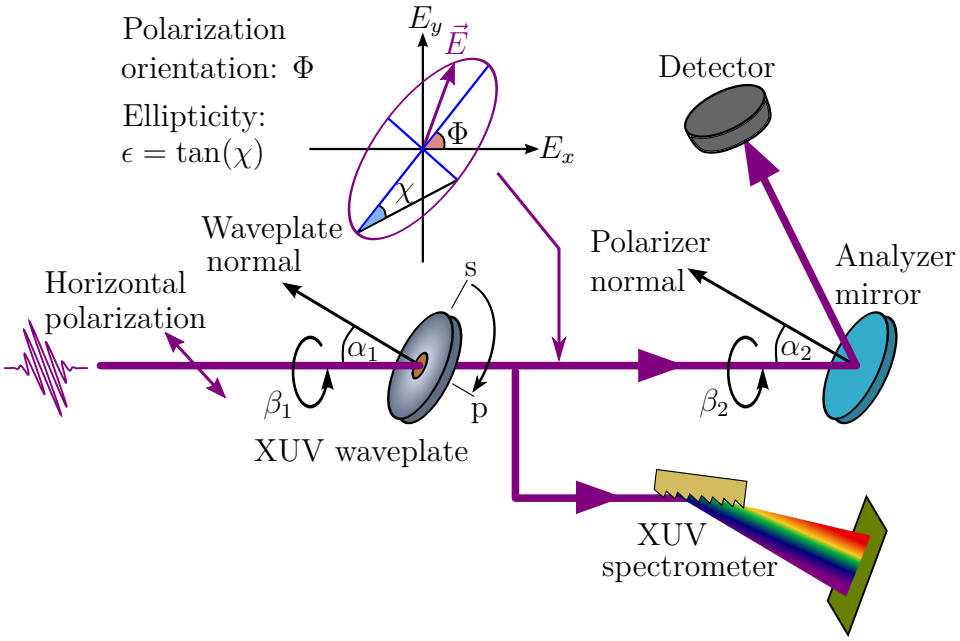

Figure 4.14: Geometrical setup of the polarimetry measurement. Wave-plate and polarizer mirror can be rotated around the beam axis by β_1 and β_2 as well as tilted by α_1 and α_2, respectively. The initial XUV polarization before the wave-plate is linear horizontal. After transmission through the wave-plate the E-field vector describes an ellipse with ellipticity ϵ and orientation Φ. The wave-plate is a thin free-standing multilayer foil glued on a 1 inch metal ring with 3 mm free aperture. A MCP detector is used to record the reflected signal. For the transmission measurement the analyzer mirror is replaced by the flat-field XUV spectrometer and α_1 is kept at a value of 45°.

supporting sub-fs pulses. Also shown is the extinction ratio R_s/R_p, i.e. the attenuation of p-reflectivity compared to s-reflectivity, which is larger than 50 within the reflection bandwidth. Both optical elements are mounted on motorized gimbal mounts enabling the independent adjustment of their incident angles $\alpha_{1,2}$ and azimuthal angles $\beta_{1,2}$. The complete polarization state of light is commonly described by the four Stokes parameters, real quantities with the dimension of intensity, which are combined to the Stokes vector $\vec{s} = (s_0, s_1, s_2, s_3)^T$, where s_0 describes the total intensity, s_1 the fraction of linear horizontal and vertical polarization, s_2 the fraction of linear polarization rotated by ±45°, and s_3 the fraction of circularly left- and right-handed polarization. The polarization degree P is given by

$$P = \frac{\sqrt{s_1^2 + s_2^2 + s_3^2}}{s_0} = \frac{s_0 - s_{\mathrm{np}}}{s_0}, \tag{4.2}$$

where $s_{\mathrm{np}} = s_0 - \sqrt{s_1^2 + s_2^2 + s_3^2}$ is the unpolarized part. Ellipticity ϵ and orientation Φ of

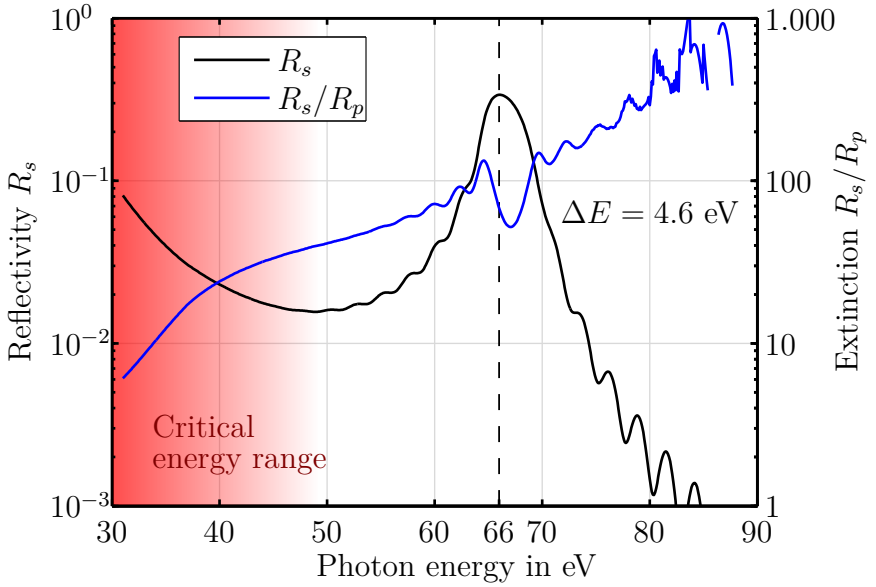

Figure 4.15: Calculated spectral behavior of the analyzer mirror. The peak reflectivity in s-orientation is 34% at 66 eV with a FWHM reflection bandwidth of 4.6 eV. The extinction ratio within this bandwidth is larger than 50. Note that the red shaded area constitutes a critical energy range within which the mirror looses its polarizing power as the extinction approaches unity and R_s starts increasing again.

the polarization ellipse are then obtained by [6]

$$\epsilon = \mathrm{sgn}(s_3)\sqrt{\frac{s_0 - s_{\mathrm{np}} - \sqrt{s_1^2 + s_2^2}}{s_0 - s_{\mathrm{np}} - \sqrt{s_1^2 + s_2^2}}} \tag{4.3}$$

$$\tan(2\Phi) = \frac{s_2}{s_1}. \tag{4.4}$$

Any interaction with an optical element is described in this formalism by the Mueller matrix [149]

$$M = \frac{1}{2}(R_p + R_s)\begin{pmatrix} 1 & -\cos(2\Psi) & 0 & 0 \\ -\cos(2\Psi) & 1 & 0 & 0 \\ 0 & 0 & \sin(2\Psi)\cos\Delta & \sin(2\Psi)\sin\Delta \\ 0 & 0 & -\sin(2\Psi)\sin\Delta & \sin(2\Psi)\cos\Delta \end{pmatrix} \tag{4.5}$$

where $\tan\Psi = r_p/r_s$, $\tan\Psi = (t_p/t_s)$ for reflecting (transmitting) optics and Δ is the induced phase shift between s- and p-orientation. The Mueller matrix which rotates the coordinate system by an angle β around the beam axis is

$$R(\beta) = \begin{pmatrix} 1 & 0 & 0 & 0 \\ 0 & \cos\beta & \sin\beta & 0 \\ 0 & -\sin\beta & \cos\beta & 0 \\ 0 & 0 & 0 & 1 \end{pmatrix}. \tag{4.6}$$

Let the polarization state after the wave-plate be $\vec{s}_i$, then the Stokes vector $\vec{s}_f$ after reflection from the analyzer mirror at the rotation angle β_2 is obtained by

$$\vec{s}_f = R(-\beta_2) \cdot M \cdot R(\beta_2) \cdot \vec{s}_i. \tag{4.7}$$

The back rotation of the coordinate system by the third Mueller matrix is necessary in order to get the polarization state in the original reference frame. The intensity which is recorded by the detector during a β_2-scan is given by the first component of $\vec{s}_f$:

$$s_{f0} = (R_p + R_s)\left(\frac{1}{2}s_0 - \frac{1}{2}s_1\cos(2\Psi)\cos(2\beta_2) - \frac{1}{2}s_2\cos(2\Psi)\sin(2\beta_2)\right), \tag{4.8}$$

which can be rewritten using equation 4.4 and the definition for $\tan\Psi$ as

$$I(\beta_2) = \frac{1}{2}(R_p + R_s)s_0 - \frac{1}{2}(R_s - R_p)\sqrt{s_1^2 + s_2^2}\cos(2\beta_2 + 2\Phi). \tag{4.9}$$

The result is a sinusoidal curve whose modulation depth encodes the ellipticity and whose phase shift represents the polarization orientation. The Stokes component s_3 is not directly accessible in this simplified polarimetry measurement since the azimuthal angle β_1 of the wave-plate is not varied. Therefore, the amount of unpolarized light is not determined and only an upper bound for the ellipticity can be obtained, as discussed in [6], by

$$\epsilon_{\max} = \sqrt{\frac{s_0 - \sqrt{s_1^2 + s_2^2}}{s_0 + \sqrt{s_1^2 + s_2^2}}} \tag{4.10}$$

which equals the true ellipticity from equation 4.3 for fully polarized light, i.e. for $P = 1$. However, as can be easily verified from the equations 4.10 and 4.3, the deviation of $\epsilon_{\max}$ from ϵ gets negligibly small for large values of s_3, i.e. for a high degree of circular polarization. A potential deviation only gets significant for small values of s_3 provided the ratio between s_{np} and s_0 is constant. The latter requirement is generally fulfilled. Using the maximum and minimum value of equation 4.9

$$I_{\min/\max} = \frac{1}{2}(R_p + R_s)s_0 \pm \frac{1}{2}(R_s - R_p)\sqrt{s_1^2 + s_2^2}, \tag{4.11}$$

equation 4.10 is recast to

$$\epsilon_{\max} = \sqrt{\frac{R_s I_{\min} - R_p I_{\max}}{R_s I_{\max} - R_p I_{\min}}}. \tag{4.12}$$

Hence, the ellipticity is directly obtained from the intensity modulation depth of the β_2-scan. The extinction ratio R_s/R_p can be determined by a β_2-scan without wave-plate. We set $\beta_2 = 0$ to the s-orientation of the analyzer mirror with respect to the initial linear polarization direction. A critical complication in the measurement arises by the unfavorable spectral characteristic of the analyzer in the low energy range. As illustrated by the red shaded area in figure 4.15, the analyzer mirror gradually looses its polarization power (the

extinction approaches unity) for energies below 40 eV. At the same time, its reflectivity increases again. This behavior is highly destructive for the polarimetry measurement when radiation in this energy range is present, see figure 4.16. Therefore, it has to be ensured that this radiation is is sufficiently suppressed by filters. (Single-element) Standard metal filters such as Al or Zr foils [40, 91] are not appropriate for this purpose, as it is evident from figure 4.16. In this test measurement, β_2-scans with different filter combinations

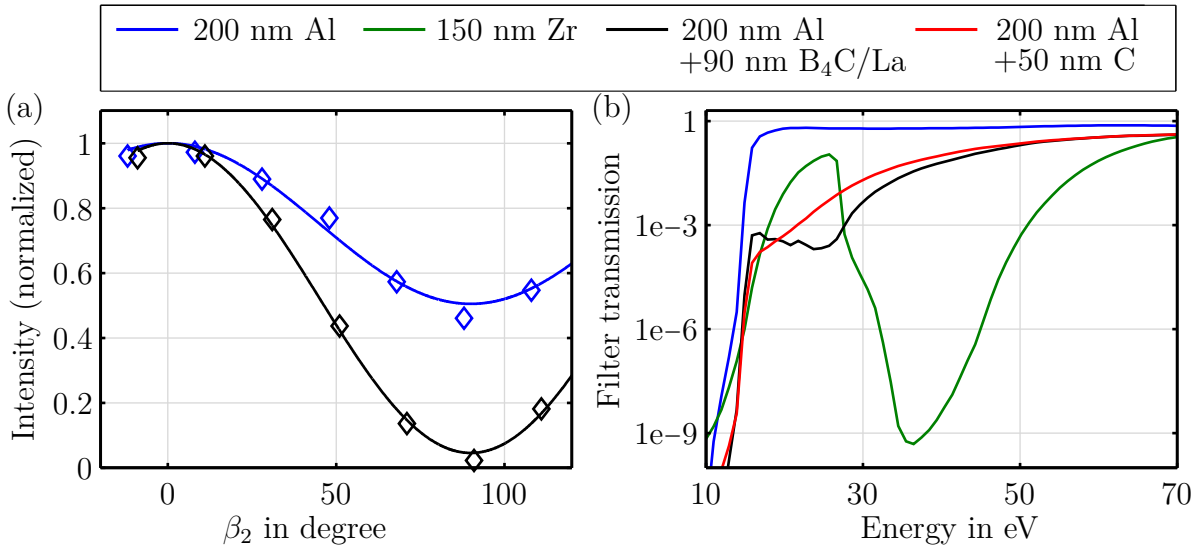

Figure 4.16: Influence of the pre-filtering on the polarimetry measurement. (a): β_2-scan without wave-plate using different foil filters to pre-filter the harmonic radiation. For the standard Al filter, the effective extinction of the analyzer mirror is reduced to about 2 since the fraction of transmitted radiation from the low energy range <40 eV, where the analyzer mirror loses its polarizing capability, is still too high. Material combinations of Al/B_4C/La or Al/C show better suppression in that energy range, leading to an improved effective extinction close to the value expected from the simulated design at 66 eV. (b): Spectral transmission behavior of different filter materials. The standard Al and Zr filters exhibit a strong transmission window between 20 eV and 40 eV. Higher suppression in this range is achieved by adding the materials La and/or C.

have been performed. The wave-plate was not inserted, i.e. the polarization is linear. Provided that the polarization degree equals unity, the β_2 scan with the Al filter yields an extinction ratio of the analyzer mirror of ≈ 2, which is far off from the simulated expectation value plotted in figure 4.15. A similar result is obtained with Zr filters. A significantly improved extinction ratio, close to the expected value, is obtained by a filter combination made of Al/La/B_4C. The transmission behavior is shown in figure 4.16(b). This observation corroborates the initial assumption: radiation leakage in the energy range below 40 eV considerably disturbs the measurements and counterfeits a polarization degree clearly smaller than unity. Furthermore, the measurement confirms that the content of really unpolarized radiation is negligible. Better suppression of radiation in the critical

energy range is attributed to the elements La and C. Unfortunately, La is highly reactive and prone to fast oxidation which makes it quite brittle. Therefore, it has to be sealed by passivating end layers, making the fabrication process quite complex. For this reason, we use a simpler filter combination consisting of Al/C for the subsequent measurements. The transmission characteristics are comparable to the Al/La/B_4C combination although the suppression below 40 eV is not quite as good, see figure 4.16(b). We first experimentally determine the effective extinction of the polarizer with this filter combination by a β_2-scan without wave-plate. We get a value of 60 which is somewhat below the bandwidth-averaged theoretical value of 80, indicating that a small, but noticeable fraction of low-energy radiation leaks through the filter combination. In a next step, we measure β_2-scans, i.e. $I(\beta_2)$ with inserted wave-plate at a fixed azimuthal angle of $\beta_1 = -45°$ and incident angles of $\alpha_1 = 45° \pm n \cdot 2°$ with $n = 1, 2$. The absolute angle uncertainty is $\pm 0.5°$. The results are plotted in figure 4.17. For each scan we fit the function 4.9 to the corresponding

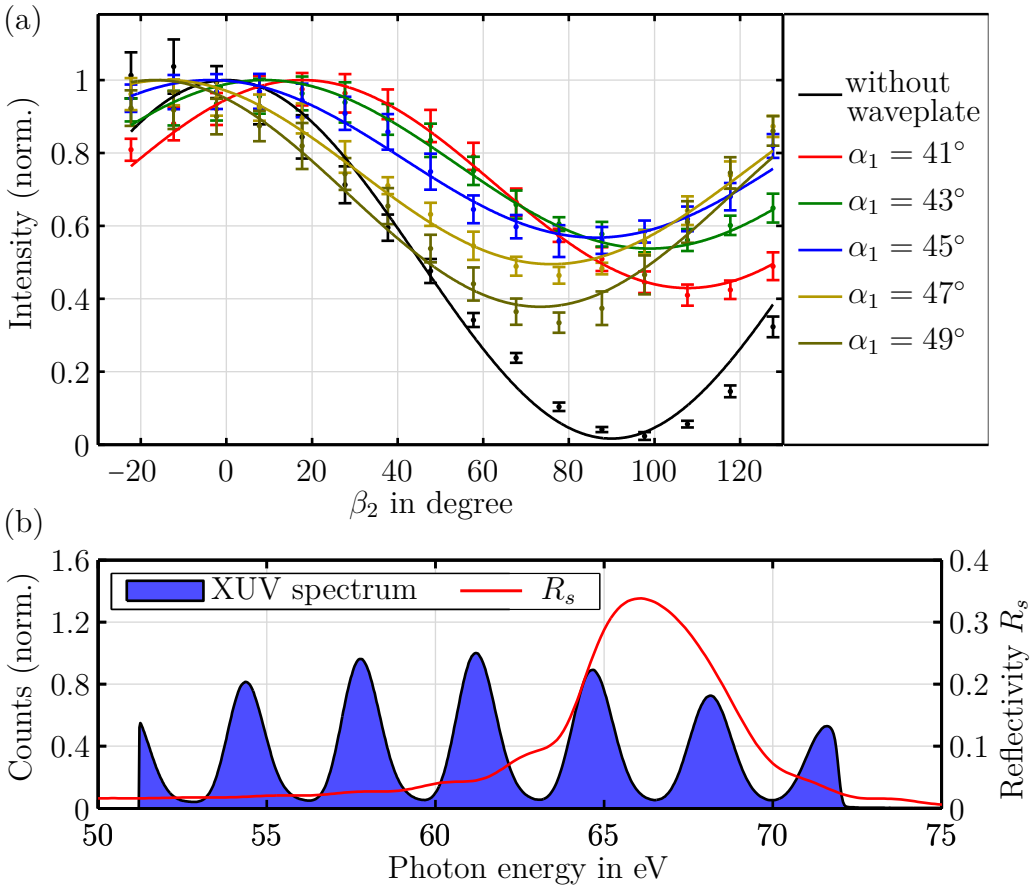

Figure 4.17: (a): Results for β_2-scans without and with wave-plate for different detuning angles. The larger the detuning angle, the stronger the modulation depth (the smaller the ellipticity) and the stronger the shift in β_2. An Al/C filter was used to pre-filter the high harmonic radiation (b): measured XUV harmonic spectrum as used for the β_2-scans and for the simulation of ϵ_{sim} and Φ_{sim}. Two neighboring harmonic peaks are cut out by the bandwidth of the analyzer mirror.

α_1	ϵ_{max}	ϵ_{sim}	Φ	Φ_{sim}
41	0.64	0.43	+18	+19
43	0.73	0.60	+9	+18
45	0.75	0.79	-4	-2
47	0.69	0.54	-17	-26
49	0.60	0.54	-17	-28

Table 4.1: Summary of measured and simulated values for the ellipticity ϵ and polarization orientation Φ of the XUV radiation after transmission through the wave-plate at different incident angles α_1.

dataset. The datasets are normalized for better visualization. The given error is three times the standard deviation of 5000 laser shots. Using equation 4.12 and the measured extinction value, we can easily deduce the ellipticity from the fitted curves. The orientation of the polarization ellipse is obtained by the β_2-offset of the I_{max} value for each curve with respect to the reference curve taken without wave-plate. The results are summarized in table 4.1.

The simulated values are obtained by calculating the intensity $I_{sim}(\beta_2)$ using the real harmonic intensity distribution, depicted in figure 4.17(b), and the simulated transmission/reflection behavior of the wave-plate and the mirror. Ellipticity and orientation angle are then extracted from $I_{sim}(\beta_2)$ as described above. Note that the simulation does not include any unpolarized radiation, i.e. the simulated value reflects the true ellipticity (not its upper bound estimation when $P < 1$). As expected, for increasing angle detuning the degree of ellipticity decreases and the orientation angle starts strongly deviating from the original (linear) polarization direction. The results for the ellipticity and orientation angle clearly show the correct tendency as expected from the theoretical design. For the nominal angle of incidence of $\alpha_1 = 45°$ the measured ellipticity well reproduces the simulated value within an error of 5%. For detuned incident angles the ellipticity naturally drops because the spectral position of the peak ellipticity shifts away from the design energy (see figure 4.12). It is also evident from table 4.1 that the deviation between measured and simulated values increases for a decreasing degree of ellipticity. This fact again encourages the assumption that a noticeable amount of low-energetic leakage radiation is present. The fraction of this leakage radiation is constant throughout the measurement and independent on the angle tuning of the wave-plate. Only the relative magnitudes between s_1, s_2 and s_3 are affected by angle tuning. In particular, s_1 and s_2 increase at the cost of s_3 when the incident angle is detuned from its nominal value. The discrepancy between ϵ_{max} and $\epsilon_{sim} \equiv \epsilon$ for decreasing s_3 gets obvious when plotting the ratio ϵ/ϵ_{max} as a function of s_3 (figure 4.18) while leaving s_{np} constant. The lower s_3 the larger the deviation. Consequently, we can assume that the obtained value of ϵ_{max} for $\alpha_1 = 45°$ (large s_3 value) is close to the true ellipticity ϵ. Regarding the orientation angles, it can be seen that they switch sign for different detuning directions, as expected from the simulation. Any offset between measured and simulated values is attributed to the adjustment uncertainty of α_1. As mentioned above, the orientation angle is very sensitive to α_1 due to its steep slope at

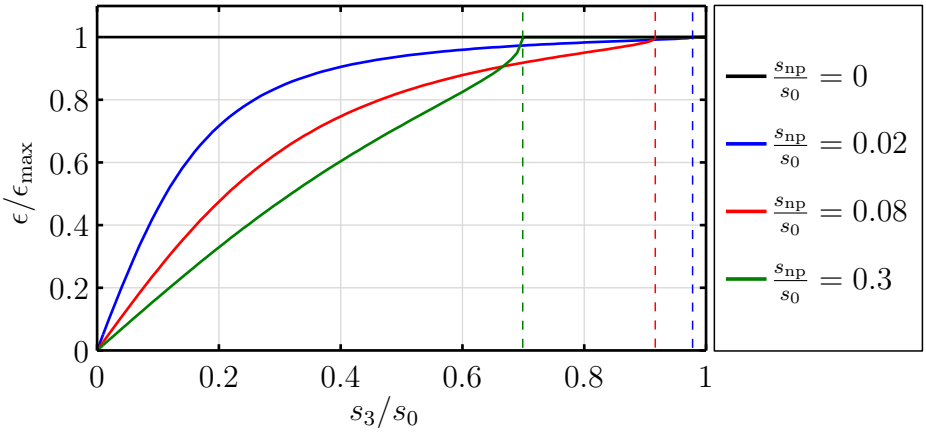

Figure 4.18: The ratio $\epsilon/\epsilon_{\max}$ is plotted against the fraction of circularly polarized radiation s_3 for different fractions of unpolarized light. It is obvious that when the value of s_3 decreases from its highest value possible (indicated by the dashed lines), the deviation of $\epsilon_{\max}$ from ϵ gets larger. The effect is stronger the higher the amount of unpolarized radiation. As the highest value for s_3 is obtained by the incident angle $\alpha_1 = 45°$, we can conclude that in this case the measured value for $\epsilon_{\max}$ is close to the true ellipticity ϵ. As any angle detuning of the wave-plate lowers the value of s_3, the deviation from the true ellipticity is expected to get larger. This is also experimentally observed, see the summary in table 4.1.

the design energy as shown in figure 4.12. Another source of error regarding angle alignment is the slightly wavy surface of the multilayer foil which was not taken into account in the simulation, but giving an additional effective angle error.

Another complication which corrupts the quality of the measurement are intensity fluctuations, see section 4.1. In particular, intensity drifts on the time scale of the acquisition time can generate systematic errors in the order of 15% as indicated by the red section in the stability plot of figure 4.19. In order to reduce such systematic errors and to improve the quality of the measurement, valid data points are restricted to a fraction of the overall spread of the intensity distribution. A 1% range around the modal value has been chosen (see figure 4.19). The latter was determined by means of a precursory stability scan. Additionally, all β_2-scans were performed both in forward and in reverse direction in order to further cancel out systematic drifts.

4.2.3 Dispersion behavior

Another important aspect in the evaluation of the wave-plate performance is the investigation of its impact on the temporal structure of the XUV input pulses. The broad reflectivity bandwidth of the analyzer mirror, in principle, supports Fourier-transform limited pulses with a duration of 400 as. However, nonlinear spectral phase distortions induced by dispersion lead to pulse broadening, temporal reshaping and chirping. From our simulations we have extracted the amount of GDD, i.e. the predominant phase effect for temporal pulse broadening, which a XUV pulse experiences while passing through the wave plate.

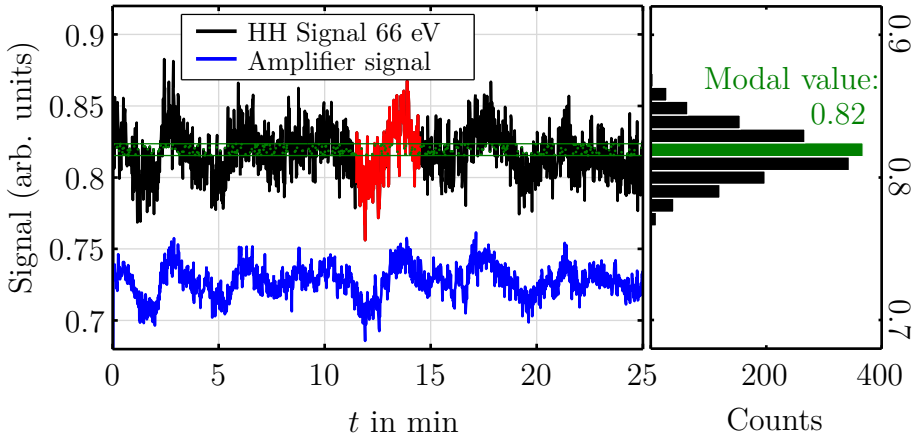

Figure 4.19: Power fluctuations of the NIR beam are (nonlinearly) transformed to the HH signal. Power drifts on the minute-scale (red section) may heavily impair the quality of the polarimetry measurement by inducing systematic errors in the order of 15%. The quality is improved by selecting valid data points only from a 1% width (green) around the modal value of the corresponding intensity distribution.

We obtain a GDD value of 33000 as^2 when the light field is p-oriented, which broadens an initially chirp-free pulse to about 460 as. This amount of broadening is comparable to the one caused by a single slab of thin metal foil with a thickness similar to the wave plate. However, the situation is quite different for the s-orientated field component. As in this case standing waves are formed within the multilayer structure, a much higher GDD value of -1.24 fs^2 is obtained which broadens the pulse to about 8.5 fs. Consequently, it seems difficult to maintain a sub-fs pulse duration of an initially unchirped attosecond pulse passing through the wave-plate.

Chapter 5

Time-, angle- and CEP-resolved PES

5.1 Calibration and performance of the electron spectrometer

In this section, the imaging quality of the electron spectrometer and its spectral resolution is investigated. In order to create a clear and distinct angle pattern as a test image, an aperture in the form of a hole array acting as an angle filter is placed between sample and the inlet of the spectrometer. The hole array is a square pattern of 5×5 pinholes with a diameter of 300 μm and a spacing of 1 mm. The distance of the aperture to the sample is 22 mm. The electron gun is used as an excitation source since the aperture blocks the XUV beam path to the multilayer mirror. The electron beam is focused onto the sample at a grazing angle of 45°. Electrons which are inelastically scattered at the sample surface are used for the imaging. The size of the illumination spot on the sample surface is, however, considerably larger than from excitation with XUV radiation. Angle images are recorded in LAD and WAM mode both with high and low retardation ratios. The measurement in LAD mode is shown in figure 5.1. It is observed that the image suffers from a strong spatial inhomogeneity, which manifests as a dark region in one half of the detection area, when the spectrometer is operated with RR > 1. The higher the retardation, the larger the dark area which evolves from the edge toward the center of the detection area. It was found that an inappropriate bias angle of the micro-channels in the MCP is the reason for this behavior. The imaging properties, given by the lens settings, determine the angle at which the electrons impinge onto the MCP surface. This angle obviously approaches the bias angle of the micro-channels for RR > 1, see figure 5.1(d). As a consequence, these electrons experience a low gain in the MCP which results in the dark area in the image. After replacing the original MCPs with a bias angle of 7° by MCPs with 12° bias angle, the spatial homogeneity of the image is restored, see figure 5.1(c). Furthermore, large retardation ratios further restrict the usable acceptance angle of the spectrometer (only 4×4 holes are completely within the field of view in this case, compare figures 5.1(a) and (c)). The straightness and regularity of the imaged hole pattern indicate good imaging quality with negligible aberrations.

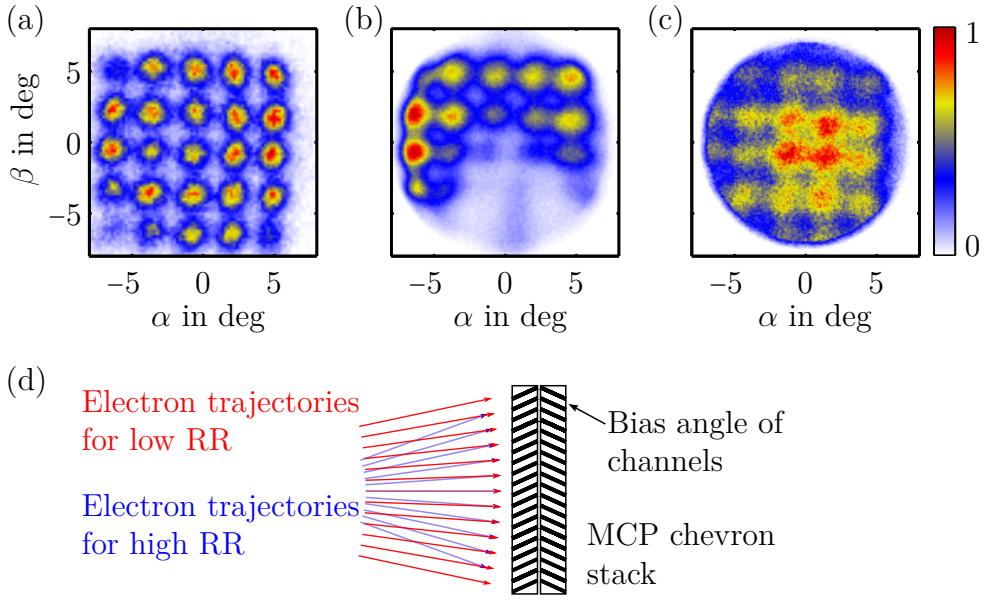

Figure 5.1: Themis image quality in LAD mode for high and low RR values. The spatial homogeneity of the image depends on the bias angle of the MCP plates. The incident angle of the electron trajectories at the MCP surface depends on the retardation ratio of the adjusted lens setting. Electrons on trajectories parallel to the bias angle of the MCP channels experience low amplification. (a): Image with RR < 1 showing spatially homogeneous signal strength. Original MCP stack with a bias angle of 7°. (b): Same image and MCP bias angle as in (a) but with RR > 1. The image is dark on one side. (c): Same image as in (b) but with a MCP bias angle of 12°. Image homogeneity is restored. (d): Geometric illustration of electron trajectories near the MCP for different RR values and their corresponding angles of incidence.

In a next step, the resolving power of the spectrometer is determined in LAD and WAM mode, again for different retardation ratios. Typically, the width of the Fermi edge is used to estimate the energy resolution. The fine structure of the valence band (VB), however, is not resolved due to the broad excitation bandwidth of 2.6 eV FWHM. Instead, all substructure features merge into a single VB peak (see also figure 5.4). Here, we use the width of the high energy slope of the VB peak as a measure of energy resolution, see figure 5.2(a). A shape-preserving weighted local regression method is utilized to smooth the dataset, and the width of the VB edge ΔE_{edge} is determined by a 10%-90% criterion, see figure 5.2. The energy resolution of the spectrometer $\Delta E_{\mathrm{Themis}}$ is finally obtained by deconvolving the excitation bandwidth ΔE_{mir} according to $\Delta E_{\mathrm{Themis}} = \sqrt{\Delta E_{\mathrm{edge}}^2 - \Delta E_{\mathrm{mir}}^2}$. The result is summarized in table 5.1. The simulated values (fourth column) are calculated from equation 3.42 as described in section 3.2.6, using the measured DLD time resolution of $\tau_{\mathrm{DLD}} = 420$ ps. The angle resolution is estimated from the measurements with the patterned pinhole aperture. It is obtained by determining the cutoff-frequency from the single-sided amplitude spectrum of the angle-image after a spatial 2D Fourier-

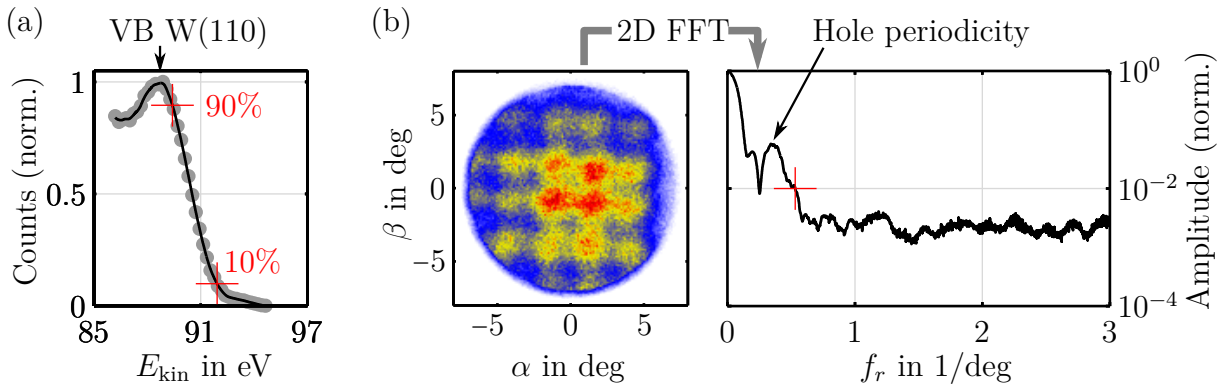

Figure 5.2: Experimental determination of the resolving power of the electron spectrometer, exemplarily shown in LAD mode with RR = 2.25. (a): Energy resolution determined by the width of the high-energy edge of the tungsten valence band based on a 10%-90% criterion, excited with 95 eV photon energy. (b): Angle image of the pinhole aperture and its single-sided amplitude spectrum derived from a 2D Fourier transform. Angle resolution is defined as the −20 dB cutoff frequency.

Mode	RR	ΔE in eV	ΔE_{sim} in eV	$\Delta\alpha$ in deg
LAD	0.23	3.8	3.5	1.9
LAD	2.25	–	0.6	1.9
WAM	0.12	6.3	4	1.7
WAM	1.5	2.2	1.2	1.7

Table 5.1: Summary of resolution values of the electron spectrometer. The values in the fourth column are ideal, simulated values calculated from equation 3.42 using the real DLD time resolution of $\tau_{\mathrm{DLD}} = 420$ ps.

transformation. In order to get a directionally independent estimation, the 2D Fourier spectrum is integrated over the polar angle. An exemplary spectrum as a function of the radial frequency component $f_r = \sqrt{f_\alpha^2 + f_\beta^2}$ is plotted in figure 5.2(b). The cutoff-level is set to 1% of the DC value (i.e. to a normalized amplitude of 0.01). The result is also summarized in table 5.1. The measured values for the energy resolution reflect the proper relative behavior as predicted by equation 3.42. Their absolute magnitude, however, is slightly higher. The deviation may arise from the finite illumination spot size and from space charge effects, see section 5.2.2. The values for the angle resolution don't show significant variation. Hence, it can be concluded that the measured resolution is limited by the influence of the large illumination spot rather than by the spectrometer itself, and therefore these values can be considered as an upper limit.

5.2 High harmonic (AR)PES on W(110)

The spectral NIR pulse properties, the corresponding PAP, and the resultant high harmonic spectrum as used for the following PES and streaking measurements are summarized in figure 5.3.

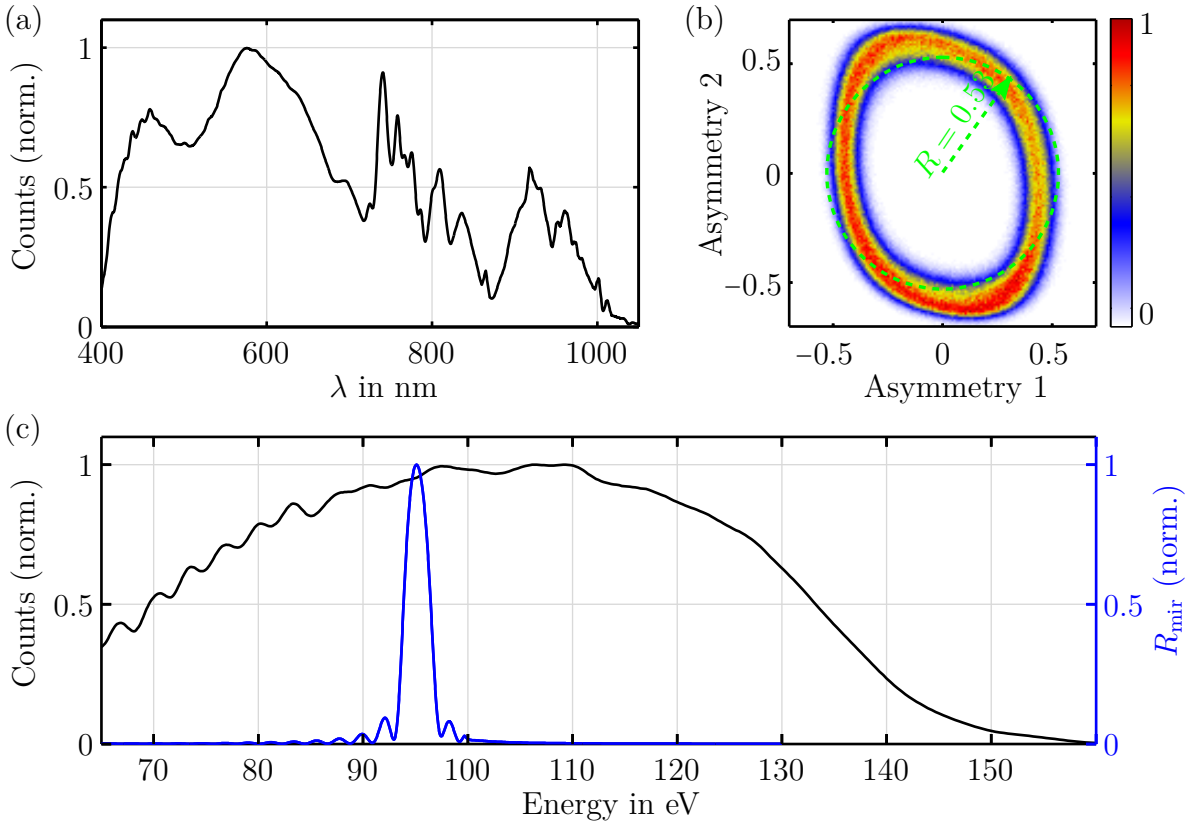

Figure 5.3: Pulse parameters and HHG spectrum as used for the PES and streaking measurements. (a): SPM broadened spectrum after the HCF. (b): PAP of the compressed pulses. The radius of $R = 0.53$ indicates a mean FWHM pulse duration of 5.1 fs. (c): Zirconium filtered HHG spectrum generated in neon at a pressure of 150 mbar. The blue line shows the spectral position and width of the multilayer bandpass filter, see also figure 5.4 for more details.

The general structure of a broadband-excited XUV photoelectron spectrum on W(110) recorded with the Themis 1000 is shown together with a high resolution synchrotron measurement (courtesy of S. Neppl) in figure 5.4(a). The excitation energy is in both cases 95 eV. Figure 5.4(b) depicts the spectral reflectivity of the utilized XUV multilayer mirror exhibiting a bandpass characteristic with a FWHM bandwidth of 2.6 eV, supporting sub-fs XUV pulses in the Fourier-limit. The spectrum is recorded in LAD mode with a retardation ratio of 0.23 and integrated over the emission angles. It is obvious from the figure that due to the limited energy resolution imposed by the broadband HH excitation, the spin-orbit split 4f-states and the 5p-state as well as the substructure of the valence

band merge into two individual, pronounced peaks with a slightly asymmetric line shape. These two peaks are simply denoted as valence band peak and 4f-peak in the following. In order to estimate the quality of the HH photoelectron spectrum, it is compared to the

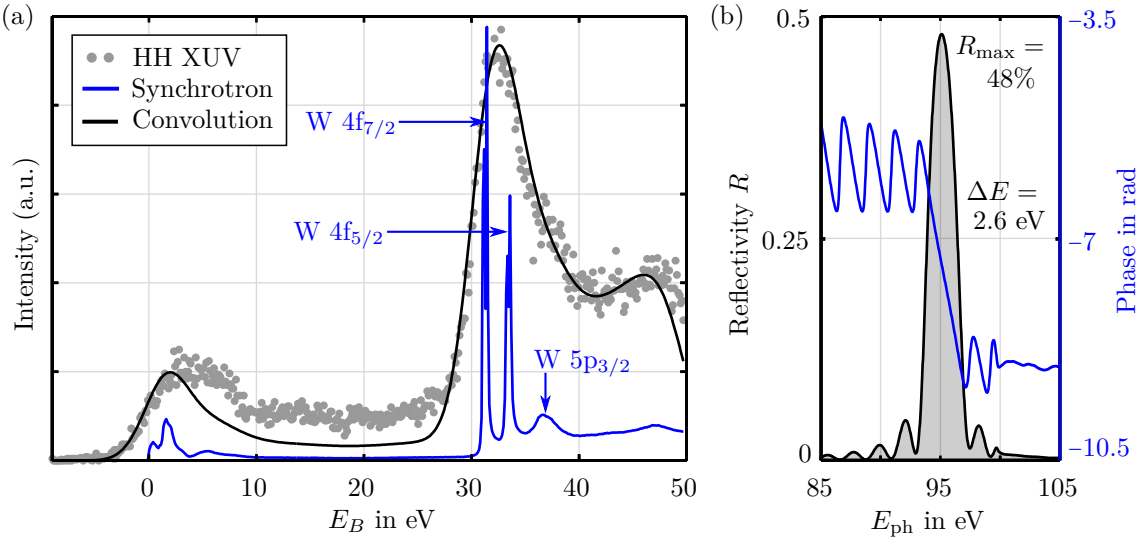

Figure 5.4: Principal structure of the photoemission spectrum from the W(110) surface. (a): Comparison of a high-resolution synchrotron PES measurement from a clean W(110) surface at an excitation energy of 95 eV (courtesy of S. Neppl) with a photoemission spectrum excited by broadband (2.6 eV FWHM) high harmonic XUV pulses energetically centered at 95 eV and taken in LAD mode at RR = 0.23. (b): Calculated spectral bandpass characteristic of the used multilayer-based XUV focusing mirror.

convolution of the synchrotron measurement with a Gaussian function which accounts for the excitation bandwidth and the resolving power of the instrumentation. The width of the Gauss function is determined by least-square optimization between the HH photoelectron spectrum and the convolution. The resulting width provides an alternative measure for the resolving power of the spectrometer. A value of 4.5 eV FWHM is obtained for the given lens setting, which results in an energy resolution of 3.7 eV after deconvolving the mirror bandwidth. This value is in good agreement with the one obtained by the simpler Fermi-edge method described above (compare to the first row of table 5.1). The convoluted synchrotron spectrum well reproduces the line shape of the 4f-peak as well as the valence band slope at the Fermi edge. However, a difference between the two spectra is apparent at the low-energy side of the valence band where the HH photoelectron spectrum exhibits a slightly broadened shoulder. This feature is attributed to adsorbed contaminants on the sample surface [96] which is investigated in more detail in the next section. The additional photoelectrons from the contaminants also contribute to an elevated, inelastic background signal.

5.2.1 Surface contamination

Before any measurement the sample surface is cleaned according to the recipe given in [154]: low temperature annealing ($T \approx 950$°C) segregates carbon from the crystal lattice which is oxidized and desorbed under an oxygen atmosphere. The remanent tungsten-oxide and the atomic oxygen are finally removed by several cycles of high temperature flashes ($T \geq 2000$°C). Typically, a pressure in the mid 10^{-9} mbar range is achieved in the experimental chamber. This pressure implies a mono-time of nearly 15 minutes. However, in order to populate the multi-dimensional dataset for a time-, angle- and CEP-resolved photoemission measurement with satisfactory statistics, a longer acquisition time is necessary with the given repetition rate of 10 kHz. Therefore, a completely contamination-free measurement cannot yet guaranteed at the current status. The structural change of the HH photoelectron spectrum as a consequence of an increasing degree of surface impurity is summarized in figure 5.5. After an exposure of the sample of several mono-times in the

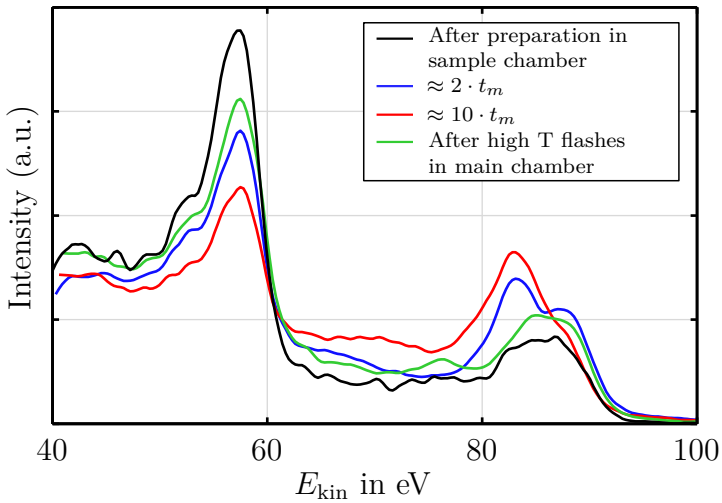

Figure 5.5: Impact of surface contamination on the structure of HH photoelectron spectra from W(110). With increasing degree of contamination, expressed as multiples of the mono-time t_m, the low kinetic energy shoulder of the valence band peak first slowly grows until it forms a distinct peak which finally dominates the valence band structure, considerably modifying the original line shape. The additional peak predominantly arises from O-2p derived states [96]. The line shape of the 4f-peak is conserved but its signal strength gets greatly reduced. Flash annealing by the in situ heating capabilities cannot completely recover the line shape of an atomically clean surface but is still useful to quickly refresh the signal strength of the 4f-peak to some extent.

residual vacuum gas atmosphere, photoelectrons from adsorbed contaminants, primarily from O-2p derived states of oxygen compounds (expected ~ 6 eV below the Fermi edge [96]) interfere with those from the tungsten valence band, considerably modifying the spectral shape of the valence band peak. The energetically specific W-4f peak is only little disturbed by adsorbed impurities, i.e. its line shape is conserved within the applied energy resolution (making a solid-state physical interpretation less complex), though its signal strength

considerably decreases with increasing degree of contamination. For a first validation of the applicability of the new, extended streaking scheme which is presented in this section, we therefore focus on the W-4f peak. Nevertheless, although the electronic properties of core-like states may be less affected by contamination than those of the valence band, surface impurities are still expected to be a dominant source of error. In order to cancel out any systematic error arising from the gradual increase of contamination during data acquisition, the acquisition process of the streaking experiment is organized as a number of quick delay-series measurements with alternating delay-direction in which the acquisition time for each delay step is kept short (a few seconds). It is also obvious from figure 5.5 that the limited heating temperature achieved by the in-situ heater ($T \sim 1600°C$) is not able to completely remove the adsorbed oxygen from the tungsten surface. However, it is still useful to refresh the signal strength of the 4f-peak between subsequent acquisition cycles.

5.2.2 Space charge distortion

Another potential nuisance in photoemission measurements is space charge, i.e. the mutual Coulomb repulsion of photo-excited electrons, leading to appreciable distortions both in the spectral and spatial domain of the photoemission signal [104,107]. In general, space charge effects become stronger the more electrons accumulate near a single point in space-time. Especially for femtosecond and sub-fs photo-excitation times, this is inevitably the case at the (only several tens of microns sized) excitation spot on the sample where the electrons are released into vacuum, and potentially at *cross-over* points of electron trajectories within the lens-column of the spectrometer. The strength of the space charge influence from cross-over points depends on the specific lens setting which in turn determines the space-time dispersion of the electrons during their excursion through the lens-column. Lens settings with RR < 1 (accelerating mode) entail a low space-time dispersion, and hence represent the worst-case scenario. Therefore, we conduct an exemplary measurement with a low retardation ratio of RR $= 0.23$ in LAD mode in order to reveal and estimate the strength of space charge distortion of sub-fs photo-excitation from tungsten. Spectra for different XUV intensities are plotted in figure 5.6. The XUV intensity is varied by adjusting the gas pressure in the HHG nozzle, see figure 4.2. With increasing number of generated photoelectrons the spectral features shift, broaden and smear out, indicated by the slope width of the valence band at the Fermi edge and the change of the W-4f peak position. Although space charge induced degradation is detrimental for the analysis of the spectra on the one hand, its appearance demonstrates on the other hand, that the high harmonic flux generated by this new source is sufficiently high in order to exploit the full potential of the source regarding its repetition rate. Driving the photoemission process into the space charge limit reveals that the maximum signal count rate, determined by the repetition rate, can be virtually reached. The only way to reduce space charge degradation is to lower the excitation intensity, which simultaneously reduces the signal count rate at the detector. As indicated in the figure, the effective count rate for an undistorted spectrum can get quite small, making up only a fraction of the repetition rate. This fact underlines

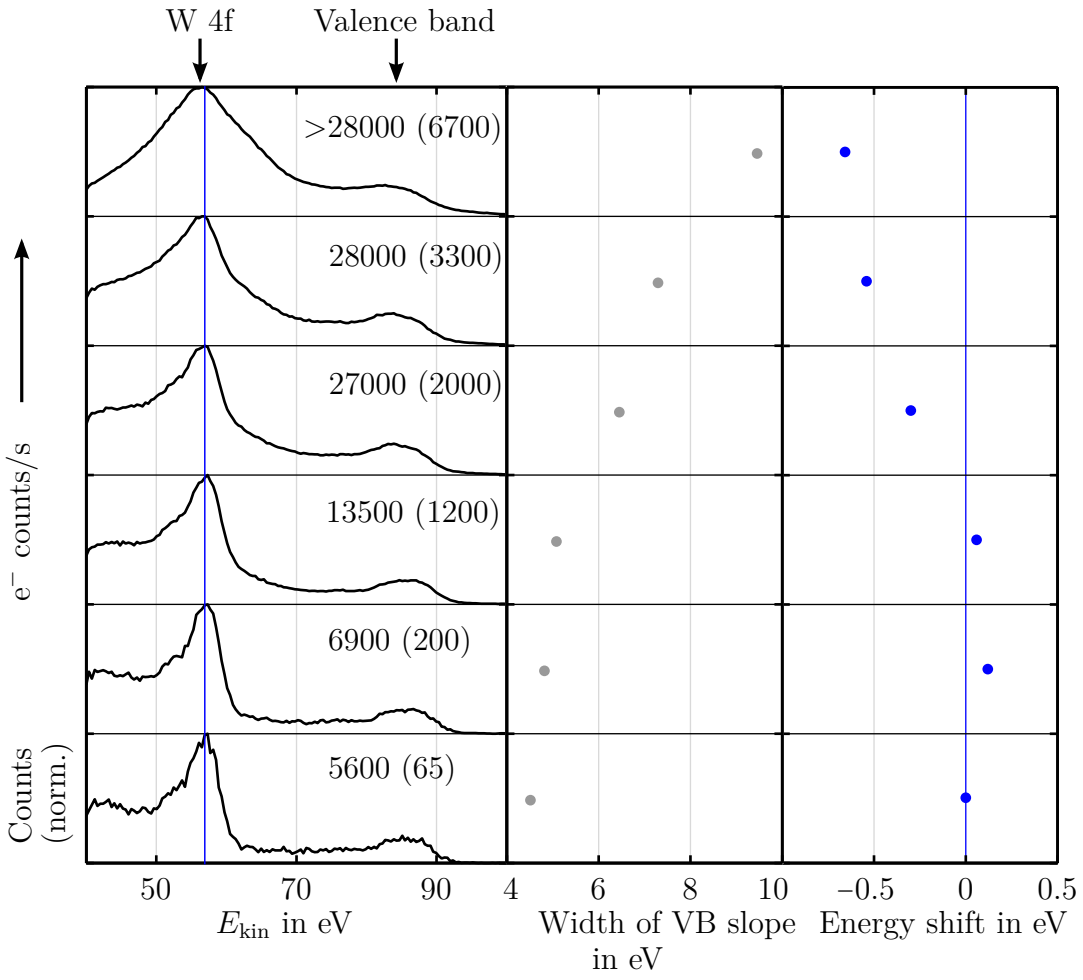

Figure 5.6: Deformation of PES spectra from W(110) due to space charge influence in an accelerating mode (RR < 1). Spectral features broaden and smear out with increasing high harmonic intensity. The width (10%-90% criterion) of the high energy slope of the valence band as well as the change of the W-4f peak position are shown in the right panels. The value attached to each curve indicates the total electron count rate on the detector (including secondary electrons) as well as, in parenthesis, the effective electron count rate considering only the electrons within the energy window adjusted by the lens settings of the spectrometer.

the importance of a high-repetition rate source and illustrates the benefit gained by 10 kHz compared to the prevailing 1-3 kHz. Moreover, space charge distortion even occurs when the effective count rate is well below the repetition rate (less than 1 detector count per laser shot within the adjusted energy window), revealing that the dominant contribution of space charge distortion stems from the numerous secondary electrons. This fact sets a stringent limit to the applicable streaking field strength which in turn generates a vast amount of slow electrons by above-threshold ionization (ATI). In order to keep space charge distortions low, the total signal count rate, as a coarse rule of thumb, should be kept below 50% of the repetition rate, as evident from figure 5.6. However, this condition can usually not be fulfilled in the presence of the NIR streaking field. Therefore, an unavoidable space charge distortion induced by the streaking field has to be accepted. A general, precise statement about the onset of space charge deformation derived from the detector count rate can not be made due to the varying complexity of the spectral transmission function and electron trajectories through the spectrometer according to the specific lens settings, but any influence of space charge effects can be easily checked experimentally by means of a comparative test spectrum with lower count rate. A similar behavior of signal degradation due to space charge can be expected for the angle image.
Finally, the influence of space charge distortion from ATI electrons generated by multi-photon ionization of the NIR streaking field is shown in figure 5.7 for the lens settings as used in the streaking measurements ($U_{\text{kin}} = 58$ V and $U_{\text{pass}} = 100$ V). Note that for

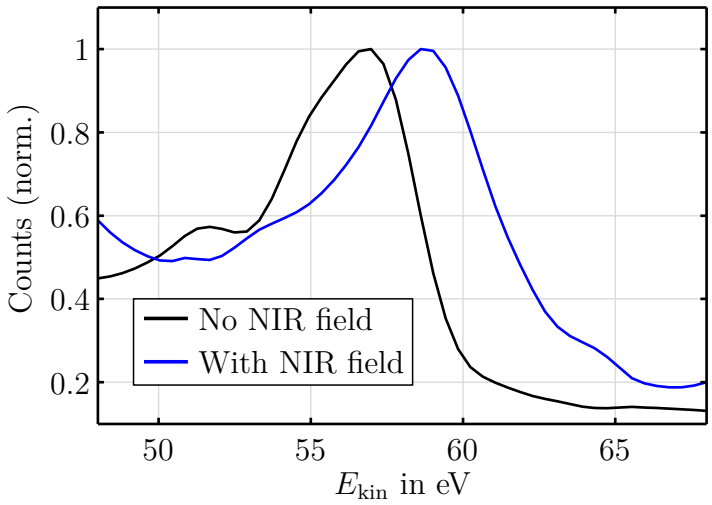

Figure 5.7: Space charge deformation of the W-4f spectrum under the influence of ATI electrons generated by the NIR streaking field.

these lens settings the W-5p line becomes already discernible. The energy resolution of the spectrometer was determined by a convolution analysis with the synchrotron data to be a few hundred meV. In the presence of the NIR field, however, the effective energy resolution is deteriorated by 0.5-1 eV. Furthermore, the spectrum shifts by ~ 2 eV to higher energies under the influence of the photoelectrons generated by the laser field, causing a systematic

error in the streaking measurements.

5.3 Angle- and CEP-resolved photoelectron streaking

The advanced photoelectron streaking scheme presented in this section provides a five-dimensional dataset $(\alpha, \beta, E_{\text{kin}}, \Phi_{\text{CEP}}, t_d)$, which incorporates a tremendous amount of information. Projections of the dataset along selected parameter ranges reduce the dimensionality and enable the extraction of desired information as well as its graphical representation. The main task addressed in this section is the verification of the proper and reliable functioning of the method. This step is indispensable due to the critical aspects related to the synchronization between electron spectrometer and phase-meter as discussed in section 3.2.8. Relevant technical issues and pitfalls are summarized in appendix A. The data are recorded in LAD mode with $U_{\text{kin}} = 58$ V and $U_{\text{pass}} = 100$ V.

5.3.1 CEP-related evaluation

In figure 5.8 we present a CEP resolved photoelectron spectrum of the W-4f peak by projecting (summing) the dataset along the entire range of emission angles for a fixed time delay $t_d \gg 1$ so that XUV and NIR laser pulse are not overlapping yet. The photoemission signal shows an appreciable modulation as a function of the CEP with a modulation depth close to 50% and a periodicity of 180°, indicating inversion symmetry of the photoemission signal with respect to the NIR field. As the only link between photoemissin process and NIR laser field for the adjusted time delay is the HHG process, it is intuitive to assume that the observed modulaton constitutes a direct imprint of the CEP dependant high harmonic yield, which is confirmed by a CEP-dependant HHG simulation (courtesy of M. Hoegner) using the Lewenstein model [83]. The simulation uses the applied laser pulse as well as gas target parameters and calculates the spatially coherent high harmonic response over the NIR beam profile at a single z-slice (where z is the propagation direction), considering transient gas ionization. The contribution of long-trajectories is programmatically suppressed (by limiting the excursion time) as this condition is also experimentally fulfilled by phase-matching adjustments. Propagation effects, however, are not accounted for. The result is plotted in figure 5.8(c) and shows the typical shift of the high harmonic peaks with respect to the CEP near the cutoff region [74, 118]. The CEP-dependant HH yield, obtained by multipliying the simulated spectrum with the spectral transmission functions of the employed XUV optics (metal foil and multilayer mirror) and integrating it along the energy-axis, is in good agreement with the measured modulation behavior of the photoemission signal. A possible reason for the deviation in the modulation depth could be due to neglectiong propagation effects in the simulation. Nevertheless, the observation of a strong CEP dependency of the photoelectron signal and the agreement between simulation and measurement confirms that the assignment of CEP values within the DLD data stream works properly and reliably. Furthermore, it is reminded that the PAP only provides relative CEP values (see equation 2.32), and therefore, the CEP-axis in figure

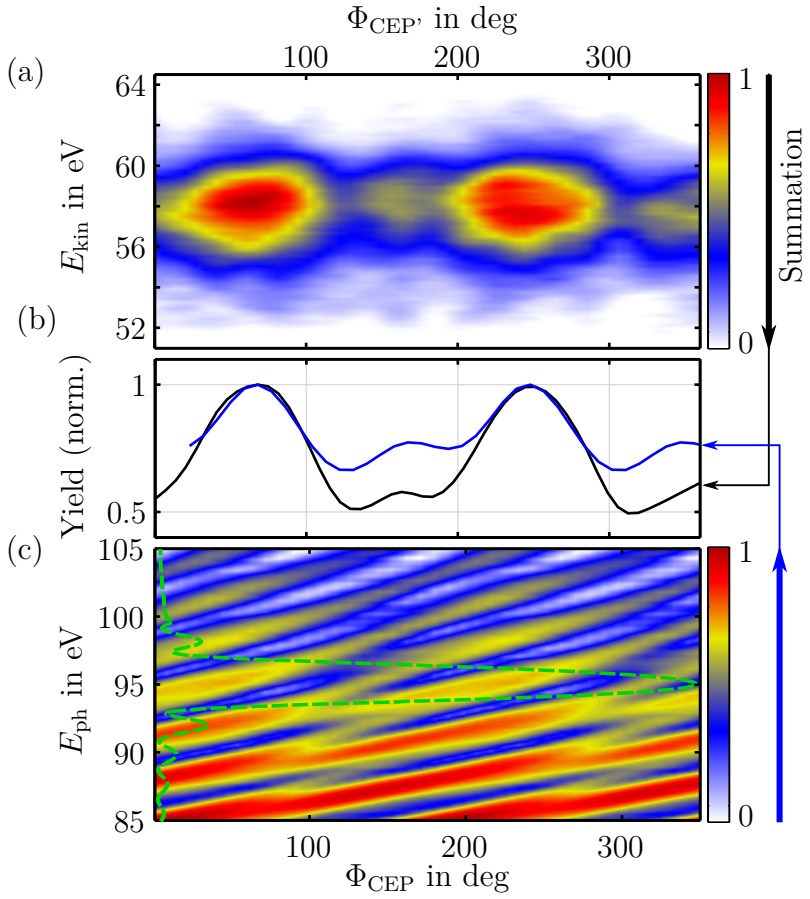

Figure 5.8: CEP resolved W-4f photoelectron spectrum and HH simulation. (a): CEP resolved photoelectron spectrum. (b): Projection of (a) and (c) along the energy axis showing the detailed evolution of the signal modulation with respect to the CEP. (c): CEP-dependent HH simulation.

5.8 is only correct except for a constant offset $\Phi_{\mathrm{CEP}}^{\mathrm{offset}}$, i.e. $\Phi_{\mathrm{CEP'}} = \Phi_{\mathrm{CEP}} + \Phi_{\mathrm{CEP}}^{\mathrm{offset}}$ [1] where Φ_{CEP} is the typical CEP referenced to a cosine-pulse. The CEP-axis of the simulated HH intensity has to be shifted by $\Phi_{\mathrm{CEP}}^{\mathrm{offset}} = 23°$ in order to match it with the measurement, i.e. a CEP value of $\Phi_{\mathrm{CEP'}} = 23° \pm n \cdot 180°$, $n \in \mathbb{N}$, corresponds to a ±cosine-pulse. The sign cannot be determined by this method due to the field inversion symmetry of the process. However, in the next paragraph it is shown how an absolute calibration of the CEP'-axis can be directly deduced from the measured dataset.

For the following investigation, the dataset is evaluated as a function of time delays around $t_d = 0$, i.e. the photo-excited electrons now experience the NIR-laser field. The common streaking trace is obtained when the kinetic energy of the field-dressed photoelectrons is plotted over the time delay. Angle-integrated streaking traces for a set of CEP

[1] For the remainder of this section, the primed denotation $\Phi_{\mathrm{CEP'}}$ refers to CEP values derived from the phase-meter.

selections, as indicated in figure 5.8(a), are depicted in figure 5.9. The appearance of an oscillating energy shift of the photoemission spectra verifies once more the successful implementation of the phase-tagging setup and the correct synchronization of phase-meter and electron spectrometer. For a first qualitative inspection of the resulting streaking traces,

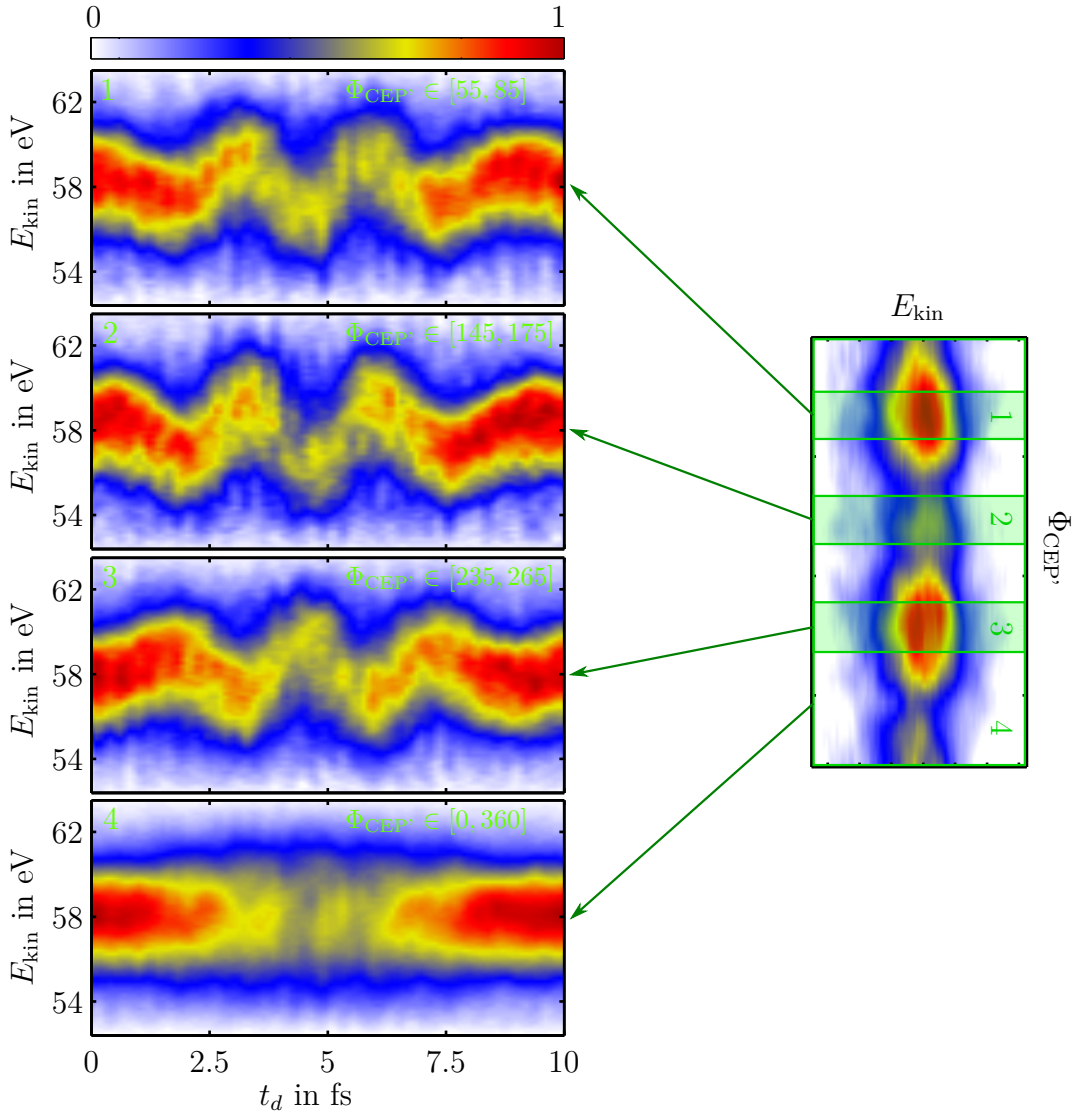

Figure 5.9: Exemplary streaking traces for selected CEP ranges as indicated in the right graph (both main maxima and the side maximum of the CEP dependent photoemission signal).

it is reminded that the oscillatory energy shift of the spectra as a function of time delay represents the temporal evolution of the vector potential of the laser field. Therefore, the field inversion of the laser pulse for a phase shift of 180° is obvious from the reversed oscillation direction of the streaking traces 1 and 3. For a CEP shift of 90° (streaking trace 1 and 2) no significant displacement of the field maxima (and minima respectively) with

respect to time is observed between the streaking traces. This fact reflects the intrinsic synchronization of the XUV pulse to a specific phase of the driving NIR laser pulse, which will be addressed in more detail in a later paragraph. Streaking trace 4 is summed over the full 360° CEP range. Due to the afore mentioned phase-locking mechanism of the harmonic pulses, it can be considered as composed of the sum of a set of mutually inverted streaking traces. However, because of the limited energy resolution of the system the two inverse traces cannot clearly be discerned, instead they merge into a single 'blurry' structure.
For the subsequent analysis, a sinusoidal vector potential with a Gaussian envelope is assumed to approximate the oscillatory energy shift of the spectra within a streaking trace. As a measure of the energetic position of the W-4f peak, the center of energy (COE) of each spectrum $E_c(t_d)$ with

$$E_c(t_d) = \frac{\int S(E_{\mathrm{kin}}, t_d) E_{\mathrm{kin}} \, \mathrm{d}E_{\mathrm{kin}}}{\int S(E_{\mathrm{kin}}, t_d) \, \mathrm{d}E_{\mathrm{kin}}} \tag{5.1}$$

is calculated for every delay step. Finally, the model function

$$E_{\mathrm{kin},f}(t_d) = E_{\mathrm{kin},i} - \Delta E_{\mathrm{kin}}^{\mathrm{max}} \exp\left(-\frac{2\,(t_d - t_{\mathrm{env}})^2}{\tau_L}\right) \sin\left(\omega_L t_d + \Phi_{\mathrm{CEP}}\right) \tag{5.2}$$

is fitted to the COE evolution, where $E_{\mathrm{kin},i}$, t_0, $\Delta E_{\mathrm{kin}}^{\mathrm{max}}$, ω_L, τ_L and Φ_{CEP} are optimization parameters. The fit procedure is based on an iterative nonlinear least-squares estimation. Error bars represent the 95% confidence interval for the parameter estimates. A set of CEP dependant spectrograms is finally generated from the dataset, in which each spectrogram is projected over a 20° CEP bin size while consecutive spectrograms are incremented by $\Delta\Phi_{\mathrm{CEP'}} = 6.8°$. In figure 5.10 we plot the CEP value Φ_{CEP}, retrieved from the model function 5.2 over the CEP value $\Phi_{\mathrm{CEP'}}$, derived from the phase-meter. Note that the CEP

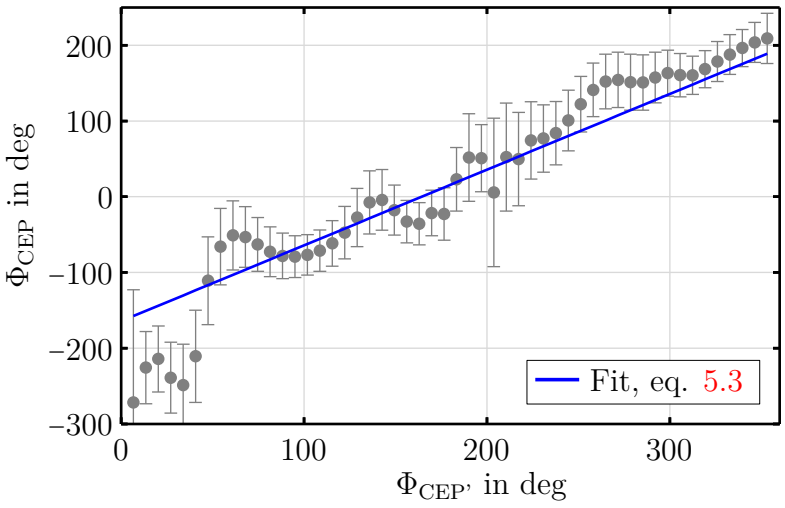

Figure 5.10: Absolute calibration of the CEP derived from the stereo ATI phase-meter.

of the model function is referenced to a cosine-pulse, therefore providing an absolute-value gauge for the calibration of the CEP deduced from the phase-meter. Both CEP terms have to be directly proportional, only differing by a constant offset, see section 2.1.2. Fitting the linear function

$$\Phi_{\text{CEP'}} = \Phi_{\text{CEP}} + \Phi_{\text{CEP}}^{\text{offset}} \tag{5.3}$$

gives an offset value of $\Phi_{\text{CEP}}^{\text{offset}} = -164° \pm 11°$, i.e. the value $\Phi_{\text{CEP'}} = 196° \pm n \cdot 360°$, $n \in \mathbb{N}$, corresponds to a +cosine-pulse. This value is in good agreement with the one estimated from the HH simulation, however, this method now allows an unambiguous assignment of the CEP to the correct sign of the corresponding cosine-pulse.
Evaluating the evolution of the parameter t_{env} in equation 5.2 in the scope of this COE analysis reveals a principal feature of the HHG process, namely the locking of the XUV pulse to a specific phase of the laser field. This mechanism is a result of the fact that the generation of a high harmonic photon of a given energy is locked to a particular ionization phase Φ_L^{ion} according to the three step model as plotted in figure 2.6. This ionization phase is unique provided that only either long-trajectories or short-trajectories contribute to the HHG process. Typically, the latter condition is experimentally fulfilled by phase-matching adjustments. The locking mechanism manifests in CEP-resolved streaking measurements in such a way that the oscillation peaks of the streaking traces (i.e. the vector potentials) for different CEP selections are mutually aligned with respect to the delay time, as already indicated in figure 5.9. As a consequence, the envelope of the vector potential has to shift by the amount t_{env} as a function of CEP in the reference system of the delay time. This behavior is illustrated in figure 5.11 and can be semi-classically understood as follows: Assuming the laser phase at the instant of ionization is required to be Φ_0 in order to produce a high harmonic photon of a certain energy. For a given CEP of $\Phi_{\text{CEP},0}$, the ionization event must happen at the time t_0 so that $\Phi_0 = \omega_L t_0 + \Phi_{\text{CEO},0}$. Correspondingly, for $\Phi_{\text{CEP},1}$ it is $\Phi_0 = \omega_L t_1 + \Phi_{\text{CEO},1}$ with now being t_1 the ionization time. Now, let's first assume a long NIR pulse (i.e. a many-cycle pulse), then Φ_0 can be considered CEP-independent. In this case the temporal shift of the envelope becomes

$$t_1 - t_0 \equiv t_{\text{env}} = \frac{1}{\omega_L}\left(\Phi_{\text{CEP},1} - \Phi_{\text{CEP},0}\right) = \frac{T_L}{2\pi}\Delta\Phi_{\text{CEP}}. \tag{5.4}$$

The temporal position of the envelope of the vector potential shifts linearly as a function of the CEP difference with a slope of $T_L/2\pi$. This CEP-dependent envelope shift, extracted by the COE analysis, is plotted in figure 5.12(b) together with a linear fit according to equation 5.4. Note that equation 5.4 only describes relative time and CEP values (also the scale of the envelope position in figure 5.12(b) is referenced to an arbitrary time offset), and therefore, an additional time offset is used as an optimization parameter in the fit. The assumption of a CEP-independent value of Φ_0 is not correct any more for few-cycle pulses. In this case, it is expected that the ionization phase required to obtain a given high harmonic photon energy experiences a CEP-dependent variation. Furthermore, this variation is expected to be stronger the shorter the pulse duration. Therefore, in the case of few-cycle pulses equation 5.4 has to be extended by an additional term $\Delta\Phi_0$ describing

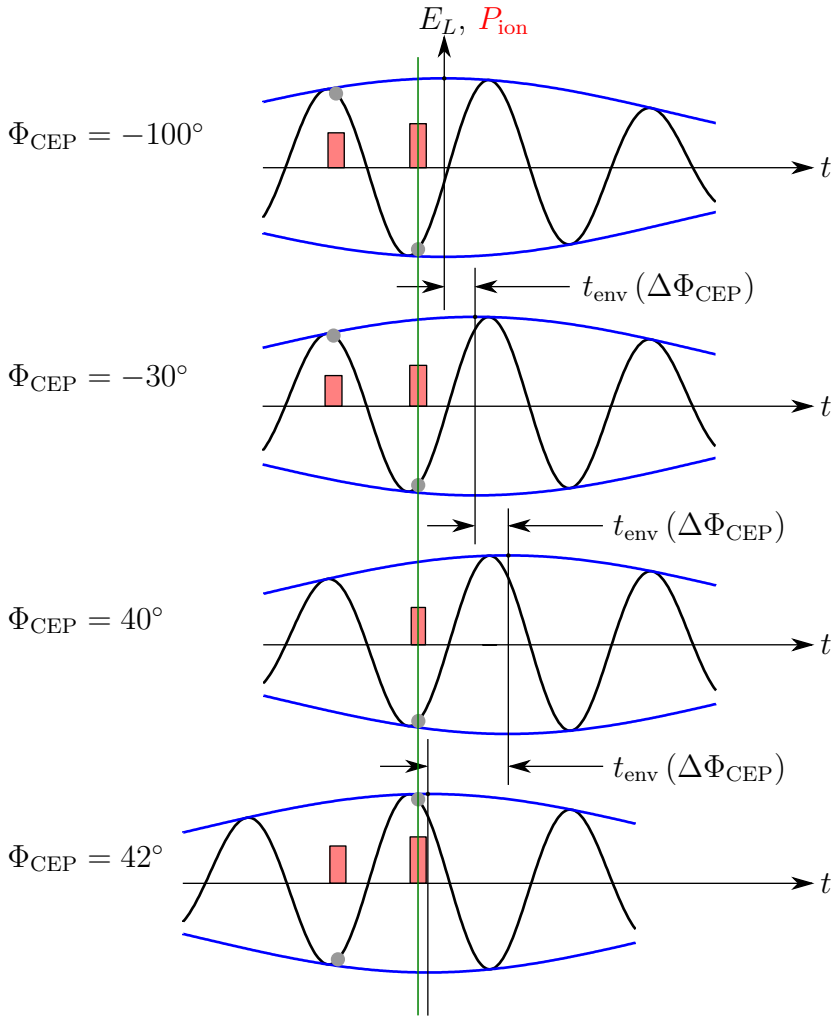

Figure 5.11: Illustration of the pulse-envelope shift in CEP-resolved streaking traces due to the phase-locking mechanism of the HHG pulses to the driving laser pulse. The electric field of the laser pulse for different CEP values is given as black solid line, its envelope is indicated as blue solid line. All instants of ionization which lead to a recombination energy of $E_{\text{kin}} = 2.9U_p$ on short-trajectories are marked by a gray dot. The ionization probability of the corresponding ionization event is indicated by the height of the red bars, using the ADK ionization rate 2.60 in the quasi-static approximation limit. Assuming a (nearly) CEP-independent excursion time of the involved electrons (which is numerically confirmed), the corresponding, spectrally filtered HHG pulse can be thought of being locked to the most-probable ionization phase. A subsequent sampling of the laser field with this HHG pulse by a streaking measurement results in the alignment of all CEP-dependent streaking traces to the instant of the most-probable ionization event for the given energy, as indicated by the green line. The phase-offset of the laser field due to its CEP finally gives rise to a shift in the envelope. When the CEP passes a value for which ionization from a neighboring half-cycle gets more likely, the envelope position experiences a sudden jump, such as at $\Phi_{\text{CEP}} = 41°$ in this illustration.

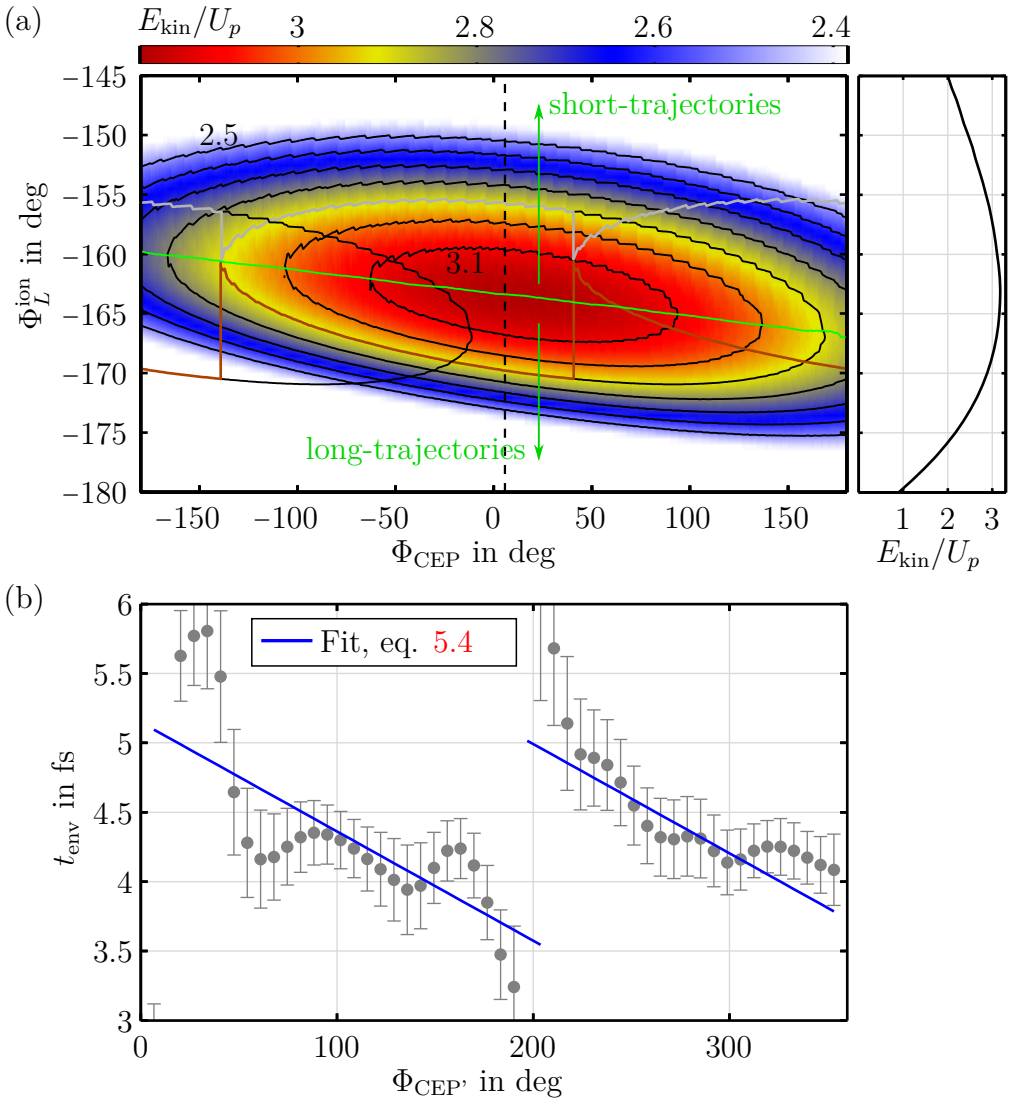

Figure 5.12: Locking of the XUV pulse to the phase of the driving laser pulse. (a): CEP-dependent ionization phase Φ_L^{ion} of a few-cycle pulse for different kinetic energies at the instant of recombination. Isolines are shown for recombination energies between $2.5U_p$ and $3.1U_p$ in steps of $0.1U_p$. The dashed line indicates the CEP with the highest-possible recombination energy of $3.17U_p$. It is close to a cosine-pulse. A cross-section is shown in the right panel. The progression of the ionization phase for the highest CEP-dependent recombination energy is indicated by the green line which also separates the graph into the region for long- and short-trajectories. The graph repeats for every $\pm 180°$ with respect to Φ_{CEP} and Φ_L^{ion} (neighboring optical half-cycles). A contracted scheme (shifting the isolines of neighboring half-cycles by $\Phi_L^{\mathrm{ion}} = \pm 180°$) for the recombination energy of $2.9U_P$ is shown. The gray and brown curves illustrate the evolution of Φ_L^{ion} of the most-probable ionization event for the short- and long-trajectory, respectively. Note that the transition from one isoline to the next manifests as a jump of the envelope position in the streaking measurement. (b): Temporal shift of the field envelope, determined from CEP-resolved streaking measurements.

this CEP-dependent variation of the ionization phase, so that

$$t_{\mathrm{env}} = \frac{T_L}{2\pi} \left(\Delta\Phi_{\mathrm{CEP}} + \Delta\Phi_0 \left(\Delta\Phi_{\mathrm{CEP}} \right) \right). \tag{5.5}$$

Figure 5.12(a) shows a calculation of the ionization phase, based on classical trajectories, for different recombination energies as a function of the CEP for a few-cycle pulse comprising 4 optical cycles within its 1/e-Gaussian field envelope. It is obvious from the graph that the highest recombination energy is only achieved by a CEP value close to a cosine pulse (which results in a continuum at the cutoff energy and which is the prerequisite for the amplitude gating technique). The ionization phase required for a given recombination energy varies nonlinearly as a function of the CEP. As a consequence, the shape of the corresponding iso-energy line maps to the CEP-dependent evolution of t_{env} (provided that the impact of the CEP on the excursion time is negligible, which is numerically confirmed). Notably, the curvature of the iso-energy lines changes from concave for long-trajectories to convex for short-trajectories. Therefore, the sign of curvature of $t_{\mathrm{env}}(\Delta\Phi_{\mathrm{CEP}})$ finally allows the determination of the type of trajectory which dominantly contributes to the HHG process. Furthermore, the XUV pulse of a given central photon energy can be thought of being locked to the corresponding ionization phase with the highest ionization probability, which in turn is determined by the instantaneous field strength in the case of tunnel ionization. Therefore, the discontinuity in $t_{\mathrm{env}}(\Delta\Phi_{\mathrm{CEP}})$ at $\Phi_{\mathrm{CEP}'} = 200°$ arises when the corresponding ionization event at a neighboring field cycle suddenly gets more likely due to the CEP-induced field shift, see also figure 5.11. The cosine-referenced CEP values for this discontinuity at a certain recombination energy are given by the outermost left edges of the corresponding iso-energy ellipses in figure 5.12(a).

Next, the parameter $E_{\mathrm{kin},i}$ of the model function 5.2 is plotted against the CEP in figure 5.13. It describes a shift of the baseline of the oscillatory part in the spectrogram due to a CEP-dependent variation of the initial kinetic energy of the photo-emitted electron. It reveals a modulated trend with a periodicity of 180°, which can be explained by the CEP-dependent spectral characteristics of the high harmonic radiation. The energetic displacement of the high harmonic peaks as a function of CEP causes a CEP-dependent variation of the energetic center of gravity E^c_{ph} within the reflection bandpass of the multilayer mirror, see figure 5.8. Based on the simulated HHG output I^{HHG} from the previous paragraph, the expected initial kinetic energy $E^{\mathrm{sim}}_{\mathrm{kin},i}\left(\Phi_{\mathrm{CEP}}\right) = E_{\mathrm{W4f}} + W - E^c_{\mathrm{ph}}\left(\Phi_{\mathrm{CEP}}\right)$ with

$$E^c_{\mathrm{ph}}\left(\Phi_{\mathrm{CEP}}\right) = \frac{\int I^{\mathrm{HHG}}(E_{\mathrm{ph}}, \Phi_{\mathrm{CEP}}) R_{\mathrm{ML}}(E_{\mathrm{ph}}) E_{\mathrm{ph}} \, \mathrm{d}E_{\mathrm{ph}}}{\int I^{\mathrm{HHG}}(E_{\mathrm{ph}}, \Phi_{\mathrm{CEP}}) R_{\mathrm{ML}}(E_{\mathrm{ph}}) \, \mathrm{d}E_{\mathrm{kin}}} \tag{5.6}$$

is plotted as blue line in figure 5.13 and shows good qualitative agreement to the experimentally derived curve. Here, E_{W4f} is the binding energy of the 4f-electrons, W is the work function of tungsten, and R_{ML} is the spectral reflectivity of the multilayer mirror.

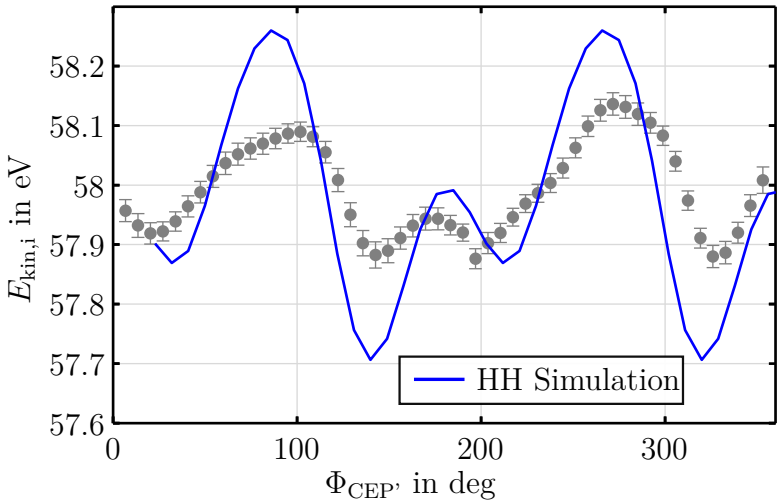

Figure 5.13: CEP-dependent variation of the initial kinetic energy of the photo-emitted electrons.

5.3.2 Angle-related evaluation

In order to validate the angle-resolving capability of the setup, the dataset is projected along a fixed CEP range of $\Phi_{\mathrm{CEP}'} \in [140°, 180°]$ while streaking traces are now generated for different selections of the emission angle, see figure 5.14(a). According to the geometric projection of the incident electric field vector onto the different emission directions, the streaking amplitude is expected to be dependent on the emission angle, following equation 2.92. Using again the model function 5.2, the streaking amplitude is obtained by the parameter $\Delta E_{\mathrm{kin}}^{\mathrm{max}}$. The result is plotted in figure 5.14(c). The experimentally measured streaking amplitude agrees well with the theoretical expectation value, confirming the viability of an angle-resolved evaluation of the streaking results from this setup.

5.3.3 Wave-packet reconstruction, relative time delays and wave-packet spread

Evaluating the fitted vector potential 5.2 in the scope of the COE analysis delivers insight into several aspects of the HHG process and provides an absolute calibration gauge for the CEP of the phase-meter. The big strength of the streaking method, however, lies in its ability to completely reconstruct the temporal profile of the photo-emitted electron wave-packet. Therefore, the full potential of the extended streaking setup is finally only exploited by investigating the wave-packet behavior for different excitation and emission parameters. Subtle changes in the temporal structure of the released wave-packets can arise from solid-state specific properties such as transport-induced dispersion, band dispersion and the screening of the NIR field [85, 86, 100]. As a first step, it is necessary to verify the plausibility of the wave-packet reconstruction obtained from CEP-tagged streaking traces

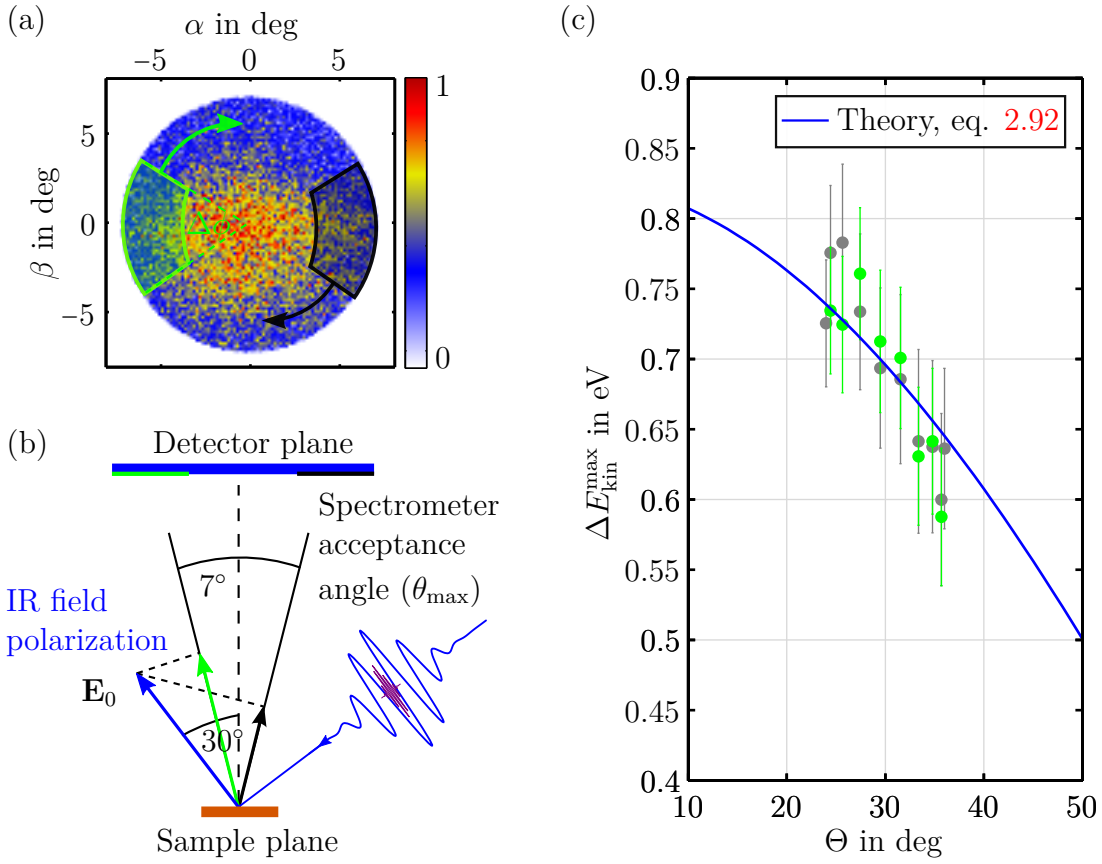

Figure 5.14: Variation of the streaking amplitude as a function of the emission angle. (a): CEP- and energy-integrated image of the emission angles. The green and black fields describe the area of angle-integration for the COE-analysis. The areas have a radial width of 3°, a polar width of 60° and are incremented by a polar angle of 20° for subsequent streaking traces. (b): Geometric illustration of the projected E-field vector of the laser field on the different electron emission directions. (c): Experimentally determined, angle-dependent streaking amplitude together with the theoretical expectation values.

recorded with an angle-resolving spectrometer. We exemplary perform a wave-packet reconstruction for an angle-integrated spectrogram which is summed over the CEP range of $\Phi_{\mathrm{CEP}} \in [140°, 180°]$ using the FROG-CRAB retrieval technique with a least-squares generalized projection algorithm (LSGPA) [41]. Figure 5.15 shows the measured trace, the retrieved trace, the vector potential and electric field of the NIR pulse, as well as the reconstructed temporal and spectral intensity of the wave-packet. The photoelectron spectra of each time delay are smoothed by a shape-preserving local regression method of second order. The retrieved spectral wave-packet width of 5.8 eV FWHM is considerably larger than the employed excitation bandwidth of 2.6 eV. Significant spectral broadening is mainly attributed to the limited resolution of the instrumentation, to space charge distortions and to the details of the background subtraction method. For the latter we apply

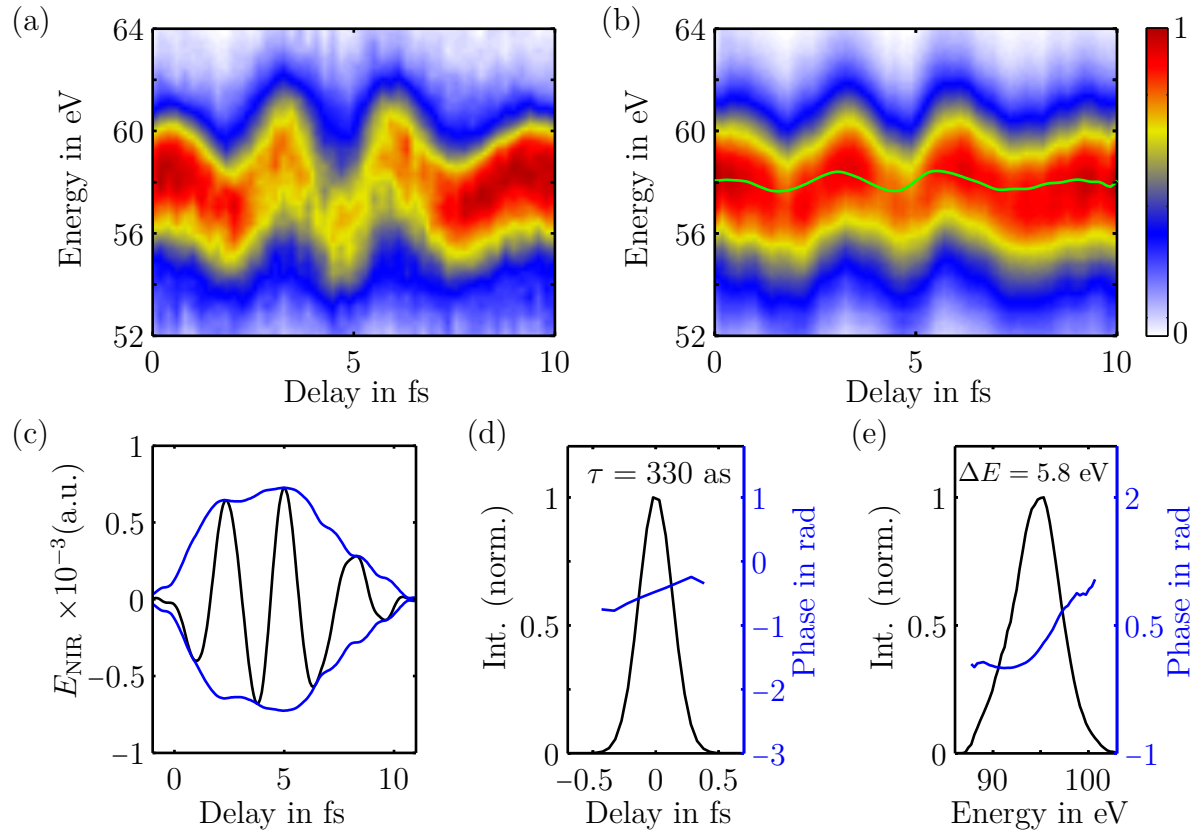

Figure 5.15: Complete electron wave packet and vector potential reconstruction of the angle-integrated streaking trace for a cosine-pulse. (a): Measured streaking trace. (b): Retrieved streaking trace and vector potential (green line). (c): Reconstructed electric field and its estimated envelope (blue lines). (d),(e): Reconstructed temporal (d) as well as spectral (e) structure and phase of the electron wave packet.

Shirley's method [136]. This method requires the definition of an energy window which encompasses the spectral feature of interest. The exact width and position of this window relies rather on a reasonably intuitive guess than on a deterministic and impartial criterion. It was found that the choice of the spectral width of this window considerably affects both the retrieved wave-packet duration and the convergence stability of the algorithm. A more stringent confinement of this energy window around the W-4f peak results in longer wave-packet durations. However, a too stringent confinement crops the tails of the photoemission peak upon its field-induced, delay-dependent energy shift, thereby artificially deforming its spectral shape, which additionally causes instabilities in the convergence behavior of the algorithm. Therefore, the width of the window is chosen a bit more generous. Stable convergence is achieved for a window width of 17 eV, symmetrically centered around the NIR field-free maximum of the W-4f photoemission peak. A typical FROG error, as defined in [41], of $0.06-0.15$ is achieved after 3000 iterations. For all of the above reasons, the reconstructed wave-packet duration is heavily underestimated compared to

the expected Fourier-limit of 700 as according to the applied excitation bandwidth. As this underestimate is a result of systematic errors which do not considerably vary within the spectral range of interest, we assume that relative changes of wave-packet parameters are still meaningful as long as the constraints for the background subtraction and for the algorithm parameters are consistently applied. The temporal width of wave-packets reconstructed from different emission angles are summarized in figure 5.16. Emission angles

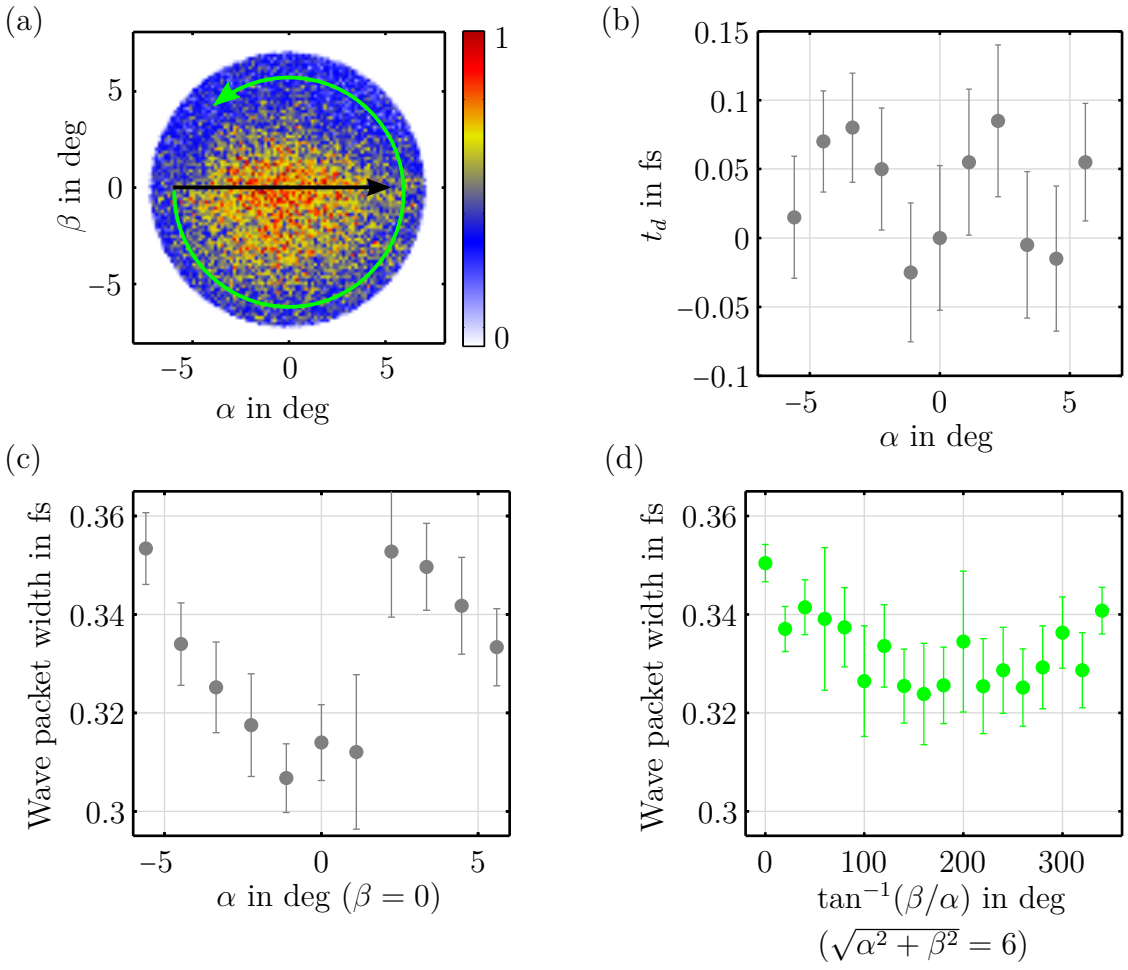

Figure 5.16: Angle-resolved wave packet spread and emission delay for a cosine-pulse. (a): Illustration of angle selections. (b): Angle-resolved electron wave packet emission delay. (c),(d): Angle-resolved wave-packet spread for different selections of the emission angle, see part (a).

with a fixed azimuthal angle, coinciding with the polarization direction of the NIR field projected onto the sample surface, and varying polar angles, including normal emission, as well as angles with a fixed polar angle of 5° and varying azimuthal angles are selected. The evolution of the wave-packet duration for different polar emission angles gives indication for a systematic wave-packet broadening from normal emission toward off-normal emission. This observation might be a result of band structure dispersion of the final states

sampled in the time domain. Interestingly, a correlating trend in the photoemission delay, deduced from a COE analysis, is not observed within the measurement error, see figure 5.16(b). So far, ballistic transport models have been quite successful in describing the transport process of photoelectrons inside a solid [96,97]. In the scope of such a model, our observation is quite surprising because this would mean that the band curvature changes considerably within the range of detected emission angles but the slope of the band does not. This discrepancy might be a result of a yet incomplete understanding or description of the underlying physics. A recent work [140] for example revealed that the band structure plays a significant role for photoemission delays in resonant excitations on the one hand, the experimentally observed magnitude of the delays, on the other hand, could not be explained by the band structure in the course of a ballistic transport model, i.e. the transport velocity of the wave-packet did not coincide with the group velocity derived from the band dispersion. It is also worthwhile to investigate the width of the wave-packet for varying azimuthal angles at a fixed polar angle. This examination should reflect the symmetry of the Brillouin zone, if band structure effects are the primary reason for the wave-packet broadening. According to figure 5.17, tungsten exhibits a two-fold symmetry. However, figure 5.16(d) gives only a vague indication for such a behavior. Besides band structure effects, screening effects may play a role. It is obvious that electrons with a momentum component parallel to the sample surface experience a slightly larger skin depth of the screened NIR field. The electron wave-packet can scatter at the potential of this screening field, leading to a change in its time structure. An influence of the screening depth has been indeed predicted by quantum-mechanical models [85, 86], its effect, however, is claimed to be very small. A similar analysis can be performed for different CEP selections. However, the pure comparison of *relative* changes in the time structure of the retrieved wave-packets is not meaningful in this case, since the CEP dependence of the HHG process naturally implies different temporal XUV pulse profiles which are imprinted on the initial photoelectron wave-packet. In order to relate solid-state effects to the deformation of the wave-packet structure, a reference wave-packet is required which contains the initial, unperturbed temporal profile, i.e. which has not been affected by interactions with the solid. Such a reference wave-packet can be obtained from accompanying streaking measurements in the gas phase as it is common for attosecond metrology. In summary, the extended streaking technique provides a multi-parametrized dataset with a tremendous amount of information which gives a multitude of possibilities for the investigation of electron dynamics in solids. A first successful application of this method to a tungsten sample lead to a series of interesting observations. A conclusive statement about the impact of band structure and screening effects, however, cannot been drawn yet. The analysis of these effects requires precise, accompanying band structure calculations and refined transport models. Furthermore, improved measurements with a better counting statistic and better energy resolution (see next paragraph) are required in order to verify the observations on the one hand and in order to quantify the effects more accurately on the other hand.

5.3.4 Prospects for band structure resolved streaking

Reasonably resolving the band structure of a solid in the course of a streaking measurement requires better energy resolution. The uncertainty principal sets a fundamental limit for the achievable energy resolution with respect to the targeted time resolution. The broad excitation bandwidth required for sub-fs pulses in combination with the resolution of the instrumentation may obliterate any band structure effects in the streaking measurement. Using the same mirror as for the streaking experiment (see figure 5.4(b)) a broadband k-space image of the valence band of tungsten around the Fermi edge is recorded in the WAM mode and depicted in figure 5.17(c). Part (b) of the figure shows a calculated Fermi

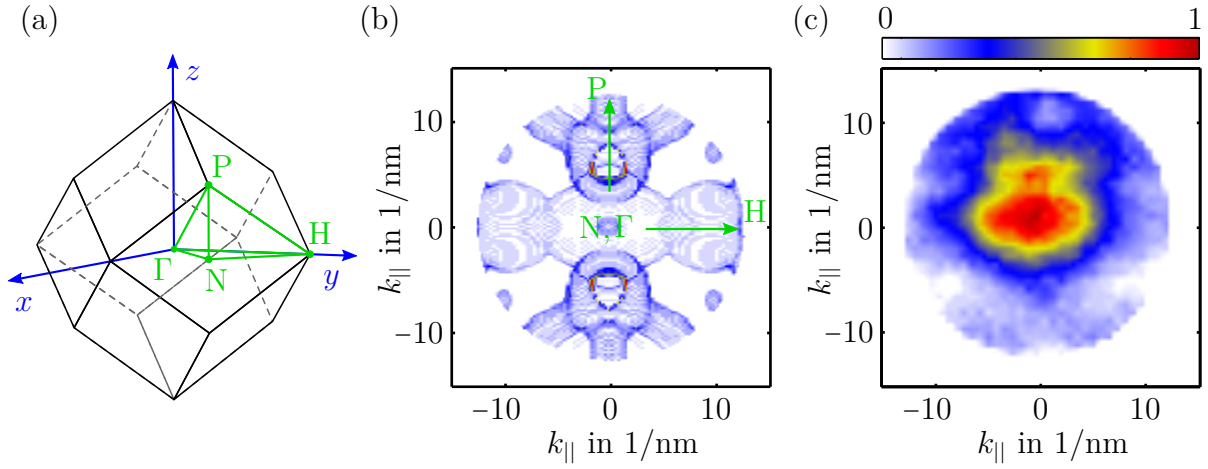

Figure 5.17: HHG XUV broadband Fermi surface imaging. (a): First Brillouin zone of bcc lattice with symmetry points. (b): Calculated Fermi surface of tungsten using the linear muffin-tin orbital method. The surface is projected onto the (110)-plane. (c): Projected Fermi surface measured with broadband (2.6 eV FWHM) XUV HHG radiation.

surface, projected onto the (110)-plane. Although the measured broadband image does not resolve any fine structure of the Fermi surface as given by the calculation, it vaguely reveals the symmetry of the Brillouin zone along the Γ,H- and ΓP-direction, demonstrating that prominent band structure features are still discernible to some extent. However, since these features are heavily smeared out they are expected to manifest as very subtle variations in the fine structure of the spectrogram, which finally imposes extremely high requirements on the signal-to-noise ratio of the streaking measurement. The statistics of the measurements conducted so far have been insufficient in order to provide spectrograms with the required quality. Additionally, space charge distortions induced by ATI electrons further impair the quality. For these reasons, a meaningful conclusion about the impact of band structure dispersion on the evolution of the electron wave-packet in the time domain and associated time delays derived from angle-resolved streaking measurements could not be made so far. Therefore, an improvement of energy resolution seems indispensable. First we examine the prospects for improving energy resolution from the instrumental side in order not to compromise time resolution. Energy resolution is generally increased by

dispersing the electrons stronger in time during their propagation within the drift tube of the spectrometer, which requires higher retardation ratios. The expected energy resolution, based on the analysis presented in section 3.2.6, as a function of the retardation ratio and kinetic energy is given in figure 5.18(c) and (d) for the LAD and WAM mode, respectively. It is evident from the plots that energy resolution is also improved by low-

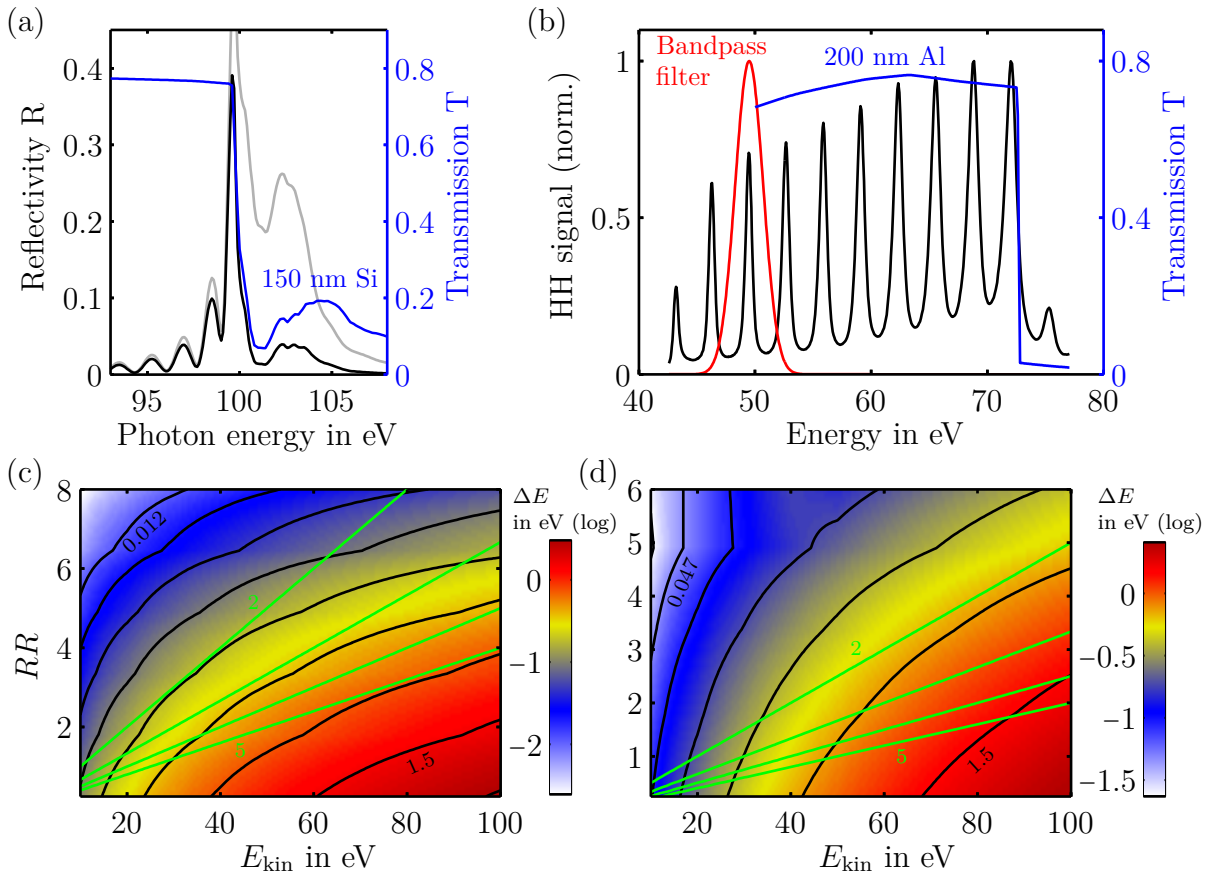

Figure 5.18: Concepts for improving energy resolution. (a): Spectral reflectivity of a Mo/Si multilayer mirror near the Si absorption edge at 100 eV (gray line). The bandwidth of the mirror can be reduced to about 500 meV in combination with an additional 150 nm thick Si foil (black line). (b): High harmonic spectrum generated with a 25 fs NIR (800 nm) driving pulse in neon. The spectral width of individual plateau harmonics is considerably below 1 eV. A single harmonic peak can be selected by an appropriate multilayer based bandpass filter. (c),(d): Contour plot of the theoretically expected energy resolution of the electron spectrometer in LAD (c) and WAM (d) mode for different lens settings and a realistic DLD time resolution of 250 ps. The value of subsequent black isolines is consecutively divided by 2. The green isolines represent the width of the energy window imaged by the corresponding lens settings in eV. They are plotted in steps of 1 eV.

ering the kinetic energy of the detection window. Limitations are finally set by residual magnetic stray field distortions and the minimum energy window required to record the

delay-dependent, NIR-field induced spectral modulation of the electron spectra without clipping important spectral features. According to the evaluation in section 3.2.6, electron energies down to $\sim$ 10 eV are not significantly affected by magnetic stray fields. In order to maintain a reasonable width of the energetic detection window the retardation ratio has to be reduced. Furthermore, the cutoff energy of the high harmonic spectrum has to be scaled down accordingly, depending on the binding energy of the electrons of interest.

In the case that a reduction of temporal resolution can be accepted, energy resolution is naturally improved by narrowing the excitation bandwidth. One option is to reduce the bandwidth of the multilayer based XUV bandpass filter. A large number of periods (bilayers) is required for this purpose as the relative bandwidth scales inversely proportional to the bilayer number. The effective number of periods experienced by the incident XUV radiation, however, is limited by the high absorptivity of the involved materials, restricting the minimum bandwidth achievable by multilayer mirrors. A minimum bandwidth of $\sim$ 500 meV near 100 eV central energy could be achieved by a Mo/Si multilayer design with extremely low gamma value (ratio of Mo thickness to bilayer thickness) containing 300 bilayers in which the thickness of the high-absorptive Mo-layer is reduced well below 1 nm [50]. The fabrication process of such a multilayer design is elaborate and requires an extremely precise and accurate control of the layer thickness. A practically more convenient alternative is to utilize a 'standard' design with less periods and a central energy in the vicinity of a sharp absorption edge of a foil filter which crops the reflection bandwidth of the mirror. A Mo/Si mirror design with 100 periods which exploits the L-absorption edge of Si at 99.6 eV, thereby reducing the effective bandwidth to $\sim$ 500 meV, is shown in figure 5.18(a). However, this method does not allow much flexibility regarding the choice of central excitation energy as the applicable photon energy is bound to the discrete energies of element-specific absorption edges. Moreover, as the reflectivity behavior of multilayer based bandpass filters is quite sensitive to the angle of incidence, even slight alignment errors of the incident angle are highly detrimental in this respect.
A second approach is to employ longer laser pulses to drive the HHG process, see figure 5.18(b). While the line width of the harmonic peaks may behave counter-intuitively when the process is driven by few-cycle pulses [39], it has been shown that for many-cycle driving pulses (30 fs at 800 nm) the line width significantly and monotonically decreases with increasing spectral distance to the cutoff energy [113]. In this case, alignment errors in the incident angle of the multilayer bandpass are less relevant, however, CEP related studies are not accessible any more.
Finally, the control of the instantaneous laser phase by chirping the pulse might provide another measure in order to improve energy resolution. Tuning the chirp of the driving NIR field allows the reduction of the harmonic line width compared to a chirp-free driving pulse, even for few-cycle pulses, as it has been shown in figure 4.7.

It is also noted that the streaking trace undergoes a fundamental structural change when the XUV excitation bandwidth is reduced, see figure 5.19. When the duration of the ionizing XUV pulse becomes comparable to, or longer than a half oscillation period of the

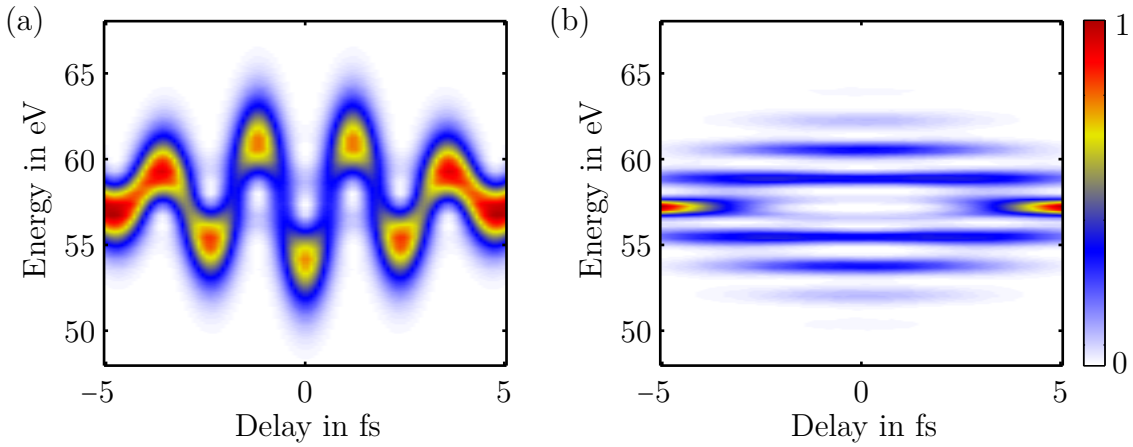

Figure 5.19: Transformation of the streaking trace for long XUV pulses. (a): Streaking trace for an excitation bandwidth of the photoemission process of 2.6 eV promoting 700 as XUV pulses in the Fourier-limit, calculated using equation 2.96. The electron wave packet is released into the electric field of a 5 fs long NIR pulse with a carrier wavelength of $\lambda_L = 720$ nm and an intensity of $6.5 \cdot 10^{10}$ W/cm^2. (b): Streaking trace for an excitation bandwidth of 500 meV. Quantum interference forms side bands which are separated by multiples of the laser photon energy.

NIR field, the streaking effect gradually vanishes and, instead, side bands at multiples of the laser photon energy are formed due to quantum interference between different parts of the same electron wave packet that receive identical momentum shift from the streaking field [36]. An accurate reconstruction of the electron wave-packet by the FROG-CRAB algorithm is not possible any more as this code relies on a number of approximations which are detrimental for such long XUV pulses. A more elaborate reconstruction using equation 2.94 could be in principle possible, but this requires considerably higher computational effort.

Chapter 6

Conclusion and outlook

In the first part of this work we presented the development of a novel, advanced HHG source which operates at an increased repetition rate of 10 kHz. This rate constitutes an improvement of a factor up to 10 compared to the predominant HHG sources which are driven by few-cycles pulses from multi-pass amplifiers. As the acquisition time in space-charge limited experiments conducted with femtosecond and sub-fs pulses scales in inverse proportion to the repetition rate, the increased rate marks an important step toward the feasibility of HHG based multi-dimensional photoelectron spectroscopy, circumventing the difficulties associated with long acquisition times such as laser drifts etc. Although the higher repetition rate is bought at the cost of a reduced pulse energy, we have demonstrated the generation of 5 fs few-cycle pulses by nonlinear compression in a hollow fiber and a subsequent high harmonic output with a cutoff energy beyond 130 eV and sufficient flux for photoemission spectroscopy, which is confirmed by the observation of the onset of space-charge limitations. While in the meanwhile a number of promising, alternative approaches for HHG at rates up to the MHz range have been conceived, the development of these sources is still in its infancy. As opposed to standard XUV beam monitors which directly image the XUV beam, we additionally employ an array of multilayer mirrors for a selection of the spectral range. This allows the simultaneous observation of the XUV beam profile, beam position, and yield only in the spectrally relevant region, greatly facilitating the optimization of XUV beam parameters for the experiment. The differential pumping section could be kept extremely compact and flexible due to the concept of a stacked sequence of interchangeable apertures within standard-sized vacuum pipes. In addition, a setup for HHG photoelectron spectroscopy with simultaneous sub-fs time-, angle- and CEP-resolution was developed. The concept of utilizing a ToF spectrometer with an angle resolving imaging lens, combined with a CEP-tagging method ensures an efficient, robust, and lossless data acquisition process. The single-shot phase meter for CEP tracking and the angle-resolving electron spectrometer have been successfully synchronized, enabling a reliable and correct assignment of entries in their data streams. The corresponding equipment has been characterized, as well as technical deficiencies identified and remediated.

A second achievement of this work is given by the successful implementation of a

multilayer-based XUV quarter wave plate, transforming linear into circular polarization. This approach could make circularly polarized HHG radiation widely available, as the majority of HHG sources today provide harmonic radiation with linear polarization. For highest transmission efficiency, it was fabricated as a free-standing foil, i.e. without additional support, with a total thickness less than 150 nm, featuring a large free aperture of 3 mm. While the fabrication of such ultra-thin, unsupported multilayer foils with reasonably good quality for practical applications has been questionable before, its feasibility is now proofed by the results of our spectral transmission and polarimetry measurement, confirming the (spectral) characteristics predicted by ab-initio simulations. In addition, natural imperfections in the foil flatness due to interface tension, leading to a wavy surface, are not destructive for the proper overall function of the wave plate, but merely induce a slight deviation from the simulated behavior. Although our analysis regarding the dispersion characteristics revealed that attosecond pulses can hardly be maintained after passing through the foil, its usability is not derogated for applications in the low-fs range. As a handy single-element device which fits in any standard 1-inch optics mount, it can be easily incorporated in any existing standard HHG beamline without any major constructional changes, upgrading it to circularly polarized radiation without deviating the original beam direction.

Finally, this work contributed to the advance of attosecond streaking spectroscopy by expanding the measurement scheme for angle- and CEP-resolution. The first application of this technique already demonstrated a number of useful and interesting implications: the sole evaluation of the laser vector potential from CEP- and angle-resolved streaking traces provides an absolute calibration gauge of the CEP for the stereographic ATI phase-meter, reveals the CEP-dependent phase-locking behavior of XUV pulses from the HHG process, and verifies the angle dependence of the streaking amplitude. Furthermore, the new streaking scheme delivers insight into the temporal evolution of the electron wave-packet as a function of CEP and emission angle, thereby uncovering a potential impact of solid state properties on the transport process of photo-emitted electrons in the time domain. An angle-dependent reconstruction of the electron wave-packet for a cosine NIR excitation pulse gives indication of a systematic broadening of the wave-packet duration from normal toward off-normal emission. Further measurements with improved counting statistics, and hence a better signal to noise ratio, are yet required to confirm this observation. Even higher repetition rates would be beneficial for this purpose. Nevertheless, the increased repetition rate of 10 kHz facilitated the first realization of such a multi-dimensional measurement. The mechanisms of systematic spectral line broadening have been discussed and the setup has been found to be quite sensitive to space charge blurring. The only way to reduce this type of distortion is the decrease of NIR intensity, which lowers the streaking amplitude and, therefore, requires appropriate energy resolution. Possible approaches for the improvement of the energy resolution have been presented, which may also enable real band-structure resolved streaking measurements in the near future. For a more detailed interpretation of the wave-packet structure, a reference streaking measurement from the gas phase or accurate HHG simulation models together with a precise knowledge of the

driving field properties are required in order to obtain the initially incident temporal XUV pulse structure. Such an experiment marks the next step and can now be easily conducted within the technical framework of the measurement infrastructure presented in this work.

Appendix A

Technical aspects of device synchronization for CEP-tagging

As already pointed out in section 3.2.8, the correct assignment of the entries between the data streams of the phase-meter and the electron spectrometer is extremely critical for a successful measurement due to the indeterministic noise fluctuations of the carrier-envelope offset frequency. The relative CEP of 200 consecutive laser pulses, as recorded with the ATI phase-meter, is shown in figure A.1(a) in which its random nature becomes evident.

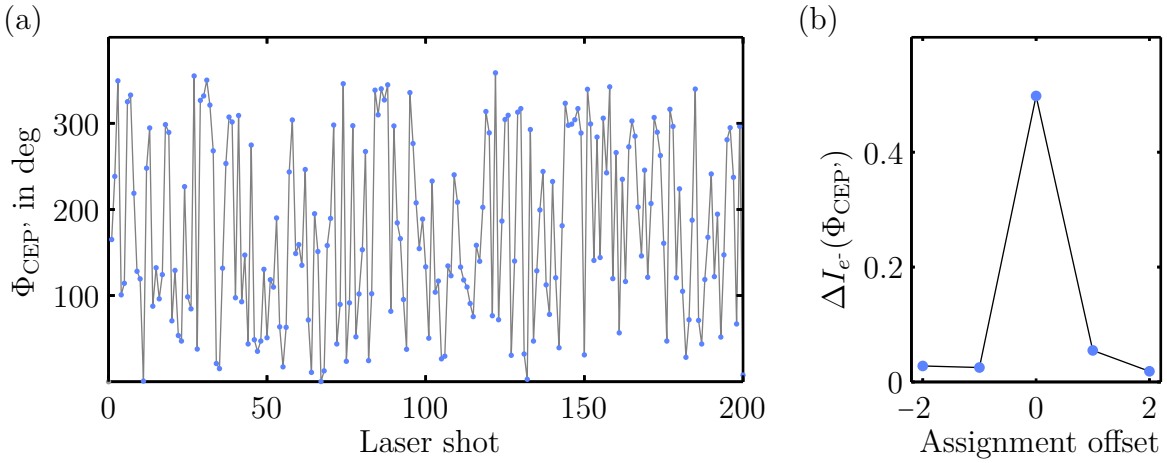

Figure A.1: Assignment offset between the data entries of the phase-meter and the electron spectrometer. (a): Relative CEP values for 300 consecutive laser shots. The random structure is evident. (b): Modulation depth of the CEP-dependent photoelectron signal as in figure 5.8. The modulation practically vanishes completely already for an assignment offset of ±1 due to the missing correlation of the CEP between consecutive laser shots.

Also shown is the behavior of the modulation strength of the CEP-dependent photoelectron signal (as plotted in figure 5.8) when the CEP list is shifted by an offset value (see figure 3.26) during the assignment process. Even for an assignment offset of ±1 the

modulation of the signal, and thus its CEP-dependence, completely disappears, confirming the absence of a temporal correlation between subsequent CEP values on the one hand, and explicitly demonstrating the drastic consequence of a potentially corrupted data list on the other hand. The latter turned out to be a real issue since the trigger recognition of the tag-input at the TDC unit was found to be unreliable for short trigger pulses. From the discussion above it is clear that even a single omitted trigger event at the position k in the data list with n entries lowers the CEP-dependence of the photoelectron signal by a factor k/n, which renders the dataset useless if $k \ll n$. Here, we investigate the cause of the problem and show the required measures to ensure a reliable and deterministic trigger recognition. Figure A.2(a) depicts the measured probability of recognizing the trigger signal as a function of its pulse width. Below a width of 13 ns, individual trigger events get lost. The reason for this failure was traced back to a trigger hold-off circuit which was

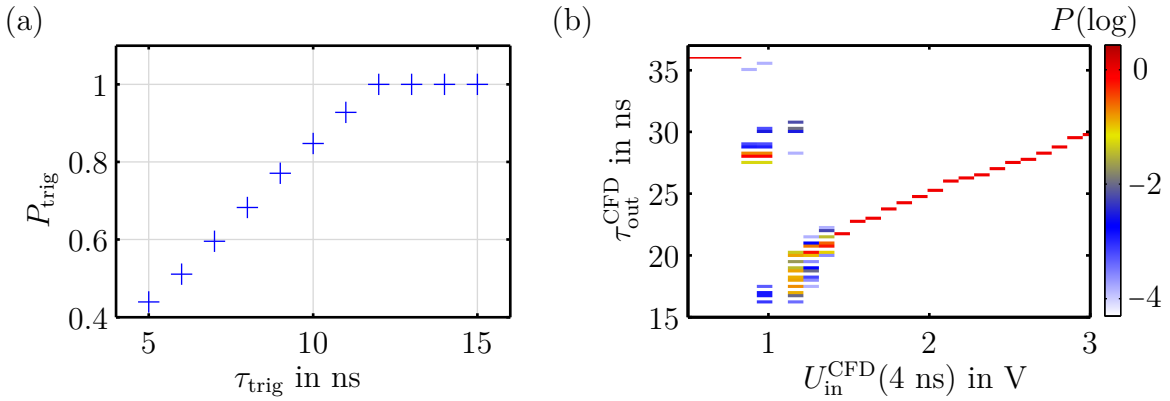

Figure A.2: Trigger pulse behavior of the CFD and TDC. (a): Probability for recognizing a rectangular trigger pulse (rise time < 1 ns) with an amplitude of $U_{\mathrm{trig}} = 4$ V at the tag-input of the TDC as a function of the pulse width. (b): Pulse width of the CFD output for a 4 ns input pulse (photo diode) as a function of input pulse amplitude.

originally intended to prevent any ringing at the rising pulse edge from incrementing the tag counter multiple times. A reinvestigation of the circuit revealed that a theoretical pulse width of 20 ns (two oscillation cycles of a reference clock) is required in order to ensure a 100% deterministic trigger recognition. The original output of the CFD, which provides the master trigger for the tagging setup (see figure 3.26), only delivers a pulse length of 4 ns. An additional circuit was implemented to extend the pulse width to 36 ns. However, it was found that this width is only stable when the pulse amplitude at the input is below a (pulse length-dependent) threshold value, see figure A.2(b). Above this threshold, the pulse width gets unstable and jitters, even ranging down to a critical width of 15 ns. Therefore, special care has to be taken that this threshold is not passed e.g. by intrinsic pulse fluctuations which are generated in the signal chain before the CFD input.

Appendix B

Time of flight filtering

The major advantage of the ToF spectrometer is its ability to intrinsically capture all electrons within the energy window of the lens system, avoiding data loss by parameter sweeps in order to scan through the desired energy range. As a side effect, most of the unwanted events, i.e. outside the energy window of interest, are also recorded. As a consequence of the chromatic imaging behavior of the electro-static lens system, a part of these electrons are focused onto the detector plane, depending on the lens adjustments. This situation is depicted in figure B.1(a) for the XUV harmonics and lens settings as used in the streaking measurements. The green shaded area indicates the useful energy range, which however only makes up a fraction of the totally collected spectrum. The majority of recorded events is formed by secondary electrons which may easily saturate the detector. In addition, a focal point is formed on the detector plane for electrons with a ToF around 140 ns. A particular problem concerning this issue arises for the streaking measurements. The NIR laser field itself generates numerous photoelectrons by multi-photon ionization. With typical NIR intensities of $\sim 10^{10} - 10^{11}$ W/cm^2 required for the streaking measurement, these additional ATI electrons can generate up to 10^4-10^5 detector events per second and are energetically positioned close to the focal point of the lens system, see figure B.1(b). As a consequence, these electrons saturate the detector on the one hand, leading to multi-hit artifacts. On the other hand, and even more destructive, the focused electron flux locally and permanently degrades the MCP gain, leading to a spatially inhomogeneous detector response. The latter is a result of the life-time characteristic of MCPs which strongly depends on the total amount of electric charge drawn from a MCP during operation. This charge-induced gain degradation is particularly pronounced for new MCPs. Figure B.2 shows the response of homogeneously illuminated MCPs after using them for 10 hours in streaking measurements according to section 5.3. The detection efficiency at the center of the MCPs has nearly dropped to zero. In order to avoid these deficiencies, a simple energy filter, consisting of a repelling anode made of a fine mesh of carbon-coated copper wire, has been installed in front of the MCPs. A corresponding retardation potential between the mesh and the MCP front prevents slow electrons from reaching the detector, see figure B.1(c). In this way, the inhomogeneous detector degradation and its saturation can be avoided. As a disadvantage, the effective

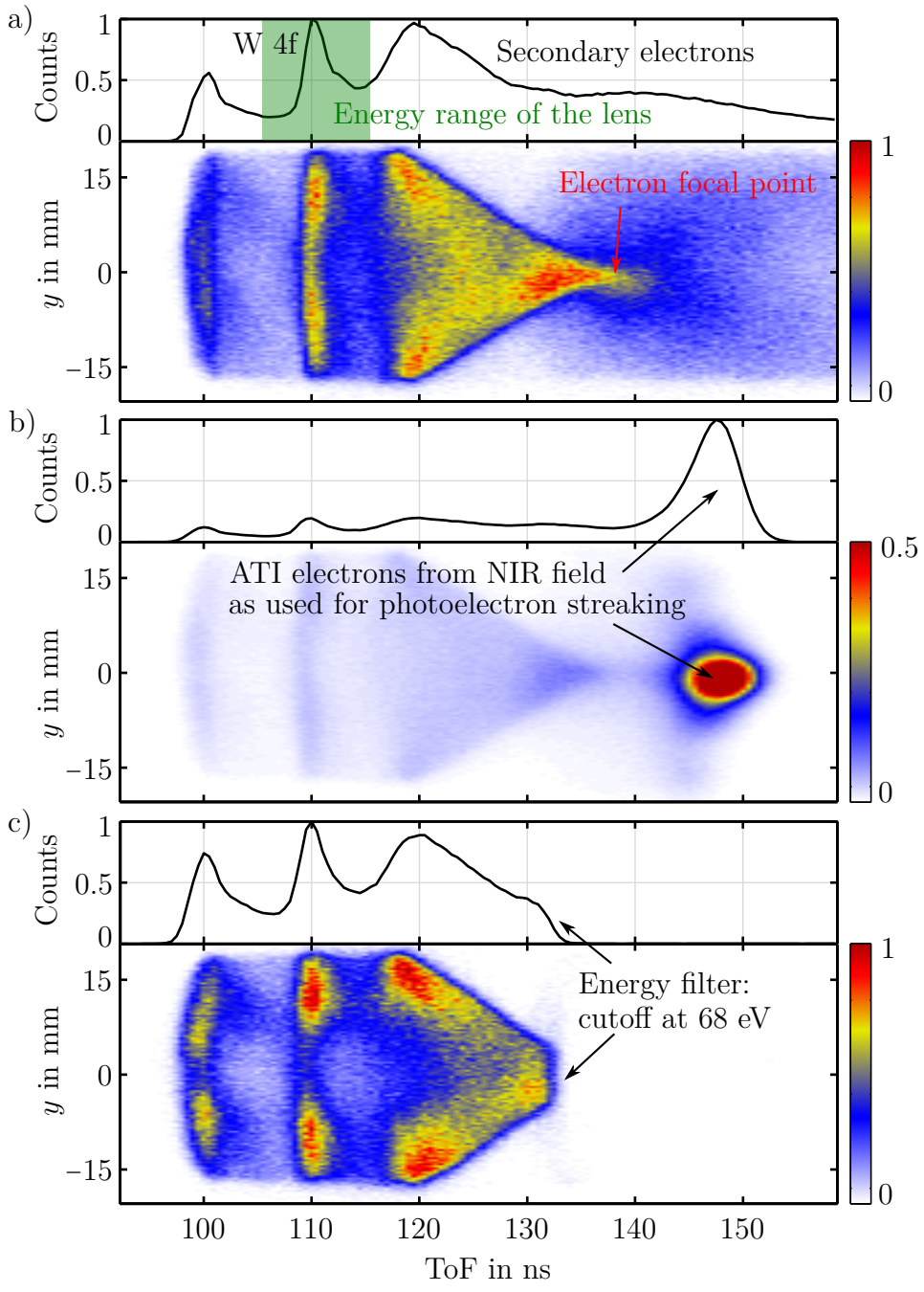

Figure B.1: ToF filtering. (a): Complete ToF spectrum of the XUV pulse as recorded for the streaking measurement. The adjusted energy window is shaded in green (lens adjustments: $U_{\mathrm{kin}} = 58$ V, $U_{\mathrm{pass}} = 100$ V). A focal point for a ToF of 140 ns is formed on the detector plane. (b): Spectrum with additional NIR beam. ATI electrons dominate the spectrum and are energetically located close to the focal point. (c): Energy-filtering prevents the ATI electrons from being recorded.

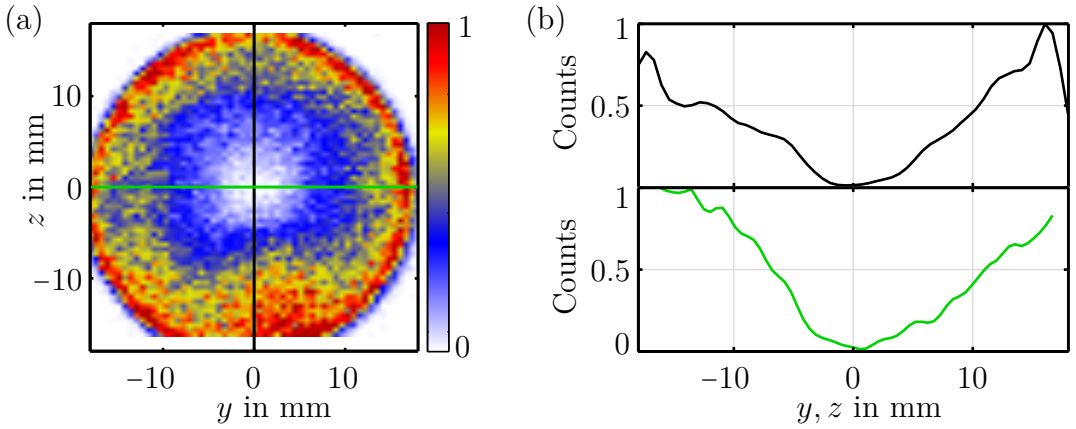

Figure B.2: Gain degradation in the MCP center due to a focused ATI electron background. (a): Inhomogeneous detector response after exposing it to focused ATI electrons for 10 hours in the streaking experiment. (b): Vertical and horizontal line-cuts. Signal amplification at the center has nearly dropped to zero.

signal rate on the detector is lowered by $\approx 20\%$ due to the limited trasmittance of the wire mesh. Moreover, this technique can only provide a cutoff-energy at the low-energy side of the spectrum. Although this setup works very well for streaking measurements, a more universal approach for future applications would be a fast gating unit, which however is more challenging to design.

Appendix C

Beam alignment concept

For the successful execution of a XUV-NIR pump-probe experiment, a multitude of components have to be accurately aligned to a well-defined beam path, see figure C.1(a). A special difficulty in this respect arises from the HHG focusing mirror, only providing a highly divergent NIR beam which is inevitably clipped by downstream components such as the apertures of the differential pumping system. From the remaining fraction of the beam, it is difficult to determine the central beam axis. Only the low-divergent XUV beam finally reveals the actual beam position. However, it is cumbersome to translate the beam once the HHG process is initiated, since it has to be assured that the orifice of the nozzle keeps always precisely aligned to the beam focus. It is easy, even by slight adjustments, to make the NIR beam strike the edge of the nozzle outlet, thereby inducing thermal effects in the nozzle material which can drastically depreciate the long-term stability of the high harmonic output (see section 4.1). Therefore, it is desirable to pre-align the NIR beam as good as possible before the HHG process is initiated. It is generally handy to establish a low-power alignment beam for basic alignment tasks. For this purpose, a HeNe-laser beam can be fed onto the NIR beam path. A telescope expands the beam size to match it with the NIR beam, imitating its focusing behavior for the HHG process. This is helpful to safely pre-align the gas nozzle to the lateral focus position. Moreover, the telescope can be detuned so that the beam is well collimated after the HHG focusing mirror, providing an easily discernible reference for the beam axis. The alignment concept which has been proven to be practical uses four alignment marks, see figure C.1. Two irises (reference 1 and 2) in front of the chirped mirror compressor define the beam path for a correct coupling condition into the compressor setup. The path after it is determined by a concentric striking position on the inner part of the double mirror. The proper beam position is adjusted and verified with the help of the beam monitoring setup at the ARPES chamber (see section 3.2.4) after the sample has been removed from the beam path. Finally, two additional alignment marks are set up to this beam reference. They are part of the XUV beam monitor unit, consisting of a retractable NIR mirror with precisely reproducible position which reflects the beam onto an alignment screen (reference 3a), and an in-vacuum iris (reference 3b) which is used for the alignment of the actual XUV beam and related XUV optics. These reference marks ensure a correct beam alignment through the vacuum

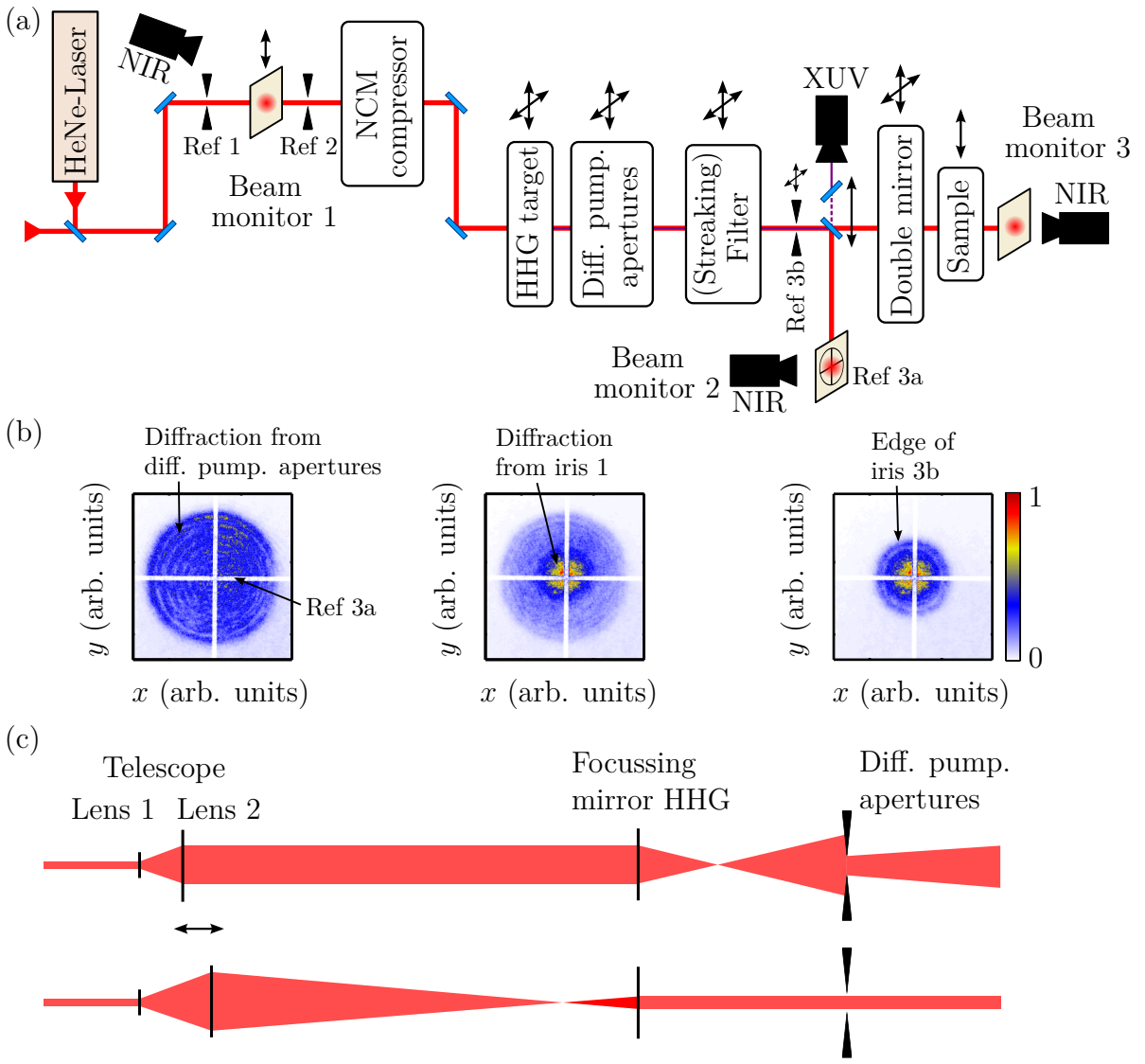

Figure C.1: (a): Schematic of the beam monitors and reference marks used to align the beam axis, apertures, and optics. (b): Diffraction patterns as recorded on beam monitor 2 assist the alignment process. Left: The apertures of the differential pumping system form thin diffraction rings. Middle: Diffraction from iris 1 reveals the position of the beam center. Right: The edge of the in-vacuum iris is used as a reference mark for the XUV beam. (c): A variable telescope optic allows the alignment beam to either emulate the size and divergence of the NIR beam or to provide a small-sized collimated beam downstream the vacuum-line.

system onto the double mirror, as the sole alignment of the beam onto reference 1 and 2 is not precise enough for this purpose. While aligning the NIR beam onto reference 1 and 2 is straightforward, it is tricky to do so for reference 3a. Fortunately, (parasitic) diffraction patterns can be used to determine the center of the beam axis with sufficient accuracy after the HHG focusing mirror. Diffraction rings which are generated by closing iris 1 can be

observed on the reference screen 3a. Their center mark the beam axis, provided the beam has been precisely aligned to the opening of iris 1 beforehand. This can be verified by an additional observation screen after iris 1. Also, this only works when the gas nozzle has been moved off the beam path as its small orifice acts a spatial filter which would smooth the beam profile again. The nozzle is finally moved in again at reduced beam power while the exact alignment of its orifice to the beam focus can be examined by reference 3a. This procedure already provides good alignment of the XUV beam, only requiring tiny adjustments for the fine tuning of its final beam axis. Reference mark 3b in combination with the XUV beam monitor is used for this purpose. Fine tuning of the nozzle position is finally performed by maximizing the XUV output. Additional XUV optics, such as the streaking filter, can now also be conveniently aligned by means of reference mark 3b.

Bibliography

[1] M. Abramowitz and I.A. Stegun: *Handbook of Mathematical Functions with Formulas, Graphs, and Mathematical Tables.* ninth dover printing, tenth gpo printing. Edition. Dover, New York, 1964.

[2] G.P. Agrawal: *Nonlinear fiber optics.* Academic press, San Diego, 2001.

[3] A.S. Alnaser, M. Kübel, R. Siemering, B. Bergues, N.G. Kling, K.J. Betsch, Y. Deng, J. Schmidt, Z.A. Alahmed, A.M. Azzeer, J. Ullrich, I. Ben-Itzhak, R. Moshammer, U. Kleineberg, F. Krausz, R. de Vivie-Riedle and M.F. Kling, *Nature Communications* **5** (2014), 3800.

[4] C. Altucci, R. Bruzzese, C. de Lisio, M. Nisoli, S. Stagira, S.D. Silvestri, O. Svelto, A. Boscolo, P. Ceccherini, L. Poletto, G. Tondello and P. Villoresi, *Phys. Rev. A* **61** (1999).

[5] M.V. Ammosov, N.B. Delone and V.P. Krainov, *Soviet Physics - JETP* **64** (1986), 1191.

[6] P. Antoine, B. Carré, A. L'Huillier and M. Lewenstein, *Physical Review A* **55** (1997), 1314.

[7] P. Antoine, A. L'Huillier, M. Lewenstein, P. Salières and B. Carré, *Phys. Rev. A* **53** (1996), 1725.

[8] A. Apolonski, P. Dombi, G.G. Paulus, M. Kakehata, R. Holzwarth, T. Udem, C. Lemell, K. Torizuka, J. Burgdörfer, T.W. Hänsch and F. Krausz, *Phys. Rev. Lett.* **92** (2004), 073902.

[9] A.L. Aquila, F. Salmassi, F. Dollar, Y. Liu and E. Gullikson, *Opt. Express* **14** (2006), 10073.

[10] A.S. Berman, *J. Appl. Phys.* **36** (1965), 3356.

[11] C. Boeglin, E. Beaurepaire, V. Halté, V. López-Flores, C. Stamm, N. Pontius, H.A. Dürr and J.Y. Bigot, *Nature* **465** (2010), 458.

[12] Á. Börzsönyi, Z. Heiner, A. Kovács, M.P. Kalashnikov and K. Osvay, *Opt. Express* **18** (2010), 25847.

[13] N. Böwering, T. Lischke, B. Schmidtke, N. Müller, T. Khalil and U. Heinzmann, *Phys. Rev. Lett.* **86** (2001), 1187.

[14] T. Brabec and F. Krausz, *Rev. Mod. Phys.* **72** (2000), 545.

[15] K.S. Budil, P. Salières, A. L'Huillier, T. Ditmire and M.D. Perry, *Phys. Rev. A* **48** (1993), R3437.

[16] N.H. Burnett, C. Kan and P.B. Corkum, *Phys. Rev. A* **51** (1995), R3418.

[17] H. Carstens, M. Högner, T. Saule, S. Holzberger, N. Lilienfein, A. Guggenmos, C. Jocher, T. Eidam, D. Esser, V. Tosa, V. Pervak, J. Limpert, A. Tünnermann, U. Kleineberg, F. Krausz and I. Pupeza, *Optica* **3** (2016), 366.

[18] A.L. Cavalieri, E. Goulielmakis, B. Horvath, W. Helml, M. Schultze, M. Fieß, V. Pervak, L. Veisz, V.S. Yakovlev, M. Uiberacker, A. Apolonski, F. Krausz and R. Kienberger, *New Journal of Physics* **9** (2007), 242.

[19] A.L. Cavalieri, N. Müller, T. Uphues, V.S. Yakovlev, A. Baltuška, B. Horvath, B. Schmidt, L. Blümel, R. Holzwarth, S. Hendel, M. Drescher, U. Kleineberg, P.M. Echenique, R. Kienberger, F. Krausz and U. Heinzmann, *Nature* **449** (2007), 1029.

[20] Z. Chang, A. Rundquist, H. Wang, I. Christov, H.C. Kapteyn and M.M. Murnane, *Phys. Rev. A* **58** (1998), R30.

[21] Z. Chang, A. Rundquist, H. Wang, M.M. Murnane and H.C. Kapteyn, *Phys. Rev. Lett.* **79** (1997), 2967.

[22] S.H. Chew, A. Gliserin, J. Schmidt, H. Bian, S. Nobis, F. Schertz, M. Kübel, Y.Y. Yang, B. Loitsch, T. Stettner, J.J. Finley, C. Späth, H. Ouacha, A.M. Azzeer and U. Kleineberg, *Applied Physics B* **122** (2016), 102.

[23] S.H. Chew, K. Pearce, S. Nobis, C. Späth, A. Spreen, S. Radünz, Y. Yang, J. Schmidt and U. Kleineberg: *Spatiotemporal characterization and control of lightfield nanolocalization on metallic nanostructures by nonlinear-PEEM*, In *Plasmonics: Metallic Nanostructures and Their Optical Properties X*, edited by M. I. Stockman. SPIE-Intl Soc Optical Eng (2012).

[24] S.H. Chew, K. Pearce, C. Späth, A. Guggenmos, J. Schmidt, F. Süßmann, M.F. Kling, U. Kleineberg, E. Mårsell, C.L. Arnold, E. Lorek, P. Rudawski, C. Guo, M. Miranda, F. Ardana, J. Mauritsson, A. L'Huillier and A. Mikkelsen: *Imaging Localized Surface Plasmons by Femtosecond to Attosecond Time-Resolved Photoelectron Emission Microscopy - "ATTO-PEEM"*. Wiley-Blackwell, 2015.

[25] S.H. Chew, F. Süßmann, C. Späth, A. Wirth, J. Schmidt, S. Zherebtsov, A. Guggenmos, A. Oelsner, N. Weber, J. Kapaldo, A. Gliserin, M.I. Stockman, M.F. Kling and U. Kleineberg, *Applied Physics Letters* **100** (2012), 051904.

[26] C.T. Chiang, A. Blättermann, M. Huth, J. Kirschner and W. Widdra, *Appl. Phys. Lett.* **101** (2012), 071116.

[27] S.B. Chikkamaranahalli, R.R. Vallance, B.N. Damazo and R.M. Silver. *Damping mechanisms for precision applications in UHV environment*, 2006.

[28] M. Chini, K. Zhao and Z. Chang, *Nature Photonics* **8** (2014), 178.

[29] I.P. Christov, J. Zhou, J. Peatross, A. Rundquist, M.M. Murnane and H.C. Kapteyn, *Phys. Rev. Lett.* **77** (1996), 1743.

[30] E. Constant, D. Garzella, P. Breger, E. Mével, C. Dorrer, C.L. Blanc, F. Salin and P. Agostini, *Phys. Rev. Lett.* **82** (1999), 1668.

[31] P.B. Corkum, *Phys. Rev. Lett.* **71** (1993), 1994.

[32] A. Damascelli, *Physica Scripta* **T109** (2004), 61.

[33] P. Dhez, *Nuclear Instruments and Methods in Physics Research Section A: Accelerators, Spectrometers, Detectors and Associated Equipment* **261** (1987), 66.

[34] P. Dombi, A. Apolonski, C. Lemell, G.G. Paulus, M. Kakehata, R. Holzwarth, T. Udem, K. Torizuka, J. Burgdörfer, T.W. Hänsch and F. Krausz, *New Journal of Physics* **6** (2004), 39.

[35] M. Drescher, *Science* **291** (2001), 1923.

[36] M. Drescher, M. Hentschel, R. Kienberger, M. Uiberacker, V. Yakovlev, A. Scrinzi, T. Westerwalbesloh, U. Kleineberg, U. Heinzmann and F. Krausz, *Nature* **419** (2002), 803.

[37] C.G. Durfee, A.R. Rundquist, S. Backus, C. Herne, M.M. Murnane and H.C. Kapteyn, *Phys. Rev. Lett.* **83** (1999), 2187.

[38] R.A.S. E. A. J. Marcatili, *Bell Syst Tech. J.* **43** (1964), 1783.

[39] J. Eden, *Progress in Quantum Electronics* **28** (2004), 197.

[40] M. Fieß, M. Schultze, E. Goulielmakis, B. Dennhardt, J. Gagnon, M. Hofstetter, R. Kienberger and F. Krausz, *Review of Scientific Instruments* **81** (2010), 093103.

[41] J. Gagnon, E. Goulielmakis and V. Yakovlev, *Applied Physics B* **92** (2008), 25.

[42] M. Geissler, G. Tempea and T. Brabec, *Phys. Rev. A* **62** (2000).

[43] E. Goulielmakis, M. Schultze, M. Hofstetter, V.S. Yakovlev, J. Gagnon, M. Uiberacker, A.L. Aquila, E.M. Gullikson, D.T. Attwood, R. Kienberger, F. Krausz and U. Kleineberg, *Science* **320** (2008), 1614.

[44] E. Goulielmakis, V.S. Yakovlev, A.L. Cavalieri, M. Uiberacker, V. Pervak, A. Apolonski, R. Kienberger, U. Kleineberg and F. Krausz, *Science* **317** (2007), 769.

[45] A. Guggenmos, M. Hofstetter, R. Rauhut, C. Späth, S. Hertrich, B. Nickel, S. Yang, E.M. Gullikson, J. Schmidt, M. Seibald, W. Schnick, F. Krausz and U. Kleineberg: *Broadband multilayer mirror and diffractive optics for attosecond pulse shaping in the 280-500 eV photon energy range*, In *XVIIIth International Conference on Ultrafast Phenomena*, edited by M. Chergui, A. Taylor, S. Cundiff, R. de Vivie-Riedle and K. Yamagouchi, Volume 41. EDP Sciences (2013) Page 01011.

[46] A. Guggenmos, M. Jobst, M. Ossiander, S. Radünz, J. Riemensberger, M. Schäffer, A. Akil, C. Jakubeit, P. Böhm, S. Noever, B. Nickel, R. Kienberger and U. Kleineberg, *Optics Letters* **40** (2015), 2846.

[47] A. Guggenmos, S. Radünz, R. Rauhut, M. Hofstetter, S. Venkatesan, A. Wochnik, E.M. Gullikson, S. Fischer, B. Nickel, C. Scheu and U. Kleineberg, *Opt. Express* **22** (2014), 26526.

[48] A. Guggenmos, R. Rauhut, M. Hofstetter, S. Hertrich, B. Nickel, J. Schmidt, E.M. Gullikson, M. Seibald, W. Schnick and U. Kleineberg, *Opt. Express* **21** (2013), 21728.

[49] A. Guggenmos, J. Schmidt, S. Heinrich, B. Nickel, F. Krausz and U. Kleineberg: *Multilayer Mirrors for VUV-XUV Attosecond Pump-Probe Experiments*, In *Frontiers in Optics 2015*. The Optical Society (2015).

[50] E.M. Gullikson, C.N. Anderson, S.S. Kim, D. Lee, R. Miyakawa, F. Salmassi and P.P. Naulleau, *Appl. Opt.* **54** (2015), 4280.

[51] S. Hädrich, A. Klenke, J. Rothhardt, M. Krebs, A. Hoffmann, O. Pronin, V. Pervak, J. Limpert and A. Tünnermann, *Nature Photonics* **8** (2014), 779.

[52] F. Helbing, G. Steinmeyer, J. Stenger, H. Telle and U. Keller, *Applied Physics B* **74** (2002), 35.

[53] B. Henke, E. Gullikson and J. Davis, *Atomic Data and Nuclear Data Tables* **54** (1993), 181.

[54] M. Hentschel, R. Kienberger, C. Spielmann, G.A. Reider, N. Milosevic, T. Brabec, P. Corkum, U. Heinzmann, M. Drescher and F. Krausz, *Nature* **414** (2001), 509.

[55] M. Hofstetter, M. Schultze, M. Fieß, B. Dennhardt, A. Guggenmos, J. Gagnon, V.S. Yakovlev, E. Goulielmakis, R. Kienberger, E.M. Gullikson, F. Krausz and U. Kleineberg, *Opt. Express* **19** (2011), 1767.

[56] K. Holldack, J. Bahrdt, A. Balzer, U. Bovensiepen, M. Brzhezinskaya, A. Erko, A. Eschenlohr, R. Follath, A. Firsov, W. Frentrup, L.L. Guyader, T. Kachel, P. Kuske, R. Mitzner, R. Müller, N. Pontius, T. Quast, I. Radu, J.S. Schmidt, C. Schüßler-Langeheine, M. Sperling, C. Stamm, C. Trabant and A. Föhlisch, *J Synchrotron Radiat* **21** (2014), 1090.

[57] S. Hüfner: *Photoelectron Spectroscopy*, Volume 2. Springer-Verlag, Berlin, 1996.

[58] N. Ishii, K. Kaneshima, K. Kitano, T. Kanai, S. Watanabe and J. Itatani, *Nature Communications* **5** (2014).

[59] N.G. Johnson, O. Herrwerth, A. Wirth, S. De, I. Ben-Itzhak, M. Lezius, B. Bergues, M.F. Kling, A. Senftleben, C.D. Schröter, R. Moshammer, J. Ullrich, K.J. Betsch, R.R. Jones, A.M. Sayler, T. Rathje, K. Rühle, W. Müller and G.G. Paulus, *Phys. Rev. A* **83** (2011), 013412.

[60] C. Kan, C.E. Capjack, R. Rankin and N.H. Burnett, *Phys. Rev. A* **52** (1995), R4336.

[61] S. Kazamias, S. Daboussi, O. Guilbaud, K. Cassou, D. Ros, B. Cros and G. Maynard, *Phys. Rev. A* **83** (2011).

[62] A.K. Kazansky and P.M. Echenique, *Phys. Rev. Lett.* **102** (2009).

[63] L.V. Keldysh, *Soviet Physics JETP* **20** (1965), 1307.

[64] O. Kfir, P. Grychtol, E. Turgut, R. Knut, D. Zusin, D. Popmintchev, T. Popmintchev, H. Nembach, J.M. Shaw, A. Fleischer, H. Kapteyn, M. Murnane and O. Cohen, *Nature Photonics* **9** (2014), 99.

[65] R. Kienberger, E. Goulielmakis, M. Uiberacker, A. Baltuska, V. Yakovlev, F. Bammer, A. Scrinzi, T. Westerwalbesloh, U. Kleineberg, U. Heinzmann, M. Drescher and F. Krausz, *Nature* **427** (2004), 817.

[66] H. Kimura, T. Miyahara, Y. Goto, K. Mayama, M. Yanagihara and M. Yamamoto, *Review of Scientific Instruments* **66** (1995), 1920.

[67] M. Kitzler, N. Milosevic, A. Scrinzi, F. Krausz and T. Brabec, *Phys. Rev. Lett.* **88** (2002).

[68] M.F. Kling and M.J. Vrakking, *Annual Review of Physical Chemistry* **59** (2008), 463.

[69] S. Koke, C. Grebing, H. Frei, A. Anderson, A. Assion and G. Steinmeyer, *Nature Photonics* **4** (2010), 462.

[70] J. Kortright and A. Fischer-Colbrie, *J. Appl. Phys.; (United States)* **61:3** (1987).

[71] J. Kortright and J. Underwood, *Nuclear Instruments and Methods in Physics Research Section A: Accelerators, Spectrometers, Detectors and Associated Equipment* **291** (1990), 272.

[72] E.E. Krasovskii, *Phys. Rev. B* **84** (2011).

[73] F. Krausz and M. Ivanov, *Reviews of Modern Physics* **81** (2009), 163.

[74] M. Krebs, S. Hädrich, S. Demmler, J. Rothhardt, A. Zaïr, L. Chipperfield, J. Limpert and A. Tünnermann, *Nature Photonics* **7** (2013), 555.

[75] M. Krüger, M. Schenk, M. Förster and P. Hommelhoff, *J. Phys. B: At. Mol. Opt. Phys.* **45** (2012), 074006.

[76] M. Krüger, M. Schenk and P. Hommelhoff, *Nature* **475** (2011), 78.

[77] M. Kübel, A.S. Alnaser, B. Bergues, T. Pischke, J. Schmidt, Y. Deng, C. Jendrzejewski, J. Ullrich, G.G. Paulus, A.M. Azzeer, U. Kleineberg, R. Moshammer and M.F. Kling, *New Journal of Physics* **16** (2014), 065017.

[78] M. Kübel, K.J. Betsch, N.G. Kling, A.S. Alnaser, J. Schmidt, U. Kleineberg, Y. Deng, I. Ben-Itzhak, G.G. Paulus, T. Pfeifer, J. Ullrich, R. Moshammer, M.F. Kling and B. Bergues, *New Journal of Physics* **16** (2014), 033008.

[79] K.C. Kulander, *Progress in Crystal Growth and Characterization of Materials* **33** (1996), 193.

[80] C. La-O-Vorakiat, M. Siemens, M.M. Murnane, H.C. Kapteyn, S. Mathias, M. Aeschlimann, P. Grychtol, R. Adam, C.M. Schneider, J.M. Shaw, H. Nembach and T.J. Silva, *Phys. Rev. Lett.* **103** (2009).

[81] D.E. Laban, A.J. Palmer, W.C. Wallace, N.S. Gaffney, R.P.M.J.W. Notermans, T.T.J. Clevis, M.G. Pullen, D. Jiang, H.M. Quiney, I.V. Litvinyuk, D. Kielpinski and R.T. Sang, *Phys. Rev. Lett.* **109** (2012).

[82] C. Lemell, B. Solleder, K. Tőkési and J. Burgdörfer, *Phys. Rev. A* **79** (2009).

[83] M. Lewenstein, P. Balcou, M.Y. Ivanov, A. L'Huillier and P.B. Corkum, *Phys. Rev. A* **49** (1994), 2117.

[84] H. Li, B. Mignolet, G. Wachter, S. Skruszewicz, S. Zherebtsov, F. Süßmann, A. Kessel, S.A. Trushin, N.G. Kling, M. Kübel, B. Ahn, D. Kim, I. Ben-Itzhak, C.L. Cocke, T. Fennel, J. Tiggesbäumker, K.H. Meiwes-Broer, C. Lemell, J. Burgdörfer, R.D. Levine, F. Remacle and M.F. Kling, *Phys. Rev. Lett.* **114** (2015), 123004.

[85] Q. Liao and U. Thumm, *Phys. Rev. Lett.* **112** (2014).

[86] Q. Liao and U. Thumm, *Phys. Rev. A* **89** (2014).

[87] X. Liu, H. Rottke, E. Eremina, W. Sandner, E. Goulielmakis, K.O. Keeffe, M. Lezius, F. Krausz, F. Lindner, M.G. Schätzel, G.G. Paulus and H. Walther, *Phys. Rev. Lett.* **93** (2004), 263001.

[88] Y. Liu, G. Bian, T. Miller and T.C. Chiang, *Phys. Rev. Lett.* **107** (2011).

[89] F. Lücking, A. Assion, A. Apolonski, F. Krausz and G. Steinmeyer, *Optics Letters* **37** (2012), 2076.

[90] W.W. M. Wutz, H. Adam: *Theorie und Praxis der Vakuumtechnik*. Friedr. Vieweg und Sohn Verlagsgesellschaft mbH, Braunschweig, 1986.

[91] E. Magerl, S. Neppl, A. Cavalieri, E. Bothschafter, M. Stanislawski, T. Uphues, M. Hofstetter, U. Kleineberg, J. Barth, D. Menzel, F. Krausz, R. Ernstorfer, R. Kienberger and P. Feulner, *The Review of scientific instruments* **82** (2011), 063104.

[92] D. Marcuse: *Theory of optical electric waveguides*. Academic press, San Diego, 1991.

[93] Y. Matsuura, M. Saito, M. Miyagi and A. Hongo, *Journal of The Optical Society of America A-optics Image Science and Vision* **6** (1989), 423.

[94] R.G. Musket, W. McLean, C.A. Colmenares, D.M. Makowiecki and W.J. Siekhaus, *Applied Surface Science* **10** (1982), 143.

[95] S. Neppl: *Attosecond Time-Resolved Photoemission from Surface and Interfaces*. Technical University of Munich, PhD thesis, 2012.

[96] S. Neppl, R. Ernstorfer, E.M. Bothschafter, A.L. Cavalieri, D. Menzel, J.V. Barth, F. Krausz, R. Kienberger and P. Feulner, *Phys. Rev. Lett.* **109** (2012).

[97] S. Neppl, R. Ernstorfer, A.L. Cavalieri, C. Lemell, G. Wachter, E. Magerl, E.M. Bothschafter, M. Jobst, M. Hofstetter, U. Kleineberg, J.V. Barth, D. Menzel, J. Burgdörfer, P. Feulner, F. Krausz and R. Kienberger, *Nature* **517** (2015), 342.

[98] R.K. Nubling and J.A. Harrington, *Optical Engineering* **37** (1998), 2454.

[99] M. Okano, K. Kajimura, S. Wakiyama, F. Sakai, W. Mizutani and M. Ono, *Journal of Vacuum Science and Technology A* **5** (1987), 3313.

[100] W.A. Okell, T. Witting, D. Fabris, C.A. Arrell, J. Hengster, S. Ibrahimkutty, A. Seiler, M. Barthelmess, S. Stankov, D.Y. Lei, Y. Sonnefraud, M. Rahmani, T. Uphues, S.A. Maier, J.P. Marangos and J.W.G. Tisch, *Optica* **2** (2015), 383.

[101] A.I. Oliva, M. Aguilar and V. Sosa, *Measurement Science and Technology* **9** (1998), 383.

[102] A.I. Oliva, V. Sosa, R. de Coss, R. Sosa, N.L. Salazar and J.L. Penã, *Review of Scientific Instruments* **63** (1992), 3326.

[103] C.H. Park and S.G. Louie, *Phys. Rev. Lett.* **109** (2012).

[104] S. Passlack, S. Mathias, O. Andreyev, D. Mittnacht, M. Aeschlimann and M. Bauer, *Journal of Applied Physics* **100** (2006).

[105] G.G. Paulus, F. Lindner, H. Walther, A. Baltuška, E. Goulielmakis, M. Lezius and F. Krausz, *Phys. Rev. Lett.* **91** (2003), 253004.

[106] K. Pearce, R. Dehde, A. Spreen, C. Späth, M. Wendl, J. Schmidt and U. Kleineberg: *Modulation of extraordinary optical transmission through nanohole arrays using ultrashort laser pulses*, In *Nanophotonics VI*, edited by D. L. Andrews, J.-M. Nunzi and A. Ostendorf. SPIE-Intl Soc Optical Eng (2016).

[107] A. Pietzsch, A. Föhlisch, M. Beye, M. Deppe, F. Hennies, M. Nagasono, E. Suljoti, W. Wurth, C. Gahl, K. Döbrich and A. Melnikov, *New Journal of Physics* **10** (2008), 033004.

[108] B. Piglosiewicz, S. Schmidt, D.J. Park, J. Vogelsang, P. Groß, C. Manzoni, P. Farinello, G. Cerullo and C. Lienau, *Nature Photonics* **8** (2013), 37.

[109] T. Popmintchev, M.C. Chen, P. Arpin, M.M. Murnane and H.C. Kapteyn, *Nature Photonics* **4** (2010), 822.

[110] T. Popmintchev, M.C. Chen, A. Bahabad, M. Gerrity, P. Sidorenko, O. Cohen, S. Backus, X. Zhang, G. Taft, I.P. Christov, M.M. Murnane and H.C. Kapteyn: *Phase Matching of High Harmonic Generation in the Soft and Hard X-Ray Regions of the Spectrum*, In *Advances in Optical Sciences Congress*. The Optical Society (2009).

[111] T. Popmintchev, M.C. Chen, D. Popmintchev, P. Arpin, S. Brown, S. Alisauskas, G. Andriukaitis, T. Balciunas, O.D. Mucke, A. Pugzlys, A. Baltuska, B. Shim, S.E. Schrauth, A. Gaeta, C. Hernandez-Garcia, L. Plaja, A. Becker, A. Jaron-Becker, M.M. Murnane and H.C. Kapteyn, *Science* **336** (2012), 1287.

[112] A. Poppe, R. Holzwarth, A. Apolonski, G. Tempea, C. Spielmann, T. Hänsch and F. Krausz, *Applied Physics B* **72** (2001), 373.

[113] E. Priori, G. Cerullo, M. Nisoli, S. Stagira, S.D. Silvestri, P. Villoresi, L. Poletto, P. Ceccherini, C. Altucci, R. Bruzzese and C. de Lisio, *Physical Review A* **61** (2000).

[114] I. Pupeza, S. Holzberger, T. Eidam, H. Carstens, D. Esser, J. Weitenberg, P. Rußbüldt, J. Rauschenberger, J. Limpert, T. Udem, A. Tünnermann, T.W. Hänsch, A. Apolonski, F. Krausz and E. Fill, *Nature Photonics* **7** (2013), 608.

[115] K. Rabinovitch, L.R. Canfield and R.P. Madden, *Appl. Opt.* **4** (1965), 1005.

[116] T. Rathje, N.G. Johnson, M. Möller, F. Süßmann, D. Adolph, M. Kübel, R. Kienberger, M.F. Kling, G.G. Paulus and A.M. Sayler, *Journal of Physics B: Atomic, Molecular and Optical Physics* **45** (2012), 074003.

[117] J. Rauschenberger, T. Fuji, M. Hentschel, A.J. Verhoef, T. Udem, C. Gohle, T.W. Hänsch and F. Krausz, *Laser Phys. Lett.* **3** (2006), 37.

[118] P. Rudawski, A. Harth, C. Guo, E. Lorek, M. Miranda, C.M. Heyl, E.W. Larsen, J. Ahrens, O. Prochnow, T. Binhammer, U. Morgner, J. Mauritsson, A. L'Huillier and C.L. Arnold, *The European Physical Journal D* **69** (2015).

[119] P. Salières, P. Antoine, A. de Bohan and M. Lewenstein, *Phys. Rev. Lett.* **81** (1998), 5544.

[120] P. Salières, A. L'Huillier and M. Lewenstein, *Phys. Rev. Lett.* **74** (1995), 3776.

[121] A.M. Sayler, T. Rathje, W. Müller, C. Kürbis, K. Rühle, G. Stibenz and G.G. Paulus, *Opt. Express* **19** (2011), 4464.

[122] A.M. Sayler, T. Rathje, W. Müller, K. Rühle, R. Kienberger and G.G. Paulus, *Optics Letters* **36** (2010), 1.

[123] F. Schäfers, H.C. Mertins, A. Gaupp, W. Gudat, M. Mertin, I. Packe, F. Schmolla, S. Di Fonzo, G. Soullié, W. Jark, R. Walker, X. Le Cann, R. Nyholm and M. Eriksson, *Appl. Opt.* **38** (1999), 4074.

[124] M. Schmid and P. Varga, *Ultramicroscopy* **42** (1992), 1610.

[125] J. Schmidt, S.H. Chew, A. Gliserin, A. Guggenmos, J. Zou and U. Kleineberg. *Carrier-Envelope phase tagged and angle-resolved photoelectron streaking.* In preparation, to be submitted in Applied Physics Letters.

[126] J. Schmidt, A. Guggenmos, S.H. Chew, A. Gliserin, M. Hoegner, J. Zou, C. Spaeth and U. Kleineberg. *Development of a 10 kHz High Harmonic Source up to 140 eV Photon Energy for Ultrafast Time-, Angle- and Phase-Resolved Photoelectron Emission Spectroscopy on Solid Targets.* Submitted to Rev. Sci. Instr.

[127] J. Schmidt, A. Guggenmos, S.H. Chew, A. Gliserin and U. Kleineberg: *Carrier-Envelope-Phase- and Angle-resolved Photoelectron Streaking Measurements on W(110)*, In *Conference on Lasers and Electro-Optics.* The Optical Society (2016).

[128] J. Schmidt, A. Guggenmos, M. Hofstetter, S.H. Chew and U. Kleineberg, *Opt. Express* **23** (2015), 33564.

[129] C.M. Schneider, M.S. Hammond, P. Schuster, A. Cebollada, R. Miranda and J. Kirschner, *Phys. Rev. B* **44** (1991), 12066.

[130] M. Schultze, E.M. Bothschafter, A. Sommer, S. Holzner, W. Schweinberger, M. Fiess, M. Hofstetter, R. Kienberger, V. Apalkov, V.S. Yakovlev, M.I. Stockman and F. Krausz, *Nature* **493** (2012), 75.

[131] M. Schultze, M. Fiess, N. Karpowicz, J. Gagnon, M. Korbman, M. Hofstetter, S. Neppl, A.L. Cavalieri, Y. Komninos, T. Mercouris, C.A. Nicolaides, R. Pazourek, S. Nagele, J. Feist, J. Burgdorfer, A.M. Azzeer, R. Ernstorfer, R. Kienberger, U. Kleineberg, E. Goulielmakis, F. Krausz and V.S. Yakovlev, *Science* **328** (2010), 1658.

[132] G. Schütz, M. Knülle and H. Ebert, *Physica Scripta* **1993** (1993), 302.

[133] M.D. Seaberg, D.E. Adams, E.L. Townsend, D.A. Raymondson, W.F. Schlotter, Y. Liu, C.S. Menoni, L. Rong, C.C. Chen, J. Miao, H.C. Kapteyn and M.M. Murnane, *Opt. Express* **19** (2011), 22470.

[134] M.P. Seah and W.A. Dench, *Surface and Interface Analysis* **1** (1979), 2.

[135] H.J. Shin, D.G. Lee, Y.H. Cha, K.H. Hong and C.H. Nam, *Phys. Rev. Lett.* **83** (1999), 2544.

[136] D.A. Shirley, *Physical Review B* **5** (1972), 4709.

[137] A.W. Snyder: *Optical waveguide theory.* Chapmann and Hall, London, 1983.

[138] A. Sommer, E.M. Bothschafter, S.A. Sato, C. Jakubeit, T. Latka, O. Razskazovskaya, H. Fattahi, M. Jobst, W. Schweinberger, V. Shirvanyan, V.S. Yakovlev, R. Kienberger, K. Yabana, N. Karpowicz, M. Schultze and F. Krausz, *Nature* **534** (2016), 86.

[139] Surface Concept GmbH. *Product information sheet, DLD-3636 3D imaging detector* (2016).

[140] Z. Tao, C. Chen, T. Szilvasi, M. Keller, M. Mavrikakis, H. Kapteyn and M. Murnane, *Science* **353** (2016), 62.

[141] H. Telle, G. Steinmeyer, A. Dunlop, J. Stenger, D. Sutter and U. Keller, *Applied Physics B* **69** (1999), 327.

[142] G. Tempea, M. Geissler, M. Schnürer and T. Brabec, *Phys. Rev. Lett.* **84** (2000), 4329.

[143] H. Tokutaka, N. Ishihara, K. Nishimori, S. Kishida and T. Takabuchi, *Japanese Journal of Applied Physics* **29** (1990), 2512.

[144] X.M. Tong and S.I. Chu, *Phys. Rev. A* **58** (1998), R2656.

[145] S. Tougaard, *Surface Science* **216** (1989), 343.

[146] B. Vodungbo, A.B. Sardinha, J. Gautier, G. Lambert, C. Valentin, M. Lozano, G. Iaquaniello, F. Delmotte, S. Sebban, J. Lüning and P. Zeitoun, *Opt. Express* **19** (2011), 4346.

[147] H. Wang, M. Chini, E. Moon, H. Mashiko, C. Li and Z. Chang, *Optics Express* **17** (2009), 12082.

[148] Y. Wang and N. Gedik, *Phys. Status Solidi RRL* **7** (2013), 64.

[149] W.B. Westerveld, K. Becker, P.W. Zetner, J.J. Corr and J.W. McConkey, *Appl. Opt.* **24** (1985), 2256.

[150] M. Wieland, C. Spielmann, U. Kleineberg, T. Westerwalbesloh, U. Heinzmann and T. Wilhein, *Ultramicroscopy* **102** (2005), 93.

[151] A. Wirth, R. Santra and E. Goulielmakis, *Chemical Physics* **414** (2013), 149.

[152] T. Wittmann, B. Horvath, W. Helml, M.G. Schätzel, X. Gu, A.L. Cavalieri, G.G. Paulus and R. Kienberger, *Nat Phys* **5** (2009), 357.

[153] V.S. Yakovlev, J. Gagnon, N. Karpowicz and F. Krausz, *Phys. Rev. Lett.* **105** (2010).

[154] K. Zakeri, T. Peixoto, Y. Zhang, J. Prokop and J. Kirschner, *Surface Science* **604** (2010), L1.

[155] A. Zangwill: *Physics at Surfaces*. Cambridge University Press (CUP), 1988.

[156] C.H. Zhang and U. Thumm, *Phys. Rev. Lett.* **102** (2009).

[157] C.H. Zhang and U. Thumm, *Phys. Rev. Lett.* **103** (2009).

[158] K. Zhao, Q. Zhang, M. Chini, Y. Wu, X. Wang and Z. Chang, *Optics Letters* **37** (2012), 3891.

[159] S. Zherebtsov and Others, *Nature Phys.* **7** (2011), 656.

[160] X. Zhou, R. Lock, W. Li, N. Wagner, M.M. Murnane and H.C. Kapteyn, *Phys. Rev. Lett.* **100** (2008).

[161] X. Zhou, R. Lock, N. Wagner, W. Li, H.C. Kapteyn and M.M. Murnane, *Phys. Rev. Lett.* **102** (2009).

[162] M. Zürch, J. Rothhardt, S. Hädrich, S. Demmler, M. Krebs, J. Limpert, A. Tünnermann, A. Guggenmos, U. Kleineberg and C. Spielmann, *Sci. Rep.* **4** (2014), 7356.

Acknowledgments

The success of this work would not have been possible without the contribution and the support of many people. First of all, I'd like to thank my supervisor Prof. Dr. Ulf Kleineberg for giving me the chance to work in an excellent scientific infrastructure and an unique professional environment. He was always open to new suggestions and ideas and supported me with the realization of new concepts. I could steadily refine my ability to work independently and could also assume responsibility by the supervision of several diploma, master and bachelor projects. Moreover, as a teaching assistant, I could actively contribute to the scientific knowledge transfer to students. By his support to join renowned international conferences, I was given the chance to keep up-to-date on cutting-edge research fields and to present latest results to an international audience of specialists.
Additionally, I cordially thank my colleagues Soo Hoon Chew, Alexander Guggenmos, Christian Späth, Kellie Pearce, Huaihai Pan and Stephan Heinrich for their support in any aspect of this work, for numerous lively and interesting discussions on scientific, technical and personal topics and for the great teamwork. Special thanks goes to Soo Hoon Chew and Alexander Gliserin for providing the framework of the phase-tagging software and for always giving useful advice on programming issues. In addition, I thank the diploma, master and bachelor students who have been under my supervision, for their various valuable contributions to the progress of the experiments.
I'm also deeply grateful to Marcus Ossiander, Johann Riemensberger and Martin Schultze for their numerous tips and tricks on the preparation and execution of the streaking measurement. Furthermore I'd like to thank Klaus Franke for helping me with a lot of administrative work as well as Johannes Wulz, Rolf Öhm and the mechanical workshop team for their assistance in mechanical engineering issues and their permanent efforts to realize the fabrication of many different types of specialized parts within a short time frame. Finally, my thanks goes to all other people who supported me in various aspects but who have not been mentioned by name, and to the entire team of the 'Munich Advanced Photonics' group for the great time and the successful collaboration.